(2)

Final Report

MECHANICS OF COMPOSITE MATERIALS FOR SPACECRAFT

by

George J. Dvorak, Mark S.Shephard
and
Yehia A.Bahei–El–Din

Rensselaer Polytechnic Institute
Department of Civil & Environmental Engineering
and
Center for Composite Materials and Structures
Troy, New York 12180–3590

Submitted to

Mechanics Division
Office of Naval Research
800 North Quincy Street
Arlington, Virginia 22217

Contract Number N00014–85–K–0733

July 1992

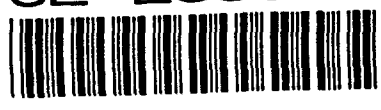

TABLE OF CONTENTS

ABSTRACT

This report presents the work performed under ONR contract number N00014–85–K–0733 during the period 1985–1990. The main objective of the project was to develop a computational facility for inelastic analysis of fibrous composite materials based on micromechanics. The theoretical work focused on development of micromechanical models for thermoplastic and thermoviscoplastic fibrous composites based on experimental observations of certain phenomena found in unreinforced and fiber reinforced metals. Implementation of the material models in computational procedures for analysis of composite materials and structures was an important part of the research. Accomplishments in these areas and in development of a layer–wise composite shell element, also performed under this contract, are described.

1. INTRODUCTION

The main goal of this research is the development of a computational facility for thermoplastic and thermoviscoplastic analysis of fibrous composite materials, and for design of composite structures for spacecraft applications. To achieve this goal, the research included formulation of a continuum plasticity theory based on micromechanics for unidirectionally reinforced fibrous composites subjected to coupled thermal and mechanical loads which simulate service conditions. A unified thermoviscoplasticity theory based on overstress was also developed, in part under this project, for homogeneous materials to represent the matrix and fiber phases. This theory can be applied to the phases of any micromechanical model to obtain the local stresses and overall response of unidirectionally reinforced composites. Subsequently, our research focused on implementation of the material models in nonlinear finite element procedures which permits analysis of more complex geometries of composite structures such as laminated plates and shells. Throughout the development of our numerical analysis procedures, the ABAQUS finite element code has represented the basic analysis engine into which our numerical formulations has been added. Standard elements available in ABAQUS have been used in conjunction of our material models to examine certain phenomena in fibrous composites such as dimensional stability under thermal and mechanical loads. In parallel, our efforts concentrated on development of new elements suitable for particular fibrous composite structures such as laminated shells.

The following accomplishments were achieved:

- Development of constitutive equations and numerical procedures for the Periodic Hexagonal Array (PHA) model.
- Development of constitutive equations and numerical procedures for the bimodal plasticity theory.

- Development of a thermoviscoplasticity theory with time recovery effects for homogeneous materials.
- Implementation of the PHA model, the bimodal theory, and the viscoplasticity constitutive equations into the ABAQUS finite element code.
- Development of a layer–wise composite shell element.

Details of these developments are described in the sequel.

2. THERMOPLASTICITY OF FIBROUS COMPOSITE MATERIALS

Evaluation of the overall properties and local fields in fibrous composites with elastic–plastic phases under thermomechanical loads was achieved with appropriate micromechanical models which can incorporate the inelastic constitutive relations that describe phase behavior, and which reflect the dominant deformation mechanisms in the microstructure. The selection of models which satisfy these requirements was motivated by our past experience with modeling of experimentally observed elastic–plastic behavior of fibrous B/Al composite systems (Dvorak et al., 1988, 1990). In particular, the periodic hexagonal array (PHA) model (Dvorak and Teply, 1985; Teply and Dvorak, 1988), and the bimodal plasticity theory (Dvorak and Bahei–El–Din, 1987) were chosen and adapted for this purpose.

In the PHA model, the centers of the aligned fibers are assumed to be arranged in a periodic hexagonal array in the transverse plane. The circular cross sections of the fibers are approximated by $(6 \times n)$ polygonal cross sections, which tend to converge rapidly when the integer $n \geq 1$ increases. The hexagonal array is divided into identical unit cells. Appropriate periodic boundary conditions are prescribed for these cells such that the solution for a single cell can be used to generate the deformation field in a fibrous composite subjected to uniform overall strains or stresses, and to a uniform thermal change. Typically, the solution is found with the finite element method for a selected subdivision of the unit cell.

The bimodal plasticity theory was originally deduced, in part, from experimental observations of elastic–plastic behavior of unidirectional B/Al systems. More recently, it was applied to several high–temperature systems, and extended to accommodate viscoplastic behavior of the matrix phase (Hall 1990). The theory recognizes two distinct deformation modes, the fiber–dominated (FDM) and the matrix–dominated (MDM) mode. In the fiber mode, the local fields in the composite are assumed to be approximately

uniform, and the overall response is evaluated from an averaging model. In the matrix mode, the dominant mode of deformation is approximated by smooth shearing on planes parallel to the fiber axis. Each of the two modes has a separate branch of the overall yield surface, and is activated according to the current position of the loading vector. The size and shape of the MDM yield surface does not depend on fiber properties and volume fraction, but these parameters do affect the FDM surface. In systems reinforced with fibers of high longitudinal shear modulus, such as boron, silicon carbide, or tungsten, the FDM surface contains a large part of the MDM surface which in turn controls the onset of yielding, and subsequent plastic flow. In contrast, systems reinforced with carbon fibers of low shear modulus may have a FDM surface which lies entirely within the MDM branch. The matrix mode is not present in such systems, but the FDM model assumptions may no longer hold and the PHA model is again indicated.

The material models described above were further developed and implemented in the ABAQUS finite element program. The work performed in this part of the contract developed into a Ph.D. dissertation (Wu, 1991). Implementation of material models into nonlinear finite element procedures and description of both the PHA model and the bimodal plasticity theory together with the procedures for their implementation in the ABAQUS program are contained in Chapters 2, 3 and 4 in Wu (1991) which appear here in Appendices A, B and C, respectively.

3. THERMOVISCOPLASTICITY OF FIBROUS COMPOSITE MATERIALS

This part of the program is concerned with modeling of the rate–dependent behavior of fibrous composites under thermomechanical loads. There are two major tasks, modeling of constituent viscoplastic behavior of the phases, and prediction of the resulting overall response.

Selection of the constitutive theory for modeling of matrix and fiber response was motivated by several requirements which were found useful in predictions of inviscid response of metal matrix composites. These include, in part, a definition of equilibrium yield surface, and ability to accommodate various hardening rules which may be indicated by experiments. Such ingredients are found, for example, in the viscoplasticity theory developed by Eisenberg and Yen (1981) which was selected for our work, albeit in a substantially modified form that includes rate effects, coupled thermal and mechanical loads, and time recovery. Since the local stress or strain path in the phases is generally nonproportional, the modifications were developed in the context of the two–surface plasticity theory motivated, in part, by the work of Dafalias and Popov (1976). The resulting phase constitutive equations include material parameters which are found by matching the results of certain experiments at room temperature, and at high temperatures (Bahei–El–Din et al. 1991, Shah 1991).

Modeling of the composite response was based again on existing models which were developed in our earlier work. In particular, we implemented the new viscoplastic constitutive equations into the ABAQUS finite element program and made comparisons with experiments using the Periodic Hexagonal Array model. The theoretical developments as well as the numerical results have been published by Bahei–El–Din, Shah and Dvorak (1991), which appear here in Appendix D, and by Shah (1991).

4. ANALYSIS OF LAYERED COMPOSITE SHELLS

Since most composite structures have one dimension which is substantially smaller than the other two, it is desirable to employ a spatial discretization assumption which reduces the amount of computation needed in the small dimension. This dimensional reduction process is particularly complex in the case of laminated structures constructed form thin orthotropic layers. This process is further complicated when lamina level nonlinear material behavior must be considered. One way to derive formulations for the behavior of shells is to apply specific kinematic constraints to the full three–dimensional elasticity equations. This 'degeneration' of the three–dimensional elasticity equations is the basis for many shell formulations. A common kinematic assumption on the behavior of shells is that the in–plane displacement components vary linearly in the thickness direction. In particular, if we assume a linear variation through the thickness of the in–plane displacement quantities in each layer (equivalently, constant transverse shear strains in each layer) we arrive at a first–order discrete layer theory. In this formulation, if we neglect the generally small direct strain in the thickness direction, there are 2N+3 displacement parameters through the thickness, where N is the number of layers, which can be a significant reduction compared to 3–D modeling.

A discrete layer theory element, called LCSLFC, was developed by K. Dorninger (1991) as part of this project. It employs C^0 linear segments for the through the thickness deformation of each layer. The LCSLFC element is based on the degeneration principle. The element is a 16–noded shell using cubic shape functions for the in–plane displacement quantities. Full account for large deformations were included in the formulation. The implementation of the LCSLFC element allows considerable flexibility in modeling composite laminates. The shell thickness may be varied through each element. Each layer may have a different orientation, thickness and material. A user defined material is incorporated into the element to allow the use of various nonlinear material modes.

Specific studies (Shephard and Beall, 1992) have been performed using this element formulation with the bimodal plasticity model in the analysis of simple composite structures. Details of relevant studies performed in this part of the project appear in Appendices G, H, and I.

5. APPLICATIONS

To demonstrate the capabilities of the methods developed for inelastic analysis of fibrous composites, we present here two applications. In the first application, the dimensional stability of metal matrix composite laminates under thermal fluctuations and thermomechanical load cycles is examined. The system considered as a model material is a Gr/Al $(\pm\varphi)_s$ laminate. The analysis is performed by the finite–element method while the underlying constitutive equations of unidirectional composites are provided by the Periodic Hexagonal Array (PHA) micromechanical model. A computationally more efficient and equally accurate method based on fiber–dominated analysis of unidirectional composites by the self–consistent method is also presented. The results show that laminates of the model system with $\varphi = 12^\circ$ are dimensionally stable in the elastic range when subjected to pure temperature changes. Plastic deformation of the matrix causes permanent dimensional changes, which can be reduced by heat treatment of the composite. Under thermomechanical loads, $(\pm\varphi)_s$ laminates are not in general dimensionally stable. Dimensional stability of the laminate was enhanced by plastic deformation of the matrix for in–phase thermal and mechanical load cycles and reduced for out–of–phase cycles. The results of this study are found in Bahei–El–Din et al. (1992) and appear here in Appendix E.

The second application considers the effect of thermomechanical loads on local fields in fibrous composites. Here, the local stresses caused by mechanical and thermal loads in high temperature intermetallic matrix composites are evaluated using a finite element solution for a periodic hexagonal array microstructure. Both uncoated and coated elastic fibers are considered. The matrix is assumed to be elastic–plastic and insensitive to loading rates. Mechanical properties of the phases are function of temperature. It was found that a CVD deposited carbon coating can be quite effective in reducing thermal stresses at the matrix/coating interface. Certain mechanical stress concentration factors,

however, may be aggravated by the compliant coating. In composite systems with a ductile matrix, plastic deformations reduce stress concentration and lead to stress redistribution. In such systems, thermomechanical loading regimes can be designed to reduce adverse local stresses introduced during fabrications, for example, by hot isostatic pressing. Details of this study have been published by Bahei–El–Din and Dvorak (1991) and appear here in Appendix F.

ACKNOWLEDGEMENT

This work was monitored by Dr. Yapa Rajapakse, who provided encouragement and useful technical suggestions.

REFERENCES

Bahei–El–Din, Y.A. and Dvorak, G.J., (1991), "Local Fields in Uncoated and Coated High Temperature Fibrous Composite Systems," Damage and Oxidation Protection in High Temperature Composites, G.K. Haritos and O.O. Ochoa, Editors, AD–Vol. 25–2, pp. 21–34.

Bahei–El–Din, Y.A., Dvorak. G.J. and Wu, J.F., (1992), "Dimensional Stability of Metal Matrix Laminates," Composites Science and Technology, Vol. 43, pp. 207–219.

Bahei–El–Din, Y.A., Shah, R.S. and Dvorak, G.J., (1991), "Numerical Analysis of the Rate–Dependent Behavior of High Temperature Fibrous Composites," Mechanics of Composites at Elevated and Cryogenic Temperatures, S.N. Singhal, W.F. Jones, C.T. Herakovich and T. Cruse, Editors AMD–Vol. 118, pp. 67–78.

Dafalias, Y.F. and Popov, E.P., (1976), "Plastic Internal Variable Formalism of Cyclic Plasticity," ASME J. Appl. Mech., Vol. 43, p. 645.

Dorninger, K., (1991), "A Nonlinear Layered Shell Finite Element with Improved Transverse Shear Behavior," SCOREC Report #3.

Dvorak, G.J. and Bahei–El–Din, Y.A. (1987), "A Bimodal Plasticity Theory of Fibrous Composite Materials," Acta Mechanica, Vol. 69, p. 219.

Dvorak, G.J., Bahei–El–Din, Y.A., Macheret, Y., and Liu, C.H., (1988), "An Experimental Study of Elastic–Plastic Behavior of a Fibrous Boron–Aluminum Composite," J. Mech. Phys. Solids, Vol. 36, p. 655.

Dvorak, G.J., Bahei–El–Din, Y.A., Shah, R.S., and Nigam, H., (1990), "Experiments and Modeling in Plasticity of Fibrous Composites," in Inelastic Deformation of Composite Materials, G.J.. Dvorak, Editor, Springer–Verlag, New York, Inc., pp. 270–293.

Dvorak, G.J. and Teply, J.L., (1985), "Periodic Hexagonal Array Models for Plasticity of Composite Materials," Plasticity Today: Modeling, Methods and Application, W. Olszak Memorial Vol., A. Sawczuk and V. Blanchi, Editors, Elsevier, p. 623.

Eisenberg, M.A. and Yen, C.F., (1981), "A Theory of Multiaxial Anisotropic Viscoplasticity," ASME J. Appl. Mech., Vol. 48, p. 276.

Hall, R., (1990), "Bimodal Viscoplasticity in Fibrous Metal–Matrix Composite Materials,", Ph.D. Dissertation, Rensselaer Polytechnic Institute, Troy, New York.

Shah, R.S., (1991), "Modeling and Analysis of High–Temperature Inelastic Deformation in Metal–Matrix Composites," Ph.D. Dissertation, Rensselaer Polytechnic Institute, Troy, New York.

Shephard, M.S. and Beall, M.S., (1992), "Analysis Idealization Control for Composite Materials with Nonlinear Behavior," in Computer Aided Design in Composite Material Technology III, pp. 313–330.

Teply, J.L. and Dvorak, G.J., (1988), "Bounds on Overall Instantaneous Properties of Elastic–Plastic Composites," J. Mech. Phys. Solids, Vol. 36, p. 29.

Wu, J.F., (1991), "Numerical Techniques for Elastic–Plastic Analysis of Fibrous Metal Matrix Composites," Ph.D. Dissertation, REnsselaer Polytechnic Institute, Troy, New York.

LIST OF PUBLICATIONS

Bahei–El–Din, Y.A. and Dvorak, G.J., (1988), "Plastic Deformation Behavior of Fibrous Composite Materials," Proceedings of the 4th Japan–U.S. Conference on Composite Materials, Washington, D.S., June 27–29, Technomic Publishing Co., Inc., pp. 118–127.

Bahei–El–Din, Y.A. and Dvorak, G.J., (1989), "New Results in Bimodal Plasticity of Fibrous Composite Materials," Advances in Plasticity 1989, edited by A.S. Khan and M. Tokuda, Pergamon Press, pp. 121–127.

Bahei–El–Din, Y.A. and Dvorak, G.J., (1989), "A Review of Plasticity Theory of Fibrous Composite Materials," Metal Matrix Composites: Testing, Analysis and Failure Modes, ASTM STP 1032, edited by W.S. Johnson, American Society for Testing and Materials, Philadelphia, pp. 103–129.

Bahei–El–Din, Y.A., Dvorak, G.J. and Shah, R.S., (1989), "Numerical Analysis of the Elastic–Plastic Behavior of Fibrous Metal Matrix Composites," Computational Experiments, edited by W.K. Liu, P. Smolinski, R. Ohayon, J. Navickas, and J. Gvildys, ASME PVP, Vol 176, pp. 125–131.

Bahei–El–Din, Y.A., Dvorak. G.J. and Wu, J.F., (1992), "Dimensional Stability of Metal Matrix Laminates," Composites Science and Technology, Vol. 43, pp. 207–219.

Bahei–El–Din, Y.A., Shah, R.S. and Dvorak, G.J., (1991), "Numerical Analysis of the Rate–Dependent Behavior of High Temperature Fibrous Composites," Mechanics of Composites at Elevated and Cryogenic Temperatures, S.N. Singhal, W.F. Jones, C.T. Herakovich and T. Cruse, eds., ASME AMD–Vol. 118, pp. 67–78.

Beall, M.W. and Shephard, M.S., (1991), "Advanced Finite Element Formulations for Composite Shells," in Proceedings of the American Society of Composites 6th Technical Conference on Composites, pp. 360–369.

Beall, M.W., Wu, J.F., and Shephard, M.S., (1991), "Lamina Level Nonlinear Composite Mixing Models in Finite Element Computations," Enhancing Analysis Techniques for Composite Materials, J.N. Reddy, Ed., ASME, New York, pp. 197–200.

Dorninger, K., (1990), "Post–Failure Analysis of Layered Composite Shells by Finite Element Analysis," Proceedings of the ABAQUS Users' Conference, Hibbitt, Karlsson & Sorensen, Inc., Providence, RI, pp. 149–164.

Dvorak, G.J., (1991), "Plasticity Theories for Fibrous Composite Materials," Metal Matrix Composites, Vol. 2, Mechanisms and Properties, R.K. Everett and R.J. Arsenault, eds., Academic Press, Boston, pp. 1–77.

Dvorak, G.J., and Bahei–El–Din, Y.A., (1987), "A Bimodal Plasticity Theory of Fibrous Composite Materials," Acta Mechanica, Vol. 69, pp. 219–241.

Dvorak, G.J., Bahei–El–Din, Y.A., Shah, R.S. and Nigam, H., (1990), "Experiments and Modeling in Plasticity of Fibrous Composites," Inelastic Deformation of Composite Materials, edited by G.J. Dvorak, Springer–Verlag, New York, Inc., pp. 270–293.

Hall, R., (1989), "Bimodal Viscoplasticity in Fibrous Metal–Matrix Composite Materials," Proceedings of the American Society of Composites Symposium on High Temperature Composites, June 13–15, 1989, Dayton, Ohio.

Lambropoulos, N.D., Wu, J.F., Shephard, M.S., Sternstein, S.S. and Dvorak, G.J. (1988), "Composite Material Models in ABAQUS," ABAQUS User's Conference Proceedings, HKS, Providence, Rhode Island, pp. 211–226.

Shephard, M.S., Baehmann, P.L., Georges, M.K., and Korngold, E.V., (1990), "Framework for Reliable Generation and Control of Analysis Idealizations," Computer Methods in Applied Mechanics and Engng., Vol. 82, pp. 257–280.

Shephard, M.S. and Beall, M.W., (1992), "Analysis Idealization Control for Composite Materials with Nonlinear Materials," Computer Aided Design in Composite Material Technology III, S.G. Advani, W.R. Blain, W.P. de Wilde, J.W. Gillespie, Jr. and O.H. Griffin, Jr., Eds., Computational Mechanics Pub. and Elsevier Applied Science, pp. 313–330.

Wu, J.F., (1991), "Numerical Techniques for Elastic–Plastic Analysis of Fibrous Metal Matrix Composites," Ph.D. Dissertation, Civil Engineering, Rensselaer Polytechnic Institute, Troy, NY.

Wu, J.F., Bahei–El–Din, Y.A, Dvorak, G.J. and Shephard, M.S., (1990), "A Bimodal Plasticity Model for Fibrous Composites Implemented in ABAQUS – I. Fiber–Dominated Mode," Proceedings of the ABAQUS Users' Conference, Hibbitt, Karlsson & Sorensen, Inc., pp. 519–528.

Wu, J.F., Shephard, M.S., Dvorak, G.J., and Bahei–El–Din, Y.A., (1989), "A Material Model for the Finite Element Analysis of Metal Matrix Composite," Composites Science and Technology, Vol. 35, pp. 347–366.

LIST OF PRESENTATIONS

Presentations by Dr. Dvorak

University of California, Los Angeles Short Course on "Metal and Ceramic Composites – Basic Science and Industrial Applications," (coordinator and lecturer), Los Angeles, California, February 3–7, 1986.

NASA–Langley Research Center Seminar, February 18, 1986.

Upstate New York Regional Student Conference, ASCE, lecture, March 1, 1986.

SDIO–IST Program Review, Washington, DC, March 7, 1986.

Midwestern Mechanics Seminar:
University of Michigan, April 9, 1986
University of Wisconsin, April 10, 1986
University of Minnesota, April 11, 1986
Michigan State University, April 29, 1986

Colloquium, Northwestern University, May 2, 1986.

ONR Workshop on Failure Mechanics, University of Maryland, May 12–13, 1986.

"Analysis of Fatigue Cracking of Fibrous Metal Matrix Laminates," General Electric Company, Seminar, May 14, 1986.

DARPA Site Visit Presentation, May 27, 1986.

SDIO/ONR Composite Consortium Program Review, Woods Hole, Massachusetts, June 2–3, 1986.

Tenth United States National Congress of Applied Mechanics, ASME, Austin, Texas, June 16–20, 1986.

Short Course on "Metal Matrix Composites," (program director and lecturer), Columbia, Maryland, June 23–27, 1986.

IUTAM Symposium on "Thermomechanical Couplings in Solids," invited lecturer, Paris, France, September 1–5, 1986.

Colloquium, Texas A&M University, November 11, 1986.

Colloquium, Rice University, November 12, 1986.

ASME Winter Annual Meeting, invited lecturer, Anaheim, California, December 7–12, 1986.

NASA Site Visit Presentation, December 18–19, 1986.

DARPA Workshop, Santa Barbara, California, January 5–9, 1987.

Applied Mechanics Seminar, Yale University, January 21, 1987.

NASA–MRC Program Review, January 26, 1987.

Symposium in Memory of Aris Phillips, Gainesville, Florida, January 28–30, 1987.

Seminar, University of California at Berkeley, February 23, 1987.

University of California, Los Angeles Short Course on "Metal and Ceramic Composites – Basic Science and Industrial Applications," (coordinator and lecturer), Los Angeles, California, February 23–26, 1987.

ONR Workshop on Composite Materials – Interface Science, Leesburg, Virginia, March 11, 1987.

ONR/SDI Review on Mechanics of Composites, University of Maryland, March 30, 1987.

Solid Mechanics Seminar, Brown University, April 5, 1987.

Lawrence Livermore Laboratories, Livermore, California, Mechanics Seminar, April 23, 1987.

RPI/DARPA–HiTASC Retreat, Lake Luzerne, New York, May 12, 1987.

Alcoa Laboratories Centennial Technical Seminar on Mechanics: Micromechanics to Product Design, Hilton Head, South Carolina, June 7, 1987.

Army Mechanics Conference, West Point, New York, June 15, 1987. Opening Lecture.

SDIO/IST Advanced Composites Program Review, Woods Hole, Massachusetts, June 23, 24, 1987.

DARPA Materials Research Council Meeting on High Temperature Composites, La Jolla, California, July 13–15, 1987.

Presentation for DARPA–HiTASC Program, monitor Steve Fishman, August 13, 1987.

Society of Engineering Science 24th Annual Meeting, Salt Lake City, Utah, 3 papers, September 20–23, 1987.

NASA–MRC Program Review, October 7, 1987.

Air Force Mechanics of Composites Review, Ft. Lauderdale, Florida, October 16, 1987.

Short Course on "Metal Matrix Composites," (program director and lecturer), Marina del Rey, California, October 26–30, 1987.

Industrial Research Institute Visit, November 19, 1987.

Aeritalia Visit, "The Mechanics of Metal Matrix Composites," December 10, 1987. Rensselaer Polytechnic Institute, Troy, New York.

ASME Winter Annual MEeting, Boston, Massachusetts, 2 lectures, December 14–15, 1987.

Gordon Research Conference, "Plasticity Effects in Metal Matrix Composites," (DARPA) Ventura, California, January 11–15, 1988.

Evandale Aircraft Plant Site Visit, (DARPA) Evandale, Ohio, February 19, 1988.

Short Course on Metal Matrix Composites, Los Angeles, California, February 22–26, 1988.

Rensselaer Composites Center Overview '88, "Plasticity and Fracture of Composite Materials," March 2, 1988.

NASA Site Visit, Center for Advanced Engineering Materials and Structures for Space Applications, March 30, 1988.

ASTM Symposium on Metal Matrix Composites: Testing, Analysis and Failure Modes, "Plasticity Theory of Fibrous Composite Materials," (presentation made by Y.A. Bahei–El–Din), Reno, Nevada, April 1988.

ABAQUS User's Conference, "Composite Material Models in ABAQUS," (presentation made by M. Shephard), Newport, Rhode Island, June 1988.

IST/SDIO/ONR Woods Hole Review, "Dimensional Stability of Metal Matrix Laminates," Woods Hole, Massachusetts, June 13–14, 1988.

Symposium on Mechanics of Composite Materials 1988, First Joint Summer Meeting of the Applied Mechanics Division of ASME and Society of Engineering Science, "Fracture of Fibrous Metal Matrix Composites," University of California, Berkeley, June 20–22, 1988.

Fourth Japan–United States Conference on Composite Materials, "Plastic Deformation Behavior of Fibrous Composite Materials," (presented by Y.A. Bahei–El–Din), Washington, DC, June 1988.

XVII International Congress of Theoretical and Applied Mechanics, "Plasticity of Composite Materials: Theory and Experiment," Invited Sectional Lecturer, Grenoble, France, August 1988.

France–U.S. Research Workshop, Strain–Localization and Size Effect Due to Cracking and Damage, "Fatigue Damage Mechanics of Metal Matrix Composite Laminates," (with E.C.J. Wung), Cachan, France, September 1988.

Third Technical Conference, American Society for Composites, "Plasticity of Composite Materials," Seattle, WA, September 1988.

Boeing Military Corporation, "Overview of Mechanics of Composites Research at RPI," Seattle, WA, September 1988.

NASA/AFOSR Composites Grant presentation, "Progress and Plans for Composite Research," NASA Headquarters, October 1988.

Center of Composite Materials and Structures, RPI presentation to Lord Corporation, "Micromechanics of Metal Matrix Composites," October 1988.

Colloquium, Rutgers University, "Thermal Expansion and Plasticity of Composite Materials," October 1988.

Invited lecture, ASME Winter Annual Meeting, "Thermal Stresses in Coated Fiber Composites," Chicago, IL, November 1988.

ONR/DARPA HiTASC program site visit, RPI, "Thermo–mechanical Compatibility," March 1989.

Invited lecture in meeting on new materials, synthesis, characterization and properties, International Center for Applied Sciences, "Damage Mechanics of Metal Matrix Composite Laminates," Gradisca d'Isonzo, Italy, March 1989.

Overview of Mechanics of Composite Research, RPI, lecture Centro Sviluppo Materiali S.p.A., (CSM), Rome, Italy, March 14, 1989.

4 invited lectures at Politechnico di Milano, Italy, "Mechanics of Composite Materials, A. Introduction, B. Elasticity, C. Plasticity, D. Damage and Fracture," March 16–17, 1989.

Invited lecture, Department of Solids and Structures, Tel–Aviv University, Israel, "Fatigue Damage Mechanics of Composite Laminates, March, 1989.

ONR Mechanics of Composites Review, "Thermo–plastic Constitutive Behavior of Metal Matrix Composites, Leesburg, VA, April 1989.

ONR Core Research Program in Composites Review, "Fracture of Metal Matrix Composites," Leesburg, VA, April 1989.

Invited lecture, "Physical and Computational Experiments in Plasticity of Composite Materials," Department of Applied Mechanics and Engineering Sciences, University of California, San Diego, May 1989.

Short Course on Metal Matrix, Ceramic Matrix, and Carbon Carbon Composites, Los Angeles, California, May 1989.

Alcoa Laboratories, Alcoa Center, PA, "Thermal Stresses in Fibrous Ceramic Matrix Laminates," May 1989.

Army Symposium on Solid Mechanics, Newport, Rhode Island, "Fracture of Fibrous Metal Matrix Composites," May 16–18, 1989.

IST–SDIO/ONR Woods Hole Review, "Overall Response and Local Fields of High Temperature Composite Laminates," June 5–6, 1989.

Second International Symposium of Plasticity and its Current Applications, "New Results in Bimodal Plasticity of Fibrous Composites," Mie University, Tsu Japan, July 30 – August 4, 1989.

AFOSR 14th Annual Mechanics of Composites Review, "Fracture in Fibrous Metal Matrix Composites," Dayton, Ohio, November 1, 1989.

ASME/WAM, "On a Correspondence Between Mechanical and Thermal Effects in Two–Phase Composites," San Francisco, CA, December 10–15, 1989.

DARPA–HiTASC Program site visit, RPI, March, 1990.

Invited lecture, Department of Applied Mechanics and Engineering Sciences, University of California, San Diego, March 5, 1990.

Short Course on "Metal Matrix Composites," (program co–director and lecturer), UCLA, March 6–8, 1990.

Montedisnial visit at RPI, April 9, 1990.

Invited Lecture, University of Illinois–Chicago, April 25, 1990.

Invited Lecture Northwestern University, April 26, 1990.

"Some Experimental Results in Plasticity of Fibrous Composites," IUTAM Symposium on Inelastic Deformation of Composites Materials, RPI, May 29 – June 1, 1990; Chairman of Symposium.

"Local Stresses in High Temperature Composites and Laminates," IST–SDIO/ONR Woods Hole IV Research Review, Woods Hole, Massachusetts, June 4, 1990.

Invited Lectures, Politecnico di Milan, Milan, Italy, June 11–12, 1990.

Invited Lecture, EniChem, Milan, Italy, June 13, 1990.

Invited Lecture, Institute of Theoretical and Applied Mechanics, Czechoslovak Academy of Sciences, Prague, Czechoslovakia, June 25, 1990.

Short Course, "Advanced Composite Materials and Structures," RPI, July 24, 1990

KAPL corporate visit, RPI, August 3, 1990.

Grumman Aircraft visit, RPI, August 8, 1990.

"On Uniform Fields in Heterogeneous Media," ASME/WAM, Dallas, Texas, 11/27/90.

"Fatigue Damage of Metal Matrix Composites: Optimization and Shakedown Analysis," ASME/WAM, Dallas, Texas, 11/27/90.

"Deformation and Damage Mechanisms in High Temperature Composites with Ductile Matrices," AFOSR, Bolling AFB, D.C., March 15, 1991.

"Static and Fatigue Damage in High Temperature Composites," AFOSR, Bolling AFB, D.C., March 15, 1991.

"Thermomechanical Compatibility in High Temperature Composites," DARPA HiTASC Program Review, March 27, 1991.

"A New Approach in Nonlinear Micromechanical Analysis of Heterogeneous Media," (with Y.A. Bahei–El–Din and A.M. Wafa), at First U.S. National Congress on Computational Mechanics, Chicago, Illinois, July 1991.

"On Thermal Hardening and Uniform Fields in Two–phase Composite Materials," Plasticity '91: Invited Lecture at The Third International Symposium of Plasticity and its Current Applications, Grenoble, France, August 12–16, 1991.

"Engineering Education in the United States," Invited lecture in the Klokner Institute of the Czech Technical University in Prague, Czechoslovakia, August 29, 1991.

"Fatigue Damage and Shakedown in Metal Matrix Composite Laminates," Invited lecture at conference on "New Trends in Structural Mechanics," Institute of Theoretical and Applied Mechanics, Czechoslovak Academy of Science, Prague, September 2, 1991.

"Experimental Evaluation of Yield Surfaces and Plastic Strains in a Metal Matrix Composite," American Society of Composites Meeting, Albany, NY, October 6–9, 1991.

"Fatigue and Shakedown in Metal Matrix Composites," 28th Annual Technical Meeting of the Society of Engineering Science, Gainesville, Florida, November 6–8, 1991.

"On Some Exact Results in Thermoplasticity of Composite Materials," Invited lecture ASME/WAM, Atlanta, GA, December 4, 1991.

"Thermal Stresses in Elastic–Plastic Composites with Coated Fibers," Invited lecture ASME/WAM, Atlanta, GA, December 6, 1991.

Presentations by Dr. Shephard

"Nonlinear Finite Element Modeling of Composites," ONR review of SDI related Composites Research, University of Maryland, College Park, Maryland, March 31, 1987.

"Nonlinear Finite Element Modeling of Composites," ONR Contractor's Review, Santa Barbara, CA, Sept. 30, 1987.

"Composite Material Models in ABAQUS," ABAQUS User's Conference, Newport, RI, June 2, 1988.

"Mechanical Behavior of Polymer Composites," S.S. Sternstein and M.S. Shephard, IBM Watson Research Center, Hopewell, NY, June 17, 1988.

"Idealized Models in Engineering Analysis," ASCE Structures Congress, San Francisco, CA, May 2, 1989.

"A Bimodal Plasticity Model for Fibrous Composites Implemented in ABAQUS – I. Fiber Dominated Mode," ABAQUS User's Conf., Newport, RI, May 30, 1990.

"Advanced Finite Element Formulations for Composite Shells," 6th Tech. Conf. on Composite Materials, Oct. 1991.

"Lamina Level Nonlinear Mixing Models in Finite Element Computations, ASME, Atlanta, GA, December 6, 1991.

LIST OF PROFESSIONAL PERSONNEL

Dr. G.J. Dvorak – Co–Principal Investigator
Dr. M.S. Shephard – Co–Principal Investigator
Dr. Y.A. Bahei–El–Din – Research Associate Professor
Dr. Y. Benveniste – Visiting Professor
Dr. H. Scarton – Associate Professor
Dr. L. Bank – Assistant Professor
Dr. N.Fares – Research Assistant Professor
S. Han – Post Doctor
T. Chen – Graduate Student
C. Creevy – Graduate Student
R. Hall – Graduate Student
B. Jenson – Graduate Student
A. Kaveh–Ahanger – Graduate Student
Kuruppu – Graduate Student
D. Mackay – Graduate Student
E. Martine – Graduate Student
N .Tutunco – Graduate Student
J.F. Wu – Graduate Student
J. Zarzour – Graduate Student
W. Mielke – Instrumentation Engineer
J. Grega – Secretary
D. Rogers – Secretary
E. Rudano – Secretary

APPENDIX A

Implementation of Material Models into Nonlinear Finite Element Procedures

CHAPTER 2
IMPLEMENTATION OF MATERIAL MODELS INTO NONLINEAR FINITE ELEMENT PROCEDURE

Application of the finite element method is widely accepted. Its application to nonlinear problems caused either by material nonlinearity or geometric nonlinearity is more complex and encounters heavy computational effort. More powerful computers and more accurate and efficient solution algorithms are required in nonlinear finite element applications. Nowadays, high-speed digital computers are available and more complex numerical operations with affordable costs can be performed. Also, the development of improved element characteristics and more efficient nonlinear solution algorithms has been demonstrated, (see for example Owen & Hinton [1980], Hughes [1987]). These achievements make it possible to incorporate the complicated material models available for composite materials into finite element procedures for the design of advanced composite structures.

2.1 Introduction

From the viewpoint of finite element modeling, the goal of this study is to develop analysis procedures based on specialized composite material models which are not available in general purpose programs.

In general, two types of nonlinearities should be considered in finite element procedures for structural mechanics:

1. Nonlinear strain-displacement relations, which is known as geometric nonlinearity.
2. Nonlinear stress-strain relations, which is known as material nonlinearity.

The objective of this study is to develop the procedure for implementation of metal matrix composite material models into the ABAQUS finite element program. Although the strains developed in fibrous composites are small due to the constraints imposed by the stiff fibers, geometrical nonlinearities may be accounted for, if necessary, by the finite strain capability available in ABAQUS. Therefore, our work focus is on the material nonlinearity caused by inelastic deformation of fibrous composites.

2.2 Nonlinear finite element procedure

Regarding the solution scheme to general nonlinear finite element system of equations, two generalized solution algorithms, namely the Newton-Raphson and initial stiffness (modified Newton-Raphson) methods are the best known methods in the literature. In the Newton-Raphson method, the instantaneous stiffness of the finite element system of equations is used for global iterations whereas in the modified Newton-Raphson method, the constant stiffness (elastic stiffness) of the system of equations is used throughout the global iterations. The instantaneous (or constant) stiffness of the finite element system is calculated from the instantaneous stiffness (or elastic stiffness) matrix of each material point and is assembled through the element routines. Any material model capable of updating the material instantaneous stiffness matrix and stress vectors under a given strain path may be implemented into the nonlinear finite element procedure. Considering metal matrix composite material models, the material nonlinearity is usually caused by inelastic deformation of the matrix material. Figure 2.1 shows a block diagram illustrating the sequence of events when composite material model is used in a finite element procedure. The standard nonlinear finite element procedure can be found in most of nonlinear finite element textbooks (see for example Zienkiewicz, [1977]).

2.3 Formulations of material models

In the nonlinear finite element procedures the strain vector and its increment are the independent variables. Most elastic-plastic composite material models, however, are formulated in stress–space which defines the material stiffness in terms of stresses and treats the stress and stress increment as independent variables. This causes some difficulty in the implementation of such material models into nonlinear finite element procedures.

The constitutive equations can be also formulated in the strain-space in which the strain and strain increment are the independent variables and the material stiffness is defined in terms of the strains. This formulation avoids the difficulties encountered in implementations of models based on the stress-space formulation. Although Drucker commented on the usage of strain-space formulation as early as 1950 [Drucker, 1950], the first detailed study was done by Naghdi & Trapp in 1975 [Naghdi & Trapp, 1975]. They proposed a strain-space formulation which was found to be free of the shortcomings of the stress-space plasticity. For example, unlike the stress-space formulation, the loading criteria for the perfectly plastic material in strain-space is exactly the same as that for work-hardening materials. In 1981, Yoder and Iwan [Yoder & Iwan, 1981] proposed and formulated a strain-space plasticity theory and demonstrated its advantages in applications involving extensive numerical techniques.

The strain-space formulation was applied to fibrous composite materials by Wung and Dvorak [1985]. They derived strain-space constitutive equation based on the vanishing fiber diameter (VFD) model. The VFD model was originally developed by Dvorak & Bahei-El-Din [Dvorak & Bahei-El-Din, 1978, 1982, and Bahei-El-Din, 1979] in a stress-space. Wu [1987] showed that the results found with the stress-space formulation and the strain-space formulation of the VFD model are in agreement.

Although composite material models based on the stress-space formulation may encounter certain difficulties in their implementation in nonlinear finite element procedure, we will consider them in our subsequent work for the following reasons:

1. The two material models, the PHA model and the BIMODAL theory are available in the stress space formulation. Substantial theoretical effort is required to reformulate these models in the strain-space.
2. Two special numerical algorithms which make the stress-space formulation of material models useful in finite element applications were developed to overcome the difficulties encountered in the stress-space formulation material models (see Chapter 3 and 4). The numerical study of these two methods has shown that both algorithms give accurate results, with minimal loss of computation efficiency.

All numerical integration schemes (i.e. solution schemes to the governing differential equations) which are based on Taylor's series expansion, such as Euler's method, Modified Euler's method, Runge-Kutta method, etc. are suitable for this application. When a Taylor's series expansion based integration scheme is employed in the constitutive calculations, the current stress increment is divided into several subincrements, which may or may not be equal in size depending on the method used. In each subincrement the stress-strain relation is then assumed to be linearly related by the instantaneous stiffness. In this way, the stress subincrement is found by multiplying the instantaneous stiffness matrix by the strain subincrement. After the stress subincrement has been found, the corresponding instantaneous stiffness matrix can then be updated. The procedure is repeated for all subincrements of each increment until the end of loading path. Numerical efficiencies of the strain-controlled and the stress-controlled algorithms are compared in Chapter 4.

In another approach, which makes the stress-controlled, stress-space formulation useful in nonlinear finite element procedures, the constitutive calculation algorithm is unaltered while manipulation is performed between constitutive calculation and finite element global iterations. Details of this procedure is given in Chapter 3 when the implementation of PHA is considered.

2.4 Connection between nonlinear material models and nonlinear finite element procedure

In a typical finite element procedure, there are as many as N1xN2xN3xm sampling points in the finite element domain, where N1, N2, and N3 are the number of sampling points in the three directions of element local coordinate system and m is the total number of elements in the finite element mesh. This means that there are N1xN2xN3xm nonlinear loading paths, which are generally different from each other, in each nonlinear finite element analysis. Therefore, the material model evaluation is required N1xN2xN3xm times in each finite element global iteration.

In strain-controlled, stress-space constitutive routines, the nonlinear finite element procedures result in accurate solutions with good computation efficiency. In stress-controlled, stress-space constitutive routines, however, accurate solutions are accompanied by "local iterations" between the constitutive routine and the finite element global procedure. These "local iterations" are necessitated due to the need of converting strain increments (from finite element global iteration) into stress increments for stress-controlled material routine.

As shown in Chapter 3, the "local iteration" provides a useful algorithm for the implementation of a nonlinear stress-controlled constitutive routine into a nonlinear finite element procedure. This makes it possible to implement any (either stress-controlled or strain-controlled) nonlinear material models into finite element procedure.

In the nonlinear finite element procedure, it is important to point out that for both stress-controlled and strain-controlled material routines one should always return elastic stiffness matrix to finite element procedure at the beginning of the global iteration for each increment. This treatment will guarantee faster convergence of the global iteration especially when the structure is unloaded from a highly nonlinear stage since too much compliant stiffness may produce very large strain increment during the unloading.

2.5 General purpose nonlinear finite element code-ABAQUS

Although the solution procedures developed can be incorporated in many general purpose finite element programs, the ABAQUS nonlinear general purpose finite element package was selected to carry out the specific finite element calculations for the study. The ABAQUS program features relevant to this study are discussed in this section.

2.5.1 ABAQUS overview

ABAQUS is a general purpose finite element analysis code developed by Hibbit, Karlson, and Sorrenson, Inc. (HKS) specifically for applications in nonlinear mechanics [User's Manual, 1988a, Theory Manual, 1987, Example Manual, 1988b, and System Manual, 1985]. It possesses a large number of standard features of a general purpose finite element code including large element and material libraries, a number of analysis classes and solution procedures, a group of post-processing options and a number of features that are of importance to the type of analyses needed for metal matrix composites.

Several attractive features exist in ABAQUS. First, it uses recently developed nonlinear solution procedures that are both efficient and stable. Second, it imposes a strong separation of element formulations, material property definitions, boundary condition prescriptions and loading history specifications. Third, it supports a large

number of user defined subroutines including element formulation, material constitutive formulation, boundary condition specification, and loading definition. In addition, the ABAQUS's element library contains a layered shell type element that should be very useful in the analysis of composite structures where differences in material behavior must be enforced at the laminate level. These features make ABAQUS attractive in employing the more advanced nonisotropic and/or nonlinear material models with various element types. Also, the ability to develop specialized material subroutines within ABAQUS is of principal importance to our research in development of finite element procedures for analysis of composite materials.

Tailoring ABAQUS to deal with functions not directly available within the program is achieved through the available user definable routines. There are twenty user definable routines in the program. Each user defined routine allows the analyst to carry out a particular type of operation that alters data within ABAQUS's data structures.

The method used to provide this functionality is to set aside a particular set of subroutines for the various purposes. Each of these subroutines has a fixed name and a fixed sequence for passing data in and out of ABAQUS. The particular user defined routines that are invoked in an analysis are specified through the input file for a particular analysis problem. For example, the user defined material routine is invoked by indicating that the material type for a particular element set is the user defined material. This keys the program to call the user defined material routine (UMAT), which will use the information passed to it as well as any information UMAT maintains to calculate the material stiffness terms and stress increments which are then sent back to the calling element routine. The user defined subroutine can access data available in the ABAQUS's data structures for other purposes.

The other functions that are also of importance to our study are the material models supported by ABAQUS's material library, such as the kinematic hardening

option, the isotropic hardening option and the Hill's anisotropic yield criteria with kinematic/isotropic hardening rule. These options accompanied with temperature dependent features make it possible to model the inelastic behavior of metal matrix composites for certain idealized domains.

2.5.2 ABAQUS input data file

In a typical ABAQUS input data file there are two major groups of input data entries including model data deck and history data deck. These input data decks are capable of completely modeling the problems of interest.

The model data deck contains the definition of the analysis model including the output heading, the data echo selections, the wavefront minimization option, the restart type of the analysis (optional), the node coordinates, the node set, element types, element connectivities, element set, the material models, the boundary conditions, orientation of the element coordinate system (if nonisotropic material is used), and the assignment of specific material model and/or its orientation to the corresponding element set.

The history data deck contains the definition of the analysis type including the submitting of subtitle for the analysis, the analysis classes, the loading history, the tolerance and other control numbers for nonlinear analysis case, and other output control options.

2.5.3 User definable routine — UMAT

This section limits its attention to the ABAQUS user definable material routine –UMAT, more specifically, the UMAT of ABAQUS version 4–7–25 which is the program we have used for the analyses presented in this study.

2.5.3.1 Basic interaction of ABAQUS with UMAT routine

When UMAT is called by an ABAQUS element routine, twenty seven variables (matrices, vectors, and values) are passed and/or returned through the UMAT subroutine

argument list including: material properties, current stress, strain, temperature, time, state variables (which are needed in material constitutive calculation), increments in strain, temperature, time, and updated stress vector and instantaneous stiffness matrix. Note that if the material stiffness matrix is symmetric in the analysis, ABAQUS will store the diagonal entries as well as the lower triangle part of the matrix, therefore users may update their instantaneous stiffness to those values only. This has the advantage of avoiding the unnecessary operations which return the entries on the upper part of the stiffness matrix to ABAQUS element routine.

2.5.3.2 Integration of material models into UMAT

In its application to composite materials, the UMAT subroutine works as the mechanism which links the micromechanical level material model to the macromechanical level behavior of a composite material. The essential part of the UMAT procedure is the material routine which calculates the constitutive law at each sampling point. Any material model which satisfies the requirements stated previously can be used in UMAT. The UMAT subroutine then performs six functions:

1. Initialize all solution dependent variables at the start of loading path.
2. Set up the counters for indicating the material point number.
3. Check the beginning of an increment, update solution dependent variables (from temporary array) and return elastic stiffness to ABAQUS element routine.
4. Calculate the stress vector and the instantaneous stiffness due to strain increment.
5. Store solution dependent variables in the temporary array.
6. Return updated instantaneous stiffness matrix and stress vector to ABAQUS.

Some operations for integration of a material model into UMAT are dependent on the type of material constitutive formulation. Details of these operations must therefore be

described for specific material models. In Chapters 3 and 4, we describe implementation of the PHA model and the BIMODAL theory, respectively, into UMAT subroutine.

2.5.4 ABAQUS post-processing capabilities

ABAQUS also supports a group of post-processing options including:

1. Output requests of line printer outputs, model plots (mesh plots - part or complete domain), result plots (contour plots - part or complete domain or even combination of several plots, deformed shape plots, and history plots - for the evolutions of specific quantity),...etc. for various of output devices.
2. Restart runs from previous results.
3. File transfer from local computer system to remote computer system for subsequent ABAQUS runs on remote computer system. The binary format for both computer systems may be different during the file transfer procedure.
4. User definable post-processing program for specific data process from the ABAQUS result files.

Detailed key features of ABAQUS post-processing capabilities can be found in Chapters 10 and 11 of ABAQUS Users Manual [1988a]. A procedure for running ABAQUS on VAX system at RPI is shown in Appendix A.

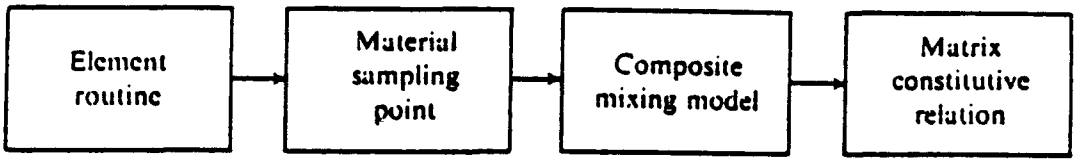

Figure 2.1 Placement of Composite Material Models into Finite Element Procedure

APPENDIX B

Periodic Hexagonal Array Model: Description and Finite Element Implementation

CHAPTER 3
PERIODIC HEXAGONAL ARRAY MODEL: DESCRIPTION AND FINITE ELEMENT IMPLEMENTATION

The development of composite material models for the application in the elastic range has been well established by two major approaches, namely, the Composite Cylinder Assembly (CCA) model [Hashin & Rosen, 1964] which provides rigorous bounds on the moduli, and the Self-Consistent Method (SCM) [Hill, 1965, and Budiansky, 1965] and the Mori-Tanaka Method [Mori & Tanaka, 1973, Benveniste, 1987, and Dvorak, 1990a] which both provide single estimate of each of the moduli. However, the application of these models for prediction of elastic-plastic responses has certain limitations (see for example, Dvorak & Rao [1976a,b], Dvorak & Wung [1984] and Dvorak & Bahei-El-Din [1979]). The Periodic Hexagonal Array (PHA) model, [Teply,1984, Dvorak & Teply, 1985, and Teply & Dvorak, 1988] overcomes the shortcomings of the above models.

3.1 Overview of the periodic hexagonal array (PHA) model

The analysis of the PHA model begins with selection of an appropriate representative volume element (RVE) and the identification of an appropriate set of periodic boundary conditions which allows an analysis of the RVE that will yield useful information on the overall behavior of the composite. One of the assumptions that yield a set of boundary conditions is uniform far-field strains on the micromechanical volume containing the RVE. Although there are gradients in the solution at the macromechanical level, the uniform strain field assumption is adequate for the purpose of determining the material properties. The second assumption which is important to the construction of a convenient set of boundary conditions is a regular packing of the fibers. In the PHA the packing is assumed to be hexagonal within an individual lamina. Since the metal matrix composites considered here are typically reinforced by large cross-section continuous filaments arranged in a fairly regular array, this is an acceptable assumption.

Using the PHA formulation, Teply [1984] has developed finite element based upper and lower bound solutions for the RVE. Since our study is concerned with implementation of the PHA model into a displacement based finite element analysis code, only the displacement based upper bound formulation is considered here.

3.1.1 Geometry and assumptions of PHA model

In the PHA model, the fibers are assumed to be periodically distributed throughout the layers of the matrix material in a topologically periodic hexagonal configuration (Fig.3.1).

Under overall uniform stress or strain applied to the periodic microstructure, a representative volume element (RVE) may be selected for the evaluation of overall properties and local fields. The RVE must satisfy the following properties:

1. When repeated it covers the entire macroscopic volume of the composite.
2. When the composite is loaded by uniform stresses or strains, the local stresses and strains must be invariant under coordinate transformations which repeat the RVE in the composite domain.

It is clear that the composite hexagons shown in Fig.3.1 may be selected as RVE.

If the area of the composite hexagon (Fig.3.1) is equal to unity, the dimensions shown in the figure can be found as function of the fiber volume fraction c_f as [Teply, 1984]

$$t = \frac{1 - \sqrt{c_f}}{\sqrt[4]{3}} \tag{3.1}$$

$$a = \frac{2\sqrt{c_f}}{\sqrt[4]{3^3}} \tag{3.2}$$

$$b = \frac{2}{\sqrt[4]{3^3}} \tag{3.3}$$

$$c = \frac{2}{\sqrt{3}} \tag{3.4}$$

As indicated by Dvorak & Teply [1985 and 1988] the composite hexagon is not a particularly convenient choice due to the difficulty encountered in the application of periodic boundary conditions. A more suitable selection of RVE is a triangle defined by connecting the centers of adjacent fibers (Fig.3.2). In this way, the composite domain is divided into triangular subdomains, these are identified by either the shaded or the unshaded triangles shown in Fig.3.2. It can be shown [Teply, 1984] that the shaded triangles can be converted into the unshaded triangles by a $-\delta$ transformation, where δ is the Kronecker's symbol. Either the shaded or the unshaded RVE is representative of the composite domain. Figure 3.3 shows two adjacent triangles with shaded triangle in X_i' coordinate system and unshaded triangle in X_i coordinate system. The transformation

$$X' = -\delta X + C_0 \tag{3.5}$$

where for the configuration of Fig.3.3, $C_0 = C\left(\sqrt{3},\ 1,\ 0\right)$, converts the shaded triangles into the unshaded ones throughout the composite domain. Also, it is shown [Teply, 1984, Dvorak & Teply, 1985, and Teply & Dvorak, 1988] that under overall uniform fields, both the overall and local stresses and strains are invariant under this transformation, and that the surface tractions and displacements in the two coordinate systems are identical. Figure 3.4 shows a 3D view of the RVE used in the PHA model, where c_f denotes the fiber volume fraction of the composite.

3.1.2 Periodic boundary conditions, overall strain- displacement relation, and overall stress-force relation of the RVE

The boundary conditions for the PHA model are imposed in the RVE to reflect the periodicity of the microstructure. These boundary conditions are derived from

the requirement that the local fields in the shaded and unshaded triangles remain invariant under the transformation (equation (3.5)). These conditions together with the requirement of displacement continuity across the RVE boundaries lead to expressions for the boundary displacement in terms of internal point and vertex displacements. Fig.3.5 shows detail of the RVE configuration. The displacement U_M of the mid-point M on the V_1V_3 boundary of the RVE can be derived from the expression of identical strain in two adjacent RVE's and equation (3.5) [Teply & Dvorak, 1988]:

$$U_M = \frac{1}{2}(U_{V_1} + U_{V_3}) \tag{3.6}$$

where U_{V_1}, U_{V_3} are the displacement at vertices V_1, V_3, respectively.

An expression for the displacement U_m of arbitrary point on the V_1V_3 boundary is derived due to the linear displacement fields in element 7 of Fig.3.5. From equation (3.6) and the linear displacement along the boundary sm of element 7 and the boundary rm of adjacent element (i.e. the element 7 of adjacent RVE), it is found that [Teply & Dvorak, 1988, and Fig.3.5]:

$$U_m = \frac{1}{2}(U_{V_1} + U_{V_3} - U_r + U_s) \tag{3.7}$$

Similar equations can be written for the boundaries V_1V_2 and V_2V_3.

The requirement of generalized plane strain of the fibrous medium in the fiber direction is imposed by the following boundary condition (Fig.3.4):

$$U_k - U_j = U_{V_4} - \frac{1}{2}(U_{V_2} + U_{V_5}) \tag{3.8}$$

where the coordinate of the point k is (1, X_2, X_3) and the coordinate of the point j is (0, X_2, X_3).

A set of support conditions for the RVE required to eliminate rigid body motions are shown in Fig.3.4. In this figure, the vertex V_2 is fixed in X_1 and X_2 directions, vertex V_3 is fixed in all three directions and vertex V_4 is fixed in X_2 direction.

An equivalent homogeneous volume (EHV) which has identical support conditions as the RVE is assumed for the derivation of the overall strain-vertex displacement relation and overall stress-vertex force relation. Let $\overline{\sigma}$ and $\overline{\epsilon}$ denote the overall stress and strain, respectively, where

$$\overline{\sigma} = [\overline{\sigma}_{11}, \overline{\sigma}_{22}, \overline{\sigma}_{33}, \overline{\sigma}_{12}, \overline{\sigma}_{13}, \overline{\sigma}_{23}]^T \tag{3.9}$$

$$\overline{\epsilon} = [\overline{\epsilon}_{11}, \overline{\epsilon}_{22}, \overline{\epsilon}_{33}, 2\overline{\epsilon}_{12}, 2\overline{\epsilon}_{13}, 2\overline{\epsilon}_{23}]^T \tag{3.10}$$

$\overline{u}$ denotes the displacements of the vertices V_1, V_2, V_3 and V_4, shown in Fig.3.5, and $\overline{F}$ denotes the nodal forces at the vertices, where

$$\overline{u} = [u_{V_1}, u_{V_4}, v_{V_1}, w_{V_1}, w_{V_2}, w_{V_4}]^T \tag{3.11}$$

and

$$\overline{F} = \left[F^x_{V_1}, F^x_{V_4}, F^y_{V_1}, F^z_{V_1}, F^z_{V_2}, F^z_{V_4}\right]^T \tag{3.12}$$

Here, u, v, w are the vertex displacements in x, y, z direction and the subscripts indicate the vertices.

For an equivalent homogeneous element with tri-linear displacement functions, the strain-displacement and is given by [Teply, 1984]:

$$\overline{\epsilon} = \overline{B}\,\overline{u} \tag{3.13}$$

where $\overline{B}$ is derived from the multiplication of the differential operator matrix (which is the matrix which relates the strain vector with the displacement vector) and the shape function matrix (which is the matrix relates vertices displacement vector with the displacement vector in the domain). For the vertices V_1, V_2, V_3 and V_4 indicated in Fig.3.4, the $\overline{B}$ is found as:

$$\overline{B} = \begin{bmatrix} 0 & 1 & 0 & 0 & 0 & 0 \\ 0 & 0 & -r & 0 & 0 & 0 \\ 0 & 0 & 0 & 0 & -\frac{s}{2} & 0 \\ -r & 0 & 0 & 0 & 0 & 0 \\ 0 & 0 & 0 & 0 & -\frac{1}{2} & 1 \\ 0 & 0 & 0 & -r & \frac{r}{2} & 0 \end{bmatrix} \tag{3.14}$$

where $r = \frac{1}{\sqrt[4]{3}}$ and $s = \sqrt[4]{3} = \frac{1}{r}$.

The stress-forces relation of the equivalent homogeneous element can be derived from the virtual work equation which equilibrates the external work done by nodal forces and the internal work done by stresses in the element. This leads to the explicit expression for the stress-nodal force relation [Teply, 1984]:

$$\overline{\sigma} = \overline{B}^{-T}\,\overline{F} \tag{3.15}$$

3.1.3 The overall instantaneous stiffness matrix ($\overline{L}$) of the RVE

To determine the overall instantaneous stiffness matrix of the RVE, the equivalent homogeneous volume of unknown material properties is again considered. It is the instantaneous stiffness parameters of the EHV that are needed to perform the macromechanical analysis. The overall properties of the EHV are found by equating the total strain energy computed for the EHV and the RVE when they are subjected to identical overall fields.

It is shown in [Teply, 1984] that the energy change in the EHV and the RVE, namely, $\Delta\Pi_{EHV}$ and $\Delta\Pi_{RVE}$, are given by:

$$\Delta\Pi_{EHV} = \frac{1}{2}\Delta\overline{u}^{T}\overline{B}^{T}\overline{L}\overline{B}\Delta\overline{u} - \Delta\overline{F}^{T}\Delta\overline{u} \tag{3.16}$$

$$\Delta\Pi_{RVE} = \frac{1}{2}\Delta\overline{u}^{T}\overline{K}\Delta\overline{u} - \Delta\overline{F}^{T}\Delta\overline{u} \tag{3.17}$$

where

Δu is a common set of nodal displacements at V_1, V_2, V_3 and V_4 for both the EHV and RVE.

$\overline{B}$ is the strain-displacement matrix shown in equation (3.15).

$\Delta \overline{F}$ is the nodal forces equivalent to surface tractions acting on the EHV and RVE.

$\overline{L}$ is the instantaneous stiffness of the EHV.

$\overline{K}$ is the stiffness matrix of the RVE finite element mesh, which is the assembly of fiber and matrix subelement stiffness matrices, L^k, and as a result, it is also a function of fiber and matrix subelement material matrices.

The composite overall instantaneous stiffness matrix $\overline{L}$ can then be found by equating the equations (3.16) and (3.17). This yields the explicit form of the overall instantaneous stiffness matrix in terms of local quantities:

$$\overline{L} = \left(\overline{B}^T\right)^{-1} \overline{K} (\overline{B})^{-1} \tag{3.18}$$

3.2 Thermomechanical loading

Under overall thermomechanical loads, the PHA boundary conditions, and stiffness matrix (equation 3.18) remain unchanged. Only the solution of the RVE must be modified. The thermomechanical correspondence derived by Dvorak [1986] can be used to convert the thermomechanical loading path to a mechanical path. This important result was derived from the following decomposition procedure.

1. In the first step of the procedure, the phases are separated and tractions applied to the surface of each phase to maintain the current local phase stresses and strains. A uniform thermal change $d\theta$ is then applied to both phases. Since

the phases have different coefficients of thermal expansion, they will deform differently under $d\theta$. Therefore, auxiliary uniform stresses must be applied to both phases to ensure compatibility of the phases when the composite is reassembled.

2. In the second step, the auxiliary stresses are computed from the requirement that the phases must be compatible. The traction equilibrium at the fiber/matrix interface and on the surface of the composite representative volume element is automatically satisfied since the auxiliary field is spatially uniform.
3. In the third step of the procedure, the phases are reassembled and the surface tractions are removed.

It was shown by Dvorak [1986] that if the phases are transversely isotropic, then the overall stress equilibrating the phase auxiliary stresses is axisymmetric (assuming that the fibers are aligned in the X_1 direction):

$$d\sigma = \begin{Bmatrix} d\sigma_{11} \\ d\sigma_{22} \\ d\sigma_{33} \\ d\sigma_{12} \\ d\sigma_{23} \\ d\sigma_{13} \end{Bmatrix} = \begin{Bmatrix} S_A \\ S_T \\ S_T \\ 0 \\ 0 \\ 0 \end{Bmatrix} d\theta \tag{3.19}$$

where

$$S_A = (a_3 b_1 - a_1 b_3)/(a_1 b_2 - a_2 b_1) \tag{3.20}$$

$$S_T = (a_2 b_3 - a_3 b_2)/(a_1 b_2 - a_2 b_1) \tag{3.21}$$

$$a_1 = (n_f + c_m l_f)/\left(k_f E_L^f\right) - 2/(3K_m) \tag{3.22}$$

$$a_2 = -l_f/\left(c_f k_f E_L^f\right) \tag{3.23}$$

$$a_3 = 2\left(\alpha_T^f - \alpha^m\right) \tag{3.24}$$

$$b_1 = l_f/\left(k_f E_L^f\right) + 1/(3K_m) + c_m/\left(c_f E_L^f\right) \tag{3.25}$$

$$b_2 = -1/\left(c_f E_L^f\right) \tag{3.26}$$

$$b_3 = -\left(\alpha_L^f - \alpha^m\right) \tag{3.27}$$

and

K_m is the matrix bulk modulus.

α^m is the matrix coefficient of thermal expansion.

E_L^f is the fiber longitudinal Young's modulus.

α_L^f is the fiber longitudinal coefficient of thermal expansion.

α_T^f is the fiber transverse coefficient of thermal expansion.

k_f, l_f, n_f are the Hill's moduli [1963] of the fibers:

$$k_f = -1/\left[1/G_T^f - 4/E_T^f + 4\left(\nu_L^f\right)^2/E_L^f\right] \tag{3.28}$$

$$l_f = 2k_f\nu_L^f \tag{3.29}$$

$$n_f = E_L^f + l_f^2/k_f \tag{3.30}$$

and

G_T^f is the fiber transverse shear modulus.

E_T^f is the fiber transverse Young's modulus.

ν_L^f is the fiber longitudinal Poison's ratio.

When the composite is in the plastic range with a loading increment of $d\sigma$ and $d\theta$ (or $d\epsilon$ and $d\theta$) , the corresponding equivalent strain (or stress) increment are found as [Dvorak, 1986]:

$$\begin{aligned} d\epsilon &= h d\theta + M(d\sigma - S_a d\theta) \\ d\sigma &= S_a d\theta + L(d\epsilon - h d\theta) \end{aligned} \tag{3.31}$$

where

$$S_a = [S_A.\ S_T.\ S_T.\ 0,\ 0,\ 0\ ]^T \tag{3.32}$$

$$h = [H,\ H,\ H,\ 0,\ 0,\ 0]^T \tag{3.33}$$

$$H = \frac{S_T}{3K_m} + \alpha^m \tag{3.34}$$

and M and L are the instantaneous compliance and stiffness matrices of the composite, respectively.

With the help of equation (3.31), the composite thermal stress can be found by setting the strain increment equals to zero (i.e. no mechanical load is applied):

$$d\sigma^{thermal} = (S_a - Lh)d\theta \tag{3.35}$$

In this way, the thermal load is converted to mechanical load. The usefulness of equations (3.31) and (3.35) is the implementation of this procedure into material constitutive models. The application of the decomposition procedure into laminate constitutive formulation is discussed Chapter 5 (see Bahei-El-Din, [1990b]).

3.3 Programming algorithm of the PHA constitutive model

The original PHA upper bound constitutive program developed by Teply [1984] has been substantially modified. The program was first, modified by Shah [1986] to include thermomechanical loading using the decomposition procedure, and later modified by the author to improve its computation efficiency. For a set of given material properties and loading path, the programming steps of the modified PHA constitutive program are summarized below:

1. Read phase material constants.
2. Calculate basic material quantities such as Hill's moduli [Hill, 1964] and S_a and h vectors (defined in equations (3.32) and (3.33)).
3. Calculate the RVE strain-displacement matrix B in equation (3.15).
4. Calculate the stiffness contributions of the fiber subelements to the stiffness of the RVE (i.e. $\overline{K}$ in equations (3.17) and (3.18)).
5. Calculate the stiffness contributions of the matrix subelement to the stiffness of the RVE.
6. From steps 3 to 5, calculate the overall composite moduli $\overline{L}$ and the stress concentration factor of the phases.
7. Read the loading path. The program stops if this is the end of the loading path. Otherwise check the plasticity condition for each matrix subelements through stress concentration factors.
8. In the PHA constitutive program, the linear kinematic hardening is assumed for all matrix subelements. Once the plasticity condition of the matrix subelement is detected, the program performs numerical integration for the plasticity quantities such as the translation of the yield center of the matrix subelements which have

already yielded, and the instantaneous stiffness of the elastic-plastic matrix subelement.

9. Repeat steps 8, 5, and 6 until the current loading increment has been completely integrated. Once the specific loading increment is absorbed, the program goes to step 7 for another new loading increment.

Note that the PHA's programming steps described here are intended to serve as a reviewing purpose mainly for the use of next section. Details of the data structure and plasticity integration used in the PHA program can be found in Chapters 3, 4, and 5 of Teply [1984].

3.4 Implementation into general purpose finite element code

As shown in Fig.2.1, in the finite element analysis of composites the material constitutive model always requires consideration of material nonlinearities of the matrix phase. The composite mixing model considered here is the PHA model, and, in the case of metal matrix composites, the matrix is an elastic-plastic material. Therefore the PHA evaluations are at the innermost loop of iteration in the nonlinear finite element analysis process. This means that the integration of the PHA model in a macromechanical finite element procedure must achieve the maximum computational efficiency of the individual PHA calculations.

Referring again to Fig.2.1, it is the individual element subroutines that call the UMAT routine at each numerical integration point at which the instantaneous material stiffness matrix is to be updated. The UMAT routine is responsible for ordering the information in the form needed for the PHA and calling the PHA. The PHA routine then determines the overall properties at the material point based on the constituent properties. This requires that the PHA routine invokes some other subroutines to calculate the material stiffness contributions of the matrix and the fiber phases through

the matrix constitutive relation (may be elastic-plastic) and the fiber constitutive relation (elastic response is assumed), respectively.

3.4.1 Integration of periodic hexagonal array model into ABAQUS

The user-defined material routine within ABAQUS must perform operations indicated in Section 2.5.3.

When the PHA model is implemented into the ABAQUS finite element procedure through the UMAT subroutine, a complexity that arises in this process is that it uses a stress increment to calculate the instantaneous stiffness and strain increment. However, ABAQUS, which is a displacement-based finite element procedure, provides the UMAT routine with a strain increment and requires back the instantaneous stiffness and corresponding stress. Therefore it was necessary to introduce the local iteration explained below into the UMAT routine. This procedure has been found, typically, to converge within two or three iterations.

3.4.2 Local iterations and initial thermal stress in UMAT

When UMAT is called during a load increment including mechanical and/or thermal loads, ABAQUS provides the current state (the results at the end of previous increment) of stress ($\sigma_{(A)}$), strain ($\epsilon_{(A)}$) and temperature (T) for each global iteration. At the start of a load increment, that is in the initial iteration of the current load step, the strain increment is zero ($\Delta\epsilon_{(A)}=0$) and the temperature increment (ΔT) is the value for that load increment. The function of this initial iteration is to provide the macromechanical analysis procedure (ABAQUS) with an appropriate instantaneous stiffness matrix and the appropriate introduction of the effects of any thermal load for that increment. Unlike the finite element procedure, where thermal effects are accounted for by the construction of an initial strain vector, the approach used here is to convert the thermal increment into an equivalent mechanical load through the use of an initial stress vector. The

determination of this initial stress vector must be carried out at the micromechanical level and account for the different thermal characteristics of the matrix and fibers. The analysis is done using Dvorak's decomposition procedure [1986] (see Section 3.2). The stiffness matrix and initial stress vector are returned to ABAQUS, where the effects of the pure mechanical load are combined with the initial stress vector to predict the strain increments for this load step. From this point through the remainder of the macromechanical ABAQUS level iterations for this load increment the UMAT routine treats all load types as pure mechanical load at a temperature equal to $T+\Delta T$.

In each of the subsequent macromechanical iterations for a load increment, UMAT receives a non-zero strain increment predicted from the given instantaneous stiffness and load increments. This strain increment must be converted into a stress increment ($\Delta\sigma_{(A)}$) and added to the stress at the current state ($\sigma_{(A)}$) to form a new stress vector ($\sigma^{(1)}_{(U)}$) for the PHA procedure:

$$\sigma^{(1)}_{(U)} = \sigma_{(A)} + L\Delta\epsilon_{(A)} \tag{3.36}$$

where

L is the stiffness at the beginning of increment.

$L\Delta\epsilon_{(A)}$ is the trial stress increment.

The PHA procedure calculates a new strain vector ($\epsilon^{(1)}_{(U)}$) which must be compared with the strain vector given to UMAT by the macromechanical level (ABAQUS) model ($\epsilon_{(A)} + \Delta\epsilon_{(A)}$). If they are not nearly equal, a local iteration in the UMAT routine is initiated where the stress vector used in the PHA is updated by

$$\sigma^{(i+1)}_{(U)} = \sigma^{(i)}_{(A)} + L^{(i)}_{(U)}\left(\epsilon_{(A)} + \Delta\epsilon_{(A)} - \epsilon^{(i)}_{(U)}\right),\ i = 0, 1, \ldots \tag{3.37}$$

where

$\sigma^{(i+1)}_{(U)}$ is the new stress vector for the PHA constitutive routine input.

$\sigma_{(U)}^{(i)}$ is the stress vector at the end of i^{th} local iteration.

$L_{(u)}^{(i)}$ is the instantaneous stiffness at the end of i^{th} local iteration.

$\epsilon_{(A)}$ is the strain vector at the beginning of the increment.

$\Delta\epsilon_{(A)}$ is the strain increment at this global iteration.

$\epsilon_{(U)}^{(i)}$ is the strain increment at the end of i^{th} local iteration.

$\sigma_{(U)}^{(0)}$ is the stress at the end of previous global iteration (maintained by the UMAT routine).

The convergence criterion used in the UMAT iteration is:

$$\frac{\left|\epsilon_{(U)}^{(i+1)} - (\epsilon_{(A)} + \Delta\epsilon_{(A)})\right|}{\left|\epsilon_{(A)} + \Delta\epsilon_{(A)}\right|} \leq \text{tolerance} \qquad (3.38)$$

The selection of the tolerance depends on the tolerance used in the nonlinear finite element procedure and the tolerance used in the nonlinear constitutive calculation. These three tolerances should be chosen so that same level of accuracy is performed in each process. Typical number for the tolerance is between 10^{-4} to 10^{-5}. In this work, 10^{-5} was chosen as tolerance for all calculation.

The local iterations will be repeated until equation (3.38) is satisfied, i.e. the convergence of the local iterations is reached. Figures 3.6 and 3.7 illustrate the iteration process given by equations (3.36) to (3.38).

3.4.3 Programming steps in UMAT with PHA model

The summary of the steps carried out in the user-defined material routine UMAT based on the PHA material model for metal matrix composites are:

1. At the beginning of an increment, update the solution-dependent variables and calculate initial stresses due to temperature change (if thermal load exists).
2. For other than the initiation of a load increment, calculate a new stress vector for PHA (equation(3.36)).

3. Invoke the PHA procedure to calculate the strain vector and instantaneous stiffness due to the new stress vector.
4. Compare the strain vector from PHA to the strain vector from ABAQUS (equation (3.38)). If the strain vector has converged, return the instantaneous stiffness and stress vector to ABAQUS, otherwise adjust the stress vector by using equation (3.37) and return to step 3.
5. The flow chart for these steps is shown in Fig.3.6.

The pseudo codes of UMAT with PHA and PHA routines and the User's guide of PHA version UMAT are summarized in Appendix B.

3.4.4 Applications

The UMAT subroutine developed for the PHA model was used to compute the response of a P100 graphite-aluminum (Gr-Al) composites and laminates subjected to cycles of uniform thermal change [Wu, et al, 1989]. The fibers are assumed to be elastic, the matrix is an elastic-plastic solid of the von Mises type. Constitutive equations of the matrix are given in the context of infinitesimal strains. The matrix hardens kinematically, according to the Ziegler rule [1959]. Table 3.1 shows constituent properties in the elastic range, the inelastic properties (i.e. the plastic tangent moduli) are indicated in the subsequent figures for individual cases.

The examples examine the response of a laminated plate that consists of many alternating layers in a $(\pm\phi)_s$ lay-up. The finite element model of the plate, Fig.3.8, consists of two eight-noded solid elements, one for each $+\phi$ and $-\phi$ layer. Uniform displacements on each surface were prescribed as boundary conditions. The selected idealization for the $(\pm\phi)_s$ of the solid finite elements allows the application of the PHA model to account for the micromechanical level plasticity of matrix material.

Figure 3.9 shows the response of the Gr-Al composite under a uniform thermal change which starts at 20°C and then follows the cycle to +120°C, -120°C and +120°C. Matrix (m) properties in the plastic range, are specified in terms of the ratio of a constant tangent modulus, to the elastic Young's modulus, $(E_{tan}/E)_m$. The axial strain is plotted as function of the temperature change. The solid line indicates the response of a unidirectionally reinforced plate, o=0°, whereas the dashed line represents laminate response. In the elastic range the $(\pm 12)_s$ laminate is dimensionally stable in axial direction, hence no axial overall strain is caused when the temperature changes from 20°C to 60°C which marks the onset of initial yielding in the plate. After that the plate is seen to undergo axial contraction while the temperature increases to +120°C. The reversal of the direction of thermal change causes elastic unloading and therefore brings back dimensionally stable response. Plastic loading sets in again at +50°C and continues until –120°C. No dimensional stability is seen in the response of the unidirectional plate. However, the rate of plastic strain change is much lower in the unidirectional plate and therefore, the total axial strain amplitude caused by the thermal change cycle is actually smaller in the unidirectional plate.

Figure 3.10 shows a similar result for the same Gr-Al composite in which the aluminum matrix has a larger tangent modulus. The unidirectional composite and the laminated plate are again subjected to the thermal change prescribed in figure 5.4. Owing to the greater stiffness of the matrix in the plastic range, both plates experience a smaller strain amplitude. Once again, the axial strain amplitude of the laminate exceeds that of the unidirectional plate.

Figure 3.11 indicates the computed variation of the axial thermal expansion coefficients in the elastic and plastic regions, as a function of the lamination angle ϕ. When linear hardening is assumed for the matrix, the composite's asymptotic tangent modulus is constant, and the CTE in the plastic region is proportional to the slope

of the asymptotic portion of the strain/temperature curve in the plastic region (see for example, Figs.3.9 and 3.10). Figure 3.11 shows that elastic composite laminates have a vanishing axial CTE at about ϕ=12°, while the laminates with the stiffer matrix in the plastic range show this property at ϕ=2°. The laminate with the lower hardening matrix has no dimensionally stable lay-up.

Figure 3.12 shows the total axial strain or amplitude of the three composites subjected to the thermal cycle of Figs.3.9 and 3.10, again as a function of the lamination angle ϕ. For ϕ=12°, the magnitudes of the strain amplitudes during the cycle are shown. As already mentioned, the results indicate that in the presence of plastic straining, the unidirectional reinforced plate may have a better dimensional stability than a laminated plate depending on the magnitude of matrix plastic tangent modulus (see Figs.3.9 and 3.10 for the comparison of different plastic tangent moduli). Of course, the actual response will also depend on the magnitude of the matrix yield stress. The value used in the present examples (Table 3.1) corresponds to an as fabricated material. Higher yield stress magnitudes and lower strain amplitudes can be achieved by heat treatment of the matrix. More specific investigation of dimensional stability of laminates is summarized in Chapter 5.

Properties	Fiber	Matrix
Volume fraction	0.5	0.5
Axial Young's modulus (MPa)	6.8955 × 10+5	7.2395 × 10+4
Axial Poison's ratio	0.41	0.33
Axial shear modulus (MPa)	1.5517 × 10+4	2.7216 × 10+4
Axial CTE (m/m°C)	-1.6200 × 10-6	2.4000 × 10-5
Transverse Young's modulus (MPa)	6.0690 × 10+3	7.2395 × 10+4
Transverse shear modulus (MPa)	2.0690 × 10+3	2.7216 × 10+4
Transverse CTE (m/m°C)	1.0800 × 10-5	2.4000 × 10-5
Initial yield stress in tension (MPa)		7.0000 × 10+1

Table 3.1 Material Properties for P100 Graphite-Aluminum Composite

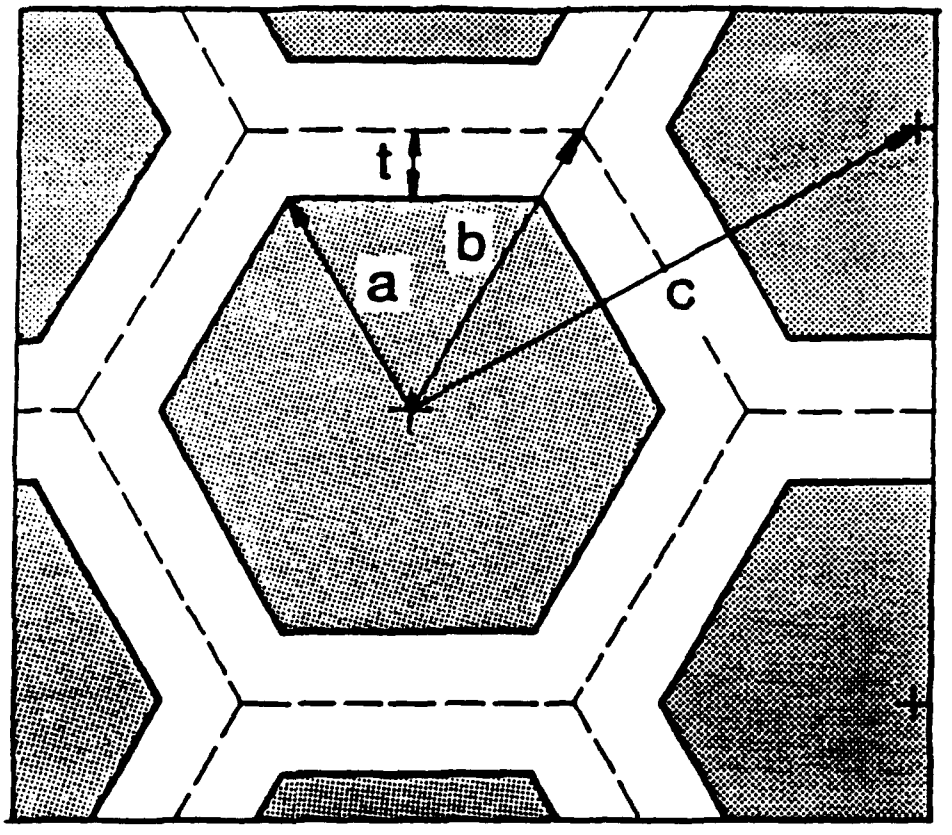

Figure 3.1 Dimension of Periodic Hexagonal Array with Cylindrical Fibers [Teply, 1984]

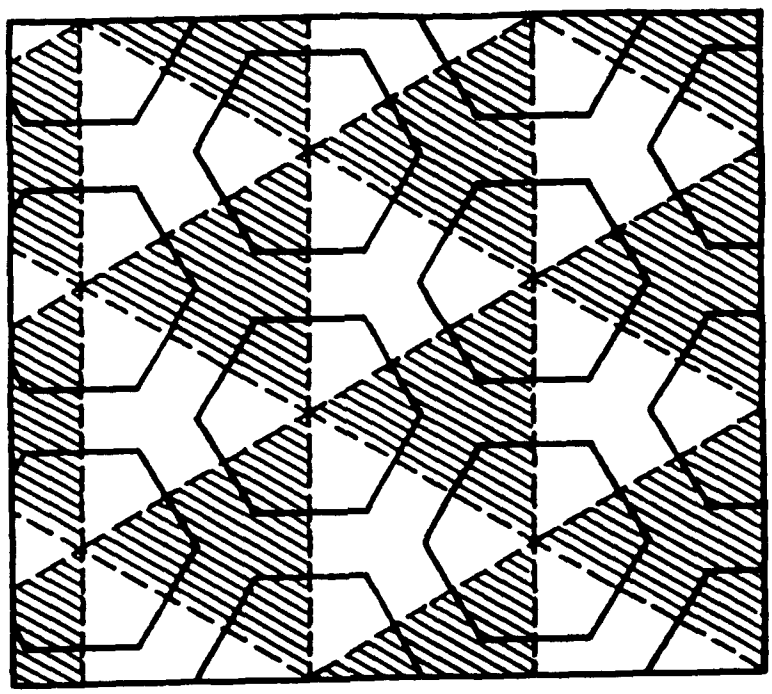

Figure 3.2 Transverse Cross Sections of Periodic Hexagonal Array Models of Fibrous Composites with Hexagonal Cylindrical Fibers [Teply, 1984]

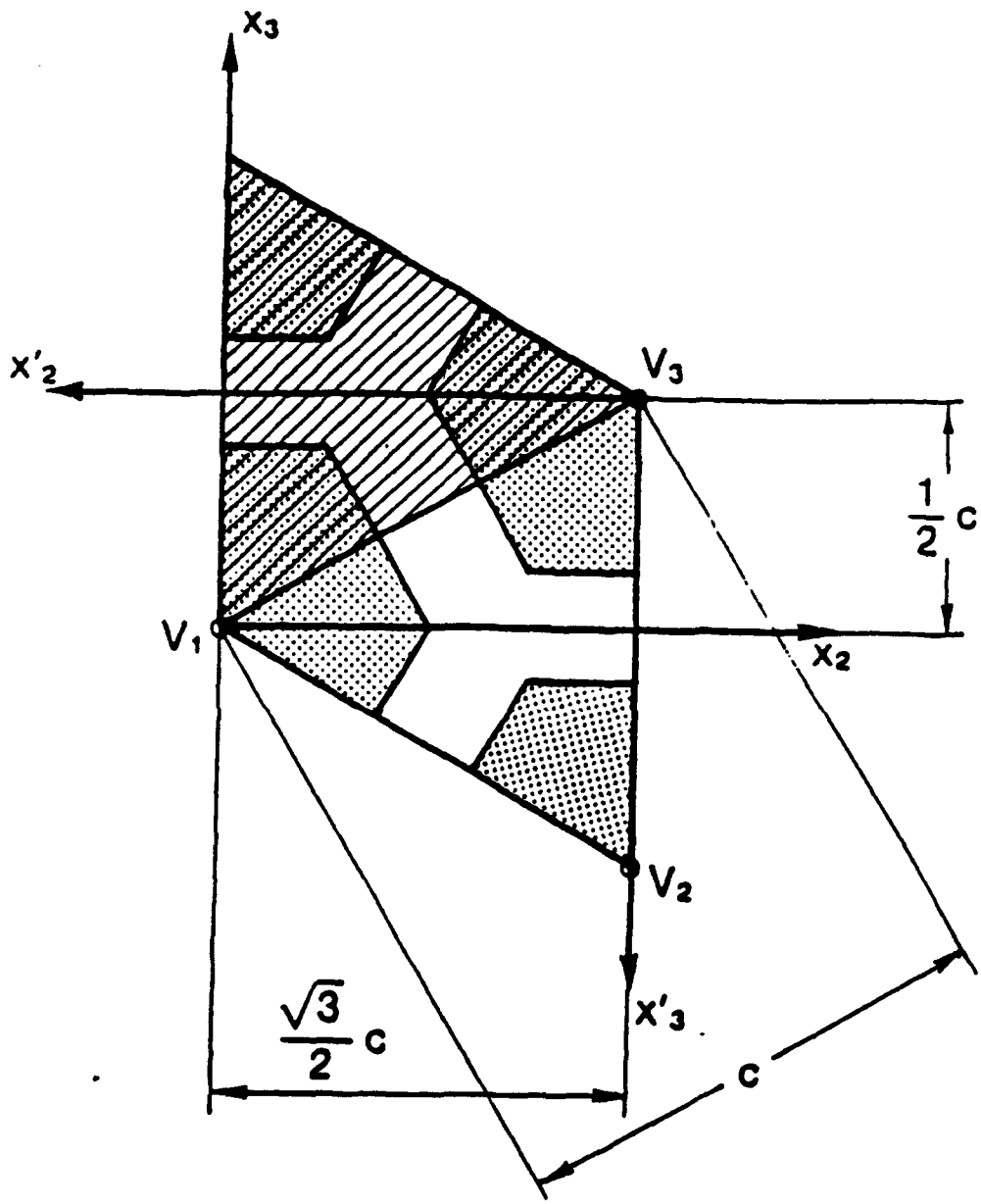

Figure 3.3 Two Adjacent Unit Cells and Their Local Coordinate Systems [Teply & Dvorak, 1988]

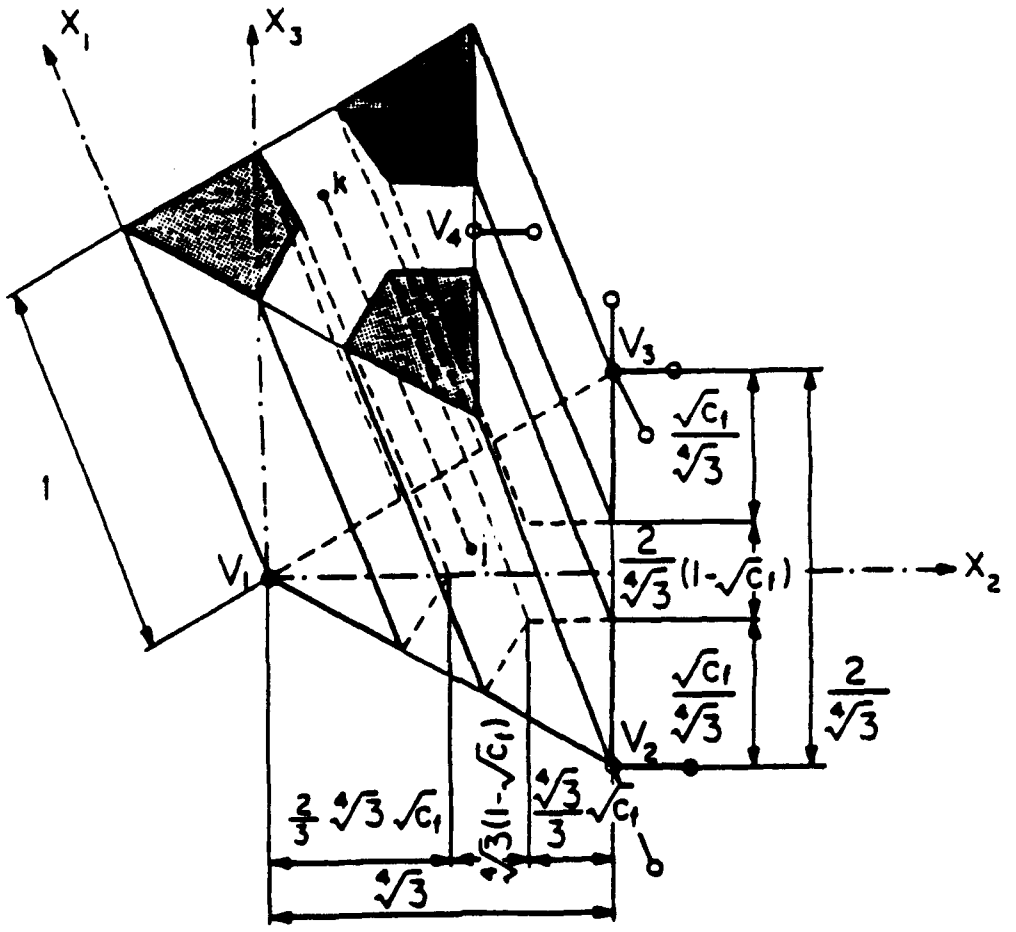

Figure 3.4 Dimension and Support Conditions of the Unit Cell in PHA Model [Teply & Dvorak, 1988]

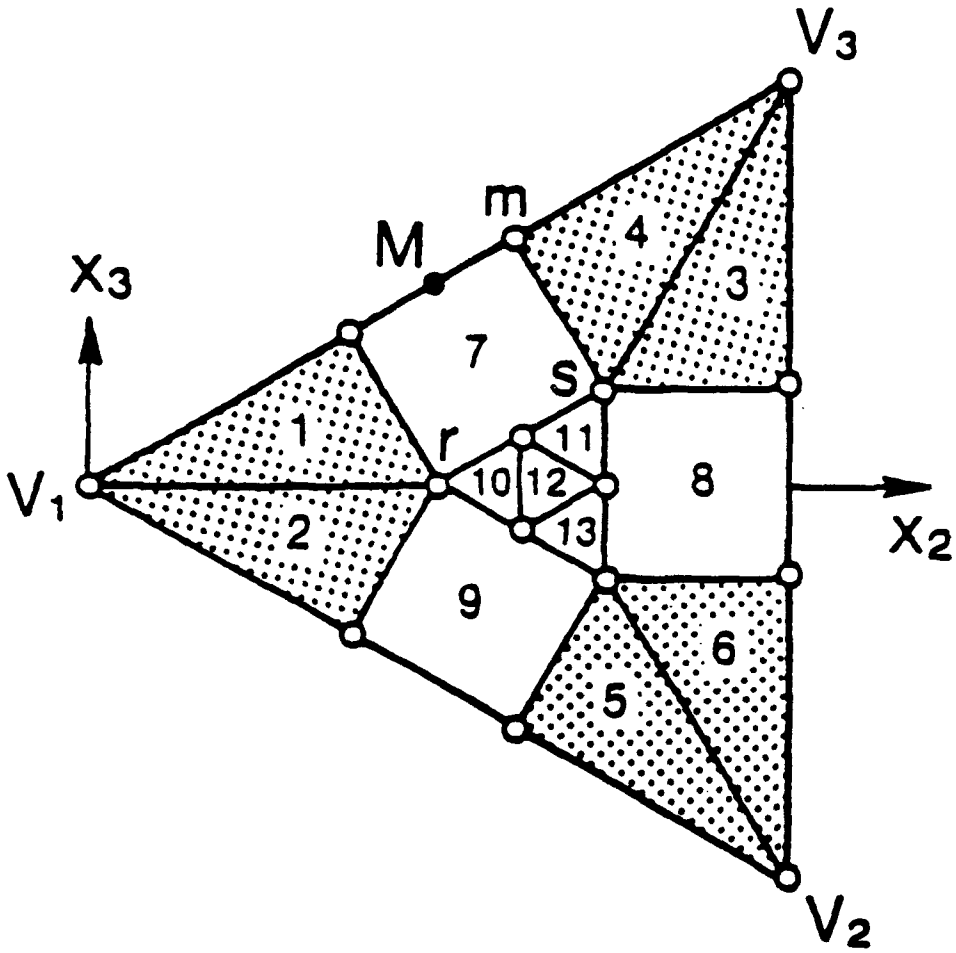

Figure 3.5 Unit Cell and the Finite Element Mesh Used in PHA Model [Teply & Dvorak, 1988]

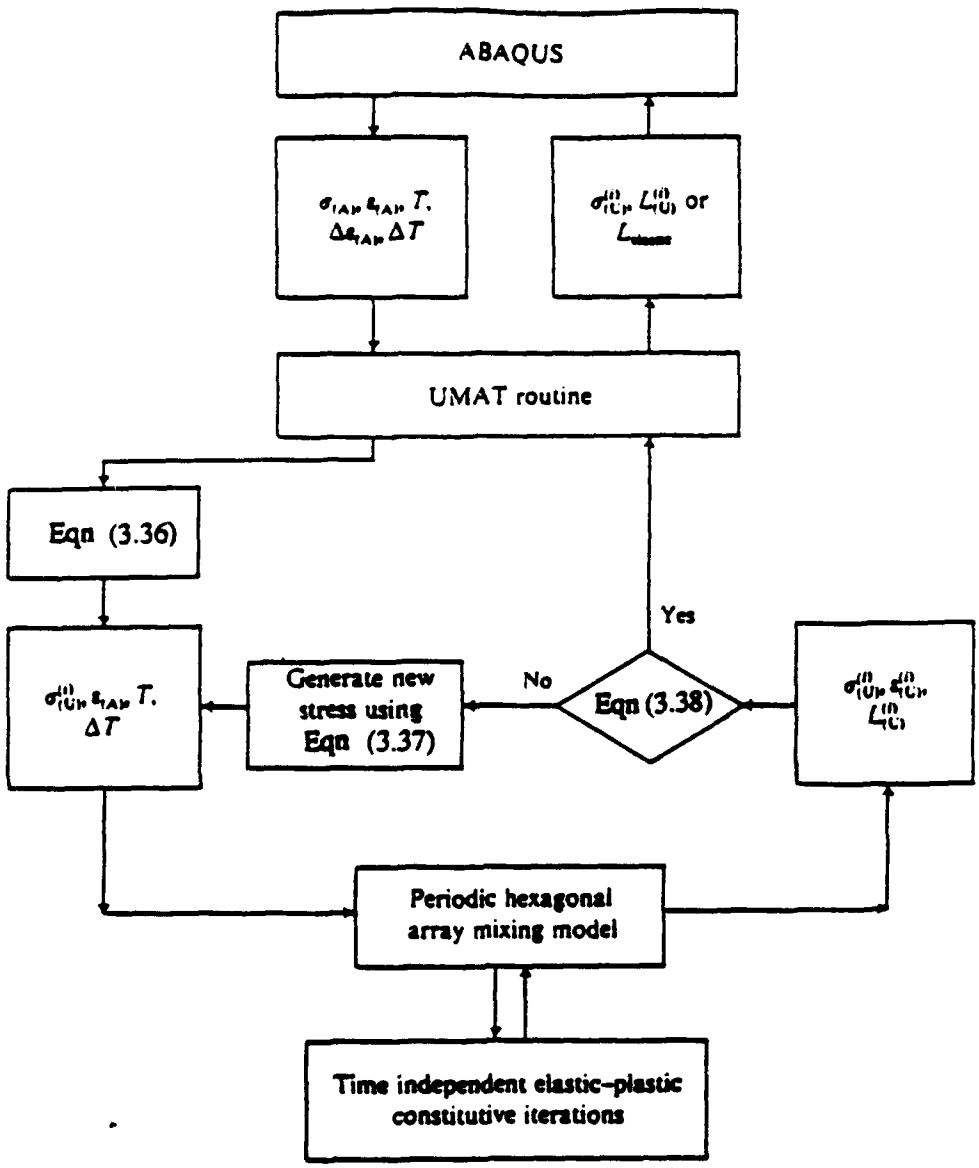

Figure 3.6 Summary of the Relationship Between ABAQUS, UMAT and PHA Constitutive Model [Wu, et al, 1989]

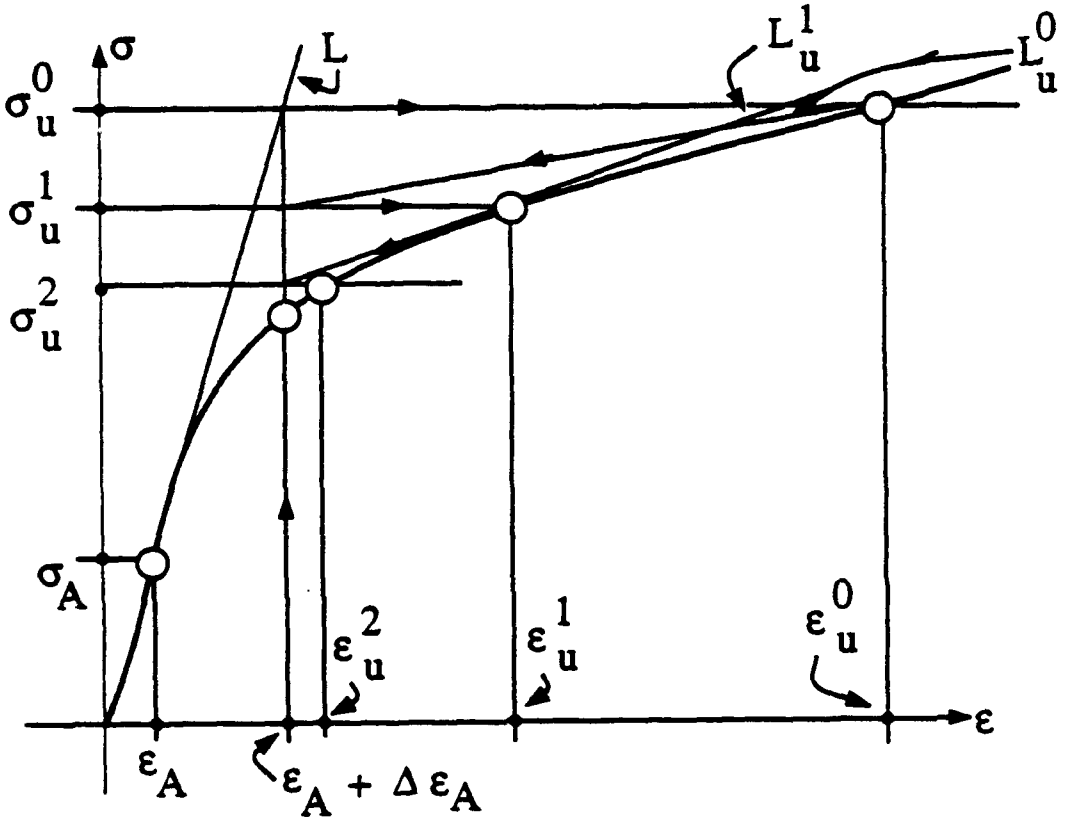

Figure 3.7 The Stress and Strain Relation in Local Iteration

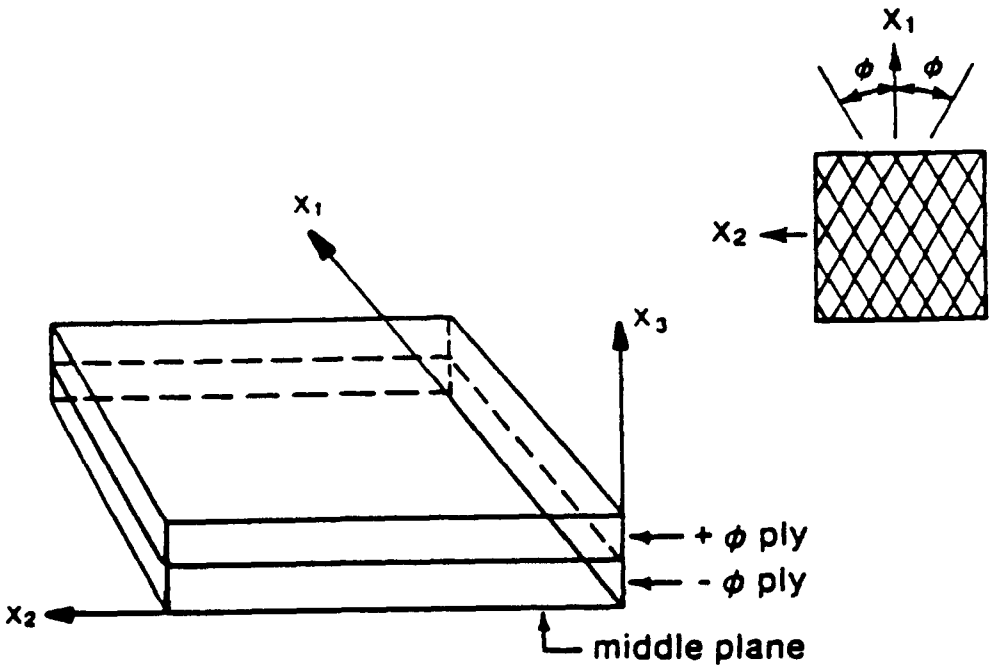

Figure 3.8 Finite Element Model

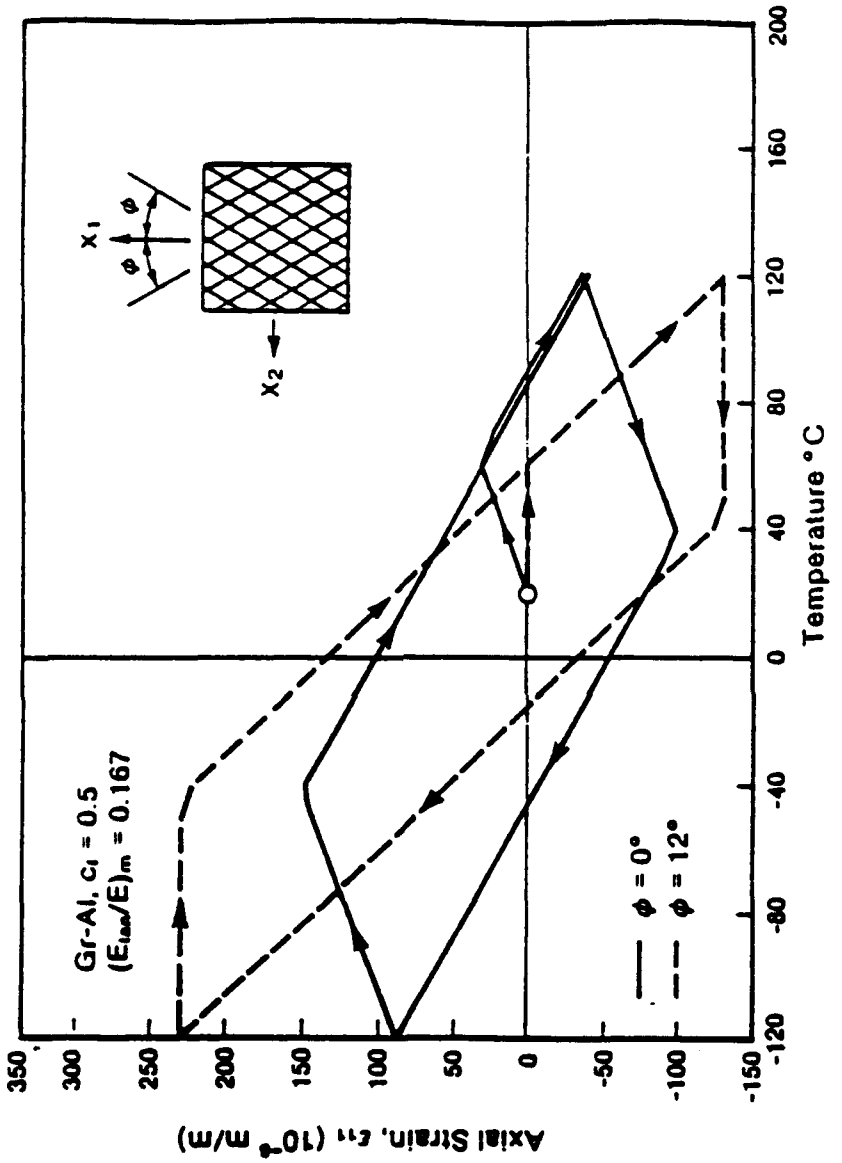

Figure 3.9 Temperature-Axial Strain Response of Angle Ply Composites with $(E_{tan}/E)_m$=0.167

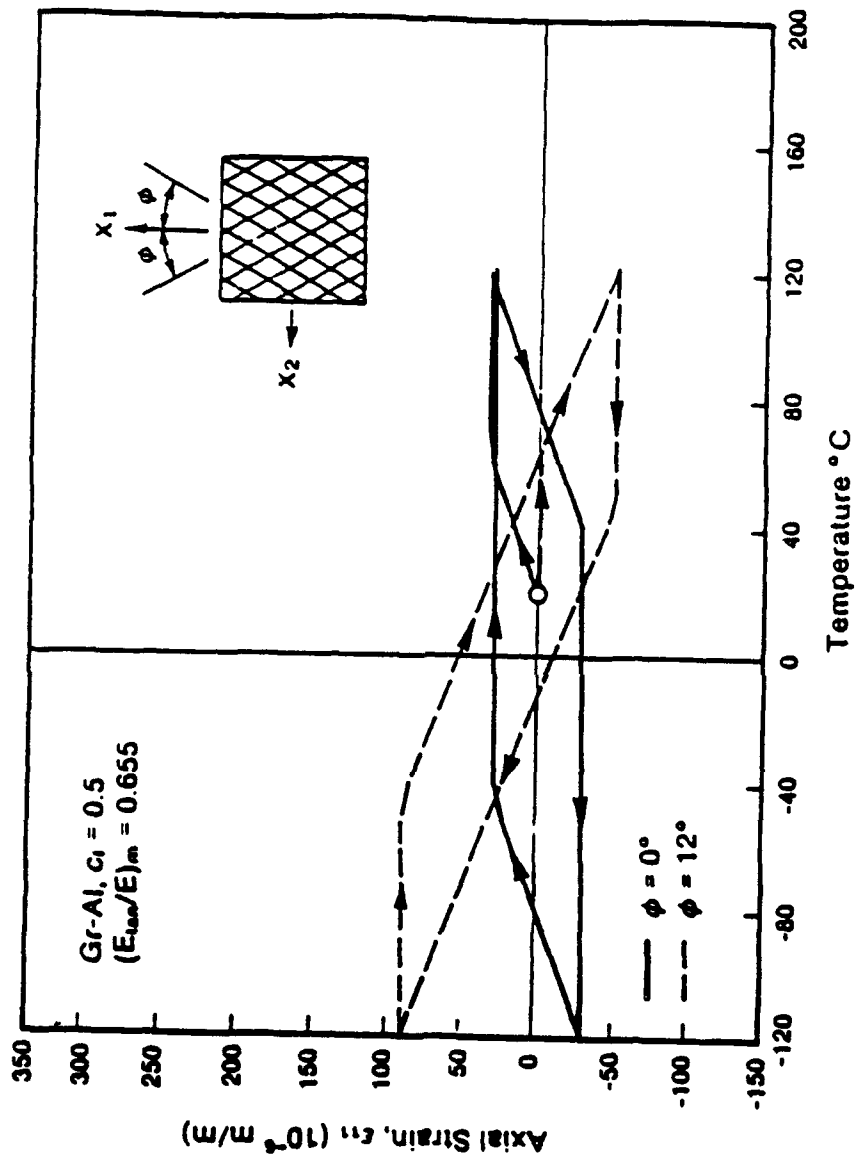

Figure 3.10 Temperature-Axial Strain Response of Angle Ply Composites with $(E_{tan}/E)_m$=0.655

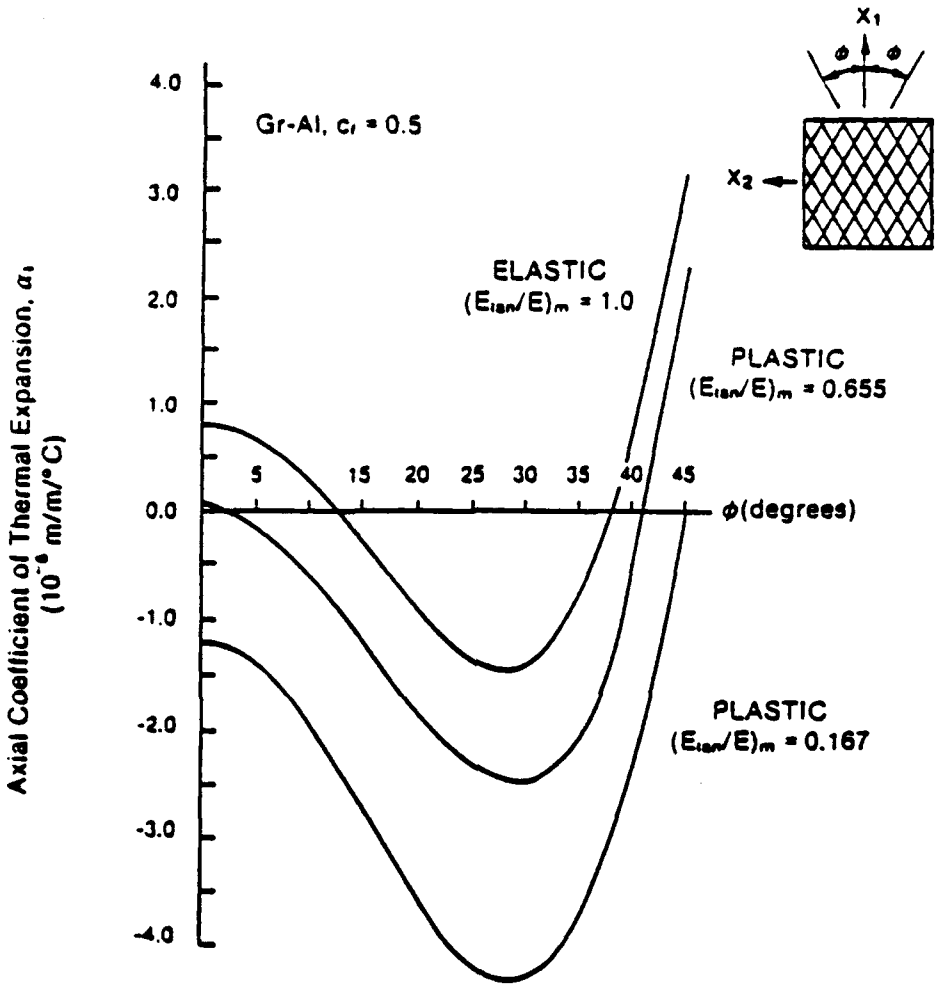

Figure 3.11 Variation of Axial C.T.E. of Composites

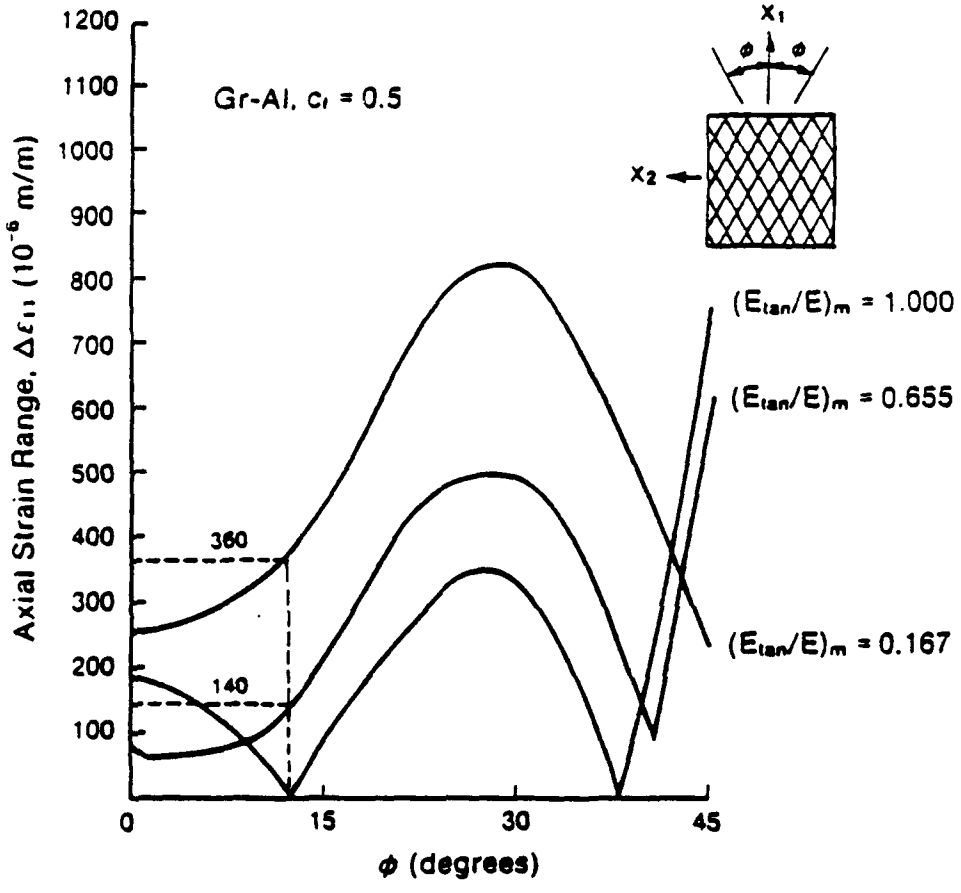

Figure 3.12 Variation of Axial Strain Range of Composite with $\Delta T = 240^0C$

APPENDIX C

Bimodal Plasticity Theory: Description and Finite Element Implementation

CHAPTER 4
BIMODAL PLASTICITY THEORY: DESCRIPTION AND FINITE ELEMENT IMPLEMENTATION

The bimodal plasticity theory proposed by Dvorak & Bahei-El-Din [1987], Bahei–El–Din & Dvorak [1989b, 1991] is a semi-phenomenological model which assumes the plastic deformation of fibrous composites consisting of elastic fibers and elastic-plastic, rate-independent matrix can be described in terms of one of two deformation modes, the fiber-dominated mode (FDM) and the matrix-dominated mode (MDM). In the fiber-dominated mode, both phases deform together in the elastic and plastic range and the composite aggregate is treated in the context of heterogeneous media elasticity and plasticity. In the matrix-dominated mode, plastic deformation is caused by slip on matrix planes which are parallel to the fiber axis. The yield condition corresponding to each mode provides a yield surface in the overall stress space. The overall yield surface of the composite is then given by the inner envelop of the FDM and MDM yield surfaces. The dominant deformation mode is determined by the elastic moduli of the phases, in particular the longitudinal shear modulus, and the overall loads. For example, in the plane stress space, the matrix-dominated mode is active in fibrous composites where the ratio of the longitudinal elastic shear modulus of the fiber and the matrix is large, for example, B/Al and SiC/Al composites. In this case, the large shear stiffness of the fiber prevents slip on matrix planes other than those allowed in the matrix-dominated mode. The fiber–dominated mode is found in composite systems where the fiber longitudinal shear modulus is comparable or smaller than the matrix elastic shear modulus. This mode is also found where the overall axial stress is dominant. Figures 4.1 and 4.2 [Dvorak & Bahei-El-Din, 1987] show examples of composite yield surface for a B/Al and a Gr/Al composite. In the plastic range, the overall instantaneous moduli of the composite are found from the deformation mode

corresponding to the yield branch containing the stress point. Recent experiments by Dvorak, et al, [1988] on a B/Al composite system have verified the existence of the deformation modes postulated by the bimodal plasticity theory. Figures 4.3. and 4.4 [Dvorak & Bahei-El-Din, 1987], show comparison of the experimental yield points and the bimodal yield surface for a B/Al composite.

In this chapter, the fiber-dominated mode and the matrix-dominated mode are described and the constitutive program for each mode is presented. Also, the connection between the two modes is investigated for a general loading path in which loading with a specific mode may have been preceded by deformation with the other mode.

4.1 Fiber-dominated plasticity

Plastic deformation in the fiber-dominated mode is described with the averaging models originally introduced by Hill [1963] for elastic phases. In this section, we describe the governing equations and programming algorithms for implementation of the constitutive relation.

4.1.1 Governing equations

The constitutive relations of the phases are assumed to be known for the volume average of the local fields. Under isothermal loads, the phase strain average $d\epsilon_r$ and stress average $d\sigma_r$, are related by

$$d\sigma_r = L_r d\epsilon_r$$
$$d\epsilon_r = M_r d\sigma_r \tag{4.1}$$

where

$r = f$ or m, f=fiber phase and m=matrix phase.

L_r = instantaneous stiffness matrix of the phases.

$M_r = L_r^{-1}$ = instantaneous compliance matrix of the phases.

Similar relations can be written for the composite overall uniform field:

$$d\sigma = L d\epsilon$$
$$d\epsilon = M d\sigma \tag{4.2}$$

where

L = instantaneous stiffness matrix of the composite.

$M = L^{-1}$ = instantaneous compliance matrix of the composite.

The volume average of the local stress and strain increments are related to their overall counterparts by [Hill, 1963]:

$$d\sigma = c_f d\sigma_f + c_m d\sigma_m$$
$$d\epsilon = c_f d\epsilon_f + c_m d\epsilon_m \tag{4.3}$$

where

c_f, c_m = fiber and matrix volume fractions; $c_f + c_m = 1$.

In addition, the local fields are assumed to be related to the overall fields by:

$$d\sigma_r = B_r d\sigma$$
$$d\epsilon_r = A_r d\epsilon \tag{4.4}$$

where

B_r = instantaneous stress concentration factor of the phases.

A_r = instantaneous strain concentration factor of the phases.

From equations (4.3) and (4.4), the phase concentration factors can be related as:

$$c_f A_f + c_m A_m = I$$
$$c_f B_f + c_m B_m = I \tag{4.5}$$

where I is a unit matrix of order 6.

From equations (4.1), (4.2), and (4.3), the composite overall stiffness and compliance matrices are found as:

$$\begin{aligned} L &= c_f L_f A_f + c_m L_m A_m \\ M &= c_f M_f B_f + c_m M_m B_m \end{aligned} \tag{4.6}$$

Simplified expressions of composite overall stiffness and compliance matrices are obtained by substituting equations (4.5) into equation (4.6):

$$\begin{aligned} L &= L_f + c_m (L_m - L_f) A_m \\ M &= M_f + c_m (M_m - M_f) B_m \end{aligned} \tag{4.7}$$

The overall response of the composite is given in terms of the known local properties of the phases, phase volume fractions, and the concentration factor of the matrix or fiber phases.

4.1.2 Concentration factors

In the elastic range, the concentration factors of the phases can be found from an averaging model. In the present work, the method developed by Mori & Tanaka [1973] was adopted for evaluation of the elastic concentration factors. The fiber stress concentration factor derived from the Mori-Tanaka method is given by [Benvenist, 1987, and Dvorak, 1990a]:

$$B_f = W(c_m I + c_f W)^{-1} \tag{4.8}$$

where W is the fiber stress concentration factor of a dilute solution defined as:

$$W = L_f T M_m \tag{4.9}$$

T is the fiber strain concentration factor of the dilute solution (i.e. found from the case when single fiber is embedded in an infinite matrix) defined as:

$$T = [I + P(L_f - L_m)]^{-1} \tag{4.10}$$

where P is a constant matrix which depends on the shape of the fibers and elastic properties of the matrix. The explicit forms of P matrix for various fiber shapes can be found in the literature (see for example, Dvorak [1990a]).

In the plastic range, a method, which was originally developed by Dvorak [1990a] for the evaluation of the overall plastic strain in the binary composite systems, is utilized to derive the instantaneous concentration factors. For the composites with elastic fibers, the plastic strain increment in the matrix phase $(d\epsilon_m^P)$ is related to the overall plastic strain increment $(d\epsilon^P)$ by

$$d\epsilon^P = c_m B_{me}^T d\epsilon_m^P \tag{4.11}$$

where B_{me}^T is the transpose of the matrix elastic stress concentration factor defined in equation (4.4).

The overall plastic strain and matrix plastic strain can also be expressed as:

$$\begin{aligned} d\epsilon_m^P &= d\epsilon_m - d\epsilon_{me} \\ d\epsilon^P &= d\epsilon - d\epsilon_e \end{aligned} \tag{4.12}$$

where $d\epsilon_{me}$ is the elastic part of the matrix strain increment, $d\epsilon_e$ is the elastic part of the composite overall strain increment, $d\epsilon_m$ is the matrix total strain increment and $d\epsilon$ is the composite overall total strain increment.

Assume that the plastic strain increment of the matrix phase is related to the matrix stress increment $(d\sigma_m)$ through the plastic compliance matrix G:

$$d\epsilon_m^P = G d\sigma_m \tag{4.13}$$

where G is derived from the constitutive model of the matrix material (see Section 4.1.3).

The matrix instantaneous stress concentration factor (B_m^{inst}) can be derived by substituting equations (4.1), (4.11), (4.12), and (4.13) into equation (4.3). The explicit form of the B_m^{inst} is shown as:

$$B_m^{inst} = \left[(M_{me} - M_f) + \left(I - B_{me}^T\right)G\right]^{-1}(M_e - M_f)/c_m \qquad (4.14)$$

where

M_e is the composite overall elastic compliance matrix [$= M_f + c_m(M_{me} - M_f)B_{me}$].

M_{me} is the matrix elastic compliance matrix.

M_f is the fiber compliance matrix (assume always elastic).

The fiber instantaneous concentration factor (B_f^{inst}) and matrix instantaneous concentration factor (B_m^{inst}) can be related by substituting equation (4.10) into equation (4.5):

$$B_f^{inst} = \left(I - c_m B_m^{inst}\right)^{-1}/c_f \qquad (4.15)$$

It can be shown from equations (4.1) to (4.4) that the phase stress concentration factor and strain concentration factor are related as:

$$A_r = M_r B_r L \qquad (4.16)$$

where L is the composite overall stiffness matrix given by equation (4.7).

Note that equation (4.16) is valid in both the elastic and plastic ranges since it is derived from its incremental form.

From equation (4.7), we know that once the instantaneous stress concentration factors of the phases are found, the overall stiffness matrix is determined. There is

alternative way of determining composite instantaneous stiffness matrix. This method is based on the numerical integration of Eshelby's S tensor [Eshelby, 1957], [Gavazzi & Lagoudas, 1990]. However, this numerical integration procedure losses computation efficiency when the material is in nonlinear range. This is because that the matrix phase is no longer isotropic in this stage.

4.1.3 Constitutive equations of the matrix

From equations (4.1.b), (4.12.a) and (4.13), it can be seen that the key quantity that the matrix constitutive equations should provide is the plastic compliance matrix G. For the associated flow rule which satisfies the normality requirement, the G matrix is found as:

$$G = \frac{nn^T}{cn^{*T}n} \tag{4.17}$$

where

$n = \frac{\partial f}{\partial \sigma}$, f is the matrix yield function.

$n_i^* = n_i$ for i=1, 2, 3, and $n_i^* = n_i/2$ for i=4, 5, 6.

$c = 2H/3$, H is the matrix plastic tangent modulus.

Equation (4.17) contains another matrix plasticity parameter H which is known as the matrix plastic tangent modulus. Several theories for evaluation of H under nonproportional loads are found in the literature. Two of the well known theories are the multisurface theory and the two surface theory. The multisurface theory model was introduced by Mroz [1967]. In this model, the yield surface is initially surrounded by a series of concentric hypersurfaces which define a series of different constant values of H. This leads to a piecewise linear stress-strain response in the loading history.

The two surface models are developed (see for example, Hashiguchi [1988], Krieg [1975] and Dafalias & Popov [1976]) mainly for the purpose of simplifying the

complexity which exists in the multisurface model. However, it turns out that the two surface model of Dafalias & Popov [1976] is the only one which allows for the specification of an arbitrary hardening rule for the yield surface. Therefore in our work, the matrix instantaneous plastic tangent modulus (H) is defined through the two surface plasticity theory which was proposed by Dafalias & Popov [1975, 1976]. The theory postulates the existence of a yield surface and a bounding surface, which are capable of defining H, ranging from infinity at the beginning of the yielding to an asymptotic value H_0 when the two surfaces are in contact. This two surface plasticity theory, as indicated in the original paper [Dafalias & Popov, 1976], has the advantage of modeling material behavior under cyclic load. A schematic representation of the two surface theory is shown in Fig.4.5 where the bounding surface is an isotropic expansion of the yield surface and these two surfaces are concentric at the initial state.

For a Mises matrix material with kinematic hardening, the yield surface $f(\sigma_m - \alpha_m)$ and the bounding surface $f(\sigma^* - \beta^*)$ can be written as:

$$f(\sigma_m - \alpha_m) = (\sigma_m - \alpha_m)^T C(\sigma_m - \alpha_m) - Y^2 = 0$$
$$f(\sigma^* - \beta^*) = (\sigma^* - \beta^*)^T C(\sigma^* - \beta^*) - \overline{Y}^2 = 0 \qquad (4.18)$$

where

α_m is the center of matrix yield surface.

β^* is the center of matrix bounding surface.

C is a constant matrix which relates the stress state to the yield function. The explicit form is found as

$$C = \begin{bmatrix} 1 & -0.5 & -0.5 & 0 & 0 & 0 \\ -0.5 & 1 & -0.5 & 0 & 0 & 0 \\ -0.5 & -0.5 & 1 & 0 & 0 & 0 \\ 0 & 0 & 0 & 3 & 0 & 0 \\ 0 & 0 & 0 & 0 & 3 & 0 \\ 0 & 0 & 0 & 0 & 0 & 3 \end{bmatrix}$$

Y is the matrix yield stress in simple tension.

$\overline{Y}$ is the size of matrix bounding surface in simple tension.

Equation (4.18) can be rewritten in terms of overall stress state:

$$f(\sigma - \alpha) = (\sigma - \alpha)^T K(\sigma - \alpha) - Y^2 = 0$$
$$f(\overline{\sigma} - \beta) = (\overline{\sigma} - \beta)^T K(\overline{\sigma} - \beta) - \overline{Y}^2 = 0 \tag{4.19}$$

where

α is the center of the composite yield surface.

β is the center of the composite bounding surface.

$K = B_{me}^T C B_{me}$ = constant matrix.

The centers of composite yield surface α and composite bounding surface β can be found from matrix α_m, β^* through the matrix elastic stress concentration factor B_{me}:

$$\sigma - \alpha = B_{me}^{-1}(\sigma_m - \alpha_m) \tag{4.20}$$

The magnitude of H is defined as [Dafalias & Popov, 1976]:

$$H = H_0 + h\left(\frac{\delta}{\delta_{in} - \delta}\right)^m \tag{4.21}$$

where

δ is the current distance between σ and $\overline{\sigma}$.

δ_{in} is the initial distance between σ and $\overline{\sigma}$ at the onset of initial or subsequent yielding.

H_0 is the asymptotic slope of stress-plastic strain curve.

h, m are material parameters to be determined from experimental data.

Note that the δ and δ_{in} in equation (4.21) are originaly calculated based on matrix stress space. However, it is possible to be evaluated on overall stress state since the composite overall yield surface and bounding surface can be found from matrix state through equations (4.19) and (4.20). The schematic presentation of equation (4.21) is shown in Fig.4.6. It can be seen from Fig.4.6 and equation (4.21) that when $\delta=\delta_{in}$, the plastic tangent modulus H is infinite whereas when $\delta=0$ the plastic tangent modulus H has the value which equals to the asymptotic slope H_0. Also, the plasticity parameters h and m define the degree of nonlinearity of the stress-strain curve.

At the current overall state, σ, α, and β, the corresponding stress point on the bounding surface, $\bar{\sigma}$, can be determined from equation (4.19) by setting the same normal. This leads to the following relation

$$\frac{K(\sigma-\alpha)}{|K(\sigma-\alpha)|}=\frac{K(\bar{\sigma}-\beta)}{|K(\bar{\sigma}-\beta)|}=n \tag{4.22}$$

where n is the unit normal of current stress state. Since $K(\sigma-\alpha)$ and $K(\bar{\sigma}-\beta)$ are parallel, the vectors $K^{-1}K(\sigma-\alpha)$ $[=(\sigma-\alpha)]$ and $K^{-1}K(\bar{\sigma}-\beta)$ $[=(\bar{\sigma}-\beta)]$ must also be parallel. Therefore, equation (4.22) becomes

$$\frac{(\sigma-\alpha)}{|\sigma-\alpha|}=\frac{(\bar{\sigma}-\beta)}{|\bar{\sigma}-\beta|} \tag{4.23}$$

Let $R=|\bar{\sigma}-\beta|/|\sigma-\alpha|$, then equation (4.23) becomes

$$(\bar{\sigma}-\beta)=R(\sigma-\alpha) \tag{4.24}$$

where the ratio R is found by substituting equation (4.24) into equation (4.19b):

$$\begin{aligned} f(\bar{\sigma}-\beta) &= R^2(\sigma-\alpha)^T K(\sigma-\alpha)-\bar{Y}^2 \\ &= R^2Y^2-\bar{Y}^2=0 \end{aligned} \tag{4.25}$$

Therefore, the ratio R becomes:

$$R=\frac{\bar{Y}}{Y} \tag{4.26}$$

and the stress point $\bar{\sigma}$ on the bounding surface is found as

$$\bar{\sigma} = \beta + \frac{\bar{Y}}{Y}(\sigma - \alpha) \tag{4.27}$$

Evaluation of the center of the bounding surface is found from equations (4.24) and (4.26) as [Dafalias & Popov, 1976]:

$$d\beta = d\alpha - Zu \tag{4.28}$$

with

$$u = \frac{(\bar{\sigma} - \sigma)}{|\bar{\sigma} - \sigma|} \tag{4.29}$$

and

$$Z = \left(1 - \frac{H_0}{H}\right)\frac{ds}{u^T n} \tag{4.30}$$

where

$$ds = n d\sigma \tag{4.31}$$

and

$$n = \frac{K(\sigma - \alpha)}{|K(\sigma - \alpha)|} \tag{4.32}$$

4.1.4 Programming algorithm for stress-controlled fiber-dominated constitutive mode

In the stress-controlled fiber-dominated constitutive program, all constitutive calculations are done based on local phase quantities. For a given overall stress increment $d\sigma$ which activates the fiber-dominated mode, the programming steps are described in the following:

1. Divide the overall stress increment $d\sigma$ into small subincrement $p^i d\sigma$, with p^i being a small number which is typically in the order of 10^{-6} to 10^{-8} at the

beginning of an increment. However, the magnitude of p^i are determined by Runge-Kutta-Fehlberg algorithm in the subsequent subincrements.

2. The corresponding stress increment of the local phases $d\sigma_r$ are then defined as:

$$d\sigma_r = B_r^{inst} p^i d\sigma \tag{4.33}$$

3. Check if this is a plastic loading or elastic unloading by use of the matrix loading-unloading criteria:

$$\frac{\partial f}{\partial \sigma_m} d\sigma_m = zz \tag{4.34}$$

where

   a. Plastic loading occurs when $zz > 0$.
   b. Neutral loading occurs when $zz = 0$.
   c. Elastic unloading occurs when $zz < 0$.

4. For plastic loading, $zz > 0$, a numerical integration/iteration scheme must be introduced to integrate the plastic equations. In the bimodal plasticity programming work, the Runge-Kutta-Fehlberg algorithm (see for example, Burden & Faires, [1988]) was chosen to perform the numerical integration. During the numerical integration, the size of the current subincrement is checked. If the current subincrement size is acceptable then the convergent solution of local plasticity quantities are saved and the size of next subincrement p^{i+1} will be computed based on the Runge-Kutta-Fehlberg algorithm. The plasticity quantities consist of:

   a. Matrix plastic strain increment $(d\epsilon_m^p)$.
   b. Shift of the center of the matrix yield surface $(d\alpha_m)$.
   c. The center of the matrix bounding surface $(d\beta_m)$.

d. The instantaneous stress concentration factor of the phases (B_r^{inst}), based on equations (4.14) and (4.15).

5. After the plasticity quantities are found for the subincrement, the local stresses ($d\sigma_r$), strains ($d\epsilon_r$), center of the yield surface (α_m), and the center of the bounding surface (β_m), are updated to their new values:

$$d\epsilon_m = d\epsilon_{me} + d\epsilon_m^p \tag{4.35}$$

$$d\epsilon_f = d\epsilon_{fe} \tag{4.36}$$

$$\sigma_r^{new} = \sigma_r^{old} + d\sigma \tag{4.37}$$

$$d\epsilon_r^{new} = \epsilon_r^{old} + d\epsilon \tag{4.38}$$

$$\alpha_m^{new} = \alpha_m^{old} + d\alpha_m \tag{4.39}$$

$$\beta_m^{new} = \beta_m^{old} + d\beta_m \tag{4.40}$$

$$d\epsilon = c_m d\epsilon_m + c_f d\epsilon_f \tag{4.41}$$

$$\epsilon^{new} = \epsilon^{old} + d\epsilon \tag{4.42}$$

$$\sigma^{new} = \sigma^{old} + p^i d\sigma \tag{4.43}$$

6. Steps 1 to 5 are repeated until the whole increment has been applied.
7. The last step for each overall loading increment is to update the overall stiffness matrix L using equations (4.7), (4.14) and (4.15).

From steps 1 to 7 and equations (4.7), (4.13), (4.14), (4.42), and (4.43), the algorithm for the stress-controlled FDM calculation is completely defined.

4.1.5 Programming steps for strain-controlled fiber-dominated constitutive mode

In the material modelling procedure, the stress-controlled constitutive formulation program has some advantages. For example, the specifications of the loading path for uniaxial or biaxial load cases are easier than the specifications of equivalent loading paths for the strain-controlled constitutive formulation program. However, the draw back of the stress-controlled formulation is the significant computation inefficiency during its finite element applications. Therefore, an alternative and more efficient algorithm for the implementation of the material model into finite element procedure is desired. In the current work, an efficient numerical procedure which is based on the strain-controlled, stress-space formulation was developed. The basic idea of this algorithm is due to the existence of equation (4.2) in each plastic subincrement. With the help of equations (4.21) to (4.32), the constitutive calculations can be carried out on the composite level. For a given overall strain increment $d\epsilon$, the programming steps of the strain-controlled algorithm afe summarized as the following:

1. Divide overall strain increment $d\epsilon$ into small subincrement $p^i d\epsilon$ with p^i being a small number (the magnitude of p^i is determined by the same procedure described in step 1 of Section 4.1.4).
2. The corresponding overall stress subincrement $d\sigma$ is found by:

$$d\sigma = Lp^i d\epsilon \tag{4.44}$$

where L is the composite instantaneous stiffness matrix.

3. The matrix stress subincrement $d\sigma_m$ is then calculated based on equation (4.33).
4. The matrix current stress state $(\sigma_m - \alpha_m)$ is computed by:

$$(\sigma_m - \alpha_m) = B_{me}(\sigma - \alpha) \tag{4.45}$$

5. With the known matrix stress state $(\sigma_m - \alpha_m)$ and its stress subincrement $d\sigma_m$, the loading-unloading criteria (i.e. equation (4.34)) is checked.
6. For the plastic loading case, the Runge-Kutta-Fehlberg numerical algorithm is again used for the integration of plasticity quantities. These quantities include the center of composite overall yield surface, $d\alpha$ and the center of the composite overall bounding surface, $d\beta$.
7. At the end of each subincrement, the plasticity quantities are then updated to their new values:

$$\alpha^{new} = \alpha^{old} + d\alpha \tag{4.46}$$

$$\beta^{new} = \beta^{old} + d\beta \tag{4.47}$$

$$\epsilon^{new} = \epsilon^{old} + p^i d\epsilon \tag{4.48}$$

$$\sigma^{new} = \sigma^{old} + d\sigma \tag{4.49}$$

and the composite instantaneous stiffness matrix L is update based on equations (4.7), (4.14), (4.17), and (4.21) to (4.32).

8. Steps 1 to 7 are repeated until a complete increment has integrated.

Steps 1 to 8 completely describe the algorithm used in the strain-controlled, stress-space FDM constitutive calculation. The advantage of using Runge-Kutta-Fehlberg integration algorithm for constitutive calculation is that this algorithm has the capability of predicting the maximum allowable subincrement size for next subincrement. Therefore, the overall computation effort is minimized during the integration procedure. The user's guide to the bimodal program and selected pseudo codes are given in Appendix D.

4.2 Matrix-dominated plasticity

In the matrix-dominated mode, the deformation of the elastic part is assumed to be the same as the fiber-dominated mode whereas the deformation of the plastic part is derived from plastic slip along the plane(s) parallel to the fiber direction [Dvorak & Bahei-El-Din, 1987, and Bahei–El–Din & Dvorak, 1991].

4.2.1 The slip systems

A typical slip system is shown in Fig.4.7 where the fibers are aligned in X_1–direction. The vector n is a unit normal to the slip plane, s is the slip direction, β is the angle between slip plane and X_1–X_3 plane, and θ is the angle between the slip direction and X_1–axis so that

$$\mathbf{n} = [0 \quad \cos\beta \quad -\sin\beta]^{\mathrm{T}} \tag{4.50}$$

and

$$\mathbf{s} = [\cos\theta \quad \sin\beta\sin\theta \quad \cos\beta\sin\theta]^{\mathrm{T}} \tag{4.51}$$

For a specific overall stress state $\sigma = [\sigma_{11} \quad \sigma_{22} \quad \sigma_{33} \quad \sigma_{31} \quad \sigma_{23} \quad \sigma_{12}]^{\mathrm{T}}$ with the center of the yield surface $\alpha = [\alpha_{11} \quad \alpha_{22} \quad \alpha_{33} \quad \alpha_{31} \quad \alpha_{23} \quad \alpha_{12}]^{\mathrm{T}}$, the resolved

shear stress τ_{ns} on the slip plane of normal n and in the slip direction of s is found as:

$$\begin{aligned}\tau_{ns} &= n_i(\sigma_{ij} - \alpha_{ij})s_j \\ &= \frac{1}{2}\sin 2\beta \sin\theta[(\sigma_{22} - \alpha_{22}) - (\sigma_{33} - \alpha_{33})] + \cos\beta\cos\theta(\sigma_{12} - \\ &\quad \alpha_{12}) - \sin\beta\cos\theta(\sigma_{31} - \alpha_{31}) + \cos 2\beta \sin\theta(\sigma_{23} - \alpha_{23})\end{aligned} \tag{4.52}$$

The resolved shear stress τ_{ns} on the slip plane is the magnitude of the shear stress center, with components τ_1 and τ_2, Fig.4.7, that can be found by substituting θ=0 and $\theta=\pi/2$ respectively, into equation (4.52):

$$\begin{aligned}\tau_1 &= \cos\beta(\sigma_{12} - \alpha_{12}) - \sin\beta(\sigma_{31} - \alpha_{31}) \\ \tau_2 &= \frac{1}{2}\sin 2\beta[(\sigma_{22} - \alpha_{22}) - (\sigma_{33} - \alpha_{33})] + \cos 2\beta(\sigma_{32} - \alpha_{32})\end{aligned} \tag{4.53}$$

Here,

$$\tau_{ns}^2 = \tau_1^2 + \tau_2^2 \tag{4.54}$$

and

$$\begin{aligned}\tau_1 &= \tau_{ns}\cos\theta \\ \tau_2 &= \tau_{ns}\sin\theta\end{aligned} \tag{4.55}$$

Among all the possible slip systems, the active slip planes are those that have the maximum resolved shear stress τ_{ns}. This means that among all β angles, the possible active slip planes are found by setting:

$$\frac{\partial(\tau_{ns})}{\partial\beta} = 0 \tag{4.56}$$

From equations (4.53) and (4.54), the condition stated in equation (4.56) becomes the following trigonometric equation:

$$g(\beta) = \{\frac{[(\sigma_{22} - \alpha_{22}) - (\sigma_{33} - \alpha_{33})]^2}{4} - (\sigma_{32} - \alpha_{32})^2\} \sin 4\beta + (\sigma_{32} - \alpha_{32})[(\sigma_{22} - \alpha_{22}) - (\sigma_{33} - \alpha_{33})] \cos 4\beta - [(\sigma_{12} - \alpha_{12})^2/2 - (\sigma_{31} - \alpha_{31})^2/2] \sin 2\beta - (\sigma_{12} - \alpha_{12})(\sigma_{31} - \alpha_{31}) \cos 2\beta = 0 \tag{4.57}$$

To solve equation (4.57) for possible β's, we should consider the following characteristics of the trigonometric equation:

1. The equation has its own period which is not necessarily equal to 2π.
2. In a specific angle range (say β=0 to π), it is possible to find several β's which all satisfy the equation (4.57). However, only some of these β's are making the magnitude of τ_{ns} an absolute maximum (since the periodic equation may have several roots that maximize the equation locally).

Since evaluation of the roots of equation (4.57) is not so straight forward, it is worth making some effort on the development of an efficient numerical solution scheme. Several useful algorithms have been investigated and summarized in the next section.

4.2.2 Numerical evaluation of the slip systems

When the solution of a specific periodic equation is concerned, two important factors must be considered, include:

1. The solution range of interest.

2. The availability of efficient numerical solution schemes.

Referring to equation (4.57), the solution range for β is $0 \le \beta \le \pi$. This means that all the roots (β's) that are found from equation (4.57) are neglected unless they are in the range from 0 to π in radians (or from 0° to 180° in degree).

Various numerical schemes for obtaining the roots of nonlinear equations exist in the literature, (see for example, [Burden & Faires, 1988]). These methods may be divided into two major families, namely iterative methods and direct methods. The iterative methods find the roots of the equation using a series of trial-and-error root searching schemes and the direct methods find the roots of the equation by numerically evaluating of the roots from explicit expression of the solutions.

The iterative methods have the following advantages

1. The roots of any nonlinear equation can be found if the method is appropriately used.
2. The programming algorithm is extremely simple.

However, there are some drawbacks which may render these methods inefficient, for example:

1. Some roots may be missed during the root searching procedure, especially when the magnitude of two (or more) roots are very close.
2. The size of each searching increment must be very small. This requires more computation effort and reduces the computation efficiency.

On the other hand, the direct methods do have some advantages such as:

1. All the roots of the nonlinear equation can always be found if the roots exist in the specified solution range.
2. No iterations are needed during the root searching procedure.

However, the disadvantage of the direct methods is that:

1. The explicit form of the solutions of the nonlinear equation is not always available.
2. The programming algorithm is more complex and require specific mathematical manipulations.

For the trigonometric equation shown in equation (4.57), it is found [Hall, 1990] that an equivalent nonlinear quartic equation could be obtained. Further development and discussion on the solution scheme to the quartic equation for various stress states was completed here. The study on the investigation of solutions to the equation (4.57) was done jointly by author and by Hall [1990]. The reasons for making this investigation are that:

1. The efficiency of the solution scheme is very critical to the MDM constitutive calculation and its finite element applications.
2. Based on the author's knowledge, almost all of the mathematics handbooks are providing incomplete solutions to the quartic equations (i.e. the solution formulae are good for some cases only). Therefore, a complete solution procedure is derived and implemented in the sequel.

In what follows, we consider the direct method and develop two methods for evaluating the roots of equation (4.57).

We begin by rewriting the equation (4.57) as:

$$A \sin 4\beta + B \cos 4\beta - C \sin 2\beta - D \cos 2\beta = 0 \qquad (4.58)$$

where

$$A = [(\sigma_{22} - \alpha_{22}) - (\sigma_{33} - \alpha_{33})]^2/4 - (\sigma_{32} - \alpha_{32})^2$$

$$B = (\sigma_{32} - \alpha_{32})[(\sigma_{22} - \alpha_{22}) - (\sigma_{33} - \alpha_{33})]$$

$$C = \left[(\sigma_{12} - \alpha_{12})^2 - (\sigma_{31} - \alpha_{31})^2\right]/2$$

$$D = (\sigma_{12} - \alpha_{12})(\sigma_{31} - \alpha_{31})$$

From properties of the trigonometric function, the equation (4.58) can be rearranged into the following form:

$$2B\cos^2 2\beta - D\cos 2\beta - B = (C - 2A\cos 2\beta)\sin 2\beta \qquad (4.59)$$

By squaring both sides of above equation and rearranging all terms, we obtain the following quartic equation:

$$\alpha_1 y^4 + \alpha_2 y^3 + \alpha_3 y^2 + \alpha_4 y + \alpha_5 = 0 \qquad (4.60)$$

where

$$y = \cos 2\beta$$

and

$$\alpha_1 = 4(A^2 + B^2)$$

$$\alpha_2 = -4(AC + BD)$$

$$\alpha_3 = -4(A^2 + B^2 - C^2 - D^2)$$

$$\alpha_4 = 2(2AC + BD)$$

$$\alpha_5 = (B^2 - C^2)$$

The quartic equation shown in the equation (4.60) may be reduced to a quardratic equation or a trivial equation under the following considerations: If $\alpha_1 = 0$, then $A = B = 0$ and $\alpha_2 = 0$. The quartic equation becomes a quadratic equation:

$$\alpha_3 y^2 + \alpha_4 y + \alpha_5 = 0 \qquad (4.61)$$

Consequently, for all stress states, there are only two possible types of equations, namely quartic equation and quadratic equation, for the active slip planes (i.e. β's). More specifically, when the composite is under transverse shear load and/or transverse tension/compression load, the quartic equation solver is needed for finding the β's. On the other hand, if the composite is under longitudinal shear and transverse hydrostatic loads, only the quadratic equation solver is needed for finding the β's. Furthermore, if the composite is under transverse hydrostatic stresses, no slip planes are activated since A=B=C=D=0 in this case and equation (4.60) is identically satisfied, then there is no effects on MDM plasticity since the trivial condition is reached.

Note that the roots found from equation (4.60) are not all good for equation (4.59) because of squaring operation from equation (4.59) to (4.60). These roots must be substituted back to equation (4.59) to determine suitable roots. Once the roots (y's) of equation (4.60) (which also satisfy equation (4.59)) have been found, the possible slip planes are known as:

$$\beta = \pm \cos^{-1}\left(\sqrt{\frac{y+1}{2}}\right) \tag{4.62}$$

From equations (4.60) and (4.62), we can find that the maximum number of slip planes under specific stress state is eight. However, the maximum resolved shear stress (in its absolute value) may not occur on each of these eight slip planes. From the numerical study on the determination of the number of slip planes, it is believed that a maximum of two active slip planes can be expected for all possible stress states (also see Hall, [1990]).

Solution of the quartic equation (i.e. α_1 term exists in equation (4.57)) begins with solution of a specific cubic equation of which the coefficients are calculated from the coefficients of the quartic equation (see for example, Spigal, [1968]).

Assume the quartic equation has the form:

$$y^4 + a_1y^3 + a_2y^2 + a_3y + a_4 = 0 \tag{4.63}$$

where a_1, a_2, a_3, and a_4 are real.

The key step for solving the quartic equation is to reduce the order of the equation. In our case, we may rearrange the equation (4.63) into the following form:

$$\left(y^2 + \frac{a_1}{2}y + \frac{X}{2}\right)^2 - (ry + s)^2 = 0 \tag{4.64}$$

where X, r, and s are numbers to be determined. After expanding equation (4.61) and comparing the coefficients with equation (4.63) term by term, we have the following equations:

$$r^2 = \frac{a_1^2}{4} - a_2 + X \tag{4.65}$$

$$s^2 = \frac{X^2}{4} - a_4 \tag{4.66}$$

$$rs = \frac{a_1X}{4} - \frac{a_3}{2} \tag{4.67}$$

Since a_1, a_2, a_3 and a_4 are known real numbers, it is possible to find X, r, and s from equations (4.65) to (4.67) by seting the following equality:

$$r^2s^2 = \left(\frac{a_1^2}{4} - a_2 + X\right)\left(\frac{X^2}{4} - a_4\right) = \left(\frac{a_1X}{4} - \frac{a_3}{2}\right)^2 = (rs)^2 \tag{4.68}$$

This leads to a cubic equation:

$$X^3 + (-a_2)X^2 + (a_1a_3 - 4a_4)X + (4a_2a_4 - a_1^2a_4 - a_3^2) = 0 \tag{4.69}$$

Equation (4.69) can be solved by the method described in Appendix C. Once the real root of equation (4.69) has been evaluated, it is possible to determine r or s (either one but not both) by substituting X into equation (4.65) or equation (4.66). However, the third unknown among X, r, and s must be calculated with caution. This is because of equation (4.67) that makes the signs of r and s coupled. Therefore, it is very important to keep in mind that only the combinations of equations (4.65) and (4.67) or equations (4.66) and (4.67) can be utilized during the solution procedure. This is the key point that almost all the mathematics references are unable to address in their formula for the solution of quartic equations.

With the known X, r, and s, the equation (4.64) can be rewritten in the following quadratic form:

$$\left[y^2+\left(\frac{a_1}{2}+r\right)y+\left(\frac{X}{2}+s\right)\right]\left[y^2+\left(\frac{a_1}{2}-r\right)y+\left(\frac{X}{2}-s\right)\right]=0 \quad (4.70)$$

Therefore the roots of the quartic equation can then be computed based on two quadratic equations:

$$\begin{aligned}\left[y^2+\left(\frac{a_1}{2}+r\right)y+\left(\frac{X}{2}+s\right)\right]&=0\\ \left[y^2+\left(\frac{a_1}{2}-r\right)y+\left(\frac{X}{2}-s\right)\right]&=0\end{aligned} \quad (4.71)$$

In the direct methods, there are two major algorithms which all the computations are based on either complex numbers or real numbers.

In the complex number version of the algorithm all numbers are treated as complex numbers and the equations (C.9) to (C.12) (see Appendix C) are used for cubic equation solver. This algorithm has the advantage of being easy to program.

In the real number version program, on the other hand, all numerical operations are carefully managed so that any possible complex number encountered in the operations is avoided. The equations (C.15), (C.16) and (C.18) (see Appendix C) are used for finding roots of cubic equation. Also in equation (4.71), the "quadratic discriminant" of each quadratic equation is checked.

The comparison of efficiency among the iterative method, direct method based on complex numbers, and direct method based on real numbers is shown next.

In the numerical study of the solution of quartic equations, the methods described in Section 4.2.2 were all coded. The CPU time was measured for each method under various cases. A large number of numerical tests had been completed. The ratios of overall (i.e. the average of all tested cases) CPU time requirements in the cases of iterative method, complex number method and real number method are approximately equal to 20:2:1. Similar conclusion was made by Hall [1990] who used the author developed solution scheme and real number version program for this numerical study.

4.2.3 The yield conditions

The yield function (f) of the matrix-dominated mode is defined, for the case of kinematic hardening, as the following:

$$f(\sigma - \alpha) = \left[\tau_{ns}^2(\sigma - \alpha)\right]_{max} - \tau_0^2 = 0 \qquad (4.72)$$

where

$(\tau_{ns})_{max}$ is the maximum resolved shear stress of $(\sigma_{ij} - \alpha_{ij})$ on the slip system(s).

τ_0 is the matrix yield stress in simple shear.

This means that the possible slip system (i.e. the slip system which contains maximum resolved shear stress) have reached the yield condition.

It is obvious from equations (4.53), (4.54), (4.56) and (4.57) that under a general stress state the MDM yield surface cannot be expresses in closed form. Construction of the overall yield surface, however, is not necessary in finite element implementations. Only the yield stress under a specific loading path is of interest.

Consider first initial yielding under proportional load defined by the stress increment $d\sigma$, Fig.4.7, the corresponding slip plane angle(s) β and resolved shear stress $(\tau_{us})_{max}$ can be calculated from equations (4.58) to (4.60). The stress magnitude (σ) on the initial yield surface is found by scaling $(\tau_{ns})_{max}$ up to its initial yield stress (see Fig.4.8):

$$\sigma = \gamma d\sigma \tag{4.73}$$

where $\gamma = |\frac{\tau_0}{(\tau_{ns})_{max}}|$

Figures 4.9 and 4.10 show various cross sections of the MDM initial yield surface. The curves in Figs.4.9 and 4.10 were found numerically by evaluating the MDM initial yield stress under stress probes applied in several directions.

Next, consider a subsequent yielding where the current stress state σ is inside an overall yield surface with center located at α. As discussed in Section 4.2.4, the center α is computed from hardening on the active slip system and is assumed to be known from the previous history. Now a stress increment $d\sigma$ is applied to the composite and we would like to compute a factor p so that the stress state $(\sigma+pd\sigma-\alpha)$ satisfies the MDM yield condition (see equation (4.72)).

Referring Fig.4.11, it is clear that different slip systems are activated as p varies (since the possible active slip systems will not remain the same along the segment from σ to $(\sigma+pd\sigma)$). Therefore, the factor p for which the stress $(\sigma+pd\sigma-\alpha)$ satisfies equation (4.72) will be found iteratively using the bisection method [Burden & Faires, 1988]. It was found that, the typical number of iterations required to compute p for MDM yielding is about 25 for a relative tolerance equals to 10^{-5}, where the "relative

tolerance" is defined as:

$$\text{tolerance} = \left| \frac{(\tau_{ns})_{max} - \tau_0}{\tau_0} \right| \tag{4.74}$$

This means that during each MDM plastic loading, the solver of the quartic equation, equations (4.58) and (4.60), must be called 25 times in order to determine the active slip plane(s). Development of an efficient solver for the quartic equations is therefore important.

As seen in Figs.4.9 and 4.10, there are some corners in the yield surface. Since the yield surfaces in Figs.4.9 and 4.10 were obtained numerically, we would like to examine if there is indeed a discontinuity in the slope at the corners as indicated in Figs.4.9 and 4.10. A symbolic solution program (MAPLE, [Char, et al, 1988]) was used for this purpose. If the slopes at the corner points are continuous, only a single valued normal will be found at each point. Therefore, the problem of discontinuity check of the slopes is reduced to the evaluation of the normal $(\partial(\tau_{ns})/\partial\sigma)$ at each of those points.

Let

$$\begin{aligned} k_1 &= \frac{\sigma_{22} - \sigma_{33}}{\tau_0} \\ k_2 &= \frac{\sigma_{21}}{\tau_0} \\ k_3 &= \frac{\sigma_{31}}{\tau_0} \\ k_4 &= \frac{\sigma_{32}}{\tau_0} \end{aligned} \tag{4.75}$$

Then the coefficients A, B, C, and D in equations (4.58) and (4.60) become:

$$
\begin{aligned}
A &= \left(\frac{\sigma_{22}-\sigma_{33}}{2\tau_0}\right)^2 - \left(\frac{\sigma_{32}}{\tau_0}\right)^2 = \left(\frac{k_1}{2}\right)^2 - k_4^2 \\
B &= \frac{\sigma_{32}}{\tau_0}\left(\frac{\sigma_{22}-\sigma_{33}}{\tau_0}\right) = k_1 k_4 \\
C &= \frac{\sigma_{21}^2-\sigma_{31}^2}{2\tau_0^2} = \frac{1}{2}(k_2^2 - k_3^2)^2 \\
D &= \frac{\sigma_{21}\sigma_{31}}{\tau_0^2} = k_2 k_3
\end{aligned}
\tag{4.76}
$$

The procedure for the evaluation of $\partial(\tau_{ns})/\partial\sigma$ is summarized in the following:

1. From equation (4.60), MAPLE is used for determining four symbolic solutions y (say, y_i, i=1,2,3,4) which are the roots of the quartic equation.
2. Substitute stress state (i.e. the stress state at the point of interest) into y_i to find real roots, say y_m (m=1,2,....j).
3. Keep y_m in its symbolic form and solve equation (4.62) for β_l (l=1,2,....,2j) symbolically.
4. From equation (4.53) with $\alpha_{ij} = 0$, we have:

$$
\begin{aligned}
\frac{\tau_1}{\tau_0} &= \cos\beta k_2 - \sin\beta k_3 \\
\frac{\tau_2}{\tau_0} &= \frac{1}{2}\sin 2\beta k_1 + \cos 2\beta k_4
\end{aligned}
\tag{4.77}
$$

and from equations (4.54) and (4.55)

$$
\frac{\tau_{ns}}{\tau_0} = \sqrt{\left(\frac{\tau_1}{\tau_0}\right)^2 + \left(\frac{\tau_2}{\tau_0}\right)^2}
\tag{4.78}
$$

5. Substitute each β_l (l=1,2,....,2j) into equations (4.75) and (4.77) to have $(\frac{\tau_{ns}}{\tau_0})_l$, (where l=1,2,....,2j) in symbolic forms.

6. Substitute stress state into each $(\frac{\tau_{na}}{\tau_0})_l$ and find the maximum $(\frac{\tau_{na}}{\tau_0})$.
7. Keep $(\frac{\tau_{na}}{\tau_0})_n$ which has the maximum value of $(\frac{\tau_{na}}{\tau_0})$ in its symbolic form.
8. Differentiate $(\frac{\tau_{na}}{\tau_0})_n$ with respect to specific component (i.e. k_1, k_2, k_3 and k_4) to find the component of the normal in each stress axis. This means that we are trying to find the symbolic expression for $\partial\left(\frac{\tau_{na}}{\tau_0}\right)_n/\partial k_i$, i=1, 2, 3, 4.
9. Evaluate $\partial\left(\frac{\tau_{na}}{\tau_0}\right)_n/\partial k_i$ numerically and check if the value is unique.

In the numerical study, selected corner points were investigated from steps 1 to 9. The typical result is found, for example in Fig.4.9, that the point of $k_1\left(=\frac{\sigma_{22}-\sigma_{33}}{\tau_0}\right)$=1.43589, $k_2\left(=\frac{\sigma_{21}}{\tau_0}\right)$=0.0, $k_3\left(=\frac{\sigma_{31}}{\tau_0}\right)$=0.90, and $k_4\left(=\frac{\sigma_{32}}{\tau_0}\right)$=0.00 was checked and the $\partial\left(\frac{\tau_{na}}{\tau_0}\right)/\partial k_2$=±0.39286. This confirms that the normal (or slope) at the corner points of MDM yield surface is discontinuous.

4.2.4 Plastic strain and overall stiffness

The plastic slip $[d\gamma_1^p \quad d\gamma_2^p]^T$ on each active slip plane caused by the shear stress $[d\tau_1 \quad d\tau_2]^T$ is found from the associated flow rule and the normality requirement [Bahei-El-Din & Dvorak, 1991]. From equation (4.72), the yield condition on a slip system is written as:

$$f(\tau) = (\tau_1 - \xi_1)^2 + (\tau_2 - \xi_2)^2 - \tau_0^2 = 0 \tag{4.79}$$

where $[d\xi_1 \quad d\xi_2]_k^T$ is the center of the MDM yield surface on the k^{th} active slip plane.

The plastic slip is then given by:

$$\begin{Bmatrix} d\gamma_1^p \\ d\gamma_2^p \end{Bmatrix}_k = \frac{1}{H^* \tau_0^2} \begin{bmatrix} (\tau_1 - \xi_1)^2 & (\tau_1 - \xi_1)(\tau_2 - \xi_2) \\ (\tau_1 - \xi_1)(\tau_2 - \xi_2) & (\tau_2 - \xi_2)^2 \end{bmatrix} \begin{Bmatrix} d\tau_1 \\ d\tau_2 \end{Bmatrix}_k \tag{4.80}$$

where H^* is the plastic tangent modulus in shear.

The overall plastic strain increment is found as the sum of the contributions of each active slip plane. The contribution of plastic strain increment of each slip plane to the composite plastic strain increment is found by coordinate transformation from local (slip plane) coordinate system to overall composite coordinate system. The final form is found as [Bahei-El-Din & Dvorak, 1991]:

$$\begin{Bmatrix} d\epsilon_{11}^p \\ d\epsilon_{22}^p \\ d\epsilon_{33}^p \\ d\epsilon_{31}^p \\ d\epsilon_{32}^p \\ d\epsilon_{21}^p \end{Bmatrix} = \sum_{k=1}^{n} \begin{bmatrix} 0 & 0 \\ 0 & \frac{1}{2}\sin 2\beta_k \\ 0 & -\frac{1}{2}\sin 2\beta_k \\ -\sin\beta_k & 0 \\ 0 & \cos 2\beta_k \\ \cos\beta_k & 0 \end{bmatrix} \begin{Bmatrix} d\gamma_1^p \\ d\gamma_2^p \end{Bmatrix}_k \tag{4.81}$$

where n is the number of the active slip planes under current stress state.

From equations (4.78), (4.79), and (4.53) we can find the MDM plastic compliance matrix G^* which is analogous to equation (4.13). The final form of G^* matrix is found as [Bahei-El-Din & Dvorak, 1991]:

$$G^* = \sum_{k=1}^{n} \frac{1}{H_k^* \tau_0^2} R_k (\sigma - \alpha)(\sigma - \alpha)^T R_k \tag{4.82}$$

where

H_k^* is the k^{th} slip plane's plastic tangent modulus found from a two-surface theory (analogous to equations (4.21) and (4.28) to (4.32)), and

$$R_k = \begin{bmatrix} 0 & 0 & 0 & 0 & 0 & 0 \\ 0 & \frac{1}{4}\sin^2 2\beta_k & -\frac{1}{4}\sin^2 2\beta_k & 0 & \frac{1}{4}\sin 4\beta_k & 0 \\ 0 & -\frac{1}{4}\sin^2 2\beta_k & \frac{1}{4}\sin^2 2\beta_k & 0 & -\frac{1}{4}\sin 4\beta_k & 0 \\ 0 & 0 & 0 & \sin^2\beta_k & 0 & \frac{1}{2}\sin 2\beta_k \\ 0 & \frac{1}{4}\sin 4\beta_k & -\frac{1}{4}\sin 4\beta_k & 0 & \cos^2 2\beta_k & 0 \\ 0 & 0 & 0 & -\frac{1}{2}\sin 2\beta_k & 0 & \cos^2\beta_k \end{bmatrix} \tag{4.83}$$

Although the plastic tangent modulus H_k^* in equations(4.80) and (4.82) is found from the bounding surface theory which analogous to equations(4.21), (4.28) and (4.32), there exist the following differences:

1. The plastic tangent modulus H used in FDM is expressed in simple tension and the plastic tangent modulus H_k^* is expressed in simple shear. However these two quantities may be related through the effective stress increment-effective plastic strain increment relation:

$$H = 3H_k^* \tag{4.84}$$

2. The movement of the yield surface ($d\alpha$) and the movement of the bounding surface ($d\beta$) in the FDM are evaluated on the composite overall level. In the MDM these quantities are evaluated on the local active slip plane level. In order to avoid the confusion on the notations for the center of bounding surface in FDM and for the position of slip plane in MDM, we shall use α^* as the center of composite bounding surface throughout this chapter. Assume that the center of the yield surface on k^{th} slip plane is $\xi^k = [\xi_1^k \quad \xi_2^k]^T$, the center of the bounding surface on that slip plane is $\eta^k = [\eta_1^k \quad \eta_2^k]^T$. In analogy with equation (4.53), ξ^k and η^k are related to the overall center α and α^*, respectively, by:

$$\begin{aligned} \xi_1^k &= \cos\beta^k \alpha_{21} - \sin\beta^k \alpha_{31} \\ \xi_2^k &= \frac{1}{2}\sin 2\beta^k (\alpha_{22} - \alpha_{33}) + \cos 2\beta^k \alpha_{32} \end{aligned} \tag{4.85}$$

and

$$\begin{aligned} \eta_1^k &= \cos\beta^k \alpha_{21}^* - \sin\beta^k \alpha_{31}^* \\ \eta_2^k &= \frac{1}{2}\sin 2\beta^k (\alpha_{22}^* - \alpha_{33}^*) + \cos 2\beta^k \alpha_{32}^* \end{aligned} \tag{4.86}$$

The center of the bounding surface can be written as (see equations (4.28) to (4.32)):

$$d\eta^k = d\xi^k - z u^k \tag{4.87}$$

$$z = \left(1 - \frac{H_0^*}{H^*}\right)_k \frac{d\tau_{ns}^k}{u^{k^T} n'} \tag{4.88}$$

where

u^k is the unit vector that connects the loading point with normal $n' = [\cos\theta \quad \sin\theta]^T$ (θ is defined in equation (4.51)) and the point on the bounding surface with the same normal.

α_{ij} are the components of the center of overall yield surface α.

α_{ij}^* are the components of the center of overall bounding surface α^*.

Equations (4.85) and (4.86) are also valid for their incremental form since all the operations are dependent on slip angle only. The reverse relations of equations (4.85) and (4.86) in their incremental forms are found as [Bahei-El-Din & Dvorak, 1991]:

$$\begin{aligned} d\alpha_{22} &= -d\alpha_{33} = \sin 2\beta^k d\xi_2^k \\ d\alpha_{31} &= -\sin\beta^k d\xi_1^k \\ d\alpha_{32} &= \cos 2\beta^k d\xi_2^k \\ d\alpha_{21} &= \cos\beta^k d\xi_1^k \end{aligned} \tag{4.89}$$

and

$$
\begin{aligned}
d\alpha^*_{22} &= -d\alpha^*_{33} = \sin 2\beta^k d\eta^k_2 \\
d\alpha^*_{31} &= -\sin \beta^k d\eta^k_1 \\
d\alpha^*_{32} &= \cos 2\beta^k d\eta^k_2 \\
d\alpha^*_{21} &= \cos \beta^k d\eta^k_1
\end{aligned}
\tag{4.90}
$$

It is shown in Section 4.3 that the equations (4.89) and (4.90) have provided an important contribution in combining FDM and MDM into complete constitutive model.

After the MDM plastic compliance matrix has been found (equations (4.82) to (4.88)), the MDM overall instantaneous stiffness matrix L is calculated as:

$$L = (M_e + G^*)^{-1} \tag{4.91}$$

where M_e is the composite elastic compliance found from equation (4.7).

4.2.5 Hardening rules used in MDM

The MDM hardening rules are determined based on experimental observation from the test performed by Dvorak, et al., [1988] on a B/Al composite. More specific description of the MDM hardening rule is found in Bahei-El-Din & Dvorak [1991].

It is shown that there are three different hardening rules in six-dimensional stress space:

1. Hardening rule I:

   This is the case when

$$(\sigma_{31} - \alpha_{31}) = (\sigma_{32} - \alpha_{32}) = 0 \tag{4.92}$$

   and

$$\left| \frac{(\sigma_{21} - \alpha_{21})}{(\sigma_{22} - \alpha_{22}) - (\sigma_{33} - \alpha_{33})} \right| \geq 1 \tag{4.93}$$

The center of the yield surface $d\alpha_{ij}$ is found as $d\alpha_{21} = d\sigma_{21}$ with all other components equal to zero.

2. Hardening rule II:

   This is the case when

$$(\sigma_{21} - \alpha_{21}) = (\sigma_{32} - \alpha_{32}) = 0 \tag{4.94}$$

   and

$$\left| \frac{(\sigma_{31} - \alpha_{31})}{(\sigma_{22} - \alpha_{22}) - (\sigma_{33} - \alpha_{33})} \right| \geq 1 \tag{4.95}$$

   The center of the yield surface $d\alpha_{ij}$ is found as $d\alpha_{31} = d\sigma_{31}$ with all other components equal to zero.

3. Hardening rule III:

   For all cases other than cases I. and II. In this case, $d\alpha_{ij} = d\sigma_{ij}$ (i.e. Phillip's hardening rule is assumed).

Note that from Fig.4.10 we can find that the hardening rules I and II are the cases when the stress state is at the flat part of the yield surface.

4.2.6 Programming algorithm for strain-controlled matrix-dominated constitutive mode

The programming algorithm for strain-controlled matrix-dominated constitutive mode is analogous to the programming algorithm described in Section 4.1.5. For a given overall strain increment $d\epsilon$, the programming steps of the strain-controlled, stress-space matrix-dominated constitutive mode are summarized as the following:

1. Divide overall strain increment $d\epsilon$ into small subincrement $p^i d\epsilon$ with p^i being a small number.

2. The corresponding overall stress subincrement $d\sigma$ is found by:

$$d\sigma = L p^i d\epsilon \tag{4.96}$$

where L is the composite instantaneous stiffness matrix.

3. With the known overall stress σ, center of overall yield surface α and overall stress increment $d\sigma$, we can calculate the trial stress state as:

$$\sigma^{new} = \sigma - \alpha + d\sigma \tag{4.97}$$

4. Substitute σ^{new} into equations (4.57) and (4.72). The plastic loading will occur when the value of equation (4.72) is greater than or equal to zero.
5. For the plastic loading case, the Runge-Kutta-Fehlberg numerical algorithm (see [Burden & Faires, 1988]) is used for the integration of the plasticity quantities. These quantities including the center of the overall yield surface $d\alpha$ and the center of the overall bounding surface $d\alpha^*$ are found from equations (4.80) to (4.95).
6. At the end of each subincrement the plasticity quantities are updated based on equations (4.46) to (4.49).
7. The composite instantaneous stiffness L is updated based on equations (4.82), (4.83) and (4.91).
8. Steps 1 to 7 are repeated until a complete increment has been integrated.

These steps completely describe the plasticity algorithm used in MDM case. Some selected MDM subroutines will be discussed in the next section.

4.3 Implementation of the bimodal theory for general loading

In the preceding two sections, the formulation of fiber-dominated mode and the formulation of matrix-dominated mode were described individually assuming that either

mode is the only active mode during the loading path. Under general loading path, activation of one mode in part of the loading regime may have been preceded by plastic deformation with the other mode. Consequently, each deformation mode should not only describe its constitutive behavior but also fully support all the data information which may be shared by the other deformation mode. The basic requirement on this issue is discussed in the next subsection. The program steps and the user's guide of the bimodal model program are described at the end of this section and Appendix D, respectively.

4.3.1 Data base exchange between FDM and MDM

It is shown in Sections 4.1 and 4.2 that in the strain-controlled, stress-space constitutive formulation, the most important plasticity quantities are the position of the center of the composite overall yield surface, α, the position of the center of composite overall bounding surface, α^*, and the composite instantaneous plastic compliance matrix G (in FDM case) or G^* (in MDM case). The composite instantaneous plastic compliance matrix is important due to the fact that the composite overall instantaneous matrix L is always found by the inverse of the sum of the elastic compliance matrix and the instantaneous plastic compliance matrix.

In the MDM, there are an infinite number of slip systems in the composite. Plastic straining on the active slip system will also affect the inactive slip planes. This is known as the latent hardening of inactive slip systems. It is shown in Bahei-El-Din & Dvorak [1991] that the overall centers of the yield surface α and bounding surface α^* can be replaced by their local counterparts from the active slip systems or inactive slip systems. Therefore it is possible to relate hardening of active slip systems with the latent hardening of inactive slip systems. This means that during the plastic deformation on the active slip system, the inactive slip systems hardens simultaneously. This simplifies

the operation of finding current centers of yield surface and bounding surface during the MDM constitutive calculation.

Once the plasticity quantities α and α^* are known, it can be shown that

1. From equations (4.21) to (4.32), the G is found based on the equation (4.17) and $d\alpha$ and $d\alpha^*$ are updated.
2. From equations(4.80) to (4.85), the G^* is found by equations (4.82) and (4.83) and $d\alpha$, $d\alpha^*$ are updated.

These mean that the response of both FDM and MDM can be calculated at any loading point. Also, both modes are capable of sharing and updating the overall instantaneous quantities (i.e. $d\alpha$, $d\alpha^*$ and L) which may be used at next loading point for either mode.

4.3.2 Programming steps for the bimodal model

The programming steps for the bimodal model can be seen as the combination of the programming steps used in FDM (Section 4.1.5) and MDM (Section 4.2.6).

The procedure is summarized as the following:

1. Divide overall strain increment $d\epsilon$ into small subincrement $p^i d\epsilon$ with p^i being a small number.
2. The corresponding overall stress subincrement $d\sigma$ is found by:

$$d\sigma = Lp^i d\epsilon \tag{4.98}$$

where L is the composite instantaneous stiffness matrix.

3. Check yield criteria for both modes (i.e. equations (4.33), (4.34) and (4.45) for FDM and equations(4.54) to (4.58), (4.72) and (4.96) for MDM) and determine which mode yield first.
4. Set up the plasticity indicator to the mode which has been activated first.

5. If FDM or MDM (with hardening rule III) is active then the composite will stay in FDM or MDM during the loading increment. However, if MDM is active and it is in the cases of hardening rule I or II, Step 4. must be checked at each subincrement since it is possible to change from the current hardening rule to the other hardening rule or even change to FDM.
6. Once the plasticity mode and type of the hardening rule (for MDM) have been determined the rest procedure described in Section 4.1.5 or Section 4.2.6 will be continued for the corresponding deformation mode.
7. Steps 1. to 6. are repeated until the current increment is completed.

A user's guide to the bimodal constitutive program is given in the Appendix L.

4.4 Implementation into general purpose finite element code

The general concepts of the integration of material model into ABAQUS have been stated in both Chapters 2 and 3. However, there still exists some differences in the implementation details due to the nature of the constitutive relations used in the individual material model. In the development of the bimodal plasticity theory based UMAT subroutine, there are several choices for the numerical implementation algorithms. We have conducted a study on the material constitutive formulations and their numerical implementation to arrive at the most efficient implementation algorithm.

From the numerical experience obtained in this study, we concluded that the strain-controlled constitutive program has the best computation performance for the composite material models, therefore the constitutive program of the bimodal theory was then developed based on stress-space, strain-controlled formulation.

During the development of the bimodal constitutive program, we discovered an efficient algorithm for the strain-controlled constitutive calculations. The most important feature of this algorithm is that almost all the constitutive calculations are done on the

composite overall level. The detail algorithm is described in Sections 4.1.5 and 4.2.6 for FDM and MDM, respectively.

Since the bimodal plasticity program is based on the stress-space, strain-controlled formulation, the programming steps are different from the programming steps used in PHA model (see Section 3.4.3). The summary of the steps which are carried out in the UMAT with bimodal plasticity theory is the following:

1. At the beginning of a load increment, ABAQUS provides the solution dependent variables to UMAT together with the load increment.
2. For an elastic response, the composite overall stiffness matrix (i.e. the stiffness matrix at material point of finite element mesh) is computed from the FDM constitutive relation.
3. For an elastic-plastic response, the overall yield branch (FDM or MDM) which contains the current stress point is determined and the corresponding constitutive equations are used to compute instantaneous stiffness matrix.
4. Finally, the overall stresses, instantaneous stiffness matrix, and the solution dependent variables are updated at the end of the load increment.

The flow chart for these steps is similar to the flow chart shown in Fig.3.6 except the local iteration loop (the loop that loops from equations (3.36) to (3.38)) since in the strain-controlled constitutive formulation case, there is no need to perform local iterations in its UMAT subroutine. The pseudo code of the bimodal theory based UMAT subroutine is given in Appendix D.

4.5 Selected results

The CPU time and overall strains found by the algorithms given in Section 4.4 for a $(\pm 10)_s$ P-100 Gr/Al composite laminate under uniaxial cycle of ±400 MPa are

shown in Tables 4.1 and 4.2. The material properties of the constituents used in these demonstration cases are listed in the Table 3.1 and the finite element model is shown in Fig.3.8.

In Table 4.1, the relative computation efficiency of each algorithm can be found by subtracting the elastic part of CPU time from total required CPU time. In this table, only the CPU time that used for finite element procedure are counted. The CPU time that used for input data syntax check is not included here. It is clear that the strain-controlled bimodal formulation algorithm which described in sections 4.1.5 and 4.2.6 has the best computation performance.

In Table 4.2 the laminate overall longitudinal and transverse strains at the end of loading cycle demonstrate the consistency of all the algorithms used in this example. In both longitudinal and transverse response, the relative differences between algorithms b, c, and d are all less than 1 percent. The difference between b and c is due to stress-controlled and strain-controlled algorithms used in these two cases.

Figures 4.12 and 4.13 show the predictions of the bimodal theory and the PHA model for the axial response and transverse response of a $(\pm 10)_s$ composite laminate consisting of P-100 Gr/Al plies under uniaxial cycle of ±400 MPa. The material properties are again shown in Table 3.1 of Chapter 3. Linear kinematic hardening behavior, which was assumed in the PHA model based UMAT subroutine, was simulated in bimodal theory based UMAT subroutine by setting the size of the yield surface equal to the size of the bounding surface so that the matrix instantaneous plastic tangent modulus reaches its asymptotic value right after yielding. These two figures are used to show the comparison between FDM and PHA model since it is in FDM under this load condition.

Figures 4.14 and 4.15 demonstrate the constitutive behavior of fibrous composite when a bounding surface is used in the theory. The composite material system used in the analysis is the B/Al where the material properties of the constituents are listed in

Table 4.3. In Fig.4.14, the loading cycle is specified so that the magnitude of unloading is small. Therefore, the reloading curve is flatter than unloading curve since the plasticity is not well developed in the unloading stage. This results in the reloading curve departures from initial loading curve. Fig.4.15 shows another loading cycle. In this case, the plasticity has been well developed in both loading and unloading segment. Therefore, when the composite is reloaded, the stress-strain curve merges to the asymptotic line. Note that the stress-strain response of the loading segment is the same as the stress-strain response shown in Fig.11 (bimodal MDM curve) of Dvorak, et al [1990].

Another illustration of the bimodal theory is shown in Fig.4.16 when the axial stress-strain response of $(\pm\phi)_s$ B/Al composite is given. A set of laminates with different orientations (ϕ=0° to 90° with 5° increment between cases) are investigated. The FDM response is found in the cases when ϕ is less than 25° and the MDM response is found when ϕ greater than 30°. As expected, the response of the laminate is stiffer under the FDM deformation because of the constraints imposed by the fibers on the matrix response.

Figures 4.17 and 4.18 show the response of B/Al unidirectional laminate under a loading path which first activates the MDM, and then the FDM. The loading path is specified as follows:

1. At point A, σ_{11}=0 MPa and σ_{22}=0 MPa (X_A=X_1).
2. At point B, σ_{11}=10 MPa and σ_{22}=100 MPa.
3. At point C, σ_{11}=10 MPa and σ_{22}=75 MPa.
4. At point D, σ_{11}=600 MPa and σ_{22}=75 MPa.

From point A to point B, the response is basically in MDM. In this loading segment, the transverse response (σ_T-ϵ_T) goes from elastic to plastic whereas the axial response (σ_L-ϵ_L) remains elastic since there is no plastic strain in fiber direction during matrix-

dominated deformation. From point B to point C, the composite is in unloading from MDM. This is indicated by linear segments of $\overline{BC}$ in both σ_A–ϵ_A curve and σ_T–ϵ_T curve. From point C to point D, the composite is reloaded to FDM. As expected, the axial response is much stiffer (compare to segment $\overline{AB}$ of σ_T–ϵ_T curve). The segment $\overline{CD}$ in σ_T–ϵ_T curve is the response which induced by the axial load (σ_{11}=10 MPa to 600 MPa). Although it is in plastic range, the nonlinear curve can not be seen in this segment since it is plotted in σ_T–ϵ_T relation where σ_T is constant during the loading segment.

Figure 4.18 is an enlarged portion of loading points A-B-C of σ_A–ϵ_A curve shown in Fig.4.17. These two figures can be used to demonstrate the data communication between MDM and FDM in the bimodal plasticity program.

Cases	Formulation and algorithm types	CPU time (Sec.)
a	PHA , stress-controlled, return instantaneous stiffness (Section 3.4)	2,538
b	Bimodal, stress-controlled, return instantaneous stiffness (Section 4.1.4)	2,115
c	Bimodal, strain-controlled, return instantaneous stiffness (Section 4.1.5)	1,655
d	Improved bimodal, return instantaneous stiffness (Sections 4.2.6 and 4.3)	616
e	Elastic response (Section 4.1)	340

Table 4.1 CPU time required in different constitutive formulation algorithms.

Cases	Axial strain (x10-3)	Transverse strain (x10-3)
a (PHA)	1.156675	-0.802513
b(Bimodal)	1.156075	-0.792350
c (Bimodal)	1.156075	-0.792488
d (Bimodal)	1.156075	-0.792488

Table 4.2 Overall Longitudinal and Transverse Strains After Loading Cycle.

Properties	Fiber	Matrix
Volume fraction	0.5	0.5
Young's modulus (MPa)	4.0000 × 10+5	7.2500 × 10+4
Poison's ratio	0.20	0.33
Initial yield stress in tension (MPa)		2.3640 × 10+1
Size of bounding surface in tension (MPa)		8.8335 × 10+1
H_0 for plastic tangent modulus (MPa)		2.1000 × 10+4
m value for plastic tangent modulus		2.0
h value for plastic tangent modulus (MPa)		3.6000 × 10+5

Table 4.3 Material Properties for Boron-Aluminum Composite

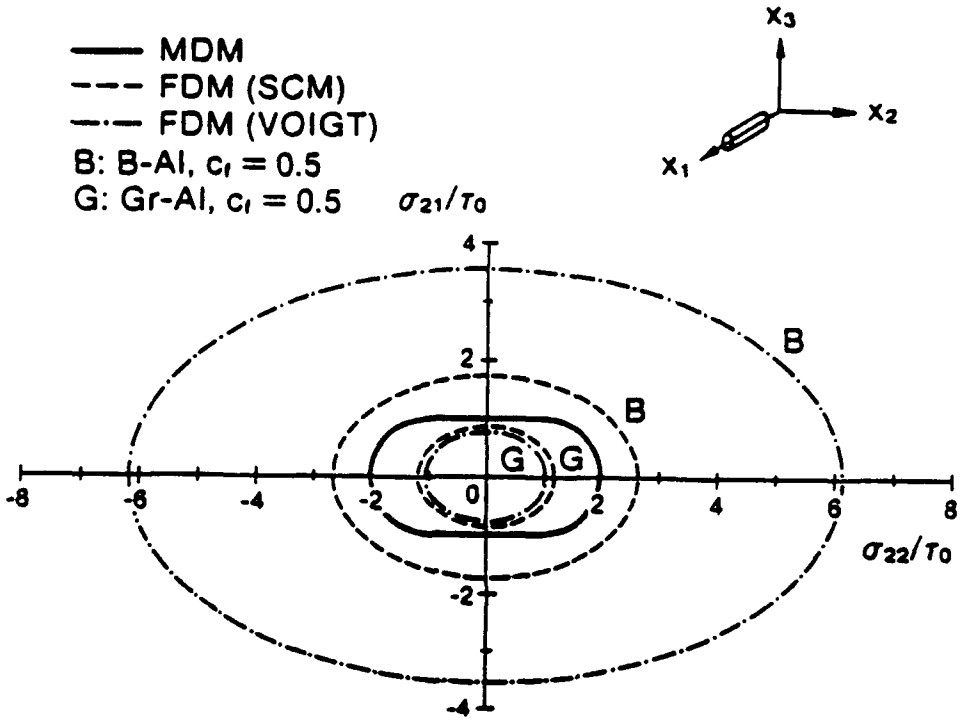

Figure 4.1 Initial Yield Surface in the $\sigma_{21}\sigma_{22}$–plane. Comparison of FDM and MDM in Boron and Graphite- Aluminum Composite Systems. [Dvorak & Bahei-El-Din & Dvorak, 1987]

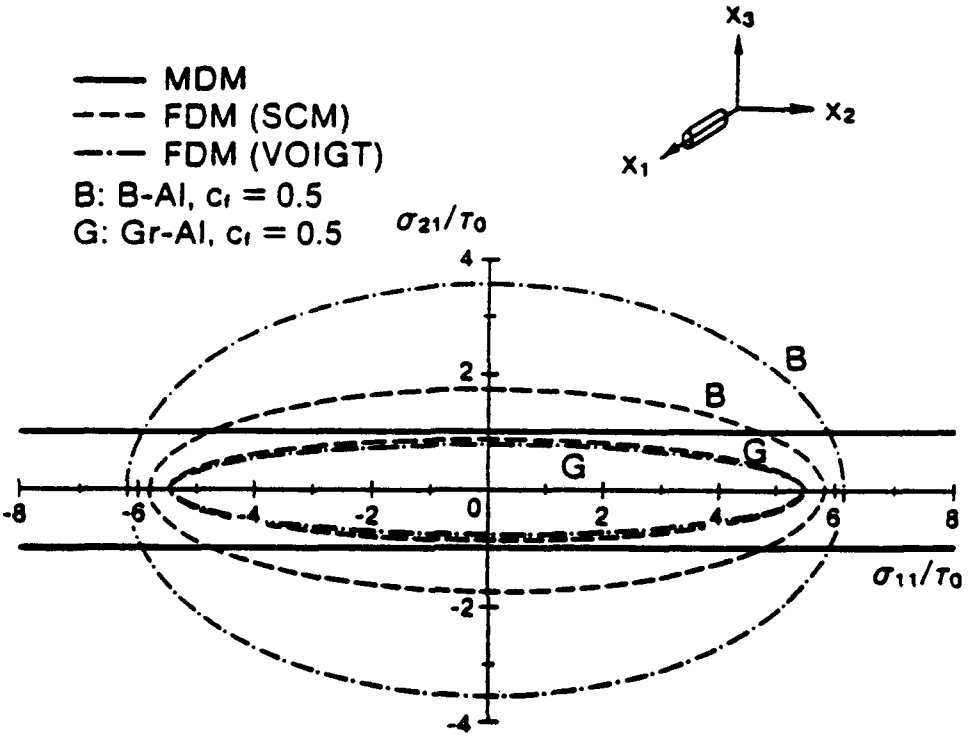

Figure 4.2 Initial Yield Surface in the $\sigma_{21}\sigma_{11}$–plane. Comparison of FDM and MDM in Boron and Graphite-Aluminum Composite Systems. [Dvorak & Bahei-El-Din & Dvorak, 1987]

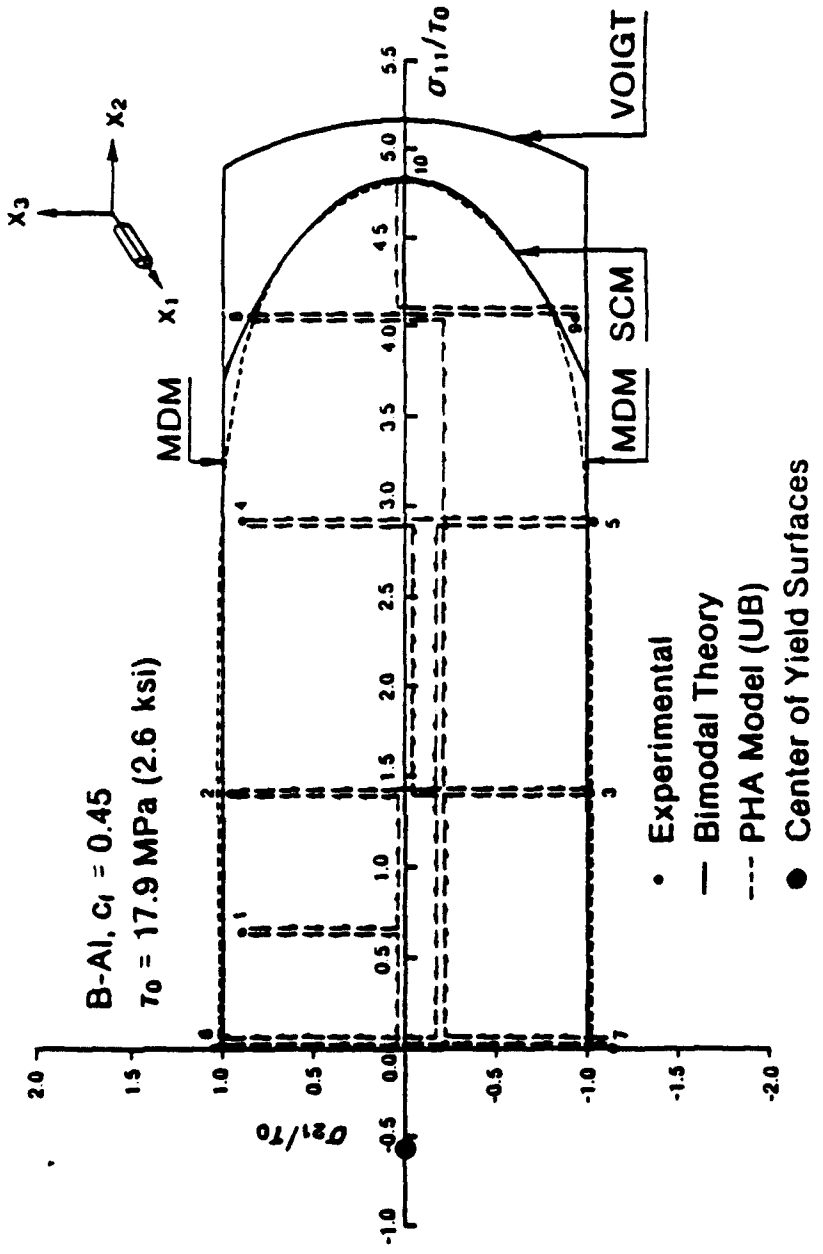

Figure 4.3 Initial Yield Surface of a B/Al Composite in the $\sigma_{21}\sigma_{11}$–plane. Comparison of Experimental Results with Yield Surface Derived from Bimodal Plasticity Theory and the Periodic Hexagonal Array (PHA) Model. [Dvorak & Bahei-El-Din & Dvorak, 1987]

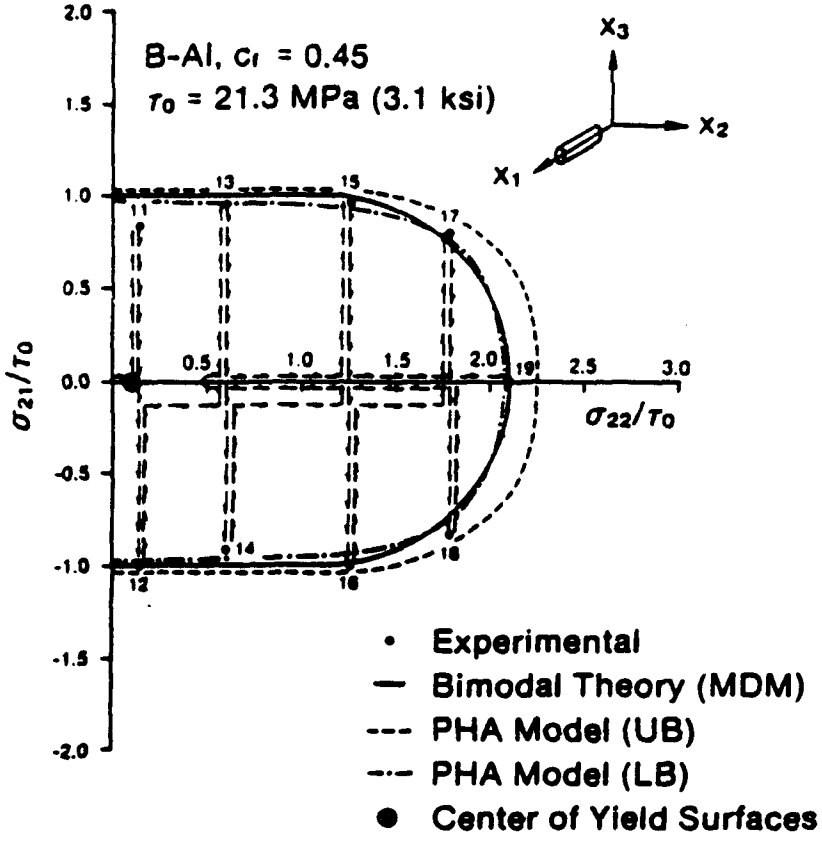

Figure 4.4 Initial Yield Surface of a B/Al Composite in the $\sigma_{21}\sigma_{22}$–plane. Comparison of Experimental Results with MDM Yield Surface and the Periodic Hexagonal Array (PHA) Model. [Dvorak & Bahei-El-Din & Dvorak, 1987]

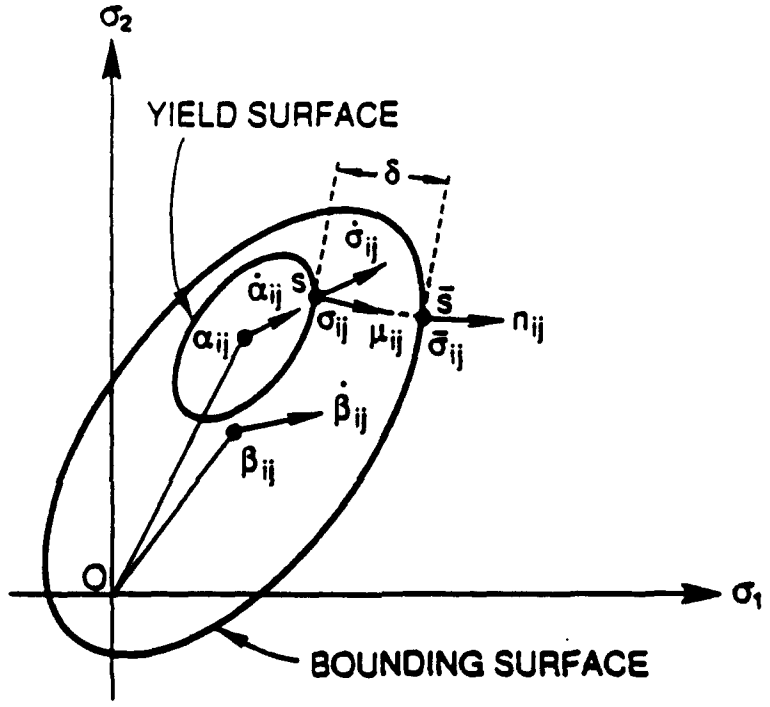

Figure 4.5 Schematic Representation of the Yield and the Bounding Surfaces and Their Motion During Plastic Flow.

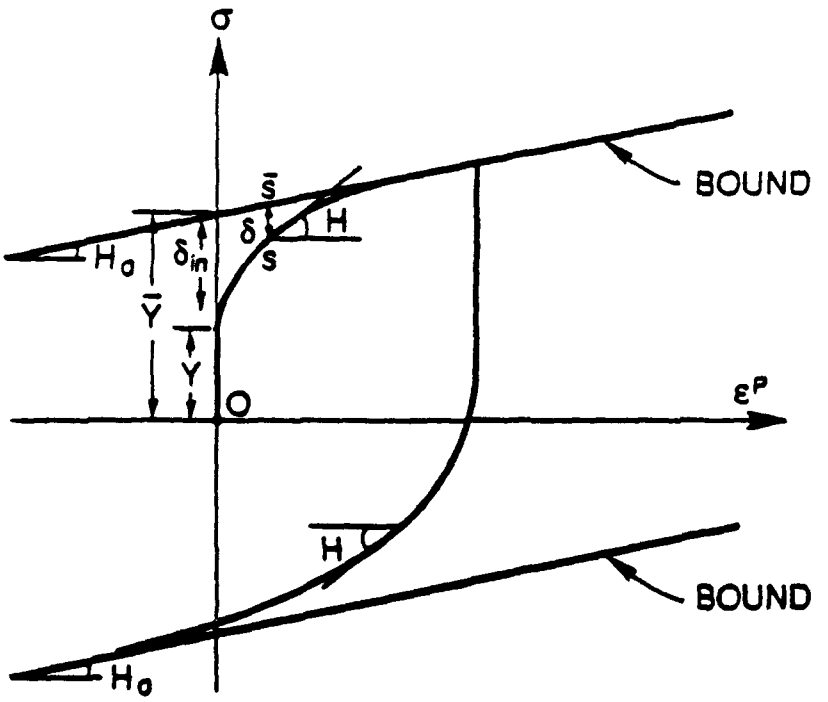

Figure 4.6 Schematic Presentation of δ_{in}, δ, H, H_0, Y and $\overline{Y}$

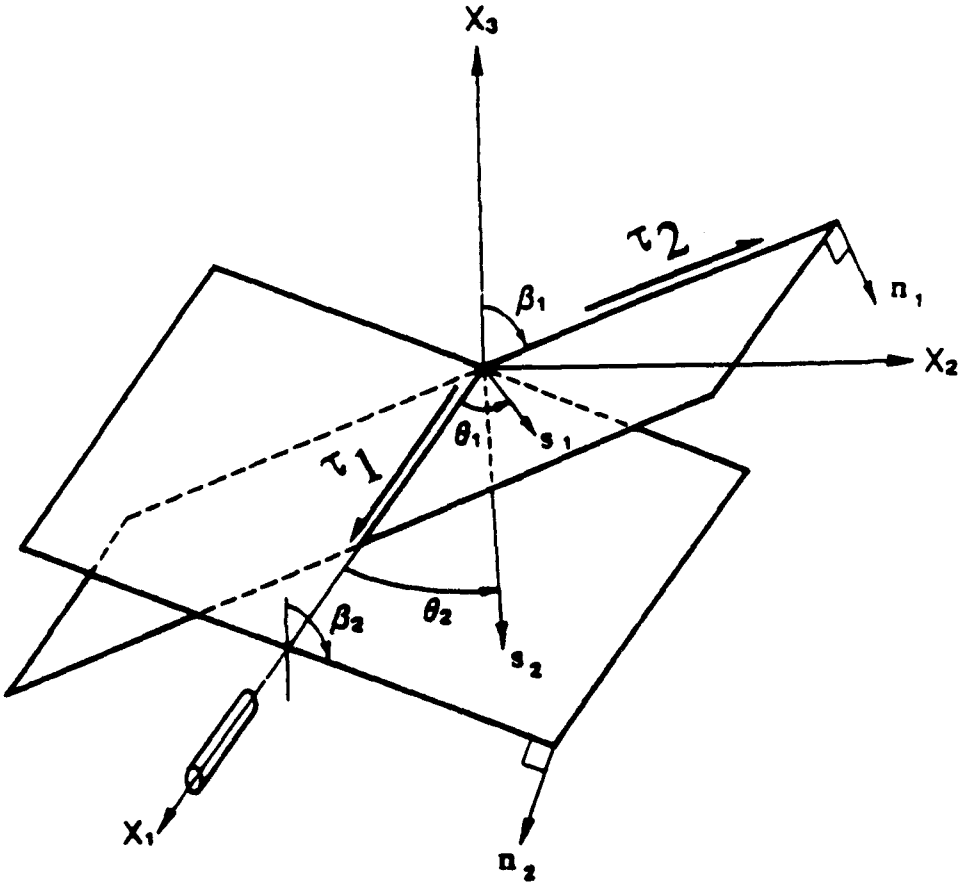

Figure 4.7 Geometry of the Slip Systems.

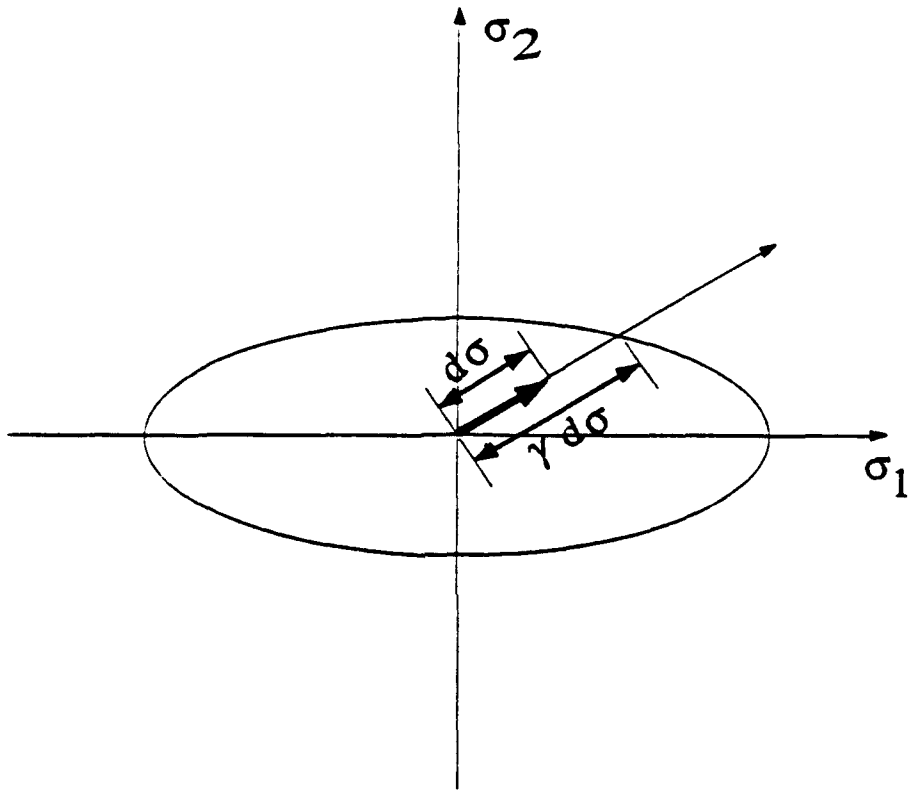

Figure 4.8 Schematic Representation of the

Method for Finding MDM Initial Yield Surface

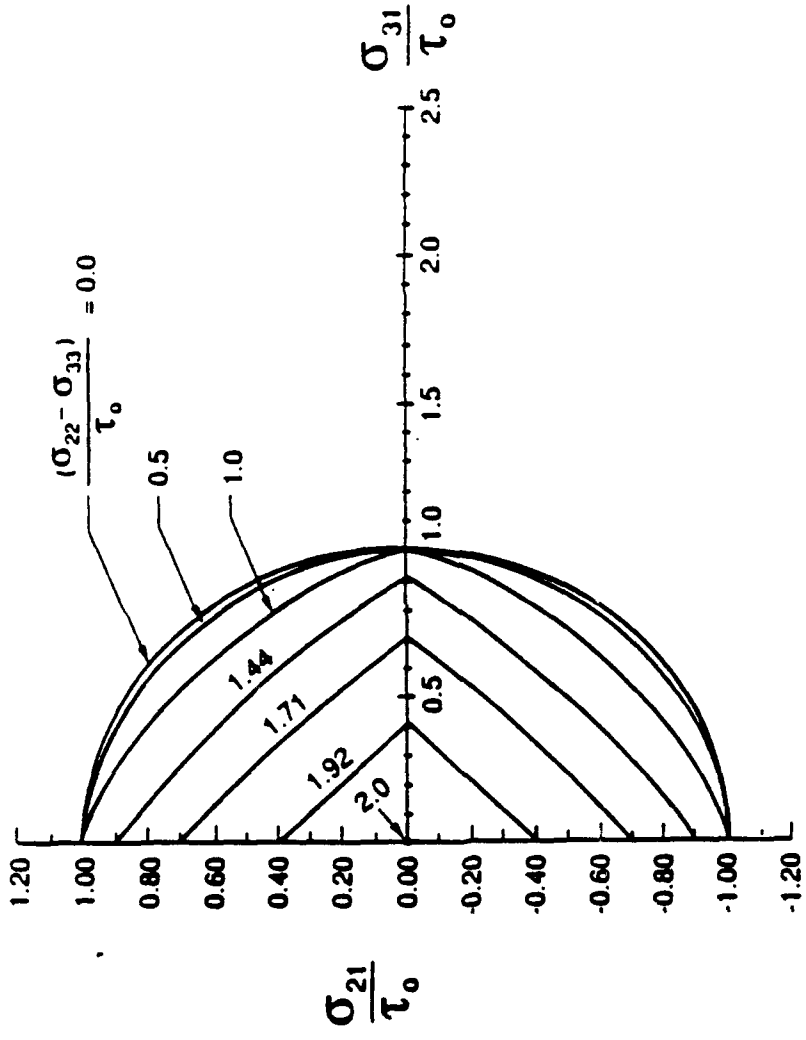

Figure 4.9 Several Sections of the MDM Yield Surface in the $\sigma_{21}\sigma_{31}$–plane.

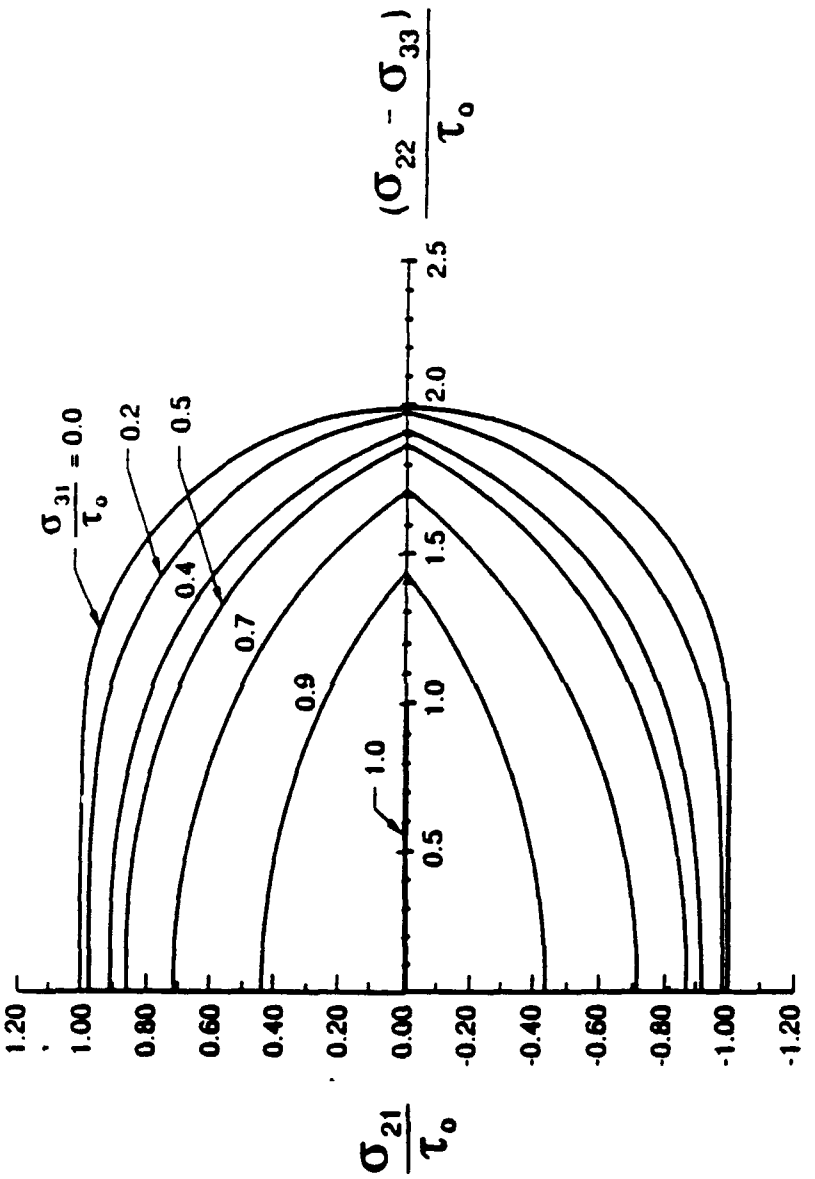

Figure 4.10 Several Sections of the MDM Yield Surface in the $\sigma_{21}(\sigma_{22}$-$\sigma_{33})$-plane.

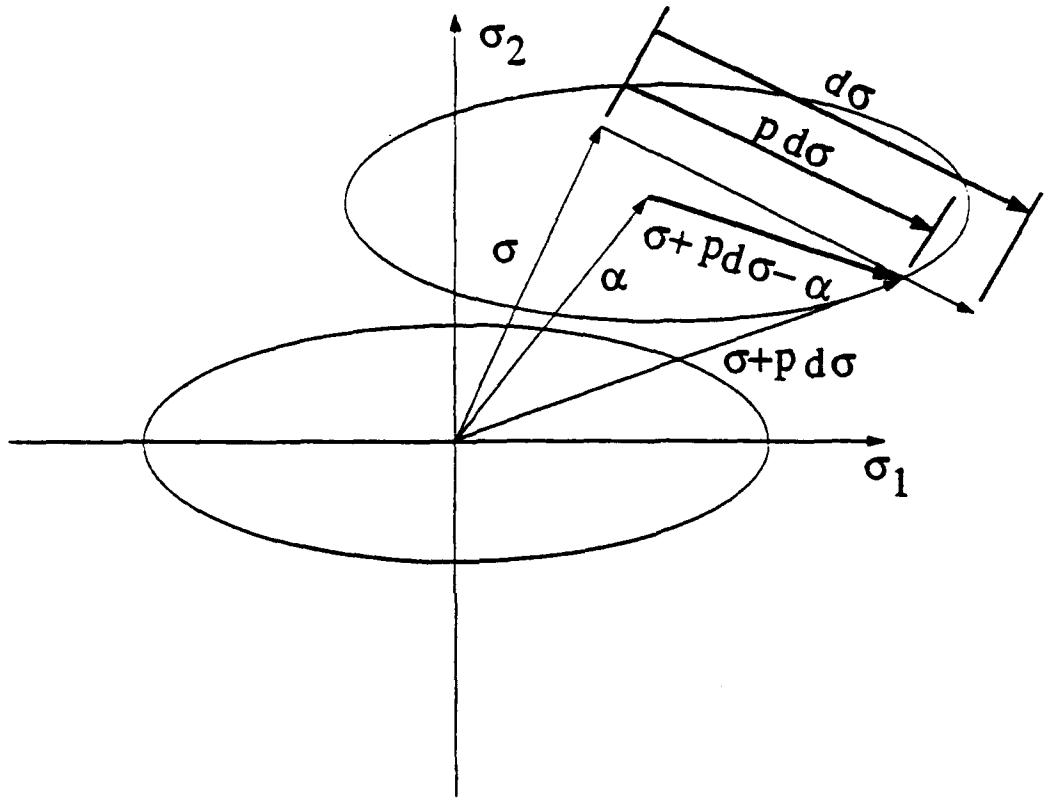

Figure 4.11 Schematic Representation of the Method for Finding MDM Subsequent Yield Surface

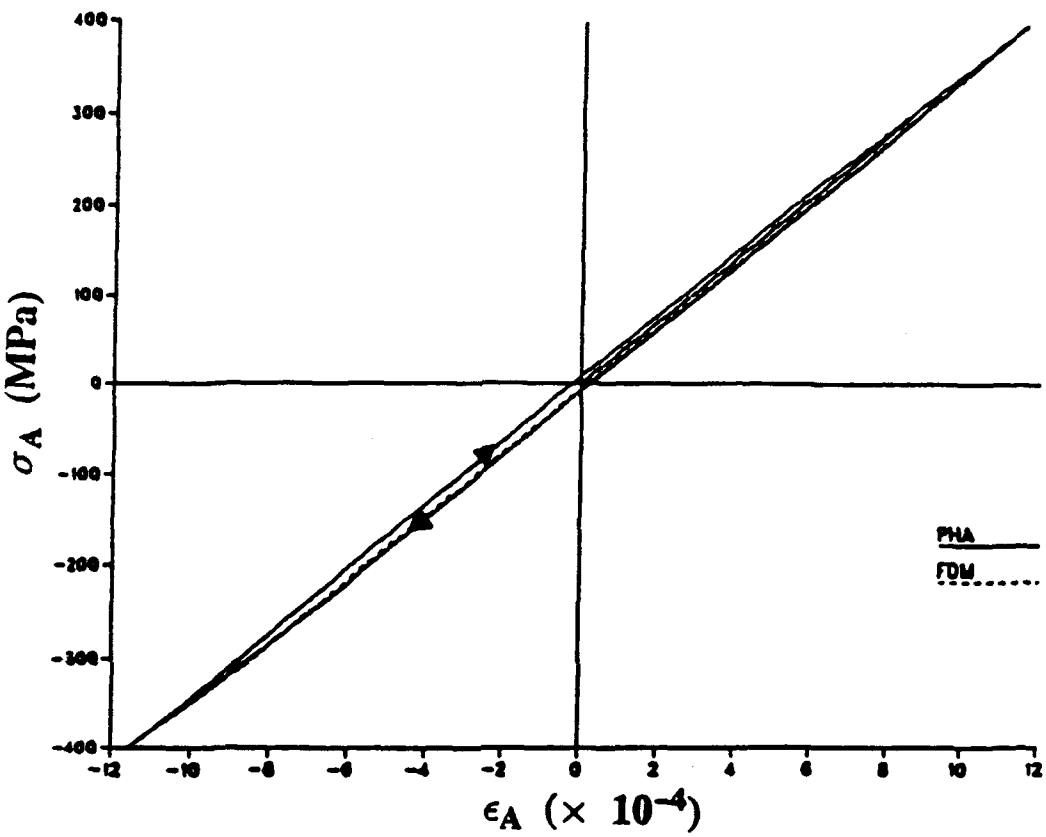

Figure 4.12 Axial Response of $(\pm 10)_s$ Gr/Al Composite Laminate Under Uniaxial Cycle of ±400 MPa. (FDM Response)

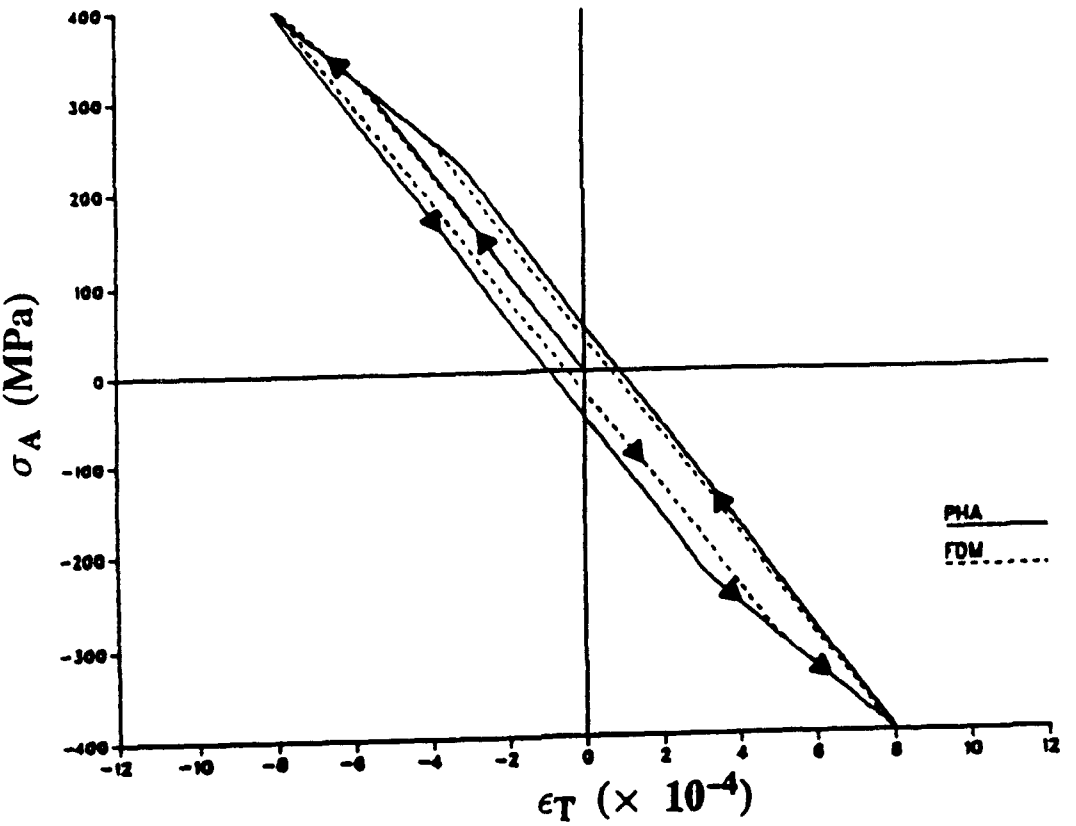

Figure 4.13 Transverse Response of $(\pm 10)_s$ Gr/Al Composite Laminate Under Uniaxial Cycle of ±400 MPa. (FDM Response)

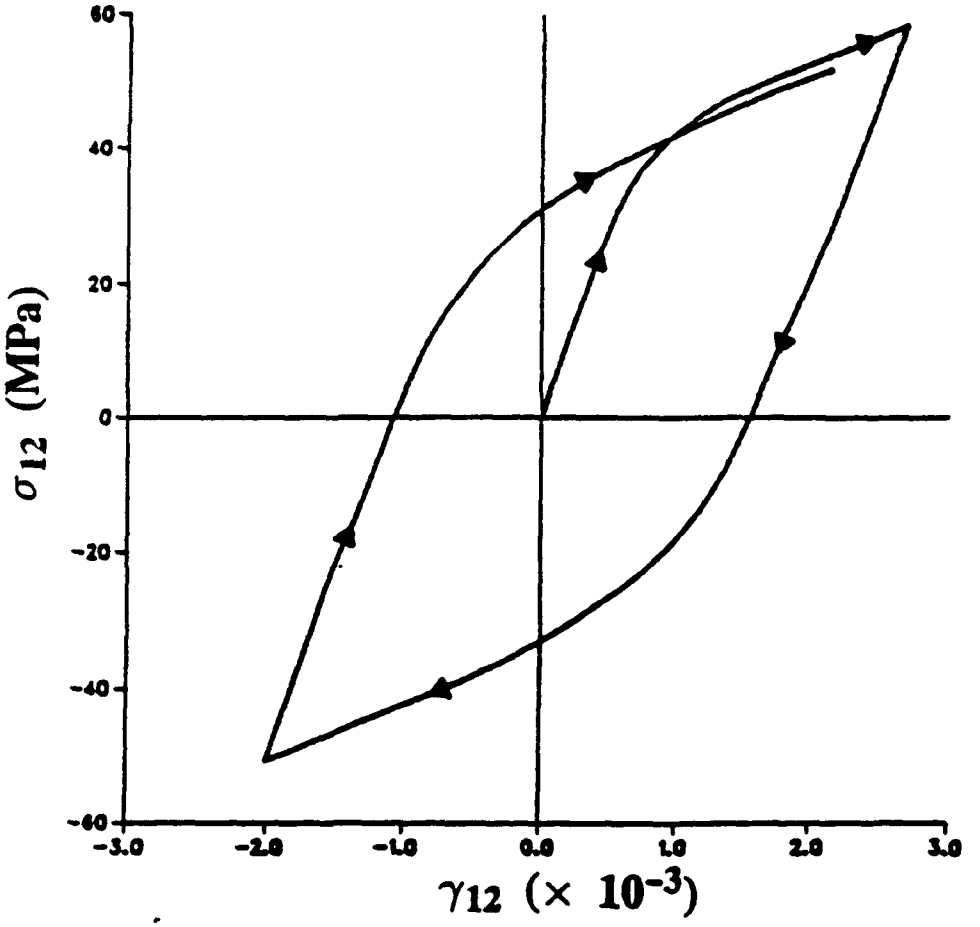

Figure 4.14 Stress-Strain Response of B/Al Unidirectional Composite Under Longitudinal Shear Cycle with Mild Unloading. (MDM Response)

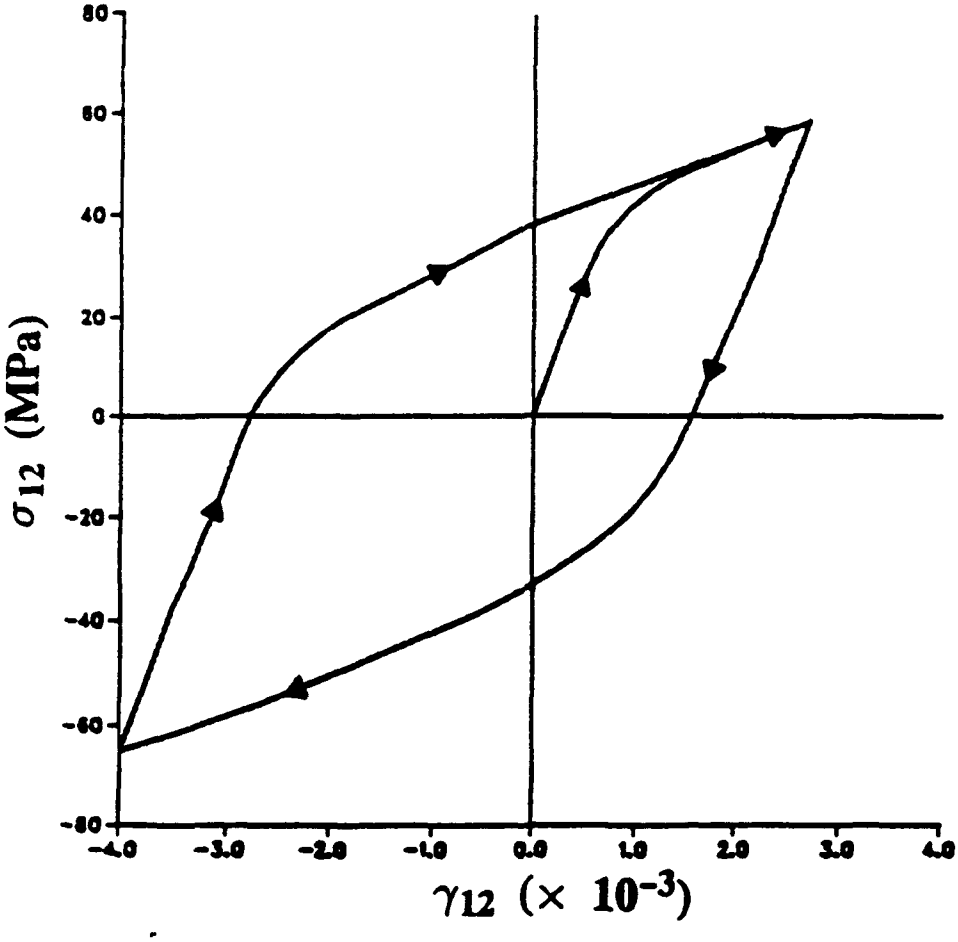

Figure 4.15 Stress-Strain Response of B/Al Unidirectional Composite Under longitudinal Shear Cycle with Large Amount of Unloading. (MDM Response)

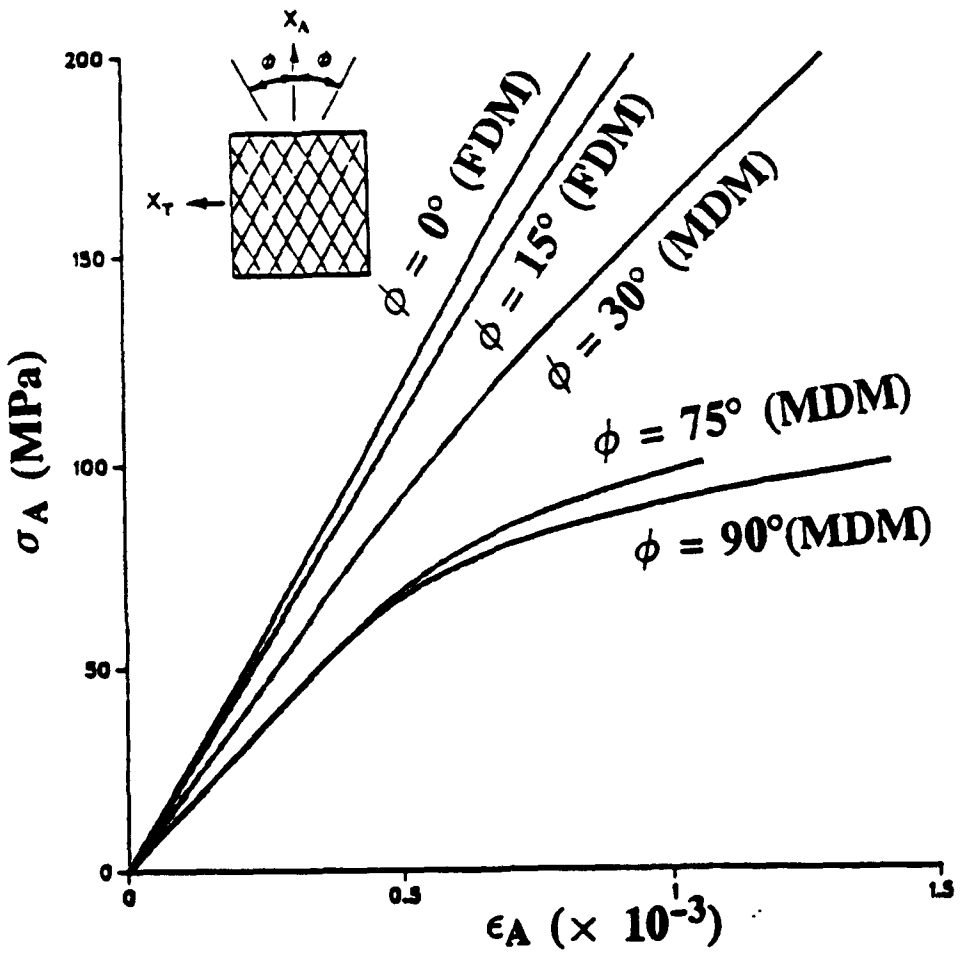

Figure 4.16 Variation of Axial Response of $(\pm\phi)_s$ B/Al Composite Laminates Under Axial Tension. (MDM and FDM Responses)

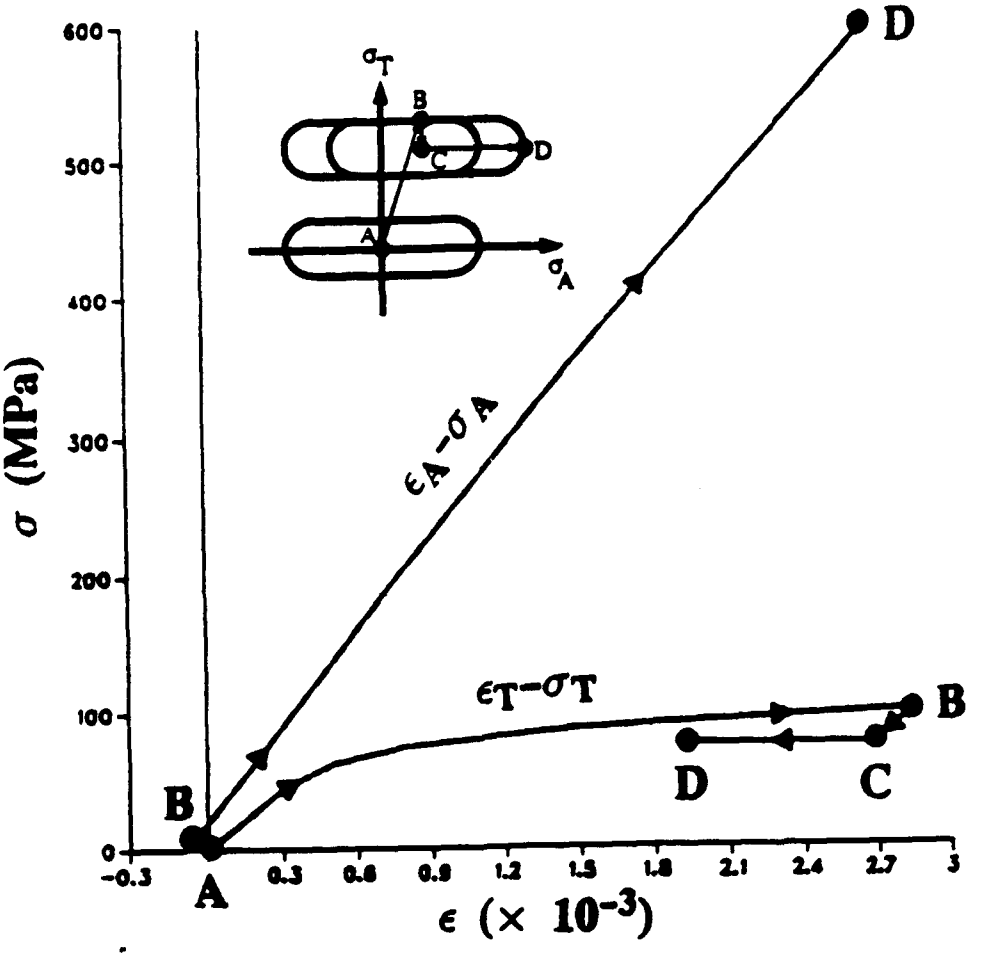

Figure 4.17 Stress-Strain Response of Unidirectional B/Al Composite Laminate Under Nonproportional Loads. (From MDM to FDM)

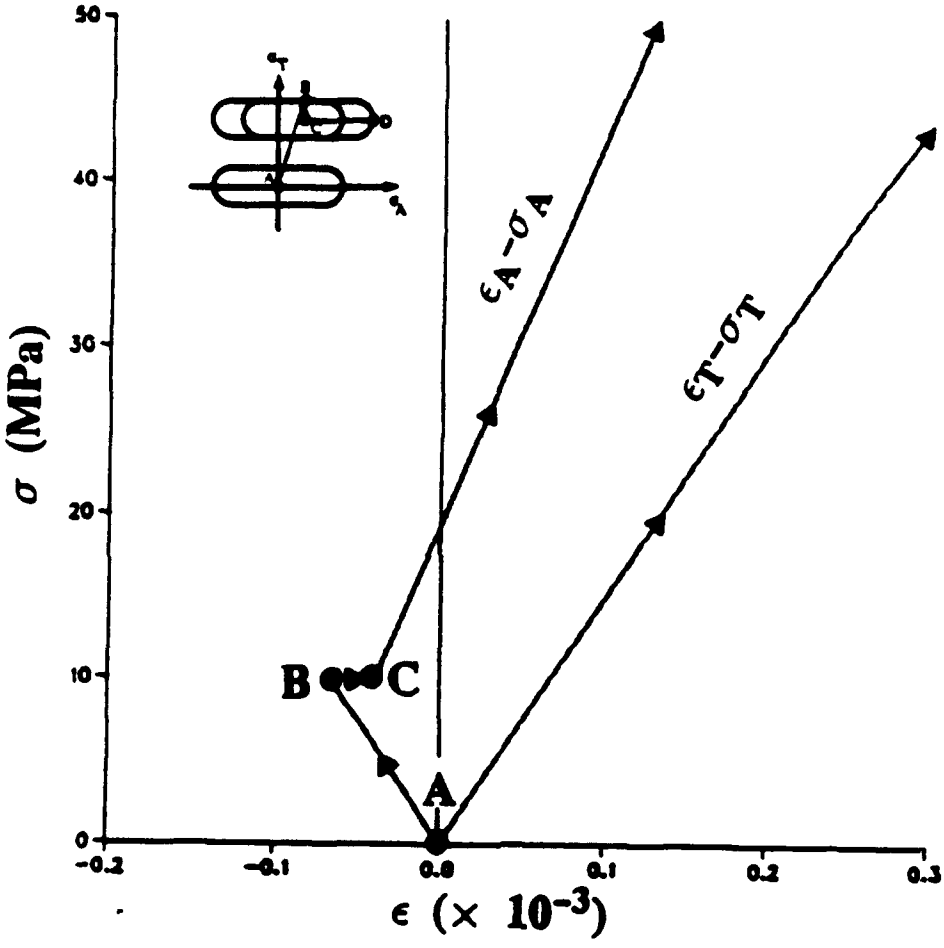

Figure 4.18 Enlarged Portion of Fig.4.17

APPENDIX D

Numerical Analysis of the Rate–Dependent Behavior of High Temperature Fibrous Composites

Reprinted From
AMD–Vol. 118, Mechanics of Composites at Elevated and Cryogenic Temperatures
Editors: S. N. Singhal, W. F. Jones, and C. T. Herakovich and T. Cruse
Book No. G00618 – 1991

The American Society of Mechanical Engineers

NUMERICAL ANALYSIS OF THE RATE-DEPENDENT BEHAVIOR OF HIGH TEMPERATURE FIBROUS COMPOSITES

Y. A. Bahei-El-Din, R. S. Shah, and G. J. Dvorak
Department of Civil Engineering and
Institute Center for Composite Materials and Structures
Rensselaer Polytechnic Institute
Troy, New York

ABSTRACT

The rate–dependent behavior of high temperature composites reinforced with aligned continuous fibers is evaluated numerically for an idealized periodic hexagonal array geometry of the microstructure. The analysis employs the finite element method for a representative volume element of the periodic geometry. Constitutive equations of the phases are derived from a new thermo–viscoplasticity theory which is based on overstess measured from an equilibrium yield surface, and a two–surface plasticity theory. Numerical predictions of multistep creep strains compared fairly well with experimental measurements for a SiC/Ti unidirectional composite.

INTRODUCTION

Future applications of fibrous metal matrix composites in aerospace and automobile industries include high temperatures that may well exceed 1000°C. In such environment, the behavior of most conventional alloys is sensitive to loading rates. Creep, relaxation, thermal recovery and other time–dependent phenomena are characteristic of their behavior under high temperatures. In heterogeneous media, in general, and fibrous composites, in particular, these phenomena take place under local stress and strain fields which are neither uniform nor proportional. The local straining rates may, therefore, vary considerably at individual material points within each phase. Under these circumstances, material models which are both geometrically and intrinsically representative of high temperature multiphase materials must be used in evaluation of their behavior.

Numerous analytical models have been proposed for prediction of the inelastic response of fibrous composites. An extensive bibliography appears in the reviews by Bahei–El–Din and Dvorak (1989) and Dvorak (1991). Implementation of these models, however, has been mostly limited to room temperature applications in which constitutive behavior of the phases can be described by rate–independent plasticity theories. In this context, a recent study by Dvorak et al. (1990) of the reliability of the predictions made by three specific models of fibrous composites in comparison to experiments showed that somewhat detailed description of the microgeometry of the composite is essential for reliable predictions of plastic strains.

This paper describes a viscoplastic analysis of fibrous composites under nonisothermal loads in a high temperature environment. The analysis employs the periodic hexagonal array (PHA) model (Dvorak and Teply, 1985; Teply and Dvorak, 1988) and the finite element method to compute the overall response of unidirectional composites. A similar analysis utilizing a rate–independent plasticity theory for the matrix was described by the

authors (Bahei–El–Din et al., 1989). In the present paper, constitutive equations of the phases were derived from a viscoplasticity theory which includes many of the phenomena observed in high temperature experiments of metallic alloys. First, we briefly describe the composite representative domain based on the PHA model. The new viscoplasticity constitutive equations are presented next and followed by comparison of predicted and measured inelastic strains of a unidirectional silicon carbide/titanium composite at elevated temperature.

COMPOSITE REPRESENTATIVE DOMAIN

The composite domain used in predictions of fibrous composites was selected according to the periodic hexagonal array (PHA) model developed by Dvorak and Teply (1985) and Teply and Dvorak (1988). In this model, the microstructural geometry in the transverse plane of a unidirectionally reinforced fibrous composite is represented by a periodic distribution of the fibers in a hexagonal array. Cross section of the fibers is approximated by a nx6–sided polygon. An example of the PHA microgeometry with dodecagonal fiber cross section is shown in Fig. 1.

The hexagonal array shown in Fig. 1 is divided into two unit cells, as indicated by the shaded and unshaded triangles. Under overall uniform stresses or strains, the two sets of unit cells have related internal fields. Accordingly, under properly prescribed periodic boundary conditions, only one unit cell from either set needs to be analyzed. Figure 2 shows a three dimensional view of one of the unit cells with hexagonal fiber cross section.

The actual analysis is performed by the finite element method. The unit cell is subdivided into a selected number of subelements, element material properties are prescribed as suggested in the sequel. The degree of mesh refinement may vary from few elements in the matrix and fiber regions to several hundred elements. Figure 3 indicates two possible subdivisions of the unit cell in the transverse plane. The effect of the mesh geometry on the computed results was examined by Bahei–El–Din et al. (1987, 1989), and Shah and Teply (1989). In general, evaluation of the local fields requires a large number of elements, while few elements are sufficient to satisfactorily compute the overall response.

THERMO–VISCOPLASTICITY OF THE PHASES

A number of viscoplasticity theories based on internal state variables have been proposed in the literature. The work by Benallal and Ben Cheikh (1987), Chaboche (1989), Krempl et al. (1986), Lindholm et al. (1985), and Walker (1981) is representative of the modeling efforts for the time–dependent behavior of unreinforced materials under thermomechanical loads. To reflect the particular inelastic behavior of ductile materials under nonisothermal, nonproportional loading conditions that exist in the phases of a high temperature composite, the present paper introduces a new rate–dependent constitutive theory which is based on overstress measured from an equilibrium yield surface, and incorporates a two–surface plasticity theory. At low homologous temperatures, and isothermal conditions, the new constitutive equations reduce to the formulation by Eisenberg and Yen (1981), albeit in a form more suitable for nonproportional loading.

Associated Flow Rule

We assume the matrix and fiber phases to be homogeneous and elastically isotropic. Either phase may exhibit nonlinear response under thermomechanical loads which exceed the elastic limit of the material. The total strain rate, $\dot{\epsilon}_{ij}$, is divided into elastic, thermal and inelastic components:

$$\dot{\epsilon}_{ij} = \dot{\epsilon}^{e}_{ij} + \dot{\epsilon}^{t}_{ij} + \dot{\epsilon}^{'}_{ij} . \tag{1}$$

Assuming the thermoelastic properties to be temperature–dependent, the elastic and thermal strain rates are given by

$$\dot{\epsilon}^{e}_{ij} = M^{e}_{ijkl}(\theta)\, \dot{\sigma}_{kl} , \tag{2}$$

$$\dot{\epsilon}^{t}_{ij} = [(dM^{e}_{ijkl}(\theta)/d\theta)\,\sigma_{kl} + m_{ij}(\theta)]\,\dot{\theta}\,, \tag{3}$$

$$m_{ij}(\theta) = \delta_{ij}\,\beta(\theta)\,, \tag{4}$$

where θ is the current temperature, $M^{e}_{ijkl}(\theta)$ is the elastic compliance, δ_{ij} is the Kronecker's tensor, and $\beta(\theta)$ is the coefficient of thermal expansion.

The inelastic part of the strain is found with the help of viscoplasticity theorems based on overstress (Eisenberg and Yen, 1981; Krempl et al., 1986). We assume the existence of an equilibrium yield surface which is the locus of all stress states that can be reached from the current state by purely elastic deformation. Inelastic deformation develops only when the stress point lies outside the equilibrium yield surface. In the presence of kinematic and isotropic hardening, a Mises form of the current equilibrium yield surface can be written as

$$f = \frac{3}{2}(s^{*}_{ij} - \alpha_{ij})(s^{*}_{ij} - \alpha_{ij}) - (Y + Q)^{2} = 0\,, \tag{5}$$

where s^{*}_{ij} is the deviatoric equilibrium stress tensor, α_{ij} denotes the center of the yield surface, $Y = Y(\theta)$ is the yield stress in tension, which is independent of the loading rate, and Q is an isotropic hardening function.

Corresponding to a given stress tensor, s_{ij}, which lies outside the yield surface (5), there exists an equilibrium stress, s^{*}_{ij}, which satisfies (5), Fig. 4. Hence,

$$s^{*}_{ij} = \left[\frac{2\,[Y(\theta) + Q(\theta)]^{2}}{3\,(s_{kl} - \alpha_{kl})(s_{kl} - \alpha_{kl})}\right]^{\frac{1}{2}}(s_{ij} - \alpha_{ij}) + \alpha_{ij}\,. \tag{6}$$

The effective overstress, R, is a measure of the distance between the actual stress point, s_{ij}, and the equilibrium stress point, s^{*}_{ij}. It vanishes if the stress point lies on, or falls inside the yield surface. In particular,

$$R = [\tfrac{3}{2}(s_{ij} - s^{*}_{ij})(s_{ij} - s^{*}_{ij})]^{\frac{1}{2}} \quad \text{if } f(s_{ij} - \alpha_{ij}) > 0\,, \tag{7}$$

$$R = 0 \quad \text{if } f(s_{ij} - \alpha_{ij}) \leq 0\,. \tag{8}$$

The inelastic strain rate is found from an associated flow rule in which the strain rate is normal to the equilibrium yield surface and its magnitude is assumed in the form of a power law of the overstress (Eisenberg and Yen, 1981):

$$\dot{\epsilon}^{\prime}_{ij} = \sqrt{(3/2)}\,k(\theta)\,R^{p(\theta)}\,n_{ij}(s^{*}_{ij})\,, \tag{9}$$

where the functions $k(\theta)$ and $p(\theta)$ are material parameters and n_{ij} is the unit normal to the yield surface (5) at the current equilibrium stress point. From (5)

$$n_{ij} = \frac{(s^{*}_{ij} - \alpha_{ij})}{[(s^{*}_{kl} - \alpha_{kl})\,(s^{*}_{kl} - \alpha_{kl})]^{\frac{1}{2}}} = \sqrt{(3/2)}\,\frac{(s^{*}_{ij} - \alpha_{ij})}{(Y + Q)}\,. \tag{10}$$

Hardening

Under thermomechanical loads applied at high temperature, evolution of the hardening variables Q and α_{ij}, eq. (5), depends not only on the loading history but also on time. In particular, thermal recovery of hardening caused by annealing may be significant. The evolution equation for Q can be written in the following form which is suggested by Nouailhas et al. (1983)

$$\dot{Q} = q(\theta)[Q_a(\theta) - Q]\,\dot{\bar{\epsilon}}' - b_r(\theta)\,|Q - Q_r(\theta)|^{(n_r(\theta)-1)}[Q - Q_r(\theta)]. \tag{11}$$

The functions $Q_a(\theta)$, $q(\theta)$, $b_r(\theta)$, $Q_r(\theta)$, and $n_r(\theta)$ are material parameters, and $\dot{\bar{\epsilon}}'$ is the effective inelastic strain rate;

$$\dot{\bar{\epsilon}}' = \left[\frac{2}{3}\dot{\epsilon}'_{ij}\,\dot{\epsilon}'_{ij}\right]^{\frac{1}{2}} = k(\theta)\,R^{p(\theta)}; \quad \dot{\epsilon}'_{kk} = 0\,. \tag{12}$$

The first term in (11) represents isotropic hardening caused by inelastic flow, and the second term represents thermal recovery of isotropic hardening. In the absence of thermal recovery, the size of the yield surface f in the deviatoric stress space reaches the asymptotic value $(Y + Q_a)$. On the other hand, if the inelastic strain rate is zero, the size of the yield surface Y in the virgin state is recovered either totally $(Q_r = 0)$, or partially $(Q_r \neq 0)$.

In analogy with (11), and permitting complete thermal recovery of kinematic hardening, the evolution equation for the center of the yield surface, α_{ij}, can be written as

$$\dot{\alpha}_{ij} = \dot{\mu}\,\nu_{ij} - c_r(\theta)\,\bar{\alpha}^{(m_r(\theta)-1)}\,\alpha_{ij}\,. \tag{13}$$

In the absence of inelastic deformation, complete thermal recovery of kinematic hardening is achieved by the second term in (13). The functions $c_r(\theta)$ and $m_r(\theta)$ are material parameters, and $\bar{\alpha}$ is the magnitude of α_{ij} defined by the invariant

$$\bar{\alpha} = (\alpha_{kl}\,\alpha_{kl})^{\frac{1}{2}}. \tag{14}$$

The first term in (13) represents kinematic hardening caused by inelastic deformation in the absence of thermal recovery. The unit tensor ν_{ij} defines the direction of translation of the yield surface in the deviatoric stress space, and can be specified according to the hardening rules applied in rate-independent plasticity theories. Here, we select the Phillips hardening rule which has been observed in room temperature, and high temperature experiments on certain materials (Phillips et al., 1972; Dvorak et al., 1988). In particular, we specify

$$\nu_{ij} = \dot{s}_{ij} / (\dot{s}_{kl}\,\dot{s}_{kl})^{\frac{1}{2}} \quad \text{if } \dot{s}_{ij} \neq 0 \tag{15}$$

$$\nu_{ij} = n_{ij} \quad \text{if } \dot{s}_{ij} = 0\,. \tag{16}$$

The factor $\dot{\mu}$ in (13) is found from Prager's consistency condition, $\dot{f} = 0$, when translation of the yield surface is specified by the first term in (13):

$$\dot{f} = (s^*_{ij} - \alpha_{ij})\dot{s}^*_{ij} - \dot{\mu}\,(s^*_{ij} - \alpha_{ij})\nu_{ij} - \frac{2}{3}(Y + Q)(\dot{Y} + \dot{Q}) = 0\,. \tag{17}$$

Using $(10)_2$, eq. (17) can be rewritten as

$$n_{ij}\,\dot{s}^{*}_{ij} - \dot{\mu}\,n_{ij}\,\nu_{ij} - \sqrt{(2/3)}\,(\dot{Y} + \dot{Q}) = 0\,. \tag{18}$$

The first term in (18) is found by equating the inelastic strain rate given by (9) and the inelastic strain rate given by the associated flow rule of rate–independent plasticity (Eisenberg and Yen, 1981). The result is

$$n_{ij}\,\dot{s}^{*}_{ij} = \sqrt{(2/3)}\,[H(\theta)\,k(\theta)\,R^{p(\theta)} + \dot{Y}(\theta)]\,, \tag{19}$$

where, $H(\theta)$ is the instantaneous tangent modulus of the inelastic stress–strain equilibrium curve. Substituting (11), retaining only the first term, and (19) into (18) and using (12), the factor $\dot{\mu}$ can be found as

$$\dot{\mu} = \sqrt{(2/3)}\,k(\theta)\,R^{p(\theta)}\Big[H(\theta) - q(\theta)[Q_a(\theta) - Q]\Big]/n_{kl}\,\nu_{kl}\,. \tag{20}$$

Two–Surface Plasticity Theory

A bounding surface is used to establish the instantaneous tangent modulus H and to describe the cyclic behavior of the material, Fig. 4. This surface is derived as an isotropic expansion of the initial equilibrium yield surface. During inelastic deformation, the bounding surface translates in the stress space and exhibits isotropic changes as well. Translation of the bounding surface is dictated by the requirement that the yield surface and the bounding surface have a common normal when they become in contact. Details of this kinematic hardening rule are given by Dafalias and Popov (1976). In analogy with the equilibrium yield surface, thermal recovery of isotropic as well as kinematic hardening of the bounding surface can be included in our model. This is omitted here for brevity. We only mention that the recovery terms for isotropic and kinematic hardening of the bounding surface assume a form similar to those suggested above for the yield surface, but with new material parameters.

The instantaneous tangent modulus, H, is found as a function of the distance, δ, between the equilibrium stress, s^{*}_{ij}, and a corresponding point on the bounding surface, $\bar{s}_{ij}$, with unit normal $\bar{n}_{ij}(\bar{s}_{ij}) = n_{ij}(s^{*}_{ij})$:

$$H(\theta) = H_o(\theta) + h(\theta)\,[\delta/(\delta_o - \delta)]\,, \tag{21}$$

$$\delta = \left[\frac{3}{2}\,(\bar{s}_{ij} - s^{*}_{ij})\,(\bar{s}_{ij} - s^{*}_{ij})\right]^{\frac{1}{2}}, \tag{22}$$

where δ_o is the distance between the yield surface and the bounding surface at the onset of inelastic deformation. When the equilibrium stress point lies on the bounding surface, the plastic tangent modulus assumes the asymptotic value $H_o(\theta)$. Both $H_o(\theta)$ and $h(\theta)$ need to be determined experimentally.

COMPARISON WITH EXPERIMENTS

The viscoplasticity constitutive equations described in the preceding section were implemented in the ABAQUS finite element program. The program was used to evaluate the rate–dependent behavior of unidirectional composites using the geometry specified by the PHA model. In the present paper, we used a coarser version of the mesh shown in Fig. 3a (40 matrix elements, and 18 fiber elements) to evaluate and compare the overall multistep creep strains of a unidirectional SCS6/Ti–15–3 composite to the experimental results provided by Tuttle et al. (1990) at 566° C.

Elastic, isotropic behavior is assumed for the silicon carbide fiber. The fiber properties are shown in Table 1 at 566° C. The titanium matrix is elastic–viscoplastic.

The material parameters required by the viscoplasticity theory described above were found by fitting the stress–strain response measured experimentally for several unreinforced titanium specimens fabricated by diffusion bonding of Ti–15–3 foils. The properties of the neat matrix are therefore expected to be representative of the *in situ* properties of the matrix phase in the composite.

Six unreinforced Ti–15–3 specimens were tested in uniaxial tension by Tuttle, Rogacki and Johnson (1990) at room temperature, 482°C, and 649°C. At each temperature, two tension tests were performed, one under stress–controlled loading at a rate of 2.6 MPa/s, the other under strain–controlled loading at a rate of 10^{-4}/s. The strain–controlled tests consisted of a number of loading and relaxation periods. The hold strain and time are given in Table 2 for the three test temperatures. Figures 5 and 6 compare the computed and measured stress–strain curves. The matrix parameters used in fitting the experimental curves are shown in Table 3. The script Latin letters shown in the first column of Table 3 indicate material parameters related to the bounding surface and have the same meaning of their yield surface counterparts. For example, $\mathscr{Y}$ is the 'radius' of the bounding surface, and c_r , m_r are material parameters which define the recovery term for kinematic hardening of the bounding surface. Material parameters not shown in Table 3 are assumed zero. For intermediate temperatures, the material constants are found by linear interpolation between the values given in Table 3.

The phase properties determined above were used in the PHA model to compute the overall strains in the fiber direction of a 0°, SCS6/Ti–15–3 composite corresponding to the multistep creep loading history shown in Fig. 7. The axial strain computed at 566°C is compared to the experimental record provided by Tuttle et al. (1990) in Fig. 8. At the onset of creep strain, marked in the figure for each stress level, the computed and measured axial strains are matched. In this way, we compare the results for the creep behavior alone, and eliminate any descripancies between the experiments and the numerical simulation that might have been caused during application of the overall stress.

CONCLUSION

The nonisothermal elastic–viscoplastic response of fibrous composites at high temperatures was modeled using the periodic hexagonal array (PHA) model. Constitutive equations of the phases were derived from a new viscoplasticity theory which is based on overstress measured from an equilibrium yield surface, and includes isotropic and kinematic hardening rules with thermal recovery terms. A two–surface plasticity theory was also incorporated in the model to account for nonproportional loading. The model involves several material parameters, the number of which increases as the material behavior becomes more complex. For example, modeling complete thermal recovery requires four parameters, two for isotropic hardening and two for kinematic hardening. Modeling partial thermal recovery in isotropic hardening requires one additional constant.

Actual calculations of the overall strains were performed with the ABAQUS finite element program for a unit cell of the composite as defined by the PHA model. Axial strains found in a high temperature multistep creep test performed on a SCS6/Ti–15–3 composite were successfully reproduced by the model.

ACKNOWLEDGEMENTS

This work was supported in part by the Aerospace Directorate of the Air Force Office of Scientific Research, and in part by the Mechanics Division of the Office of Naval Research. Lt. Col. George Haritos and Dr. Yapa Rajapakse served as project monitors for the AFOSR and the ONR, respectively.

REFERENCES

Bahei–El–Din, Y.A., and Dvorak, G.J., 1989, "A Review of Plasticity Theory of Fibrous Composite Materials," *Metal Matrix Composites: Testing, Analysis, and Failure Modes*, ASTM STP 1032, W.S. Johnson, ed., American Society for Testing and Materials, Philadelphia, pp. 103–129.

Bahei–El–Din, Y.A., Dvorak, G.J., Lin, J., Shah, R.S., and Wu, J.F., 1987, "Local Fields and Overall Response of Fibrous and Particulate Metal Matrix Composites," ALCOA Laboratories, Contract No. 379(52R)053(22L).

Bahei–El–Din, Y.A., Dvorak, G.J., and Shah, R.S., 1989, "Numerical Analysis of the Elastic–Plastic Behavior of Fibrous Metal Matrix Composites," *Computational Experiments*, W.K. Liu, P. Smolinski, R. Ohayon, J. Navickas, and J. Gvildys, eds., ASME PVP, Vol. 176, pp. 125–131.

Benallal, A., and Ben Cheikh, A., 1987, "Modelling of Anisothermal Effects in Elasto–Viscoplasticity," *Thermomechanical Coupling in Solids*, Bui, H.D. and Nguyen, Q.S., eds., Elsevier, North Holland, p. 403.

Chaboche, J.L., 1989, "Constitutive Equations for Cyclic Plasticity and Cyclic Viscoplasticity," *Int. J. Plasticity*, Vol. 5, pp. 247–302.

Dafalias, Y.F., and Popov, E.P., 1976, "Plastic Internal Variables Formalism of Cyclic Plasticity," *J. Appl. Mech.*, Vol. 43, pp. 645–651.

Dvorak, G.J., 1991 "Plasticity Theories for Fibrous Composite Materials," *Metal Matrix Composites, Vol. 2, Mechanisms and Properties*, R.K. Everett and R.J. Arsenault, eds., Academic Press, Boston, pp. 1–77.

Dvorak, G.J., Bahei–El–Din, Y.A., Macheret, Y., and Liu, C.H., 1988, "An Experimental Study of Elastic–Plastic Behavior of a Fibrous Boron–Aluminum Composite," *J. Mech. Phys. Solids*, Vol. 36, pp. 655–687.

Dvorak, G.J., Bahei–El–Din, Y.A., Shah, R.S., and Nigam, H., 1990, "Experiments and Modeling in Plasticity of Fibrous Composites," *Inelastic Deformation of Composite Materials*, G.J. Dvorak, editor, Springer–Verlag, New York, Inc., pp. 270–293.

Dvorak, G.J., and Teply, J.L., 1985, "Periodic Hexagonal Array Models for Plasticity of Composite Materials," *Plasticity Today: Modeling, Methods and Applications*, A. Sawczuk and V. Bianchi, eds., Elsevier, Amsterdam, pp. 623–642.

Eisenberg, M.A. and Yen, C.F., 1981, "A Theory of Multiaxial Anisotropic Viscoplasticity," *J. Appl. Mech.*, Vol. 48, pp. 276–284.

Krempl, E., McMahon, J.J., and Yao, D., 1986, "Viscoplasticity Based on Overstress with a Differential Growth Law for the Equilibrium Stress," *Mechanics of Materials*, Elsevier, North Holland, p. 35.

Lindholm, U.S., Chan, K.S., Bodner, S.R., Weber, R.M., Walker, K.P., and Cassenti, B.N., 1985, "Constitutive Modeling for Isotropic Materials," NASA CR–174980.

Nouailhas, D., Policella, H., and Kaczmarek, H., 1983, "On the Description of Cyclic Hardening Under Complex Loading History," *Proceedings of the International Conference on Constitutive Laws for Engineering Materials*, Desai and Gallagher, eds., Tucson, Arizona.

Phillips, A., Liu, C.S., and Justusson, J.W., 1972, "An Experimental Investigation of Yield Surfaces at Elevated Temperatures," *Acta Mechanica*, Vol. 14, pp. 119–146.

Shah, R.S., and Teply, J.L., 1989, "A Finite Element Convergence Study of the Periodic Hexagonal Array Model," Alcoa Laboratories Technical Report No. 57–89–32.

Teply, J.L., and Dvorak, G.J., 1988, "Bounds on Overall Instantaneous Properties of Elastic–Plastic Composites," *J. Mech. Phys. Solids*, Vol. 36, pp. 29–58.

Tuttle, M., Rogacki, J. and Johnson, W.S., 1990, Private Communication.

Walker, K.P., 1981, "Research and Development Program for Nonlinear Structural Modeling with Advanced Time–Temperature Dependent Constitutive Relationships," Report PWA–5700–50, National Aeronautics and Space Administration.

Table 1 Thermoelastic constants of SCS6 fiber

Temperature (°C)	E * (GPa)	ν †	β ‡ (10^{-6}/°C)
566	397.1	0.25	4.6

*Young's Modulus.
†Poisson's Ratio.
‡Coefficient of Thermal Expansion.

Table 2 Hold strain and time applied in relaxation tests of Ti–15–3 experiments

	Hold Time (s)		
Strain (%)	21°C	482°C	649°C
0.75	–	690	450
1.50	300	300	300
2.25	300	540	300
3.00	300	480	300
3.75	300	600	300
4.50	300	480	300
5.25	300	540	300
6.00	–	480	300
6.75	–	660	–

Table 3 Elastic–thermoviscoplastic constants of Ti–15–3 matrix

Material Constant	Units	21°C	482°C	649°C
E	GPa	92.4	72.2	55.0
ν		0.351	0.351	0.351
Y	MPa	790	45	15.5
H_0	MPa	1400	40	50
h	GPa	21	350	162
γ	MPa	915	1100	316
p		3.75	1.85	1.43
k	$(\text{MPa})^{-p}/\text{s}$	$1.6\text{x}10^{-7}$	$4.2\text{x}10^{-7}$	$3.2\text{x}10^{-6}$
Q_a	MPa	–120	–10	–5.0
ℓ_a	MPa	350	100	95
q		800	5.5	2.61
φ		800	5.5	2.61
m_r		1.2	1.29	1.35
m_r		1.2	1.29	1.35
c_r	$(\text{MPa})^{-m_r+1}/\text{s}$	$8.0\text{x}10^{-5}$	$5.0\text{x}10^{-4}$	$2.0\text{x}10^{-3}$
c	$(\text{MPa})^{-m_r+1}/\text{s}$	$8.0\text{x}10^{-5}$	$5.0\text{x}10^{-4}$	$2.0\text{x}10^{-3}$

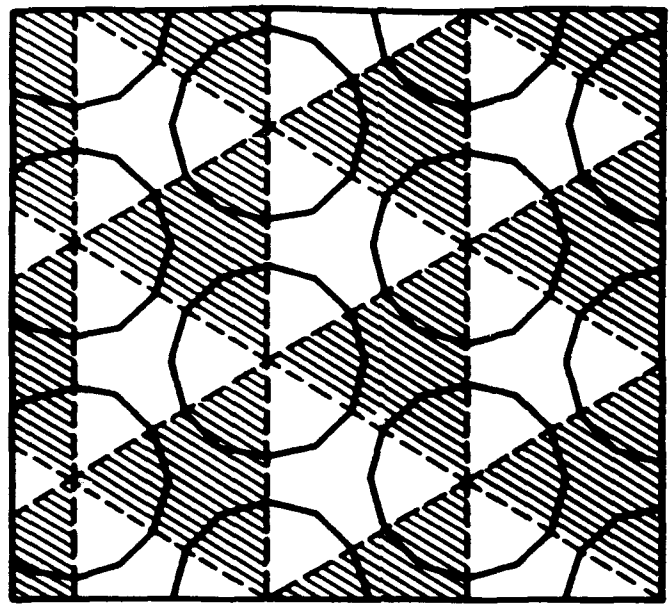

Fig. 1 Transverse plane geometry of the PHA model with dodecagonal fiber cross section.

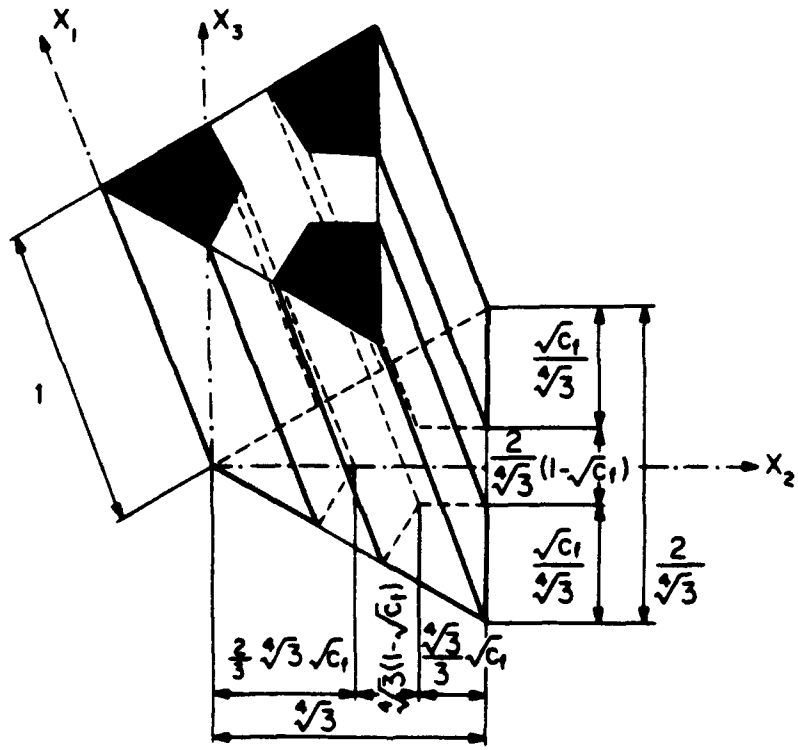

Fig. 2 Unit cell of the PHA model.

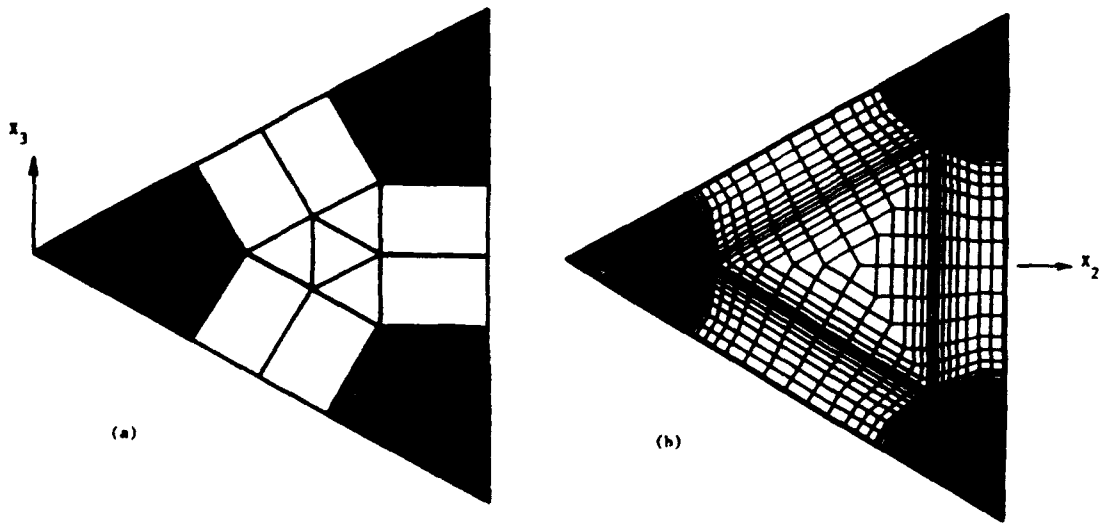

Fig. 3 Examples of finite element subdivisions of the PHA unit cell in the transverse plane.

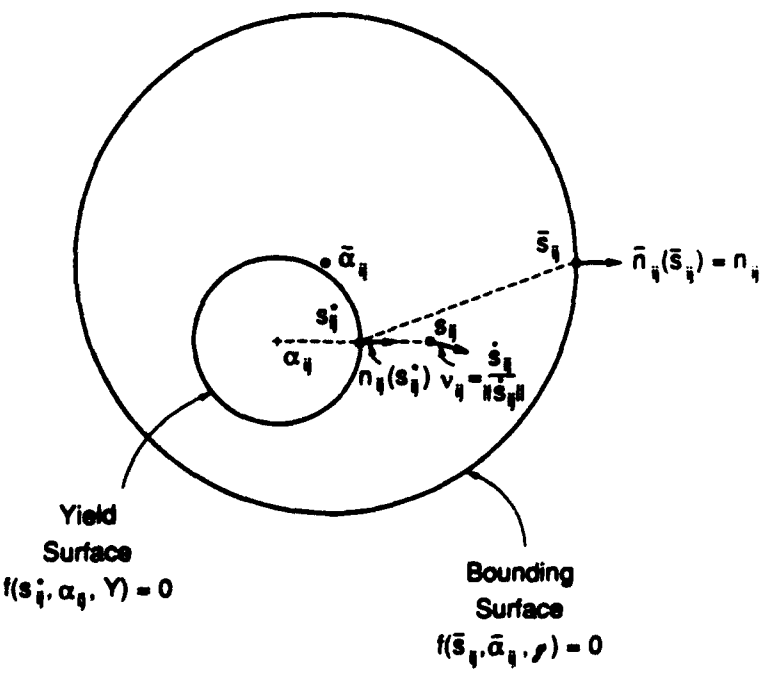

Fig. 4 Schematic of equilibrium yield surface and bounding surface in the deviatoric stress space of an elastically isotropic material.

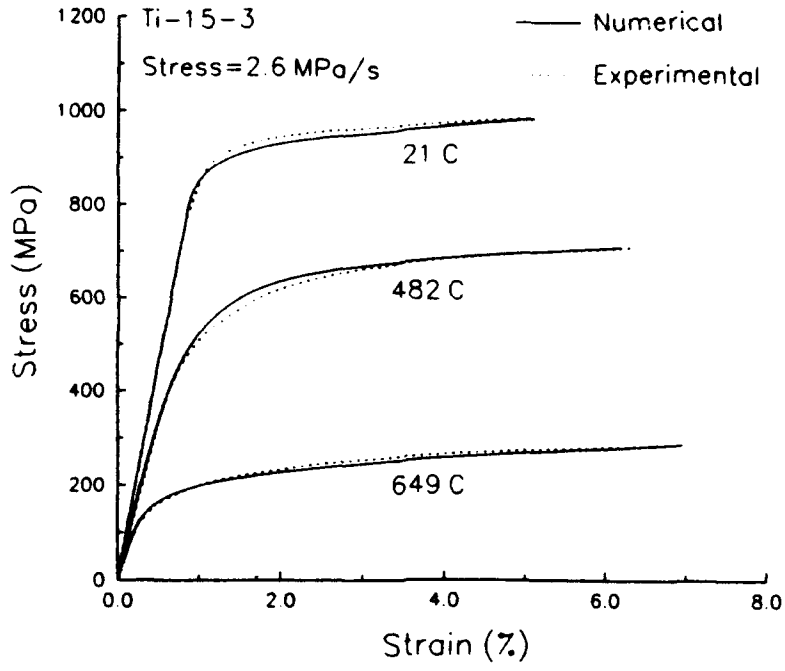

Fig. 5 **Comparison of measured and computed isothermal response of a Ti–15–3 specimen at room temperature, 482°C, 649°C, and stress rate of 2.6 MPa/s.**

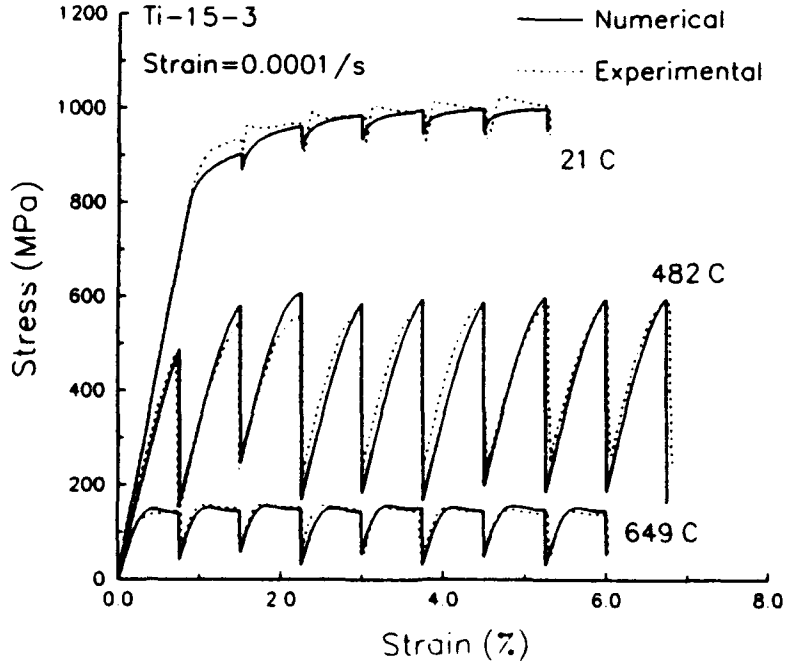

Fig. 6 **Comparison of measured and computed response of a Ti–15–3 specimen at room temperature, 482°C, 649°C, and strain rate of 10^{-4}/s.**

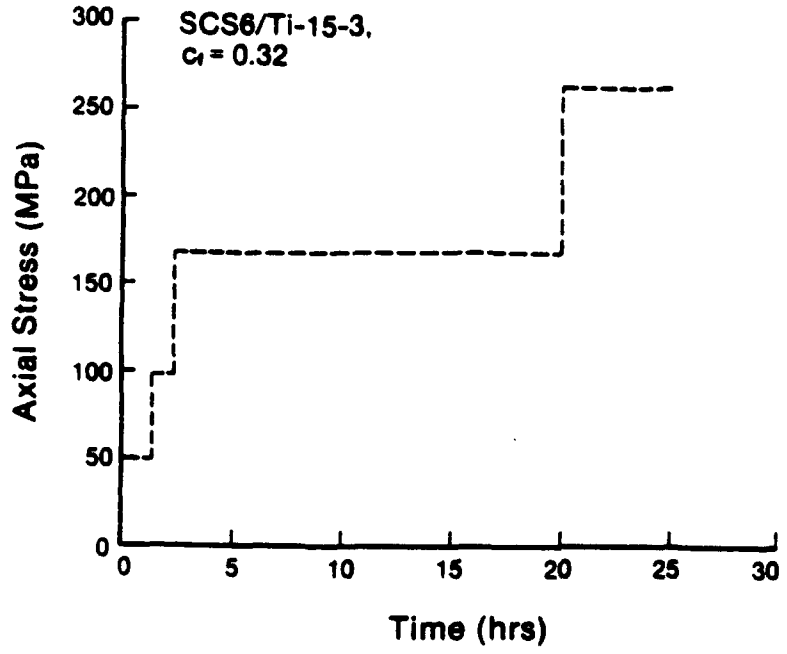

Fig. 7 Stress history applied in multistep creep test of a SCS6/Ti–15–3 composite.

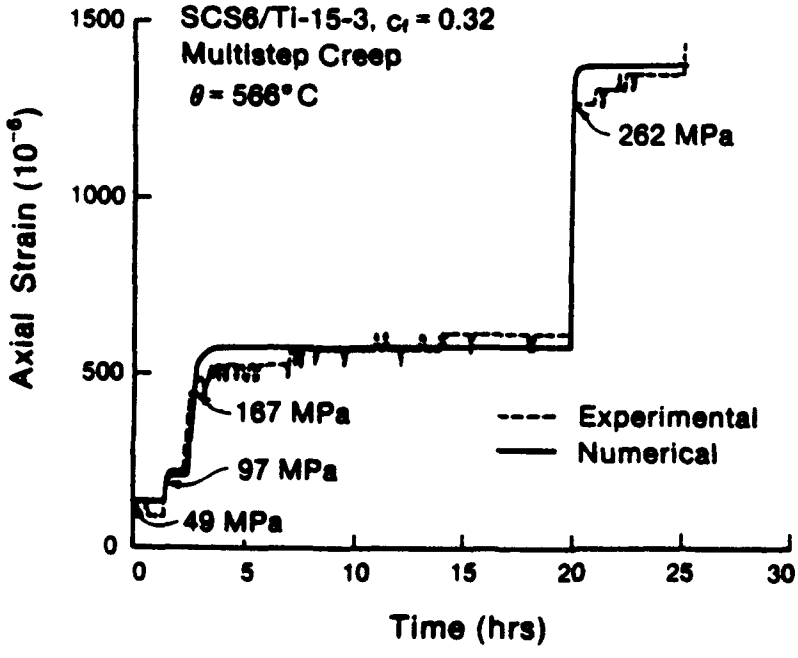

Fig. 8 Comparison of computed and measured strain found in multistep creep test on a SCS6/Ti–15–3 composite.

APPENDIX E

Dimensional Stability of Metal–Matrix Laminates

Composites Science and Technology 43 (1992) 207–219

Dimensional stability of metal-matrix laminates

Yehia A. Bahei-El-Din,* George J. Dvorak & Jer-Fang Wu

Department of Civil Engineering, Rensselaer Polytechnic Institute, Troy, New York 12180–3590, U.S.A.

(Received 11 September 1990; accepted 4 January 1991)

The dimensional stability of metal matrix composite laminates under thermal fluctuations and thermomechanical load cycles is examined. The system considered as a model material is a Gr/Al $(\pm\varphi)_s$ laminate. The analysis is performed by the finite-element method while the underlying constitutive equations of unidirectional composites are provided by the periodic-hexagonal-array (PHA) micromechanical model. A computationally more efficient and equally accurate method based on fiber-dominated analysis of unidirectional composites by the self-consistent method is also presented. The results show that laminates of the model system with $\varphi = 12°$ are dimensionally stable in the elastic range when subjected to pure temperature changes. Plastic deformation of the matrix causes permanent dimensional changes, which can be reduced by heat treatment of the composite. Under thermomechanical loads, $(\pm\varphi)_s$ laminates are not in general dimensionally stable. Dimensional stability of the laminate was enhanced by plastic deformation of the matrix for in-phase thermal and mechanical load cycles and reduced for out-of-phase cycles.

Keywords: metal matrix laminates, dimensional stability, thermoplasticity, thermomechanical loads, finite elements, micromechanics.

1 INTRODUCTION

In certain aerospace structures, high specific stiffness and strict dimensional tolerances are major design criteria. The typical loads consist of thermal fluctuations in the range of ±200°C, which may be accompanied by mechanical load cycles. Among the leading material candidates in these applications are metal matrix composites. In particular, continuous graphite-fiber-reinforced metals are considered for their high axial stiffness and low coefficient of thermal expansion.

The thermal mismatch in the axial direction between the fiber and matrix phases in graphite-reinforced composites, however, is large. This causes large local stresses to develop in the phases and it leads to plastic deformation in the matrix under small temperature changes. For example, a simple calculation of the matrix axial stress in a unidirectional 6061-F Al/Gr composite reveals that the composite yields after a temperature change of about 40°C.[1] Similar observations were found in tests performed on Gr/Al and Gr/Mg composites.[2–4] Under these circumstances, dimensional stability of metal matrix composite materials and laminates should be examined with accurate micromechanical models, which permit plastic deformation of the matrix.

In this paper, dimensional stability of Gr/Al composite laminates is evaluated for purely thermal as well as thermomechanical load cycles. The effects of matrix yield stress, hardening, and coupling between thermal and mechanical loads on the dimensional stability of $(\pm\varphi)_s$ laminates are of primary interest. The elastic–plastic

* Structural Engineering Department, Cairo University, Giza, Egypt.

Composites Science and Technology 0266-3538/91/$03.50

analysis used in this study is a finite-element-based procedure that incorporates micromechanical models for unidirectionally reinforced materials.[5,6] The results presented here were obtained from the ABAQUS finite-element program with the constitutive equations derived from the periodic hexagonal array (PHA) model.[6-8] The paper also presents a laminate analysis, which can be used in lieu of the finite-element method for composite systems that exhibit fiber-dominated deformation,[9] such as graphite-fiber-reinforced composites.

The plan of the paper is as follows. In Section 2, we address the thermomechanical loading problem for laminates and discuss available methods of analysis. A laminate analysis based on correspondence between mechanical and thermal loads is presented in this section. In Section 3, we present finite element results for the dimensional stability of $(\pm\varphi)_s$ Gr/Al laminates. Finally, the method of Section 2 is used to generate master curves for evaluation of axial strains in $(\pm\varphi)_s$ laminates corresponding to a wide range of axial load/temperature ratios.

2 THERMOMECHANICAL ANALYSIS OF LAMINATES

Consider a symmetric laminate consisting of several identical unidirectionally reinforced thin laminae in which the matrix is isotropic, and the fiber is transversely isotropic and their properties are not a function of temperature. The plane of the laminate coincides with the x_1x_2 plane of a Cartesian co-ordinate system that is parallel to the $\bar{x}_1\bar{x}_2$ planes associated with the laminae. The $\bar{x}_3$ and x_3 axes are perpendicular to the plane of the laminate. The fiber orientation of lamina i is specified by the angle φ_i between the local $\bar{x}_1$ axis and the overall x_1 axis. If the laminate is subjected to the in-plane stress increments $d\sigma_{11}$, $d\sigma_{22}$, $d\sigma_{12}$, together with the temperature increment $d\theta$, we wish to evaluate the local stresses in the matrix and fiber as well as the overall strain.

The solution to this problem can be obtained in several different ways. One approach, which is employed in Section 3, uses the finite-element method for a stack of elements, each of which represents a unidirectional lamina with specified fiber orientation. In the present study, we used the ABAQUS program, in which constitutive equations of the unidirectional composite are provided by the PHA model.[6-8] Figure 1 shows an example of the finite-element mesh for a $(\pm\varphi)_s$ laminate. It consists of two eight-noded brick elements, one for each $+\varphi$ and $-\varphi$ ply. Uniform displacements were prescribed on each surface of the finite-element domain. To simulate the symmetric layup, the displacements in the x_3 direction were prescribed as zero for the nodal points in the x_1x_2 plane.

Another approach to the solution of the stated laminate problem is the laminate theory, which assumes that the plies have equal in-plane strains. As before, the response of each ply is derived from a micromechanical model of the composite. Bahei-El-Din and Dvorak[10] found the solution for mechanical loads by using the laminate theory and the vanishing-fiber-diameter (VFD) model.[11] Their approach was used for thermomechanical loading of unidirectional composites and laminates by Bahei-El-Din[1] and Min and Crossman.[2] Alternatively, Bahei-El-Din[12] converted the thermomechanical problem for laminates to a mechanical loading problem that can be solved by the laminate theory. The method used is based on a decomposition procedure which was introduced by Dvorak[13] for unidirectional composites (see Appendix A). In this method, the plies are separated and in-plane tractions are applied to each ply in order to maintain the current stresses. A temperature increment $d\theta$ is then applied to the plies according to the procedure given by Dvorak.[13] This leaves each ply with axisymmetric auxiliary stresses, $s_A\,d\theta$ in the axial direction and $s_T\,d\theta$ in the transverse plane. The corresponding over-all

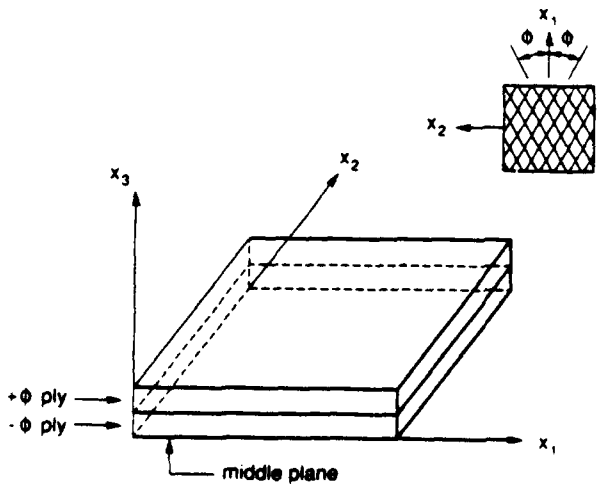

Fig. 1. Finite element mesh for $(\pm\varphi)_s$ laminates.

strains are isotropic and uniform in the entire composite (see Appendix A). Hence, the strains are compatible in the x_1x_2 plane regardless of the fiber orientation, and the laminate can be reassembled. Upon reassembly, the laminate supports an overall stress $d\boldsymbol{\sigma}$, which equilibrates the lamina stresses.

For the $(\pm\varphi)_s$ laminates considered in the present paper, the stress components of $d\boldsymbol{\sigma}$ are given by:[12]

$$d\hat{\sigma}_{11} = s_1\,d\theta, \quad d\hat{\sigma}_{22} = s_2\,d\theta, \quad d\hat{\sigma}_{33} = s_T\,d\theta, \tag{1}$$

$$d\hat{\sigma}_{23} = d\hat{\sigma}_{31} = d\hat{\sigma}_{12} = 0, \tag{2}$$

$$\begin{aligned} s_1 &= s_A\cos^2\varphi + s_T\sin^2\varphi, \\ s_2 &= s_A\sin^2\varphi + s_T\cos^2\varphi. \end{aligned} \tag{3}$$

The stresses s_A and s_T are given in Appendix A. The actual fields caused by the temperature change $d\theta$ are found by superposition of the fields developed in the plies of the decomposed laminate and those caused by removal of the over-all stress $d\hat{\boldsymbol{\sigma}}$. Simultaneous application of the in-plane stress increments $d\sigma_{11}$, $d\sigma_{22}$, $d\sigma_{12}$ and the temperature increment $d\theta$ to the laminate is therefore equivalent to application of the mechanical load:

$$\begin{aligned} d\boldsymbol{\sigma}^* = [&(d\sigma_{11} - s_1\,d\theta)(d\sigma_{22} - s_2\,d\theta) \\ &- s_T\,d\theta\;d\sigma_{12}\;\;0\;\;0]^T. \end{aligned} \tag{4}$$

The equivalent mechanical load (4) consists of in-plane stresses and out-of-plane normal stress.

Let a superimposed prime on the stress or strain vectors indicate (3×1) arrays listing quantities associated with the x_1x_2 plane of the laminate, e.g.

$$\begin{aligned} d\boldsymbol{\sigma}' &= [d\sigma_{11}\,d\sigma_{22}\,d\sigma_{12}]^T, \\ d\boldsymbol{\epsilon}' &= [d\epsilon_{11}\,d\epsilon_{22}\,2d\epsilon_{12}]^T. \end{aligned}$$

The over-all in-plane strains caused by simultaneous application of $d\boldsymbol{\sigma}'$ and $d\theta$ are then found as:[12]

$$d\boldsymbol{\epsilon}' = h\mathbf{1}\,d\theta + \mathcal{M}[d\boldsymbol{\sigma}' - (\mathbf{s}\,d\theta + \mathcal{k}s_T)\,d\theta] \tag{5}$$

where $\mathbf{s} = [s_1\;\;s_2\;\;0]^T$, $\mathbf{1} = [1\;\;1\;\;0]^T$, and h is given in Appendix A. Matrix $\mathcal{M}$ is the instantaneous compliance of the laminate associated with in-plane loads, and $\mathcal{k}$ defines in-plane stresses caused by unit out-of-plane normal stress when the in-plane strain $d\boldsymbol{\epsilon}'$ equals zero. Expressions for $\mathcal{M}$ and $\mathcal{k}$ are given in Appendix B. The first term in eqn (5) is the uniform strain generated in each ply of the decomposed laminate by the axisymmetric stresses $s_A\,d\theta$ and $s_T\,d\theta$. The second term is the strain caused by application of the equivalent stress $d\boldsymbol{\sigma}^*$, eqn (4), to the laminate.

The non-zero matrix stresses in the plies are the in-plane stresses $d\boldsymbol{\sigma}'_m = [d\sigma^m_{11}\,d\sigma^m_{22}\,d\sigma^m_{12}]^T$ and the out-of-plane component $d\sigma^m_{33}$. The matrix stresses are non-uniform in reality.[14] Here, however, we adopt Hill's approach[15] and compute the average stress in the phases. Let $\mathcal{G}$ and $\mathcal{g}$ define the in-plane average stress concentrations for the matrix of a specific ply under over-all in-plane stresses and out-of-plane normal stress, respectively. The first column of $\mathcal{G}$ is the stress $d\boldsymbol{\sigma}'_m$ caused by over-all stress $d\sigma_{11} = 1$ applied to the laminate, the second column corresponds to $d\sigma_{22} = 1$, etc. Similarly, $\mathcal{g}$ is the stress $d\boldsymbol{\sigma}'_m$ caused by $d\sigma_{33} = 1$. Now, the matrix in-plane stress in the ply under consideration caused by $d\boldsymbol{\sigma}$ and $d\theta$ can be written as:

$$d\boldsymbol{\sigma}'_m = s_T\mathbf{1}\,d\theta + \mathcal{G}(d\boldsymbol{\sigma}' - \mathbf{s}\,d\theta) - \mathcal{g}s_T\,d\theta. \tag{6}$$

The stress $d\sigma^m_{33}$ is written as:

$$d\sigma^m_{33} = s_T\,d\theta + \mathcal{j}^T(d\boldsymbol{\sigma}' - \mathbf{s}\,d\theta) - \mathcal{e}s_T\,d\theta, \tag{7}$$

where $\mathcal{j}^T$, $\mathcal{e}$ are stress concentration factors for matrix out-of-plane normal stress corresponding to over-all in-plane stresses and out-of-plane normal stress, respectively. Formulae for the concentration factors $\mathcal{G}$, $\mathcal{g}$, $\mathcal{j}^T$, $\mathcal{e}$ are given in Appendix B. They are functions of the fiber orientation, local instantaneous properties of the phases, and phase volume fractions. The first term in eqns (6), (7) is the isotropic stress caused in the matrix by the axisymmetric stresses $s_A\,d\theta$ and $s_T\,d\theta$ in the decomposed laminate (see Appendix A). In a plastically incompressible matrix, this isotropic stress state does not cause plastic deformation. The second term in eqns (6), (7) is the stress caused by the in-plane mechanical load $(d\boldsymbol{\sigma}' - \mathbf{s}\,d\theta)$, and the third term is the stress caused by removing the out-of-plane normal stress $s_T\,d\theta$.

3 DIMENSIONAL STABILITY OF $(\pm\varphi)_s$ LAMINATES

3.1 Elastic coefficient of thermal expansion

The system under consideration is a graphite-fibre-reinforced composite. This is a particularly attractive system in dimensionally accurate

Table 1. Material properties for graphite fiber and aluminium matrix

	E_A (GPa)	E_T (GPa)	G_A (GPa)	ν_A	α_A (10^{-6}/°C)	α_T (10^{-6}/°C)
P100 Graphite	690	6·07	15·5	0·41	−1·62	10·8
Aluminum	72·4	72·4	27·2	0·33	24·0	24·0

applications, since the graphite fiber has a negative coefficient of thermal expansion (CTE) in the axial direction, which tends to reduce the axial thermal strain developed in metal matrix composites. A dimensionally stable laminated system can therefore be designed by variation of the fiber volume content and/or the fiber orientation. Here, we assume that the fiber-volume fraction is constant in all laminae at 0·5 and select aluminum for the matrix material. Elastic properties of the matrix and fiber are shown in Table 1.

The effect of the fiber orientation in $(\pm\varphi)_s$ laminates on the over-all axial CTE is examined in Fig. 2. Computation of the over-all response of the laminate was made with the ABAQUS program and the implemented PHA model by using the finite-element mesh of Fig. 1. It is seen that the unidirectional composite does not exhibit dimensional stability in the elastic range. Dimensionally stable systems are found at $\varphi = 12°$, 38°. Strength and stiffness considerations exclude the system with $\varphi = 38°$. Our subsequent analysis will therefore, focus on $(\pm 12)_s$ laminates.

3.2 Initial yielding

The over-all initial yield surface of a composite laminate is the envelope of all stress states that can be reached from the current state by purely elastic deformation in the matrix phase for all plies. The yield surface may translate in the over-all stress space as a result of hardening of the matrix and/or the constraint imposed on the matrix deformation by the fibers.[10,11] Matrix hardening takes place only when plastic strain develops in the matrix, whereas constraint hardening is present for both elastic and elastic–plastic systems when mechanical loads are coupled with thermal changes. It was shown by Dvorak, Rao, and Tarn[16] and Bahei-El-Din[17] that the over-all yield surfaces of unidirectional composites and laminates translate in the stress space if the composite is subjected to a thermal change.

For elastic laminates, the translation is given by the stress vector $d\hat{\boldsymbol{\sigma}}$ (eqns (1)–(3)).[17] Evaluation of the yield surface translation for elastic–plastic laminates is more complex. In the examples given in the sequel, the over-all yield surface and its translation were found from the laminate analysis given in Refs 10 and 17.

Figure 3 shows three sections of the initial yield surface ($\Delta\theta = 0$) of $(\pm 12)_s$ Gr/Al laminates in the plane stress space. The yield surfaces were computed for a von Mises matrix and a

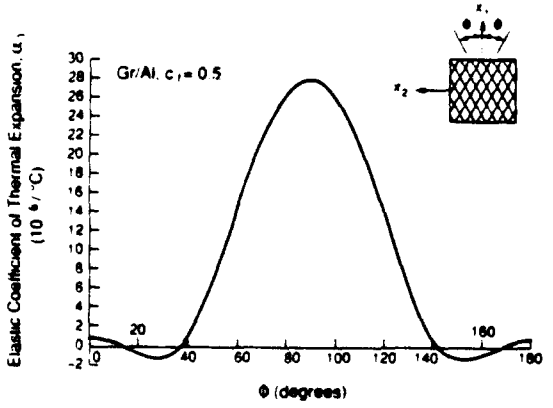

Fig. 2. Variation of axial elastic coefficient of thermal expansion of $(\pm\varphi)_s$ laminates.

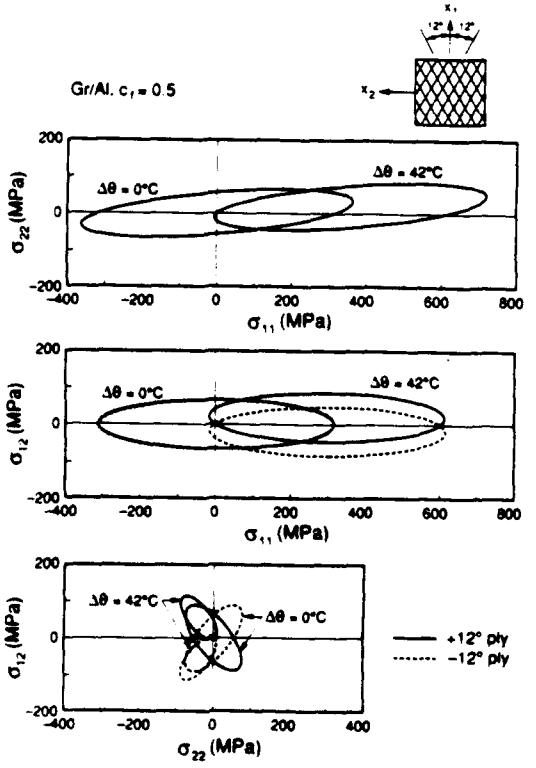

Fig. 3. Initial yield surfaces for a $(\pm 12)_s$ laminate.

matrix tensile-yield stress of 70 MPa. The latter is approximately the magnitude of the yield stress for 6061 aluminum in the as-fabricated condition. For each ply, there is a yield surface in the over-all stress space. The over-all yield surface is the inner envelope of the two surfaces shown in Fig. 3. Note that, in the $\sigma_{11}\sigma_{22}$ plane, the yield surfaces of the $+\varphi$ and $-\varphi$ plies coincide.

Under a temperature change $d\theta$, the centers of the yield surfaces for the $+\varphi$ and $-\varphi$ plies are located at $d\hat{\boldsymbol{\sigma}}$ (eqns (1)–(3)). At the onset of yielding, at least one of the yield branches contains the stress origin. This is shown in Fig. 3, where yield surfaces of the $(\pm 12)_s$ laminate are drawn at the yield temperature $\Delta\theta = 42°C$. Note that both plies yield together and that the response under subsequent mechanical loading will be very much affected by the temperature change. For example, after the temperature change indicated, the laminate response is elastic under axial tensile stress σ_{11} and elastic–plastic under axial compression. In the $\sigma_{11}\sigma_{12}$ plane, the over-all elastic domain is reduced substantially after the temperature change, while it completely disappears in the $\sigma_{22}\sigma_{12}$ plane.

The implication is that relatively small temperature changes may cause yielding of laminates and that the over-all deformation under thermal loading can be affected significantly by the presence of mechanical loads and vice versa. Moreover, the mechanical-loading direction is expected to influence dimensional stability under thermal loads. These effects are examined in the subsequent sections.

3.3 Dimensional stability under pure thermal loading

It was shown that initial yielding of the composite laminate occurs for a temperature change of only 42°C. In this section, we consider applications in which the laminate is subjected to thermal cycles in the range ±120°C. Consequently, plastic deformation develops in the aluminum matrix, which may affect the dimensional stability of the composite. Linear work-hardening was assumed for the matrix response in the plastic range. Two values were considered for the elastic–plastic tangent modulus, E_{tan}, of the matrix, $(E_{tan}/E)_m = 0{\cdot}167, 0{\cdot}667$, which correspond to plastic tangent moduli, H, of 14·5 GPa and 145 GPa, respectively.

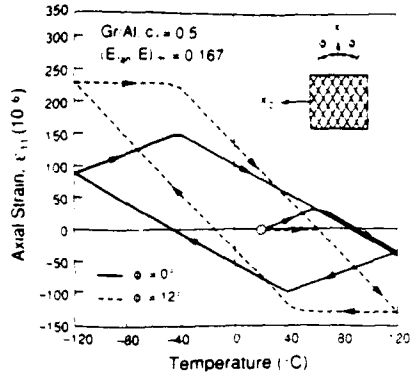

Fig. 4. Temperature/axial-strain response of a unidirectional composite and $(\pm 12)_s$ laminate with $(E_{tan}/E)_m = 0{\cdot}167$.

Figures 4 and 5 show the axial thermal strains generated in unidirectional and $(\pm 12)_s$ Gr/Al laminates under the temperature cycle $20 \rightarrow 120 \rightarrow -120 \rightarrow 120°C$. Although the composite is dimensionally stable for $\varphi = 12°$ in the elastic range, it is not stable in the plastic range. Furthermore, the 0° lamina, which did not exhibit stability in the elastic range, developed a total strain during the thermal cycle much smaller than that found for $\varphi = 12°$. Hence, the dimensional stability of the laminate was enhanced by plastic deformation of the matrix for the 0° laminate and reduced for the $(\pm 12)_s$ laminate. As expected, the over-all strains found for the composite with $(E_{tan}/E)_m = 0{\cdot}667$ (Fig. 5) are much smaller than the strains found for $(E_{tan}/E)_m = 0{\cdot}167$ (Fig. 4).

The axial CTE in the elastic and elastic–plastic ranges are compared in Fig. 6 for $0 \leq \varphi \leq 45°$. The magnitudes of the over-all CTE were found as the slopes of the linear parts of the strain–temperature curves computed for each

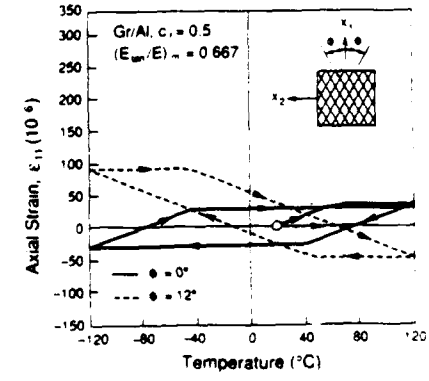

Fig. 5. Temperature/axial-strain response of a unidirectional composite and $(\pm 12)_s$ laminate with $(E_{tan}/E)_m = 0{\cdot}667$.

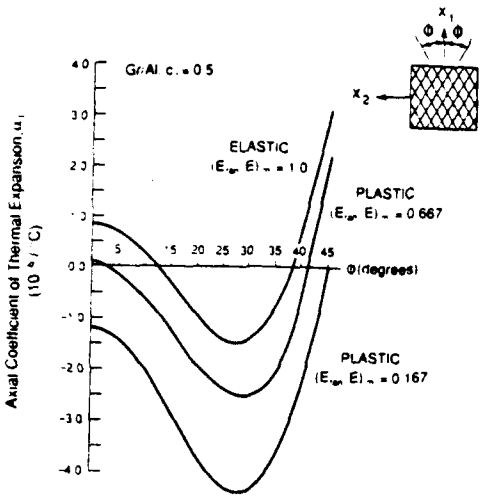

Fig. 6. Variation of axial coefficient of thermal expansion for $(\pm\varphi)_s$ laminates.

layup by using ABAQUS (see, for example, Figs 4, 5). It is clear that plastic deformation of the matrix affects the dimensional stability of composites to a great extent. For example, elastic laminates have a vanishing CTE for $\varphi = 12°$, 38°, whereas laminates with the stiffer matrix in the plastic range show this property at $\varphi = 2°$, 41°. On the other hand, laminates with the softer matrix in the elastic–plastic range have a vanishing CTE at $\varphi = 45°$. The large lamination angles are obviously not useful in real applications since they lead to large plastic strains and reduce the composite stiffness substantially.

Figure 7 shows the total axial-strain range found during the thermal loading cycle indicated in Figs 4, 5 as a function of the lamination angle, φ. The strain magnitudes found for $\varphi = 12°$ during the cycle are indicated. It is seen that the

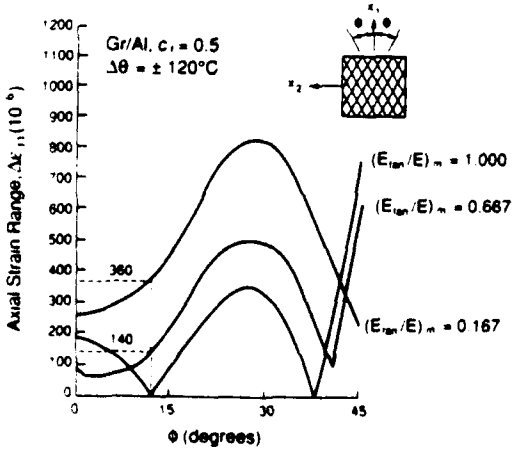

Fig. 7. Variation of axial strain range for $(\pm\varphi)_s$ laminates under ±120°C cycles.

unidirectional composite experiences dimensional changes during thermal cycling that are much smaller than those found for other layups. In actual applications, however, small off-axis angles may be required to enhance the transverse stiffness and strength of the composite.

The results are, of course, affected by the matrix properties, as is evident from the response of the two matrices considered here. Different matrix responses can be achieved by heat treatment, which affects both the magnitude of the matrix yield stress and the plastic tangent modulus. The effect of the matrix yield stress on dimensional stability of laminates is examined in the sequel.

3.4 Dimensional stability under thermomechanical loads

In certain structural applications of fibrous composites, temperature changes generate mechanical loads. Statically indeterminate truss beams considered for space structures[18] are examples of this situation. To examine the effect of combining mechanical and thermal loads on the dimensional stability of composites, we consider again the $(\pm 12)_s$ Gr/Al laminate with $(E_{tan}/E)_m = 0{\cdot}167$. The response under three separate loading cycles is examined: (*a*) the thermal-loading cycle applied in the previous section ($20 \rightarrow 120 \rightarrow -120 \rightarrow 120$°C), (*b*) the same thermal-loading cycle combined with the axial tension/compression load cycle ($0 \rightarrow 300 \rightarrow -300 \rightarrow 300$ MPa), (*c*) the thermal cycle combined with the axial compression/tension load cycle ($0 \rightarrow -300 \rightarrow 300 \rightarrow -300$ MPa). Let r and p indicate the ratio of axial load to temperature (MPa/°C) and the axial load amplitude (MPa), respectively. Hence, the three loading cases indicated above specify thermal cycling in the range ±120°C with $(r, p) = (0, 0)$, $(2{\cdot}5, \pm 300)$, $(-2{\cdot}5, \mp 300)$, respectively.

The over-all strain computed in all three loading cases is plotted as a function of temperature in Fig. 8. The mechanical-loading parameters r, p and the total strain range, $\Delta\epsilon_{11}$, found in each case are tabulated. As expected, dimensional stability is lost in the elastic range when the laminate is subjected to mechanical loads. Since the axial elastic CTE vanishes, the strain developed in the elastic range is only mechanical. The elastic–plastic response under thermomechanical loads is also very different

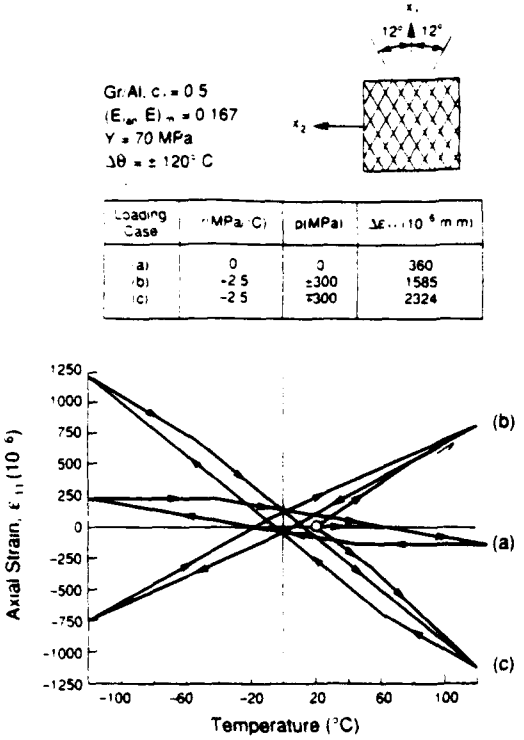

Fig. 8. Temperature/axial strain response of a $(\pm 12)_s$ laminate with matrix yield stress $Y = 70$ MPa under thermomechanical load cycles in the range ± 120°C.

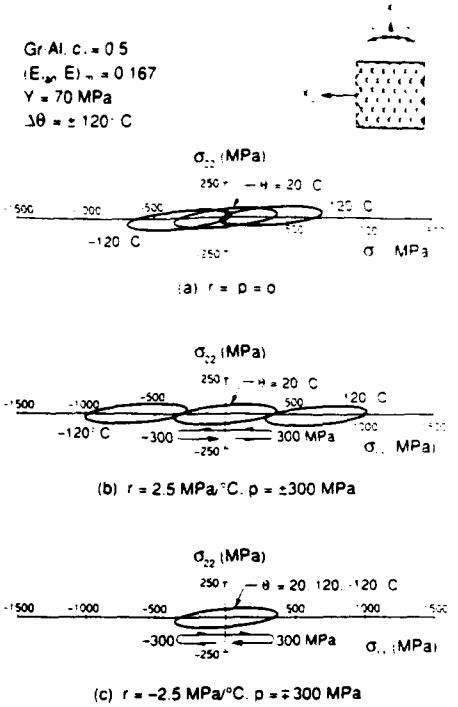

Fig. 9. Over-all yield surfaces of a $(\pm 12)_s$ laminate in the $\sigma_{11}\sigma_{12}$ plane corresponding to the thermomechanical load cycles of Fig. 8.

from the pure thermal loading case as indicated by the slopes of the strain/temperature segments. The loading direction affects the results significantly. The results show that larger strains occur when r is negative (case (c)). In this case, both the temperature change and the mechanical load produce axial compressive stresses in the matrix. This causes the composite to yield at a lower temperature as compared with the cases with $r = 0$ (case (a)) and $r > 0$ (case (b)) and results in larger plastic strains during the same thermal cycle. As may be seen in Fig. 8, the dimensional stability of the laminate is enhanced by plastic deformation of the matrix for $r > 0$, and reduced for $r \leq 0$.

The effect of thermomechanical loading on plastic deformation of laminates is illustrated with the help of the yield surface in Fig. 9. The initial yield surface of the $(\pm 12)_s$ laminate together with the yield surfaces corresponding to 120°C and -120°C are shown for the three loading cases indicated above. In case (a), $r = 0$, $p = 0$, the yield surface translates in the direction of the positive σ_{11} axis and contains the stress origin at 62°C ($\Delta\theta = 42$°C) as indicated previously. As the temperature increases from 62 to 120°C, the yield surface remains in contact with the origin and the matrix deforms plastically. On the reversed part of the cycle from 120 to -120°C, the yield surface translates in the direction of the negative σ_{11} axis, where it comes into contact with the origin at about 42°C. At this temperature, plastic deformation again develops in the matrix, and the yield surface remains in contact with the origin to the end of this thermal-loading segment. In loading case (b), $r = 2{\cdot}5$, $p = \pm 300$ MPa, both the loading point and the yield surface move along the positive σ_{11} axis but with different rates relative to the temperature. This delays yielding of the laminate, which occurs at about 80°C (see Fig. 8) and axial load of 180 MPa (note that $r = 3$ for the first loading segment). The yield surface translates at a higher rate than to the stress point, and as such the yield surface comes into contact with the loading point at the trailing end of the surface. The process is repeated when the load and temperature are reversed.

Yielding of the composite is accelerated, on the other hand, when $r < 0$ (loading case (c), $r = -2{\cdot}5$, $p = \mp 300$ MPa), where the loading point and the yield surface move in opposite directions. The composite in this case yields at about 50°C (see Fig. 8) and an axial load of

−90 MPa. Continued loading results in translation of the yield surface in the direction of the negative σ_{11} axis where it remains in contact with the loading point. At 120°C and −300 MPa, the yield surface is pulled back by the loading point to a position that is almost identical with the initial position.

3.5 Effect of elevated yield stress

In the preceding sections, we showed that plastic deformation of the matrix may enhance or reduce the dimensional stability of composites. Through heat treatment, it is possible to change the matrix properties in such a way that the dimensional stability of the composite is enhanced. We have already shown that increasing the plastic tangent modulus of the matrix reduces the thermal strains significantly (Figs 4–7). In this section, we examine the effect of the magnitude of the matrix yield stress, particularly when it is elevated by heat treatment (for example, by the T6 temper).

Consider again the (±12), Gr/Al laminate and assume that the matrix yield stress in simple tension has been increased from 70 MPa to 280 MPa. The computed axial strain is shown in Fig. 10 for the three loading cases described previously. For the temperature range indicated

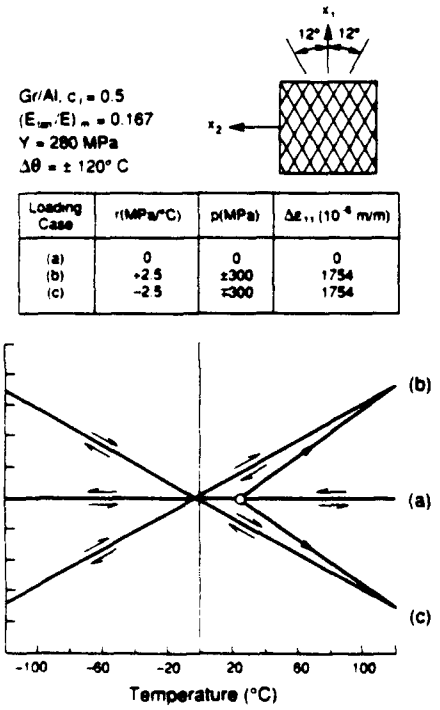

Fig. 10. Temperature/axial strain response of a (±12), laminate with matrix yield stress $Y = 280$ MPa under thermomechanical load cycles in the range ±120°C.

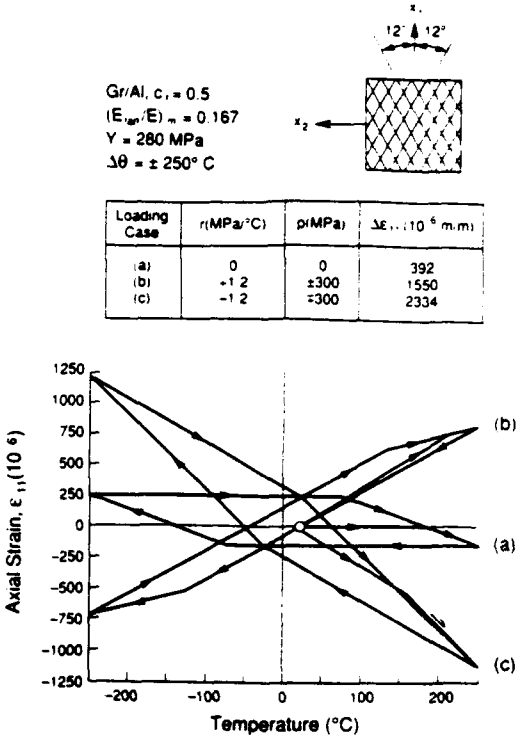

Fig. 11. Temperature/axial strain response of a (±12), laminate with matrix yield stress $Y = 280$ MPa under thermomechanical load cycles in the range ±250°C.

(±120°C), the laminate remains elastic. Comparing the strains found in this case with those given in Fig. 8, we find that increasing the yield stress by 400% reduced the strains developing under temperature coupled with compression/tension loading ($r = -2{\cdot}5$, $p = \mp 300$) by about 25%. The strains found under temperature and tension/compression loading ($r = 2{\cdot}5$, $p = \pm 300$), however, increased by about 10% when the matrix yield stress increased.

Figure 11 shows the response when the composite is cycled between 250°C and −250°C. The axial strains developed in this case are comparable with those developed under ±120°C cycles and 70 MPa matrix yield stress (Fig. 8). Consequently, if a certain tolerance is imposed on dimensional changes of the laminate, they can be met for various temperature and mechanical load ranges by changing the matrix yield stress through heat treatment. In Section 5, we present master curves that may aid in design for specific dimensional tolerances in Gr/Al laminates.

3.6 Summary

The results presented in the preceding sections are summarized in Table 2. The case of a matrix

Table 2. Summary of dimensional-stability results for P100 Gr/Al, (±12)$_s$ laminate [$c_f = 0{\cdot}5$, $(E_{mm}/E)_m = 0{\cdot}167$]

Loading path			Total axial-strain range, $\Delta\epsilon_{11}(10^{-6}$ m/m)	
$\Delta\theta$ °C	r (MPa/°C)	p (MPa)	6061-O Al ($Y = 70$ MPa)	6061-T6 Al ($Y = 280$ MPa)
±120	0	0	360	0
±120	2·5	±300	1585	1754
±120	−2·5	∓300	2324	1754
±250	0	0	905	392
±250	1·2	±300	1002	1550
±250	−1·2	∓300	2879	2334

yield stress of 70 MPa and temperature range of ±250°C is added to the cases discussed previously for comparison.

For the model (±12)$_s$ laminate considered here and the temperature and axial loading ranges indicated, we find:

(i) dimensional stability is achieved for the T6 temper of the matrix alloy and pure thermal loading of ±120°C;
(ii) overaging enhances dimensional stability under pure thermal loads ($r = 0$), and under out-of-phase thermal and mechanical loads ($r < 0$);
(iii) the dimensional stability of the composite is enhanced by plastic deformation of the matrix when the temperature change and the mechanical load are in-phase ($r > 0$); otherwise it is reduced;
(iv) the dimensional stability was unaffected when the operating temperature range increased from ±120°C to ±250°C and the matrix yield stress increased from 70 MPa to 280 MPa.

4 DESIGN CURVES FOR GR/AL LAMINATES

In this section, we use the thermomechanical analysis described in Section 2 to produce master curves for calculation of the axial strain in Gr/Al $(\pm\varphi)_s$ laminates. The load consists of proportional axial stress σ_{11} and temperature change θ from a reference temperature θ_0. We assume a von Mises matrix with a bi-linear stress/strain curve.

Figure 12 shows a schematic representation of the over-all axial-strain/temperature curve. The

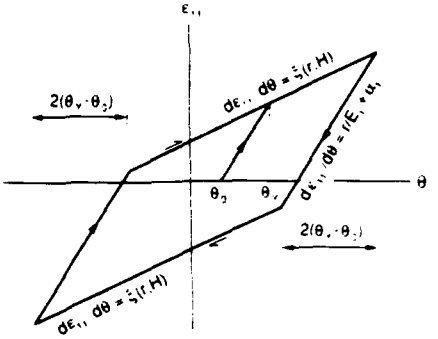

Fig. 12. Schematic representation of temperature–axial-strain curve for a laminate under thermomechanical loads.

curve is bi-linear and consists of an elastic part, $\theta_0 \le \theta \le \theta_Y$ where θ_Y is the yield temperature, and an elastic–plastic part, $\theta > \theta_Y$. The slope of the elastic segment of the curve is given by $(r/E_1 + \alpha_1)$, where $r = \sigma_{11}/(\theta - \theta_0)$, E_1 is the laminate axial elastic Young's modulus, and α_1 is the laminate axial elastic coefficient of thermal expansion. The slope of the elastic–plastic segment is a function of the loading path, r, and the matrix plastic tangent modulus, H. Let $\xi(r, H)$ denote the slope of the elastic–plastic portion of the overall strain–temperature curve. The over-all axial strain is written as:

$$\epsilon_{11} = (r/E_1 + \alpha_1)(\theta - \theta_0), \quad \theta_0 \le \theta \le \theta_Y \quad (8)$$

$$\epsilon_{11} = (r/E_1 + \alpha_1)(\theta_Y - \theta_0) + \xi(r)(\theta - \theta_Y), \quad \theta > \theta_Y. \quad (9)$$

The overall axial-strain/temperature curve can easily be constructed for a cyclic proportional axial-load/temperature regime as shown in Fig. 12.

The elastic over-all coefficient of thermal expansion, α_1 and Young's modulus, E_1, are given in Figs 6 and 13 for a Gr/Al composite and

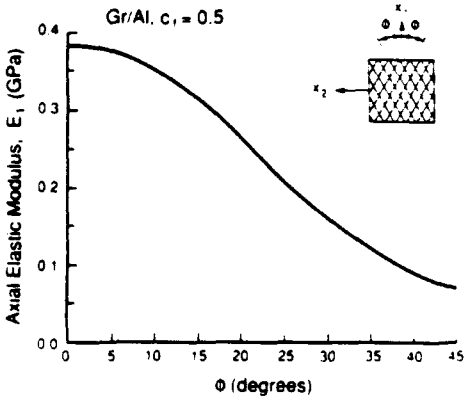

Fig. 13. Variation of axial elastic modulus for $(\pm\varphi)_s$ laminates.

$0 \le \varphi \le 45°$. The magnitude of the yield temperature is a function of the matrix yield stress and the ratio r between the mechanical load and the temperature change. Figure 14 shows yield curves generated by the analysis of Section 2 for selected values of the lamination angle φ. Given r, the curves provide the value of $(\theta_Y - \theta_0)$ and the corresponding stress at the onset of yielding in the laminate. For $\varphi = 0$, the relationship between the axial stress and the temperature change is linear with slope $r = 0{\cdot}115$. Under this load/temperature ratio, the response of the 0° lamina remains elastic. The slope, ξ, of the elastic–plastic segment of the over-all strain–temperature curve, computed for selected values of the angle φ and $H = 14{\cdot}5$ GPa, is given in Fig. 15 as a function of the ratio r between the axial load and temperature change. Similar curves can easily be generated for other composite systems and layups with the analysis presented in Section 2. Comparison of the computed over-all response for various $(\pm\varphi)_s$ Gr/Al laminates under thermomechanical loads with the finite-element

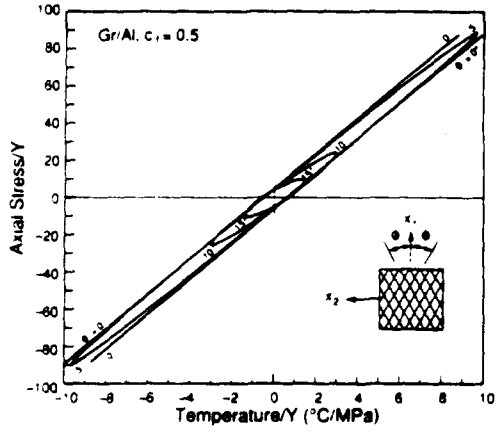

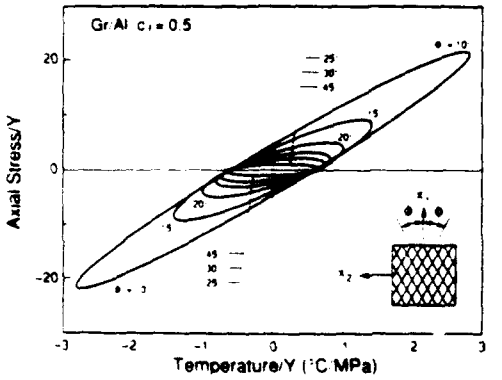

Fig. 14. Initial yield curves for selected $(\pm\varphi)_s$ laminates under combined axial stress and temperature change, normalized with the matrix yield stress Y.

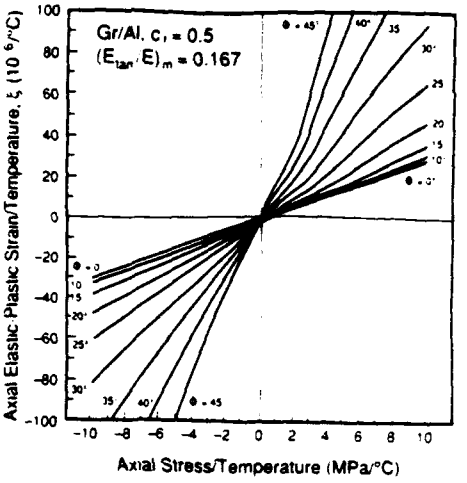

Fig. 15. Computed axial elastic–plastic strain for selected $(\pm\varphi)_s$ laminates subjected to proportional axial-stress–temperature loading.

results showed excellent agreement. The analysis in Section 2, however, may not provide accurate results for composite systems that deform in the matrix-dominated mode[9] such as B/Al and SiC/Al composites.

5 CONCLUSION

Dimensional changes caused in metal-matrix composites and laminates may be restricted within specified tolerances by variation of the laminate layup and the matrix yield stress and stress/strain response through heat treatment. Depending on the operating temperature range and the ratio of mechanical load to temperature change, the proper heat treatment can be determined such that the dimensional stability of the composite is enhanced. For example, a 6061 Al/Gr $(\pm 12)_s$ laminate is dimensionally stable in the temperature range ±42°C for the as-fabricated composite (matrix yield stress $Y =$ 70 MPa) and stable in the range ±168°C for the T6 condition ($Y = 280$ MPa). The matrix plasticity may enhance or reduce the dimensional stability of laminates subjected to combined thermal and mechanical loads. The onset of plastic deformation of the matrix is reduced for out-of-phase thermal and axial mechanical loads and enhanced for in-phase loads. Accordingly, the dimensional stability is affected by the way in which the mechanical load and thermal change are synchronized. In any case, accurate plasticity analysis must be performed for specific design loads and parameters.

Recent developments in the theory of plasticity of unidirectional composites were utilized in the present paper to examine the response of composite laminates under thermomechanical loads. One approach used here is based on the finite-element method, where the underlying constitutive equations of unidirectional plies are derived from a representative volume of the microstructure. Although highly accurate, this method is not cost-effective and requires availability of a finite-element routine. A more economical and equally accurate analysis, which may be performed on a personal computer, is based on the laminate theory and fiber-dominated micromechanical models of unidirectional composites. The analysis was outlined and used in the present paper to generate master design curves for the evaluation of axial strains in laminates subjected to axial stress/temperature cycles.

ACKNOWLEDGEMENT

This work was supported by a grant from the Office of Naval Research under contract number N000014-85-K-0733. Dr. Yapa Rajapakse served as contract monitor.

REFERENCES

1. Bahei-El-Din, Y. A., Plasticity analysis of fibrous composite laminates under thermomechanical loads. In *Thermal and Mechanical Behavior of Ceramic and Metal Matrix Composites* (ASTM STP 1080), ed J. M. Kennedy, H. H. Moeller & W. S. Johnson. American Society for Testing and Materials, Philadelphia, PA, U.S.A., 1990, pp. 20–39.
2. Min, B. K. & Crossman, F. W., History-dependent thermomechanical properties of graphite/aluminium unidirectional composites. In *Composite Materials: Testing and Design (Sixth Conference)* (ASTM STP 787), ed. I. M. Daniel. American Society for Testing and Materials, Philadelphia, PA, USA, 1982, pp. 371–92.
3. Wolff, E. G., Stiffness–thermal-expansion relationships in high-modulus carbon fibers. *J. Composite Materials*, **21** (1987) 81–97.
4. Tompkins, S. S. & Dries, G. A., Thermal expansion measurement of metal matrix composites. In *Testing Technology of Metal Matrix Composites* (ASTM STP 964), ed. P. R. DiGiovanni & N. R. Adsit. American Society for Testing and Materials, Philadelphia, PA, USA, 1988, pp. 248–58.
5. Bahei-El-Din, Y. A., Dvorak, G. J. & Utku, S., Finite element analysis of elastic–plastic fibrous composite structures. *Computers & Structures*, **13** (1981) 321–30.
6. Wu, J. F., Shephard, M. S., Dvorak, G. J. & Bahei-El-Din, Y. A., A material model for the finite element analysis of metal matrix composites. *Compos. Sci. Technol.*, **35** (1989) 347–66.
7. Dvorak, G. J. & Teply, J. L., Periodic array models for plasticity analysis of composite materials. In *Plasticity Today: Modeling, Methods and Applications (W. Olszak Memorial Volume)*, ed. A. Wawczuk & V. Bianchi. Elsevier Science Publishers, Amsterdam, 1985, pp. 624–42.
8. Teply, J. L. & Dvorak, G. J., Bounds on overall instantaneous properties of elastic–plastic composites. *J. Mech. Phys. Solids*, **36** (1988) 29–58.
9. Dvorak, G. J. & Bahei-El-Din, Y. A., A bimodal plasticity theory of fibrous composite materials. *Acta Mech.*, **69** (1987) 219–41.
10. Bahei-El-Din, Y. A. & Dvorak, G. J., Plasticity analysis of laminated composite plates. *J. Appl. Mech.*, **49** (1982) 740–6.
11. Dvorak, G. J. & Bahei-El-Din, Y. A., Plasticity analysis of fibrous composites. *J. Appl. Mech.*, **49** (1982) 327–35.
12. Bahei-El-Din, Y. A., Thermomechanical uniform fields in fibrous composte laminates. (Submitted).
13. Dvorak, G. J., Thermal expansion of elastic–plastic composite materials. *J. Appl. Mech.*, **53** (1986) 737–43.
14. Bahei-El-Din, Y. A., Dvorak, G. J., Lin, J., Shah, R. S. & Wu, J. F., Local fields and overall response of fibrous and particulate metal matrix composites. Final Technical Report, Alcoa Laboratory, Contact No. 379(52R)053(22L), November, 1987.
15. Hill, R., Elastic properties of reinforced solids: some theoretical principles. *J. Mech. Phys. Solids*, **11** (1963) 357–72.
16. Dvorak, G. J., Rao, M. S. M. & Tarn, J. Q. Generalized initial yield surfaces for unidirectional composites. *J. Appl. Mech.*, **41** (1974) 249–53.
17. Bahei-El-Din, Y. A., Yielding and thermal hardening in fibrous composite laminates. (Submitted).
18. Miller, M. F., Christian, J. L. & Wennhold, W. F., Design, manufacture, development, test, and evaluation of boron/aluminum structural components for space shuttle. General Dynamics/Convair Aerospace, Contract No. NAS 8-27738, 1973.
19. Hill, R., Theory of mechanical properties of fiber-strengthened materials: I. Elastic behaviour. *J. Mech. Phys. Solids*, **12** (1964) 199–212.
20. Hill, R., Theory of mechanical properties of fiber-strengthened materials: III. Self-consistent model. *J. Mech. Phys. Solids*, **13** (1965) 189–98.
21. Mori, T. & Tanaka, K., Average stress in matrix and average elastic energy of materials with misfitting inclusion. *Acta Metal.*, **21** (1973) 571–4.
22. Dvorak, G. J., Plasticity theories for fibrous composite materials. In *Metal Matrix Composites, Vol. 2: Mechanisms and Properties*, ed. R. K. Everett & R. J. Arsenault. Academic Press, Boston, MA, USA, 1990, pp. 1–77.

APPENDIX A

In this Appendix, we consider the problem of a unidirectional composite subjected to a temperature change $d\theta$. Both the fiber and matrix phases

are elastic; the fiber is transversely isotropic, and the matrix is isotropic. The solution of this problem was found by Dvorak,[13] using a decomposition scheme in which the fiber and matrix phases are separated from each other and subjected to the thermal change $d\theta$ while applying surface tractions to the surfaces of the phases to maintain the current stresses. Since the phases deform differently under temperature variations, auxiliary phase stresses are needed to ensure compatibility of the phases. The auxiliary stresses are found by satisfying compatibility of the phase deformations and equilibrium of the tractions at phase interfaces. In this way, the composite can be reassembled. Upon reassembly, the unidirectional composite supports overall stresses $d\hat{\boldsymbol{\sigma}}$, that equilibrate the phase auxiliary stresses. The over-all stress is axisymmetric and given by:

$$\begin{aligned} d\hat{\sigma}_{11} &= s_A\, d\theta, \\ d\hat{\sigma}_{22} &= d\hat{\sigma}_{33} = s_T\, d\theta, \\ d\hat{\sigma}_{23} &= d\hat{\sigma}_{31} = d\hat{\sigma}_{12} = 0. \end{aligned} \tag{A1}$$

Equivalent expressions for s_A and s_T can be found in Refs 12 and 13. The latter are recorded here for phase thermoelastic properties that are not functions of temperature:

$$s_A = (a_3 b_1 - a_1 b_3)/(a_1 b_2 - a_2 b_1) \tag{A2}$$

$$s_T = (a_2 b_3 - a_3 b_2)/(a_1 b_2 - a_2 b_1) \tag{A3}$$

$$a_1 = (n_f + c_m l_f)/(k_f E_L^f) - 2/(3K_m) \tag{A4}$$

$$a_2 = -l_f/(c_f k_f E_L^f), \quad a_3 = 2(\alpha_T^f - \alpha_m) \tag{A5}$$

$$b_1 = l_f/(k_f E_L^f) + 1/(3K_m) + c_m/(c_f E_L^f) \tag{A6}$$

$$b_2 = -1/(c_f E_L^f), \quad b_3 = -(\alpha_L^f - \alpha_m). \tag{A7}$$

where K_m is the matrix bulk modulus, α_m is the matrix coefficient of thermal expansion, E_L^f is the fiber longitudinal Young's modulus, n_f, k_f, l_f are Hill's moduli[19] of the fiber, and α_L^f and α_T^f are coefficients of thermal expansion of the fiber in the longitudinal direction and transverse plane, respectively.

The auxiliary local stresses are given by:[13]

$$d\hat{\boldsymbol{\sigma}}_m = s_T[1\ 1\ 1\ 0\ 0\ 0]^T\, d\theta \tag{A8}$$

$$\begin{aligned} d\hat{\boldsymbol{\sigma}}_f &= s_T[\gamma\ 1\ 1\ 0\ 0\ 0]^T\, d\theta, \\ \gamma &= (s_A/s_T - c_m)/c_f. \end{aligned} \tag{A9}$$

The strain field corresponding to eqn (A1) is uniform in the entire composite:

$$\begin{aligned} d\hat{\boldsymbol{\epsilon}} = d\hat{\boldsymbol{\epsilon}}_f = d\hat{\boldsymbol{\epsilon}}_m &= [h\ h\ h\ 0\ 0\ 0]^T\, d\theta, \\ h &= s_T/3K_m + \alpha_m. \end{aligned} \tag{A10}$$

APPENDIX B

Here we give expressions for the instantaneous compliance matrix $\mathcal{M}$ and in-plane stress vector k for $(\pm\varphi)_s$ laminates, together with expressions for the matrix stress-concentration factors $\mathcal{G}$, g, j^T, e.

Consider a laminate loaded by in-plane stress $d\boldsymbol{\sigma}'$ and out-of-plane normal stress $d\sigma_{33}$, where x_1x_2 is the plane of the laminate. The over-all in-plane strains can be written as:

$$d\boldsymbol{\epsilon}' = \mathcal{M}\, d\boldsymbol{\sigma}' + m\, d\sigma_{33}. \tag{B1}$$

The over-all stress $d\boldsymbol{\sigma}'$ can be written in terms of $d\boldsymbol{\epsilon}'$ and $d\sigma_{33}$ as

$$d\boldsymbol{\sigma}' = \mathcal{L}\, d\boldsymbol{\epsilon}' + k\, d\sigma_{33}, \tag{B2}$$

where

$$\mathcal{L} = \mathcal{M}^{-1}, \quad k = -\mathcal{L}m. \tag{B3}$$

Equations similar to eqns (B1) and (B2) can be written for each $+\varphi$ and $-\varphi$ ply. The over-all $\mathcal{M}$ and m are given by:[12]

$$\mathcal{M} = 2(\mathcal{L}_{+\varphi} + \mathcal{L}_{-\varphi})^{-1}, \quad m = \tfrac{1}{2}\mathcal{M}(k_{+\varphi} + k_{-\varphi}), \tag{B4}$$

where

$$\mathcal{L}_i = \mathcal{M}_i^{-1}, \quad k_i = -\mathcal{L}_i m_i, \quad i = +\varphi, -\varphi. \tag{B5}$$

The subscripts $+\varphi$ and $-\varphi$ indicate over-all quantities for the $+\varphi$ and $-\varphi$ plies, respectively, in the laminate co-ordinate system x_j.

The ply compliances $\mathcal{M}_i$ and m_i are given by:

$$\mathcal{M}_i = \mathcal{R}_i^T \bar{\mathcal{M}} \mathcal{R}_i, \quad m_i = \mathcal{R}_i^T \bar{m}, \quad i = +\varphi, -\varphi, \tag{B6}$$

where

$$\mathcal{R}_{+\varphi} = \begin{bmatrix} \cos^2\varphi & \sin^2\varphi & \sin 2\varphi \\ \sin^2\varphi & \cos^2\varphi & -\sin 2\varphi \\ -\tfrac{1}{2}\sin 2\varphi & \tfrac{1}{2}\sin 2\varphi & \cos 2\varphi \end{bmatrix}$$

$$\mathcal{R}_{-\varphi} = \begin{bmatrix} \cos^2\varphi & \sin^2\varphi & -\sin 2\varphi \\ \sin^2\varphi & \cos^2\varphi & \sin 2\varphi \\ \tfrac{1}{2}\sin 2\varphi & -\tfrac{1}{2}\sin 2\varphi & \cos 2\varphi \end{bmatrix}, \tag{B7}$$

and $\bar{\mathcal{M}}$, $\bar{m}$ are the over-all compliances of a unidirectional composite in the local co-ordinate system $\bar{x}_j$, where $\bar{x}_1$ is the fiber direction. Matrix

$\mathcal{M}$ is associated with in-plane loading and $\bar{m}$ with out-of-plane normal-stress loading. Expressions for $\mathcal{M}$ and $\bar{m}$ are given in Appendix C.

The ply in-plane stresses $d\boldsymbol{\sigma}_i'$ and out-of-plane normal stress $d\sigma_{33}^{(i)}$ can be written in terms of their over-all counterparts $d\boldsymbol{\sigma}'$ and $d\sigma_{33}$ as:

$$d\boldsymbol{\sigma}_i' = \mathcal{H}_i\, d\boldsymbol{\sigma}' + k_i\, d\sigma_{33}, \quad d\sigma_{33}^{(i)} = d\sigma_{33}. \tag{B8}$$

The distribution factors $\mathcal{H}_i$, k_i, $i = +\varphi, -\varphi$, are given by:[12]

$$\mathcal{H}_i = \mathcal{L}_i\mathcal{M}, \quad k_i = \mathcal{L}_i(\mathcal{m} - \mathcal{m}_i). \tag{B9}$$

In the co-ordinate system $\bar{x}_j$, the ply stresses are given by:

$$d\bar{\boldsymbol{\sigma}}_i' = \mathcal{R}_i\, d\boldsymbol{\sigma}_i', \quad d\bar{\sigma}_{33}^{(i)} = d\sigma_{33}, \tag{B10}$$

where the transformation matrix $\mathcal{R}_i$, $i = +\varphi, -\varphi$, is given by eqn (B7).

The matrix average stresses in a specific ply can be written in terms of the ply stresses as:

$$d\boldsymbol{\sigma}_m = \mathcal{B}\, d\bar{\boldsymbol{\sigma}}^{(i)} + b\, d\bar{\sigma}_{33}^{(i)}, \tag{B11}$$

$$d\sigma_{33}^m = c^T\, d\bar{\boldsymbol{\sigma}}^{(i)} + \eta\, d\bar{\sigma}_{33}^{(i)}, \tag{B12}$$

where $\mathcal{B}$, b, c^T, η are instantaneous stress-concentration factors for the ply under consideration (see Appendix C).

Finally, the matrix stresses can be written in terms of the laminate stresses $d\boldsymbol{\sigma}_i'$ and $d\sigma_{33}$ as:

$$d\boldsymbol{\sigma}_m = \mathcal{G}\, d\boldsymbol{\sigma}' + g\, d\sigma_{33} \tag{B13}$$

$$d\sigma_{33}^m = j^T\, d\boldsymbol{\sigma}' + e\, d\sigma_{33}. \tag{B14}$$

From eqns (B8)–(B14), we find:

$$\mathcal{G} = \mathcal{B}\mathcal{R}_i\mathcal{H}_i, \quad g = \mathcal{B}\mathcal{R}_i k_i + b \tag{B15}$$

$$j^T = c^T\mathcal{R}_i\mathcal{H}_i, \quad e = c^T\mathcal{R}_i k_i + \eta. \tag{B16}$$

APPENDIX C

The over-all compliances $\mathcal{M}$ and $\bar{m}$ of a lamina in the $\bar{x}_j$ co-ordinate system ($\bar{x}_1 \equiv$ axial direction) can be found in terms of the local properties and the concentration factors that relate the average local fields to the over-all uniform fields.[15] In the notation used here, the over-all compliances $\mathcal{M}$, $\bar{m}$ of a unidirectional lamina are given by:

$$\mathcal{M} = \mathcal{M}_f + c_m[(\mathcal{M}_m - \mathcal{M}_f)\mathcal{B} + (\mathcal{m}_m - \mathcal{m}_f)c^T] \tag{C1}$$

$$\bar{m} = m_f + c_m[(\mathcal{M}_m - \mathcal{M}_f)b + (m_m - m_f)\eta], \tag{C2}$$

where $\mathcal{M}_r$, m_r, $r = f, m$, are phase compliances associated with loading in the $\bar{x}_1\bar{x}_2$ plane, and with out-of-plane normal-stress loading, respectively.

The concentration factors $\mathcal{B}$, b, c^T, η relate matrix-stress averages to over-all stresses as expressed in eqns (B11) and (B12). For elastic phases, the concentration factors can be found by using an averaging model such as the self-consistent[20] or Mori–Tanaka[21] method. In this case, the concentration factors are functions of the elastic moduli of the fiber and matrix phases and their volume fractions. If the matrix deforms plastically, the method described by Dvorak[22] can be used to compute the instantaneous stress-concentration factors in terms of their elastic counterparts, the over-all instantaneous compliances $\mathcal{M}$, $\bar{m}$, the fiber elastic compliances $\mathcal{M}_f$, m_f and the matrix instantaneous compliances $\mathcal{M}_m$, m_m. The latter can be found from a constitutive model of the matrix as described in Ref. 1.

APPENDIX F

Local Fields in Uncoated and Coated High Temperature Fibrous Composite Systems

The American Society of Mechanical Engineers

Reprinted From
AD – Vol. 25 – 2, Damage and Oxidation Protection in High Temperature Composites
Editors: G. K. Haritos, and O. O. Ochoa
Book No. H0692B – 1991

LOCAL FIELDS IN UNCOATED AND COATED HIGH TEMPERATURE FIBROUS COMPOSITE SYSTEMS

Yehia A. Bahei-El-Din and George J. Dvorak
Department of Civil Engineering
Institute Center for Composite Materials and Structures
Rensselaer Polytechnic Institute
Troy, New York

ABSTRACT

Local stresses caused by mechanical and thermal loads in high temperature intermetallic matrix composites are evaluated using a finite element solution for a periodic hexagonal array microstructure. Both uncoated and coated elastic fibers are considered. The matrix is assumed to be elastic–plastic and insensitive to loading rates. Mechanical properties of the phases are function of temperature. It was found that a CVD deposited carbon coating can be quite effective in reducing thermal stresses at the matrix/coating interface. Certain mechanical stress concentration factors, however, may be aggravated by the compliant coating. In composite systems with a ductile matrix, plastic deformations reduce stress concentration and lead to stress redistribution. In such systems, thermomechanical loading regimes can be designed to reduce adverse local stresses introduced during fabrication, for example, by hot isostatic pressing.

INTRODUCTION

It is well known that the overall behavior of fibrous composites is directly affected by the local phenomena. For example, the overall performance of a composite may be impaired if damage or instability is initiated in the phases or at their interfaces. On the other hand, the overall strength may be enhanced by plastic flow of the matrix. Therefore, evaluation of local stresses in fibrous composites is important in material selection, evaluation and design under both thermal and mechanical loads.

The present paper is concerned with evaluation of the local stresses in high temperature fibrous composites under thermomechanical loads. Specifically, the stresses in uncoated and coated fiber reinforced intermetallic matrix composites are examined. For unidirectional composites, the analysis was performed for an idealized geometry of the microstructure using the Periodic Hexagonal Array (PHA) model (Dvorak and Teply, 1985; Teply and Dvorak, 1988). This geometry permits selection of a representative unit cell, the response of which is identical with the response of the composite aggregate under overall uniform stress or strain fields. The overall response and local fields are then found in the unit cell using the finite element method.

The results reported in this paper focus on the effect of fiber coating on the local thermal and mechanical stress concentration factors in elastic as well as elastic–plastic matrices. Thermal residual stresses generated by cooldown of unidirectional composites from fabrication temperatures are also evaluated. The present study examines various thermomechanical loading regimes that may be applied during the fabrication process to reduce the tensile stresses in the matrix.

The paper begins with a brief description of the PHA model for unidirectionally reinforced composites. Next, material properties for the composite system examined in this study are given. Two principal results obtained with the PHA model for intermetallic matrix composites reinforced by uncoated and coated fibers are then presented and discussed. One is concerned with the effect of fiber coating on thermal and mechanical stresses, the other examines the effect of the thermomechanical loading regime applied during fabrication of composites by hot isostatic pressing on the local stresses.

THE COMPOSITE MODEL

Several material models have been developed for elastic–plastic fibrous composites under various approximations of the microgeometry. While averaging models, such as the self–consistent model (Hill, 1965) and the Mori–Tanaka (1973) method, approximate the microgeometry by a single inclusion embedded in an infinite mass of a different material, periodic models (Aboudi, 1986; Dvorak and Teply, 1985; Nemat–Nasser et al., 1982) consider actual details of the microstructure. The latter class of models assumes certain periodic arrangements of the fiber in the transverse plane of the composite and performs the analysis on a unit representative cell of the periodic microstructure. Other models which are phenomenological in nature have been also developed (see for example the Vanishing Fiber Diameter (VFD) model by Dvorak and Bahei–El–Din, 1982; and the Bimodal Plasticity Theory (BPT) by Dvorak and Bahei–El–Din, 1987) but are more suitable for prediction of the overall response of composites. A survey of the above models can be found in the reviews by Bahei–El–Din and Dvorak (1989) and Dvorak (1991).

An essential requirement in the theoretical model used in the present study is the ability to represent details of the local stress and strain fields in the phases of a unidirectionally reinforced composite subjected to uniform overall stress and thermal change. This narrows down our choices to the periodic models. In particular, we employed the PHA model developed by Dvorak and Teply (1985) and Teply and Dvorak (1988) which we have verified experimentally (Dvorak et al., 1988; Dvorak et al., 1990). In this model, the microstructural geometry in the transverse plane of a unidirectionally reinforced fibrous composite is represented by a periodic distribution of the fibers in a hexagonal array. Cross section of the fibers is approximated by a nx6–sided polygon. An example of the PHA microgeometry with dodecagonal fiber cross section is shown in Fig. 1a. The hexagonal array shown in Fig. 1a is divided into two unit cells, as indicated by the shaded and unshaded triangles. Under overall uniform stresses or strains, the two sets of unit cells have related internal fields. Accordingly, under properly prescribed periodic boundary conditions, only one unit cell from either set needs to be analyzed. Figure 1b shows a three dimensional view of one of the unit cells.

The actual analysis is performed by the finite element method. The unit cell is subdivided into a selected number of subelements in the matrix, fiber, and coating subdomains. A fairly refined subdivision is required for evaluation of the local fields. Figure 2 shows two examples of such a finite element mesh. The results reported here were found with the ABAQUS finite element program. Resident constitutive relations were used for the homogeneous phases. The fiber and the coating were assumed elastic, whereas the matrix was assumed elastic–plastic, inviscid, and follows the Mises yield criterion. Stress–plastic strain response of the matrix was assumed to follow a linear strain hardening behavior, and the matrix yield surface to follow the Prager–Ziegler kinematic hardening rule. Thermoelastic properties of the phases as well as the matrix yield stress and plastic tangent modulus are piecewise linear functions of temperature.

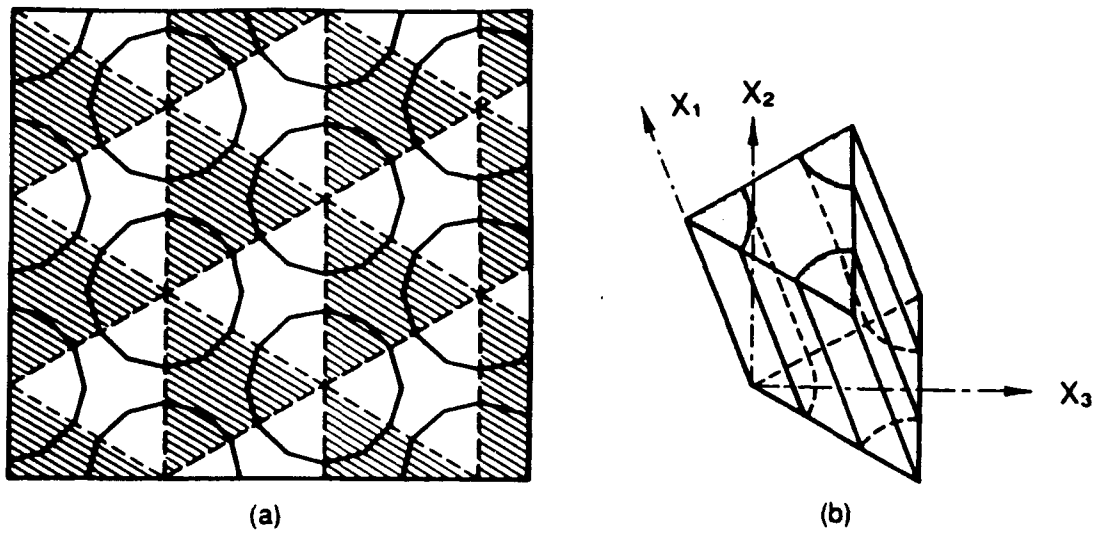

Fig. 1 Microgeometry of the Periodic Hexagonal Array (PHA) model, (a) Transverse plane, (b) Unit cell.

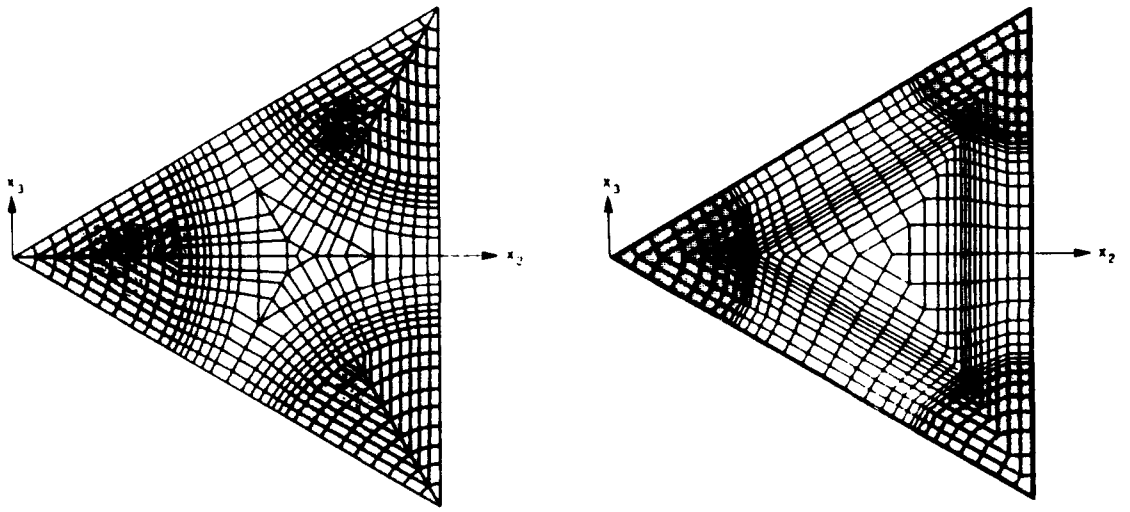

Fig. 2 Two refined meshes of the PHA unit cell.

THE COMPOSITE SYSTEM

An intermetallic matrix composite system reinforced by aligned continuous fibers is considered. The matrix is a nickel–aluminide compound ($Ni_3A\ell$), and the reinforcement is a carbon–coated or uncoated silicon–carbide fiber (SCS6) at 25% volume fraction. The carbon coating thickness is 10 μm. Tables 1 and 2 show material properties of the phases. Thermoelastic constants of the silicon–carbide fiber and the carbon coating are not function of temperature, while those of the nickel–aluminide matrix vary with temperature. Also, the yield stress and the plastic tangent modulus of the $Ni_3A\ell$ compound vary with temperature. Figure 3 shows variation of the tensile yield stress with temperature for the $Ni_3A\ell$ matrix. Unlike other aluminide compounds, for example $Ti_3A\ell$, for which the yield stress increases monotonically with decreasing temperature (see Fig. 3), the yield stress of the nickel–aluminide compound decreases with decreasing temperature if the latter is below 600°C. This causes plastic deformation of the matrix during cooldown of $Ni_3A\ell$–based system which may help in reducing the adverse thermal residual stresses.

RESULTS

Effect of Fiber Coating on Local Stresses

To examine the effect of fiber coating on the local thermal and mechanical stresses, we plotted stress contours in the unit cell for the transverse local stress σ_{22}. Figures 4 and 5 show the results for the SCS6/$Ni_3A\ell$ composite in the elastic range under thermal loading and overall transverse tension, respectively. It was assumed that the composite is stress free at the fabrication temperature of 1200°C, and small increments of a temperature decrease and transverse tensile stress were applied separately. The local stress σ_{22} found from finite element solution of the unit cell was then normalized by the applied load and plotted in the transverse plane. The unit cell is indicated in Figs. 4 and 5 by the dashed triangular boundary. The contours outside the unit cell were generated using the periodic properties of the local stress field.

It is seen from Fig. 4a that tensile hoop stresses, and compressive radial stresses develop in the matrix if the temperature is decreased, whereas compressive hoop stresses develop in the fiber. These stresses are caused by the mismatch between the thermal strains generated in the fiber and the matrix. At the fiber/matrix interface in the system under consideration, the matrix tends to move in the volume occupied by the fiber when the temperature is decreased, but is prevented by the stiff fiber which deforms at a much smaller temperature rate. Consequently, radial cracks may develop in the matrix under cooling from the fabrication temperature. If, on the other hand, the coefficient of thermal expansion of the fiber was larger than that of the matrix, local damage under temperature reduction would take the form of disbonds at the fiber/matrix interface, and radial cracks in the fibers.

Applying a carbon coat to the fiber causes significant reductions in the local thermal stresses, particularly at the fiber/matrix interface, Fig. 4b. Compared to the matrix and the fiber, the carbon coating has a much smaller elastic stiffness in the transverse plane, and as such it can accommodate the thermal strains developed in the phases. Conversely, the coating enhances sharply the mechanical transverse stresses as seen in Fig. 5. This tradeoff must be carefully considered in design of composites.

If the matrix deforms plastically, the local stresses are reduced substantially, particularly under thermal loads. This is seen in the contours plotted in Figs. 6 and 7 after loading the composite well into the plastic region so that the matrix subdomain is fully plastic. In this case, the matrix is very much compliant compared to the fiber and therefore can deform without developing large stresses. In fact, the stiffness of the matrix in the plastic range is comparable to the stiffness of the carbon coating so that the differences in the stresses developing in the coated and the uncoated systems are not significant.

These results indicate that material selection may favor uncoated fibrous systems with ductile matrices over coated elastic systems. Under repeated loads, however, low cycle fatigue may develop in the matrix under cyclic plastic straining leading to nucleation of small cracks. Certain tradeoffs therefore exist and must be applied in material selection and evaluation.

Table 1 Material properties of SCS6 fiber and carbon coating

	E_L[1]	E_T[2]	G_L[3]	G_T[4]	ν_L[5]	α_L[6]	α_T[7]
	GPa	GPa	GPa	GPa		$(10^{-6}/°C)$	
SCS6 fiber	413.6	413.6	159.1	159.1	0.3	4.6	4.6
Carbon coating	172.4	6.9	14.5	3.8	0.3	1.8	28

[1]Longitudinal Young's modulus
[2]Transverse Young's modulus
[3]Longitudinal shear modulus
[4]Transverse shear modulus
[5]Longitudinal Poisson's ratio
[6]Longitudinal coefficient of thermal expansion
[7]Transverse coefficient of thermal expansion

Table 2 Material properties of $Ni_3A\ell$ matrix (Stoloff, 1989)

T[1]	E[2]	ν[3]	α[4]	Y[5]	H[6]
°C	GPa		$10^{-6}/°C$	MPa	GPa
1200	134	0.32	20.6	137	6.70
994	142	0.32	19.0	279	7.10
776	150	0.32	17.2	459	7.50
673	154	0.32	16.4	557	7.70
642	155	0.32	16.1	564	7.75
578	158	0.32	15.6	535	7.90
376	165	0.32	14.3	356	8.25
327	167	0.32	14.0	279	8.35
206	172	0.32	13.4	156	8.60
127	175	0.32	13.0	110	8.75
21	179	0.32	12.5	79	8.95

[1]Temperature
[2]Young's modulus
[3]Poisson's ratio
[4]Coefficient of thermal expansion
[5]Tensile yield stress
[6]Tensile plastic tangent modulus

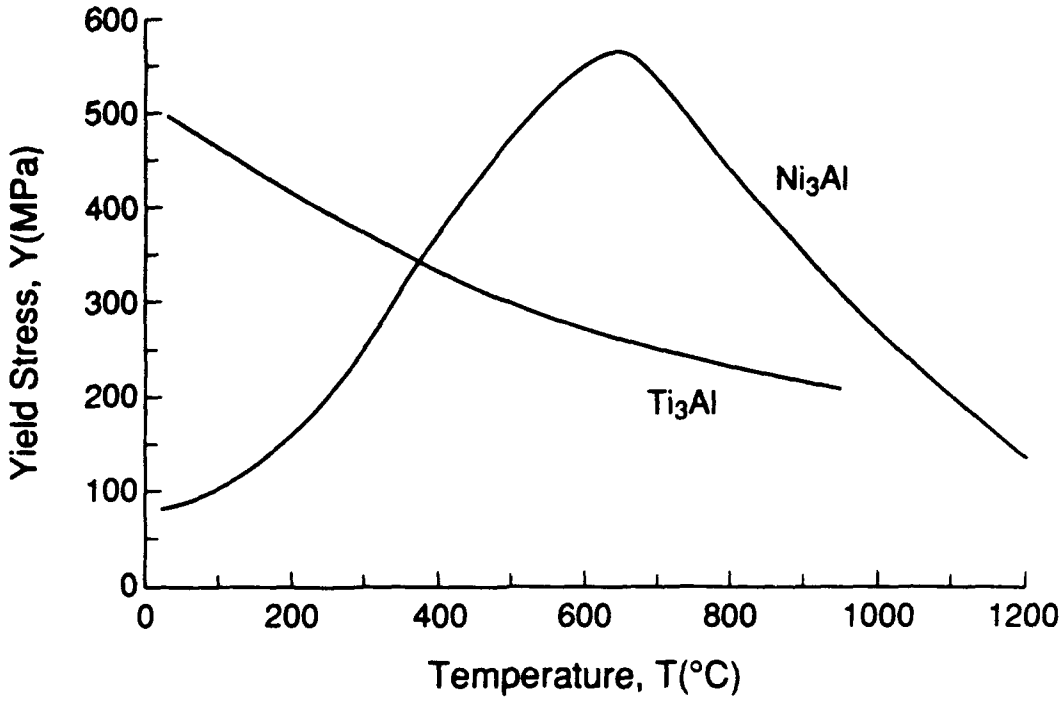

Fig. 3 Yield stress–temperature curve for $Ni_3A\ell$ and $Ti_3A\ell$ compounds.

Effect of Fabrication Parameters on Residual Stresses

This part of our study of local stresses in fibrous system is concerned with evaluation of the thermal residual stresses generated during fabrication and examination of possible thermomechanical loading regimes that can be applied during cooldown to room temperature so that high tensile thermal stresses in the matrix can be reduced. The results presented in the preceding section indicate that plastic flow of the matrix causes redistribution of the local stresses and reduction of the interfacial stresses in the matrix. Consequently, in fabrication of intermetallic matrix composites by hot isostatic pressing (HIP), one can select the optimum temperature/pressure path to follow so as to minimize the adverse local stresses in the phases, particularly the matrix. This, of course, can be accomplished only for composites with a ductile matrix.

Considering the SCS6/$Ni_3A\ell$ composite, we first examined the local stresses retained in the system at room temperature after exposure to HIP temperature of 1200°C and hydrostatic pressure, σ_0, of 200 MPa when the room temperature/zero pressure condition is reached through the various unloading options shown in Fig. 8. In particular, we compared the magnitude of the local interfacial stresses in the phases of uncoated and coated systems for the various cases listed in Fig. 8. In each case, the composite was assumed to be free of internal stresses at the fabrication temperature (1200°C), and the hydrostatic pressure σ_0 was applied in small increments up to 200 MPa. Although the overall load applied in this segment of the loading path is isotropic, the matrix stress is not necessarily isotropic. Nonetheless, the matrix isotropic stress was dominant so that the matrix phase, which was assumed to be plastically incompressible, remained elastic under 200 MPa hydrostatic pressure and 1200°C. In a typical HIP process, the composite is treated at the HIP condition for a specific duration. In our simulation, however, we assumed that the matrix is inviscid, and continued to unload the composite from the HIP conditions to the room temperature and atmospheric pressure. Plastic flow of the nickel–aluminide matrix occurred in all the cases shown in Fig. 8 but the onset of yielding varied among these cases. The local stresses retained in the composite at room temperature are, therefore, expected to vary as well among the loading cases shown in Fig. 8.

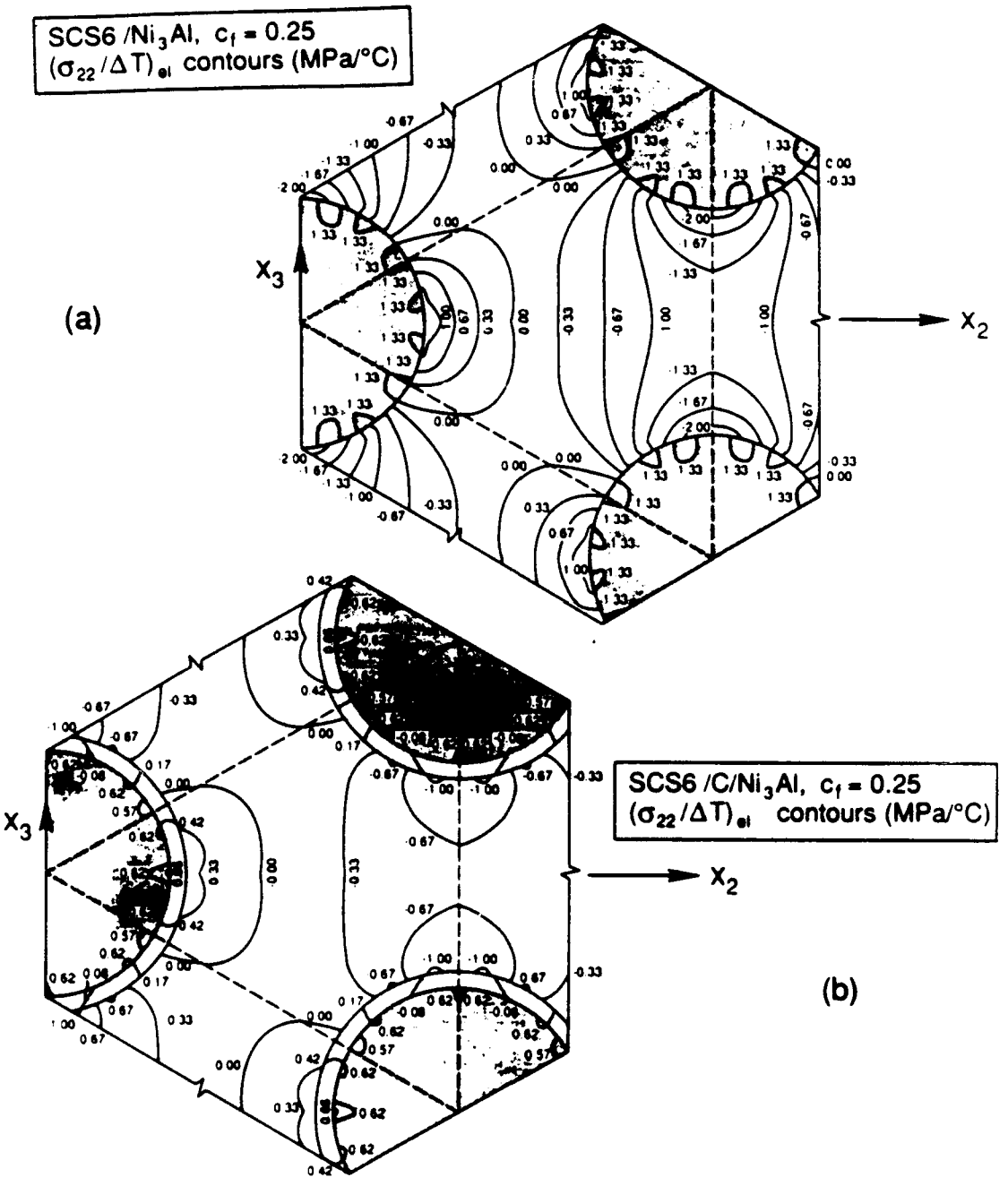

Fig. 4 Transverse thermal stress concentration factors computed in a SCS6/Ni_3Al composite in the elastic range, (a) uncoated fiber, (b) carbon–coated fiber.

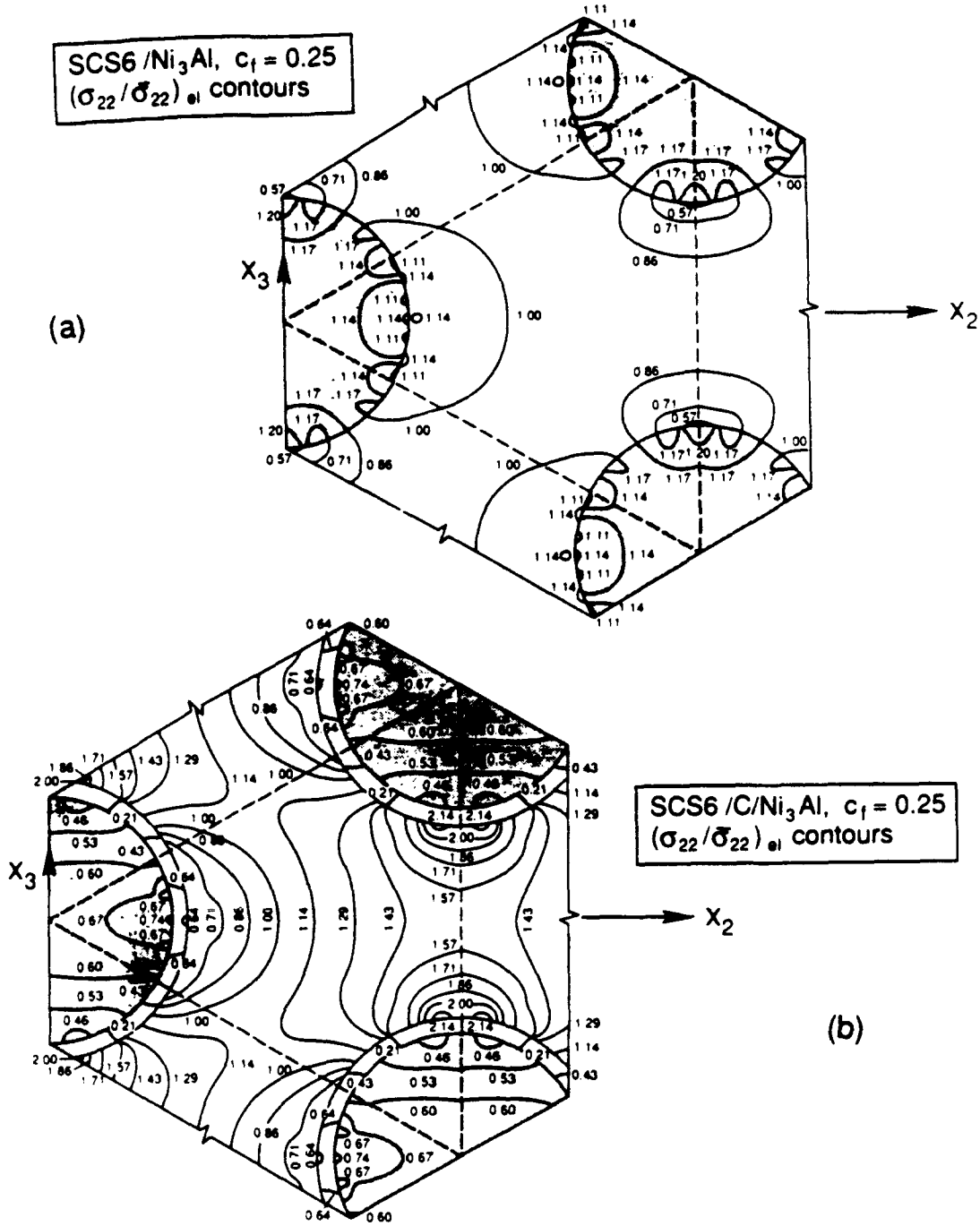

Fig. 5 Transverse mechanical stress concentration factors computed in a SCS6/Ni_3Al composite in the elastic range under overall transverse tension, (a) uncoated fiber, (b) carbon–coated fiber.

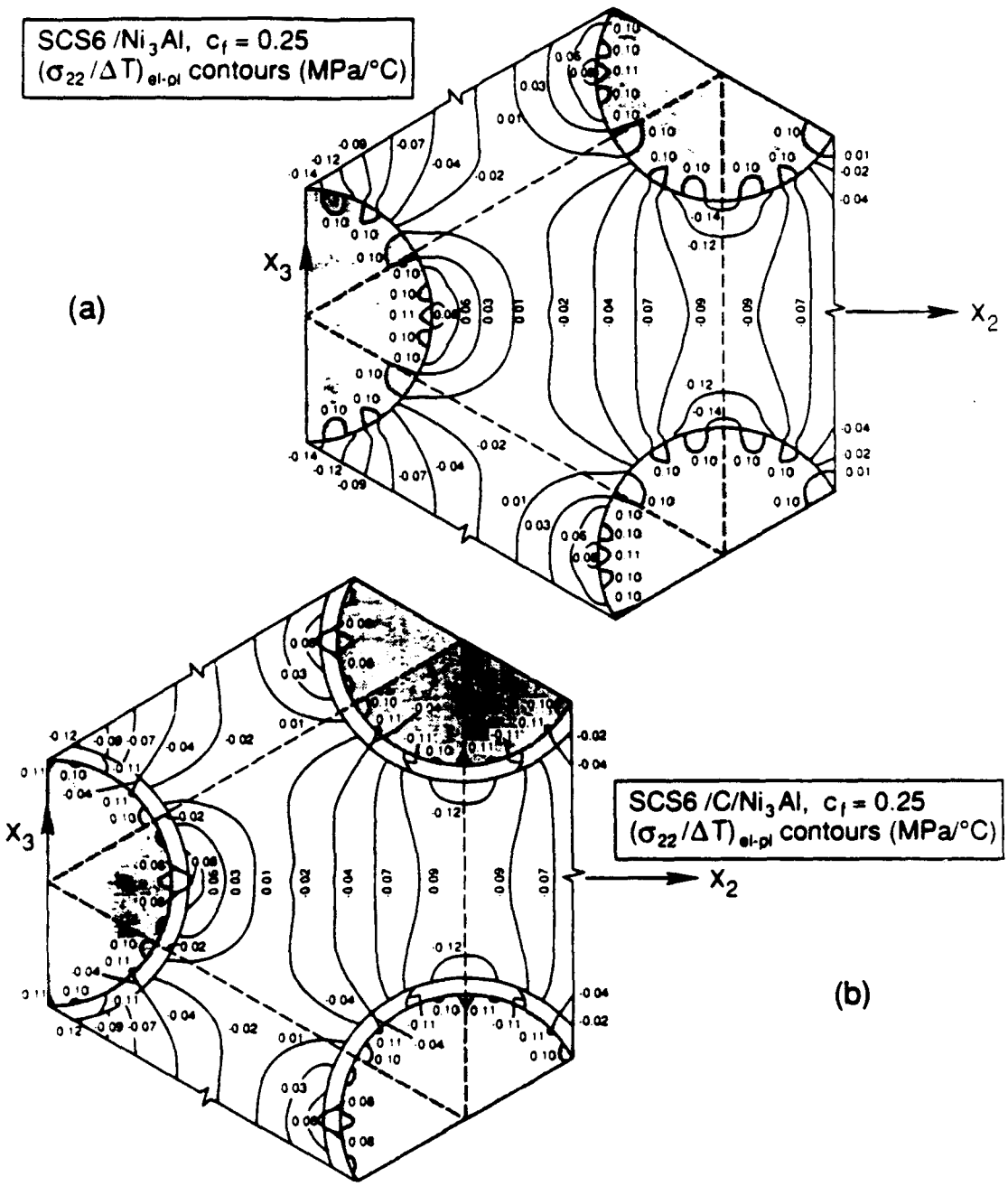

Fig. 6 Transverse thermal stress concentration factors computed in a SCS6/Ni_3Al composite in the elastic–plastic range, (a) uncoated fiber, (b) carbon–coated fiber.

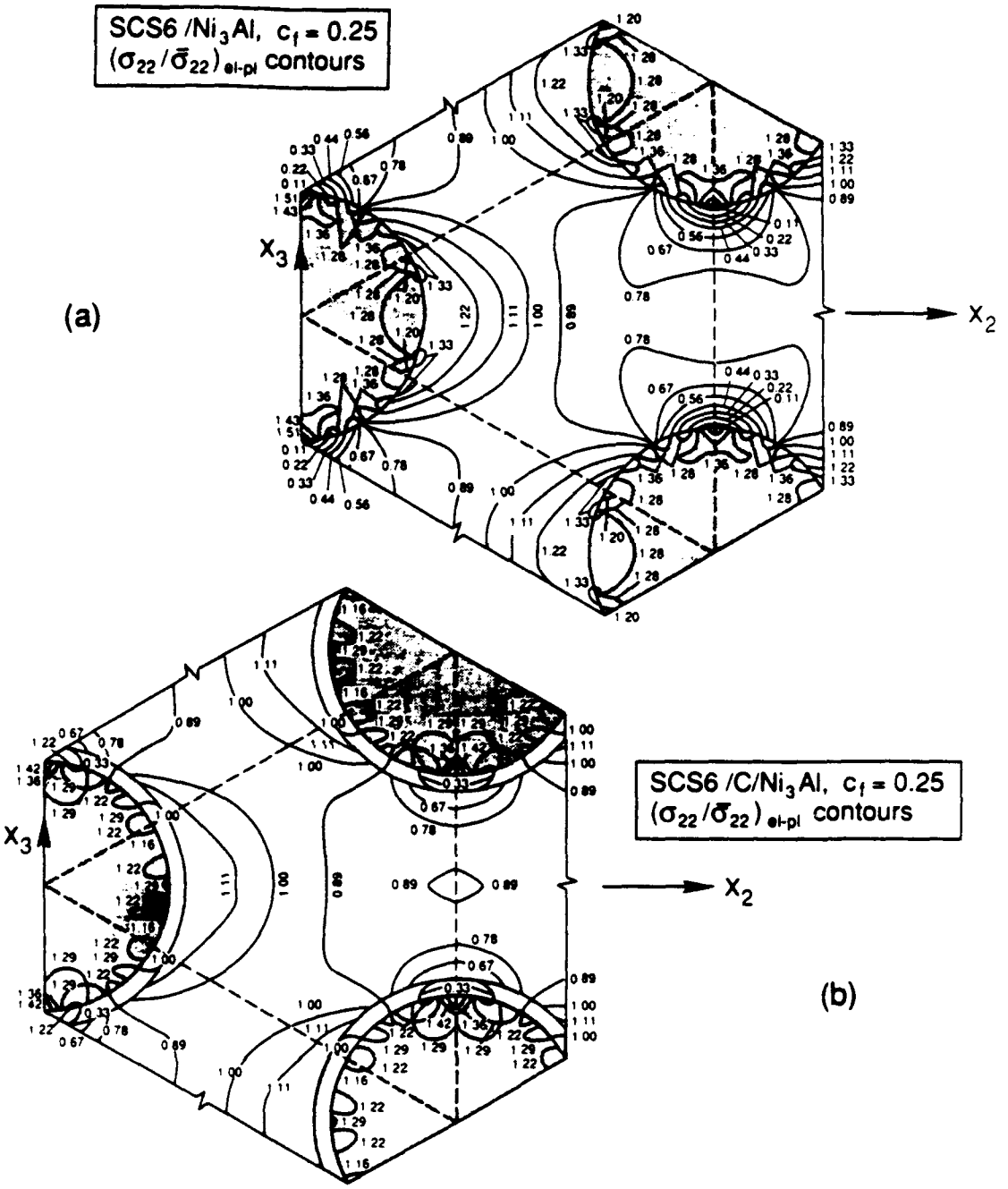

Fig. 7 Transverse mechanical stress concentration factors computed in a SCS6/Ni_3Al composite in the elastic–plastic range under overall transverse tension, (a) uncoated fiber, (b) carbon–coated fiber.

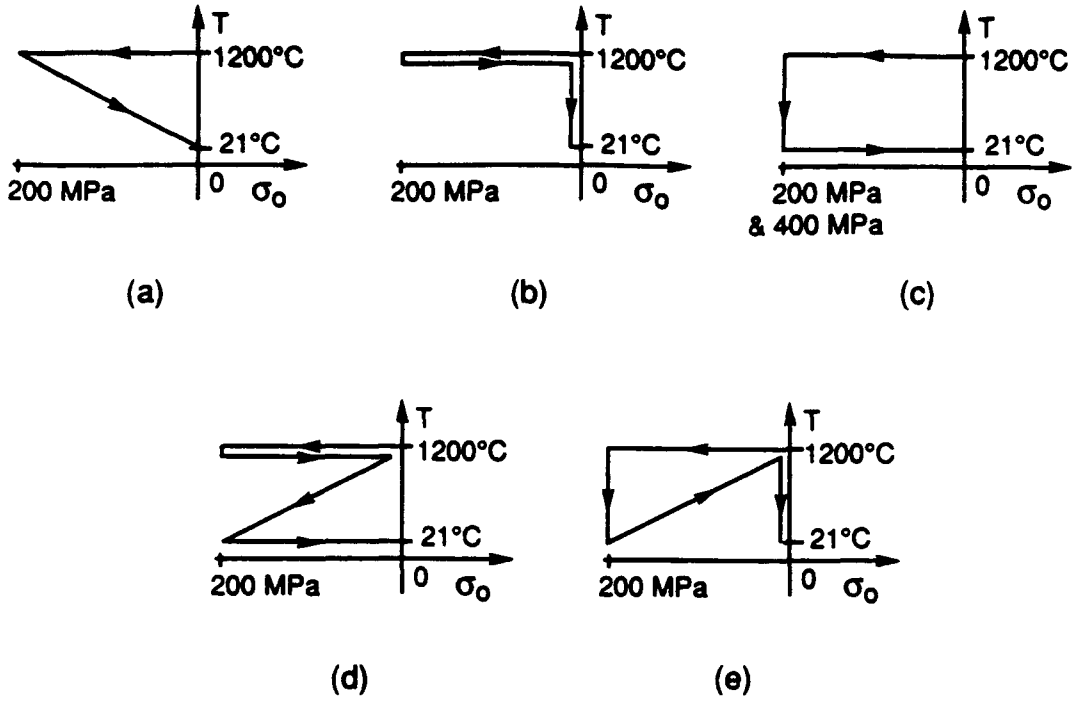

Fig. 8 Possible variations of the temperature/hydrostatic pressure loading path applied to unidirectional composites during hot isostatic pressing.

Comparing the magnitude of the local interfacial stresses in the phases of the uncoated and the coated SCS6/$Ni_3A\ell$ composite, we found that the stresses computed in cases (a), (b), (d)–(e), Fig. 8, are very similar. On the other hand, the adverse stresses were substantially reduced when the hydrostatic pressure, σ_o, was sustained during cooldown of the composite, Fig. 8c. Moreover, the stresses benefit from increasing the magnitude of the hydrostatic pressure applied during the HIP process. Specifically, the tensile stresses found in the phases were reduced substantially when σ_o was increased from 200 MPa to 400 MPa.

Table 3 compares the interfacial stresses computed in uncoated and coated SCS6/$Ni_3A\ell$ composites when the thermomechanical loading paths shown in Figs. 8a,c were applied. The stresses found in case (c) under hydrostatic pressure of 200 MPa and 400 MPa are shown. The table lists the radial stress, σ_{rr}, tangential stress, σ_{tt}, and axial stress, σ_{ll}, found at the interface at either point 'a' or point 'b' indicated on the unit cell shown in the inset in Table 3. The isotropic stress in the matrix, $(\sigma_o)_m$, found in each case is also indicated. It is seen that the tensile stresses at the fiber/matrix interface have been reduced in the uncoated composite by maintaining the hydrostatic pressure while cooling the composite down to room temperature. More reductions in the tensile stresses are achieved by elevating the hydrostatic stress to 400 MPa. For example, the matrix hoop stress is reduced by 18% when the pressure is 200 MPa, and by 37% when the pressure is 400 MPa. It appears that the tensile stresses can be reduced further by increasing the hydrostatic pressure during the HIP process. However, the magnitude of the pressure that can be applied during fabrication is usually limited by the equipment used in the HIP process.

The matrix interfacial tensile stresses in the coated system have been also reduced, but to a lesser extent, by following the loading path indicated in Fig. 8c, Table 3. The hoop stress in the coating, however, is not affected by the thermomechanical path applied during fabrication. Except for the axial stress, elevating the pressure applied during the

Table 3 Maximum interfacial stresses found in a SCS6/Ni_3Al composite at room temperature following hot isostatic pressing

Interfacial Stress (MPa)	Uncoated Fiber	Coated Fiber	Uncoated Fiber	Coated Fiber	Uncoated Fiber	Coated Fiber
$(\sigma_{rr})_m$	–98●b	–84●b	–79●b	–94●b	–60●b	–91●b
$(\sigma_{tt})_m$	190●b	158●b	155●b	152●b	120●b	152●b
$(\sigma_{ll})_m$	198●b	186●b	179●b	143●b	161●b	141●b
$(\sigma_{tt})_c$	–	185●a	–	188●a	–	188●a
$(\sigma_{ll})_c$	–	–668●b	–	–633●b	–	–624●b
$(\sigma_{rr})_f$	–98●b	–110●b	–79●b	–122●b	–60●b	–121●b
$(\sigma_{tt})_f$	–94●a	–108●a	–76●a	–117●a	–59●a	–116●a
$(\sigma_{ll})_f$	–605●b	–364●b	–552●b	–280●b	–500●b	–261●b
$(\sigma_o)_m$	97●b	87●b	85●b	67●b	74●b	67●b

Table 4 Matrix internal stresses found in a SCS6/Ni_3Al composite at room temperature following hot isostatic pressing

Stress at 'c' (MPa)	Uncoated Fiber	Coated Fiber	Uncoated Fiber	Coated Fiber	Uncoated Fiber	Coated Fiber
$(\sigma_{11})_m$	213	213	195	179	177	177
$(\sigma_{22})_m$	115	128	96	162	76	164
$(\sigma_o)_m$	101	105	90	106	79	106

HIP process does not affect the stresses in the coated system. In any case, the matrix isotropic stress, and consequently damage initiation, is affected by the thermomechanical loading path followed during the HIP run.

Table 4 lists the local stresses found in the matrix internal point 'c' (see inset of unit cell). The axial stress, $(\sigma_{11})_m$, the transverse stress, $(\sigma_{22})_m$, and the isotropic stress, $(\sigma_0)_m$, are shown for three thermomechanical loading regimes applied during the HIP process. It is seen that the stresses in the uncoated system are affected by the HIP regime. Substantial reductions in the matrix stresses are achieved by cooling down the composite under constant pressure, and by elevating the hydrostatic pressure applied during the HIP run. While these factors reduce the matrix axial stress in the coated system, the transverse stress is increased and the isotropic stress is unchanged.

The stresses found in the phases after the composite was reheated to 1200°C were not affected by the loading path, or the magnitude of the hydrostatic pressure, σ_0, applied during the HIP process.

DISCUSSION

A particular CVD deposited carbon coating can be quite effective in reducing the adverse thermal residual stresses generated during fabrication of fibrous composites. The fiber coating, however, enhances certain local mechanical stresses. In any case, the significance of these effects depends on the relative stiffness of the matrix, the fiber, and the coating. In particular, plastic flow of the matrix causes substantial reductions in the tensile interfacial stresses in the phases. The implication is that mechanical compatibility in fibrous composites is not only a function of the thermal properties of the phases, but also depends on the constitutive behavior of the phases. Accurate evaluation of thermal residual stresses, therefore, can be only performed with appropriate micromechanical models.

Plastic flow of the matrix can be utilized to reduce the tensile local stresses generated during hot isostatic pressing (HIP) of fibrous composites. Selection of the temperature/pressure path as well as the magnitude of the hydrostatic pressure applied during the HIP treatment should focus on inducing plastic deformation in the matrix early during the cooldown cycle. In our study of the local stresses in a unidirectional SCS6/$Ni_3A\ell$ composite we found that the matrix interfacial tensile stresses are lowest when the isotropic pressure applied during the HIP process was maintained during cooling to room temperature. Also the local stresses can be reduced by increasing the HIP isotropic pressure. Our yet unpublished results indicate that more reductions in the thermal residual stresses can be achieved through plastic deformation of the matrix if the hydrostatic pressure applied during the HIP process is confined to the composite's transverse plane. The results which qualify this proposition are published elsewhere (Bahei–EL–Din et al., 1991).

ACKNOWLEDGEMENT

This work was supported, in part, by the Air Force Office of Scientific Research, the Office of Naval Research, and the DARPA–HiTASC program at RPI. Dr. J.F. Wu assisted in the finite element calculations using the ABAQUS program.

REFERENCES

Aboudi, J., 1986, "Elastoplasticity Theory for Composite Materials," *Solid Mech. Archives*, Vol. 11, pp. 141–183.

Bahei–El–Din, Y.A., and Dvorak, G.J., 1989, "A Review of Plasticity Theory of Fibrous Composite Materials," *Metal Matrix Composites: Testing, Analysis, and Failure Modes*, ASTM STP 1032, W.S. Johnson, ed., American Society for Testing and Materials, Philadelphia, pp. 103–129.

Bahei–El–Din, Y.A., Dvorak, G.J., and Wu, J.F., 1991, "Fabrication Stresses in High Temperature Fibrous Composites with Ductile Matrices," to be published.

Dvorak, G.J., 1991 "Plasticity Theories for Fibrous Composite Materials," *Metal Matrix Composites, Vol. 2, Mechanisms and Properties*, R.K. Everett and R.J. Arsenault, eds., Academic Press, Boston, pp. 1–77.

Dvorak, G.J., and Bahei–El–Din, Y.A., 1982, "Plasticity Analysis of Fibrous Composites," *J. Appl. Mech.*, Vol. 49, pp. 327–335.

Dvorak, G.J., and Bahei–El–Din, Y.A., 1987, "A Bimodal Plasticity Theory of Fibrous Composite Material," *Acta Mechanica*, Vol. 69, pp. 219–241.

Dvorak, G.J., Bahei–El–Din, Y.A., Macheret, Y., and Liu, C.H., 1988, "An Experimental Study of Elastic–Plastic Behavior of a Fibrous Boron–Aluminum Composite," *J. Mech. Phys. Solids*, Vol. 36, pp. 655–687.

Dvorak, G.J., Bahei–El–Din, Y.A., Shah, R.S., and Nigam, H., 1990, "Experiments and Modeling in Plasticity of Fibrous Composites," *Inelastic Deformation of Composite Materials*, G.J. Dvorak, editor, Springer–Verlag, New York, Inc., pp. 270–293.

Dvorak, G.J., and Teply, J.L., 1985, "Periodic Hexagonal Array Models for Plasticity of Composite Materials," *Plasticity Today: Modeling, Methods and Applications*, A. Sawczuk and V. Bianchi, eds., Elsevier, Amsterdam, pp. 623–642.

Hill, R., 1965, "Theory of Mechanical Properties of Fiber–Strengthened Materials–III, Self–Consistent Model," *J. Mech. Phys. Solids*, Vol. 13, pp. 189–198.

Mori, T., and Tanak, K., 1973, "Average Stress in Matrix and Average Elastic Energy of Materials with Misfitting Inclusions," *Acta Metal.*, Vol. 21, pp. 571–574.

Nemat–Nasser, S., Iwakuma, T., and Hejazi, M., 1982, "On Composites with Periodic Structure," *Mech. of Materials*, Vol. 1, pp. 239–267.

Stoloff, N.S., 1989, "The Physical and Mechanical Metallurgy of Ni_3Al and its Alloys," *Intl. Materials Reviews*, Vol. 34.

Teply, J.L., and Dvorak, G.J., 1988, "Bounds on Overall Instantaneous Properties of Elastic–Plastic Composites," *J. Mech. Phys. Solids*, Vol. 36, pp. 29–58.

APPENDIX G

A Nonlinear Layered Shell Finite Element with Improved Transverse Shear Behavior

A Nonlinear Layered Shell Finite Element with Improved Transverse Shear Behavior

Konrad Dorninger

SCOREC Report #3 -1991
Scientific Computation Research Center

Scientific Computation Research Center
Rensselaer Polytechnic Institute
Troy, NY 12180-3590
voice 5182766795
fax 5182764886

A NONLINEAR LAYERED SHELL FINITE ELEMENT WITH IMPROVED TRANSVERSE SHEAR BEHAVIOR

by

Konrad Dorninger*

Introduction

During a stay at RPI, Rensselaer Polytechnic Institute, Troy, NY, from August 1989 to September 1990 as a visiting researcher, and while being supported by a grant form the Fonds zur Förderung der Wissenschaftlichen Forschung, Vienna, Austria, a Finite Element for layered fiber reinforced composite shells has been developed by the author, implemented into a commercial Finite Element code (ABAQUS), and tested extensively.

The displacement based degeneration principle is used in combination with specific kinematic assumptions for deriving the governing equations. By treating each layer as an individual shell and introducing kinematic constraints between the layer DOFs and the conveniently chosen global DOFs a very good representation of the mechanical behavior of the shell, including transverse shear, has been obtained.

Currently there are two material models available:

- A linear elastic model, in which the thermo-elastic material is either described by the behavior of the local components, i.e. fiber and matrix material laws and geometrical configuration in each layer, or by the overall orthotropic layer material laws.
- An elasto-plastic composite model, that is based on the assumption of linear elastic behavior of the fibers and metal-type elasto-plastic behavior of the matrix.

Other material models can easily be implemented by using the specially designed interface, LCSMAT.

* Current address: 144 Highland Ave., Apt. 302, East Lansing, MI 48823, Tel. (517) 351-1207

CONTENTS

1. FORMULATION OF THE LCSLFC-ELEMENT

1.1 INTRODUCTION

The **LCSLFC**-element (Layerwise Constant Shear Laminated Fiber Composite) is based on the degeneration principle [1,2]. Each layer is treated as a seperate shell element with orthotropic material behavior. The layer DOFs (degrees of freedom) of all layers are transformed to a set of element DOFs along with the corresponding stiffnesses and nodal forces. This procedure improves the transverse shear behavior of the shell element since normal vectors of the shell are now able to undergo piecewise (layerwise) linear deformations (due to the assumptions included in the degeneration principle, normal vectors in each layer remain straight).

As a reminder, the well known linearized incremental equilibrium equation, including thermal loading, derived from the virtual work principle, is given here [2]:

$$\underbrace{[\underset{\approx}{K}_0 + \underset{\approx}{K}_g]}_{=\underset{\approx}{K}}(\Delta \underset{\sim}{u})^1 = \underset{\sim}{R} - \underbrace{(\underset{\sim}{f} - \Delta \underset{\sim}{f}_{th})}_{=\underset{\sim}{f}_{th}} \tag{1}$$

For the updated Lagrange formulation the stiffness matrices and the nodal force vectors for one general element (e) are given by the following integrals over the volume of the element at the beginning of the increment:

$$\underset{\approx}{K}_0^{(e)} = \int_V \underset{\approx}{B}_l^T \, \underset{\approx}{C} \, \underset{\approx}{B}_l \, dV \tag{2}$$

$$\underset{\approx}{K}_g^{(e)} = \int_V \underset{\approx}{B}_{nl}^T \, \underset{\approx}{T} \, \underset{\approx}{B}_{nl} \, dV \tag{3}$$

$$\underset{\sim}{f}^{(e)} = \int_V \underset{\approx}{B}_l^T \, \underset{\sim}{\tau} \, dV \tag{4}$$

$$\Delta \underset{\sim}{f}_{th}^{(e)} = \int_V \underset{\approx}{B}_l^T \, \underset{\approx}{C} \, \underset{\sim}{\alpha} \Delta\vartheta \, dV \tag{5}$$

In Eq. (1) the sum in square brackets represents the global tangent stiffness matrix $\underset{\approx}{K}$ at the beginning of the increment, consisting of the following contributions:

a) the material stiffness matrix, $\underset{\approx}{K}_{\sigma}$, which depends on the material behavior (expressed by the current material matrix $\underset{\approx}{C}$) and the reference geometry (expressed by the linear strain-displacement matrix $\underset{\approx}{B}_{l}$);

b) the initial stress or geometrical stiffness matrix, $\underset{\approx}{K}_{\sigma}$, which depends explicitly on the current stresses (matrix $\underset{\approx}{\mathcal{T}}$) and the reference geometry (expressed by the nonlinear strain-displacement matrix $\underset{\approx}{B}_{nl}$);

The external load vector at the end of the increment, $\underset{\sim}{R}$, is given by the surface and body forces, concentrated or distributed; $\underset{\sim}{f}$ is the vector of internal forces corresponding to the stresses at the beginning of the increment (vector $\underset{\sim}{\tau}$); $\Delta \underset{\sim}{f}_{th}$ is the vector of internal nodal forces equivalent to stress increments resulting from a temperature increment $\Delta\vartheta$ and computed by using the coefficients of linear thermal expansion (vector $\underset{\sim}{\alpha}$).

1.2 STIFFNESS EXPRESSIONS FOR ONE LAYER

Each layer n is treated as a homogeneous shell with constant material properties over the layer thickness. The degeneration principle is employed to derive the shell element stiffness expressions from the 3/D continuum. This includes two assumptions [1,2]:

I. The normal vectors of the layer's reference surface remain straight and inextensible during deformation.

II. The contribution of the strain energy caused by stress components perpendicular to the reference surface is set to zero by using a modified material law.

1.2.1 Description of Geometry

With assumption I the geometry of the layer can be described by one reference surface and its corresponding normal vectors. With appropriate shape functions the matrices $\underset{\approx}{B}_{l}$ and $\underset{\approx}{B}_{nl}$ (in Eqs. (2–5)) can be constructed. Due to the isoparametric element formulation these matrices are functions of natural coordinates r, s, t, where r, s lie in the layer's reference surface and t indicates the thickness direction, see Fig. 1.1.

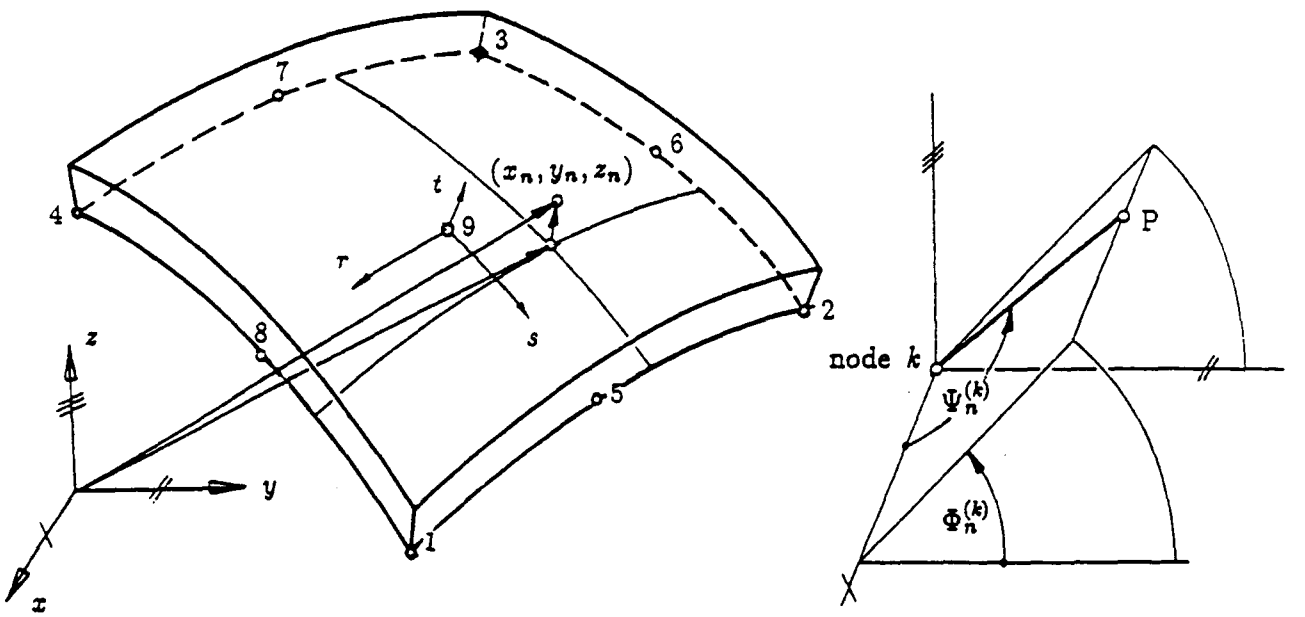

Fig. 1.1 Geometry of the degenerated shell (=layer) element

Interpolation of geometry (subscript n indicates the layer number):

$$
\begin{aligned}
x_n(r,s,t) &= \sum_{k=1}^{M} \phi^{(k)}(r,s)[x_n^{(k)} + t\,\mathrm{h}_n^{(k)} \cos\Psi_n^{(k)}] \\
y_n(r,s,t) &= \sum_{k=1}^{M} \phi^{(k)}(r,s)[y_n^{(k)} + t\,\mathrm{h}_n^{(k)} \sin\Psi_n^{(k)} \cos\Phi_n^{(k)}] \\
z_n(r,s,t) &= \sum_{k=1}^{M} \phi^{(k)}(r,s)[z_n^{(k)} + t\,\mathrm{h}_n^{(k)} \sin\Psi_n^{(k)} \sin\Phi_n^{(k)}]
\end{aligned}
\tag{6}
$$

with $\phi^{(k)}(r,s)$ being standard 2/D shape functions (i.e. Lagrangian polynomials); M is the number of nodes forming the element, $\mathrm{h}_n^{(k)}$ is the thickness of the layer at node k, and $\Psi_n^{(k)}$ and $\Phi_n^{(k)}$ are used to determine the position of the layer's normal at node k, see Fig.1.1.

Given the geometry at the beginning of the increment (denoted by x_n, y_n, z_n) and the initial geometry (denoted by ${}^0x_n$, ${}^0y_n$, ${}^0z_n$) the total displacements follow as:

$$
\begin{aligned}
u_n(r,s,t) &= x_n - {}^0x_n \\
v_n(r,s,t) &= y_n - {}^0y_n \\
w_n(r,s,t) &= z_n - {}^0z_n
\end{aligned} \tag{7}
$$

The incremental displacements $\Delta u_n, \Delta v_n, \Delta w_n$ are defined similarly. They are related to the nodal DOFs through the same interpolation functions as used for describing the geometry (=isoparametric formulation). A linearization with respect to the increments of the angles $\Phi_n^{(k)}, \Psi_n^{(k)}$ is necessary for the subsequent derivation of the stiffness expressions.

$$
\begin{pmatrix} \Delta u_n(r,s,t) \\ \Delta v_n(r,s,t) \\ \Delta w_n(r,s,t) \end{pmatrix} = \phi^{(k)}(r,s) \begin{pmatrix} 1 & 0 & 0 & t\,\mathrm{h}_n^{(k)}\,\mathrm{g}_x^{(k)} & t\,\mathrm{h}_n^{(k)}\,\overline{\mathrm{g}}_x^{(k)} \\ 0 & 1 & 0 & t\,\mathrm{h}_n^{(k)}\,\mathrm{g}_y^{(k)} & t\,\mathrm{h}_n^{(k)}\,\overline{\mathrm{g}}_y^{(k)} \\ 0 & 0 & 1 & t\,\mathrm{h}_n^{(k)}\,\mathrm{g}_z^{(k)} & t\,\mathrm{h}_n^{(k)}\,\overline{\mathrm{g}}_z^{(k)} \end{pmatrix} \underbrace{\begin{pmatrix} \Delta u_n^{(k)} \\ \Delta v_n^{(k)} \\ \Delta w_n^{(k)} \\ \Delta\overline{\varphi}_n^{(k)} \\ \Delta\overline{\psi}_n^{(k)} \end{pmatrix}}_{=\Delta\underset{\sim}{u}_n^{(k)}} \tag{8}
$$

where $\Delta\underset{\sim}{u}_n^{(k)}$ represents the vector of DOFs at node k for layer n. The functions $\mathrm{g}_j^{(k)}, \overline{\mathrm{g}}_j^{(k)}$ can be found in the appendix, Eq. (*A*10).

1.2.2 Description of Material

Assumption II for the degeneration principle is satisfied by forcing the normal stresses in thickness direction to be zero. This results in a material law similar to that used under plane stress conditions.

Usually the material matrix and the vector of coefficients of linear thermal expansion of the unidirectionally reinforced layer (UD-layer) are defined in the local layer coordinate system denoted by subscript L:

$$
\underset{\sim}{\mathrm{C}}_L = \begin{pmatrix} \mathrm{E}_{11} & \mathrm{E}_{12} & 0 & 0 & 0 & 0 \\ & \mathrm{E}_{22} & 0 & 0 & 0 & 0 \\ & & 0 & 0 & 0 & 0 \\ & sym. & & \mathrm{E}_{44} & 0 & 0 \\ & & & & \mathrm{E}_{55} & 0 \\ & & & & & \mathrm{E}_{66} \end{pmatrix}, \qquad \underset{\sim}{\alpha}_L = \begin{pmatrix} \alpha_l \\ \alpha_q \\ 0 \\ 0 \\ 0 \\ 0 \end{pmatrix} \tag{9}
$$

Each layer is assumed to exhibit orthotropic material behavior with respect to its individual fiber-fixed local coordinate system l, q, t (with l denoting the fiber direction; q

and t transverse and thickness directions, resp.). This system is related to the element fixed r, s, t system via the fiber angle Θ. The definitions of the different coordinate systems and the fiber angle are shown in Fig. 1.2.

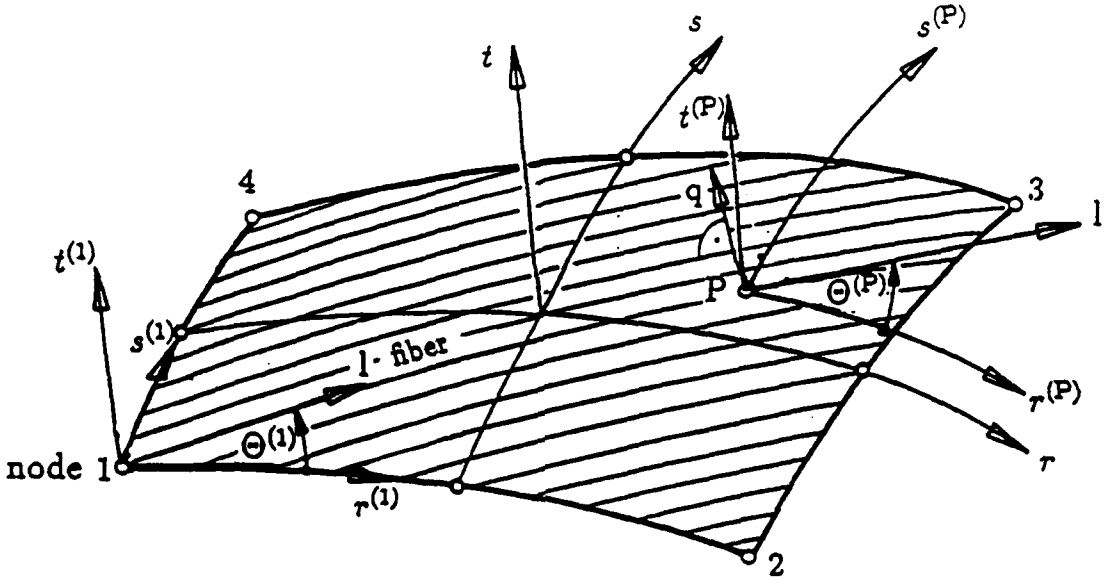

Fig. 1.2 Element fixed r, s, t coordinate system, local layer system l, q

Since element geometry and fiber-direction are independent of each other the fiber angle Θ is not necessarily constant within the element (see Fig. 1.2). Two ways of taking this fact into account are implemented in the **LCSLFC**-element:

a) By assuming the fibers to be parallel within the layer's reference surface one can find a geometric relationship that considers the variation of Θ (see [3]).

b) By specifying the Θ-angles at each nodal point of the element and using the 2/D shape functions $\phi^{(k)}(r,s)$ (from the interpolation of the geometry, Eq. (6)) one can interpolate the Θ-angle at any point.

The E_{ij} in $\underset{\sim}{C}_L$ can either be calculated from material data given for the layer, or from the material data of fiber and matrix along with the fiber volume fraction.

If engineering material properties E_l, E_q, ν_{ql}, G_{lq}, G_{lt}, G_{qt} for the layer are given, the E_{ij} values in $\underset{\approx}{C}_L$ can be computed as

$$
\begin{aligned}
E_{11} &= \frac{E_l}{1 - \nu_{ql}^2 \frac{E_q}{E_l}} & E_{44} &= G_{lq} \\
E_{12} &= \nu_{ql} E_{22} & E_{55} &= G_{lt} \\
E_{22} &= \frac{E_q}{1 - \nu_{ql}^2 \frac{E_q}{E_l}} & E_{66} &= G_{qt}
\end{aligned}
\tag{10}
$$

If material properties of the constituents of the composite are given, a homogenization technique has to be used to determine the $\underset{\approx}{C}_L$ matrix. For that purpose a software package, developed at RPI, Troy, NY, by C.M. Huang [4] which is based on the Mori-Tanaka averaging scheme, has been adapted and implemented. Using this technique the effective properties (E_{ij} and α_{ij}) of a wide variety of composite materials can be computed from fiber and matrix data, the volume fraction, and the geometrical setup. The fibers are assumed to behave orthotropically (transversely isotropic) and the matrix isotropically. Four options for the fiber arrangement are implemented in the **LCSLFC**-element:

- Aligned continuous fibers
- Randomly oriented continuous fibers
- Aligned whiskers
- Randomly oriented whiskers

When dealing with metal matrix composites one has to take into account the elasto-plastic behavior of the matrix material. In the **LCSLFC**-element a special version of the "VFD" model [5] is implemented in combination with classical plasticity theory including kinematic hardening. This part of the element code was developed by A.J. Svobodnik, TU Vienna, Austria; a detailed description of the theories used can be found in [6].

1.2.3 Integration of the Stiffness Expressions

An efficient way to reduce the numerical effort for computing the stiffness matrix and the internal nodal force vector is the use of an analytical thickness integration as described e. g. in [7,8,9]. However, a necessary requirement for this procedure is the neglection of the t−dependence of the Jacobian matrix. In [3] detailed analyses show that this

approximation is acceptable as long as the shells are thin, their curvature is moderate, and their thickness does not vary too much. The definition of the Jacobian matrix is given in the appendix, Eq. (A1).

In order to be able to perform the thickness integration analytically, the $t-$dependence of all relevant terms of the integrands in Eqs. (2–5) must be clarified. From Eqs. (6,7) and with the assumption mentioned above, the $t-$dependence of the displacement derivatives can be expressed explicitly:

$$\begin{aligned} u_{n,j}(r,s,t) &= \overline{u}_{n,j}(r,s) + t\,\widehat{u}_{n,j}(r,s) \\ v_{n,j}(r,s,t) &= \overline{v}_{n,j}(r,s) + t\,\widehat{v}_{n,j}(r,s) \qquad\qquad j = x,y,z \\ w_{n,j}(r,s,t) &= \overline{w}_{n,j}(r,s) + t\,\widehat{w}_{n,j}(r,s) \end{aligned} \tag{11}$$

The specific formulas for $\overline{u}_{n,j}, \overline{v}_{n,j}, \overline{w}_{n,j}, \widehat{u}_{n,j}, \widehat{v}_{n,j}, \widehat{w}_{n,j}$ can be found in the appendix, Eqs. (A4, A5). In a similar way the derivatives of the displacement increments $\Delta u_{n,j}$, $\Delta v_{n,j}$, $\Delta w_{n,j}$ can be computed, see appendix, Eqs. (A7–A9).

With the definition of the Almansi strains and by invoking Eq. (11), one can extract the $t-$dependence of the strains:

$$\varepsilon_{ij}(r,s,t) = \overline{\varepsilon}_{ij}(r,s) + t\,\widehat{\varepsilon}_{ij}(r,s) + t^2\,\widetilde{\varepsilon}_{ij}(r,s) \qquad i,j = x,y,z \tag{12}$$

with the different components, e.g. for strain ε_{xy}:

$$\begin{aligned} \overline{\varepsilon}_{xy} = \;& \tfrac{1}{2}(\overline{u}_{n,y} + \overline{v}_{n,x} - \overline{u}_{n,x}\,\overline{u}_{n,y} - \overline{v}_{n,x}\,\overline{v}_{n,y} - \overline{w}_{n,x}\,\overline{w}_{n,y}) \\ \widehat{\varepsilon}_{xy} = \;& \tfrac{1}{2}(\widehat{u}_{n,y} + \widehat{v}_{n,x} - \overline{u}_{n,x}\,\widehat{u}_{n,y} - \overline{v}_{n,x}\,\widehat{v}_{n,y} - \overline{w}_{n,x}\,\widehat{w}_{n,y} \\ & \qquad - \widehat{u}_{n,x}\,\overline{u}_{n,y} - \widehat{v}_{n,x}\,\overline{v}_{n,y} - \widehat{w}_{n,x}\,\overline{w}_{n,y}) \\ \widetilde{\varepsilon}_{xy} = \;& -\tfrac{1}{2}(\widehat{u}_{n,x}\,\widehat{u}_{n,y} + \widehat{v}_{n,x}\,\widehat{v}_{n,y} + \widehat{w}_{n,x}\,\widehat{w}_{n,y}) \end{aligned} \tag{13}$$

After transforming the material matrix and the vector of thermal expansion (Eq. (9)) to the global x,y,z system, and combining it with Eq. (12), the vector of Cauchy stress components becomes:

$$\underset{\sim}{\sigma}(r,s,t) = \underset{\approx}{\mathbf{C}}(r,s)\Big(\big[\underset{\sim}{\overline{\varepsilon}}(r,s) - \underset{\sim}{\alpha}(r,s)\,\overline{\vartheta}(r,s)\big] + t\big[\underset{\sim}{\widehat{\varepsilon}}(r,s) - \underset{\sim}{\alpha}(r,s)\,\widehat{\vartheta}(r,s)\big] + t^2\,\underset{\sim}{\widetilde{\varepsilon}}(r,s)\Big) \tag{14}$$

where

$$\underset{\approx}{\mathbf{C}}(r,s) = \underset{\approx}{\mathbf{T}}^{T}(r,s)\,\underset{\approx}{\mathbf{C}}_L\,\underset{\approx}{\mathbf{T}}(r,s) \tag{15}$$

$$\underset{\sim}{\alpha}(r,s) = \underset{\approx}{\mathbf{T}}^{-1}(r,s)\,\underset{\sim}{\alpha}_L(r,s) \tag{16}$$

The matrix $\underset{\approx}{\mathbf{T}}$ represents the transformation from the global x, y, z system to the local l, q, t system. $\underset{\approx}{\mathbf{T}}$ is composed of the elements of the Jacobian matrix (and depends on the fiber angle Θ). Therefore, since $\underset{\approx}{\mathbf{J}}$ is independent of t, so is $\underset{\approx}{\mathbf{T}}$. The temperature field is assumed to be linearly distributed over the thickness of the shell (and therefore over the thickness of the layer), with $\overline{\vartheta}$ being the temperature load at the $t = 0$ surface and $\widehat{\vartheta}$ being the temperature difference between the surfaces of the layer.

The $\underset{\approx}{\mathbf{B}}_l$ and $\underset{\approx}{\mathbf{B}}_{nl}$ matrices are constructed from derivatives of the displacement increments, therefore they can be decomposed similarly:

$$\underset{\approx}{\mathbf{B}}_l(r,s,t) = \overline{\underset{\approx}{\mathbf{B}}}_l(r,s) + t\,\widehat{\underset{\approx}{\mathbf{B}}}_l(r,s) \tag{17}$$

$$\underset{\approx}{\mathbf{B}}_{nl}(r,s,t) = \overline{\underset{\approx}{\mathbf{B}}}_{nl}(r,s) + t\,\widehat{\underset{\approx}{\mathbf{B}}}_{nl}(r,s) \tag{18}$$

The detailed formulas for the matrices $\overline{\underset{\approx}{\mathbf{B}}}_l$, $\widehat{\underset{\approx}{\mathbf{B}}}_l$, $\overline{\underset{\approx}{\mathbf{B}}}_{nl}$, $\widehat{\underset{\approx}{\mathbf{B}}}_{nl}$ can be found in the appendix, Eqs. ($A13, A14, A17, A18$).

Substituting Eqs. (14–18) into the expressions for the stiffness matrices (Eqs. (2–5)) and invoking some abbreviations lead to:

$$\underset{\approx}{\mathbf{K}}_{\sigma}^{(n)} = \int_{-1}^{+1}\int_{-1}^{+1} \left(\overline{\underset{\approx}{\mathbf{B}}}_l^T \underset{\approx}{\mathbf{C}} \left(\overline{\underset{\approx}{\mathbf{B}}}_l + \tfrac{1}{2}\widehat{\underset{\approx}{\mathbf{B}}}_l\right) + \widehat{\underset{\approx}{\mathbf{B}}}_l^T \underset{\approx}{\mathbf{C}} \left(\tfrac{1}{2}\overline{\underset{\approx}{\mathbf{B}}}_l + \tfrac{1}{3}\widehat{\underset{\approx}{\mathbf{B}}}_l\right)\right) \det|\underset{\approx}{\mathbf{J}}|\, dr\, ds \tag{19}$$

$$\underset{\approx}{\mathbf{K}}_{\vartheta}^{(n)} = \int_{-1}^{+1}\int_{-1}^{+1} \left(\overline{\underset{\approx}{\mathbf{B}}}_{nl}^T \left(\underset{\approx}{\mathbf{S}}_1 \overline{\underset{\approx}{\mathbf{B}}}_{nl} + \underset{\approx}{\mathbf{S}}_2 \widehat{\underset{\approx}{\mathbf{B}}}_{nl}\right) + \widehat{\underset{\approx}{\mathbf{B}}}_{nl}^T \left(\underset{\approx}{\mathbf{S}}_2 \overline{\underset{\approx}{\mathbf{B}}}_{nl} + \underset{\approx}{\mathbf{S}}_3 \widehat{\underset{\approx}{\mathbf{B}}}_{nl}\right)\right) \det|\underset{\approx}{\mathbf{J}}|\, dr\, ds \tag{20}$$

$$\underset{\sim}{\mathbf{f}}^{(n)} = \int_{-1}^{+1}\int_{-1}^{+1} \left(\overline{\underset{\approx}{\mathbf{B}}}_l^T \underset{\sim}{\mathbf{S}}1 + \widehat{\underset{\approx}{\mathbf{B}}}_l^T \underset{\sim}{\mathbf{S}}2\right) \det|\underset{\approx}{\mathbf{J}}|\, dr\, ds \tag{21}$$

$$\Delta\underset{\sim}{\mathbf{f}}_{\mathrm{th}}^{(n)} = \int_{-1}^{+1}\int_{-1}^{+1} \left(\overline{\underset{\approx}{\mathbf{B}}}_l^T \underset{\approx}{\mathbf{C}}\underset{\sim}{\alpha} \left(\Delta\overline{\vartheta} + \tfrac{1}{2}\Delta\widehat{\vartheta}\right) + \widehat{\underset{\approx}{\mathbf{B}}}_l^T \underset{\approx}{\mathbf{C}}\underset{\sim}{\alpha} \left(\tfrac{1}{2}\Delta\overline{\vartheta} + \tfrac{1}{3}\Delta\widehat{\vartheta}\right)\right) \det|\underset{\approx}{\mathbf{J}}|\, dr\, ds \tag{22}$$

with superscript (n) denoting layer n. $\underset{\sim}{\mathbf{S}}1, \underset{\sim}{\mathbf{S}}2, \underset{\sim}{\mathbf{S}}3$ represent "stress integrals" and are computed by:

$$\underset{\sim}{\mathbf{S}}i(r,s) = \underset{\approx}{\mathbf{T}}^T(r,s) \int_0^1 \underset{\sim}{\sigma}(r,s,t)\, t^{i-1}\, dt \qquad i = 1,2,3 \tag{23}$$

$\underset{\approx}{S}_1, \underset{\approx}{S}_2, \underset{\approx}{S}_3$ are equivalent to $\underset{\sim}{S}_1, \underset{\sim}{S}_2, \underset{\sim}{S}_3$ but the elements are rearranged in special matrix form, see appendix, Eq. (A19).

For elastic material these stress integrals can be computed analytically:

$$\begin{aligned}
\underset{\sim}{S}_1 &= \underset{\approx}{C}\left(\quad \underset{\sim}{\varepsilon} - \underset{\sim}{\alpha}\,\overline{\vartheta} \;+ \tfrac{1}{2}(\widehat{\underset{\sim}{\varepsilon}} - \underset{\sim}{\alpha}\,\widehat{\vartheta}) + \tfrac{1}{3}\widetilde{\underset{\sim}{\varepsilon}}\right) \\
\underset{\sim}{S}_2 &= \underset{\approx}{C}\left(\tfrac{1}{2}(\underset{\sim}{\varepsilon} - \underset{\sim}{\alpha}\,\overline{\vartheta}) + \tfrac{1}{3}(\widehat{\underset{\sim}{\varepsilon}} - \underset{\sim}{\alpha}\,\widehat{\vartheta}) + \tfrac{1}{4}\widetilde{\underset{\sim}{\varepsilon}}\right) \\
\underset{\sim}{S}_3 &= \underset{\approx}{C}\left(\tfrac{1}{3}(\underset{\sim}{\varepsilon} - \underset{\sim}{\alpha}\,\overline{\vartheta}) + \tfrac{1}{4}(\widehat{\underset{\sim}{\varepsilon}} - \underset{\sim}{\alpha}\,\widehat{\vartheta}) + \tfrac{1}{5}\widetilde{\underset{\sim}{\varepsilon}}\right)
\end{aligned} \tag{24}$$

For other material models (where the stresses cannot be computed directly from the total strains) a 2-point integration is used. By assuming the layer to be thin, a linear variation of the stresses across the thickness is valid:

$$\underset{\sim}{\sigma}(r,s,t) = \overline{\underset{\sim}{\sigma}}(r,s) + t\,\widehat{\underset{\sim}{\sigma}}(r,s) \tag{25}$$

with

$$\begin{aligned}
\overline{\underset{\sim}{\sigma}} &= \underset{\sim}{\sigma}^{(t=0)} \\
\widehat{\underset{\sim}{\sigma}} &= \underset{\sim}{\sigma}^{(t=1)} - \underset{\sim}{\sigma}^{(t=0)}
\end{aligned} \tag{26}$$

With Eq. (25) the stress integrals can be computed as follows:

$$\begin{aligned}
\underset{\sim}{S}_1 &= \underset{\approx}{T}\left(\quad \overline{\underset{\sim}{\sigma}} + \tfrac{1}{2}\widehat{\underset{\sim}{\sigma}}\right) \\
\underset{\sim}{S}_2 &= \underset{\approx}{T}\left(\tfrac{1}{2}\overline{\underset{\sim}{\sigma}} + \tfrac{1}{3}\widehat{\underset{\sim}{\sigma}}\right) \\
\underset{\sim}{S}_3 &= \underset{\approx}{T}\left(\tfrac{1}{3}\overline{\underset{\sim}{\sigma}} + \tfrac{1}{4}\widehat{\underset{\sim}{\sigma}}\right)
\end{aligned} \tag{27}$$

With Eqs. (26,27) the stress integrals can be evaluated from the stresses at $t = 0$ and $t = 1$, which, in turn, are computed either from the Svobodnik's elasto-plastic material law [6], or by a user defined material law (using the LCSMAT interface).

The integrals in Eqs. (19–22) are computed numerically using a standard Gaussian quadrature procedure.

1.3 ASSEMBLAGE OF ELEMENT STIFFNESSES

The procedure for establishing a connection between the individual layers is based on kinematic assumptions. Using this assumptions a relationship between conveniently chosen element DOFs and the layer DOFs can be derived.

1.3.1 Definition of Degrees of Freedom

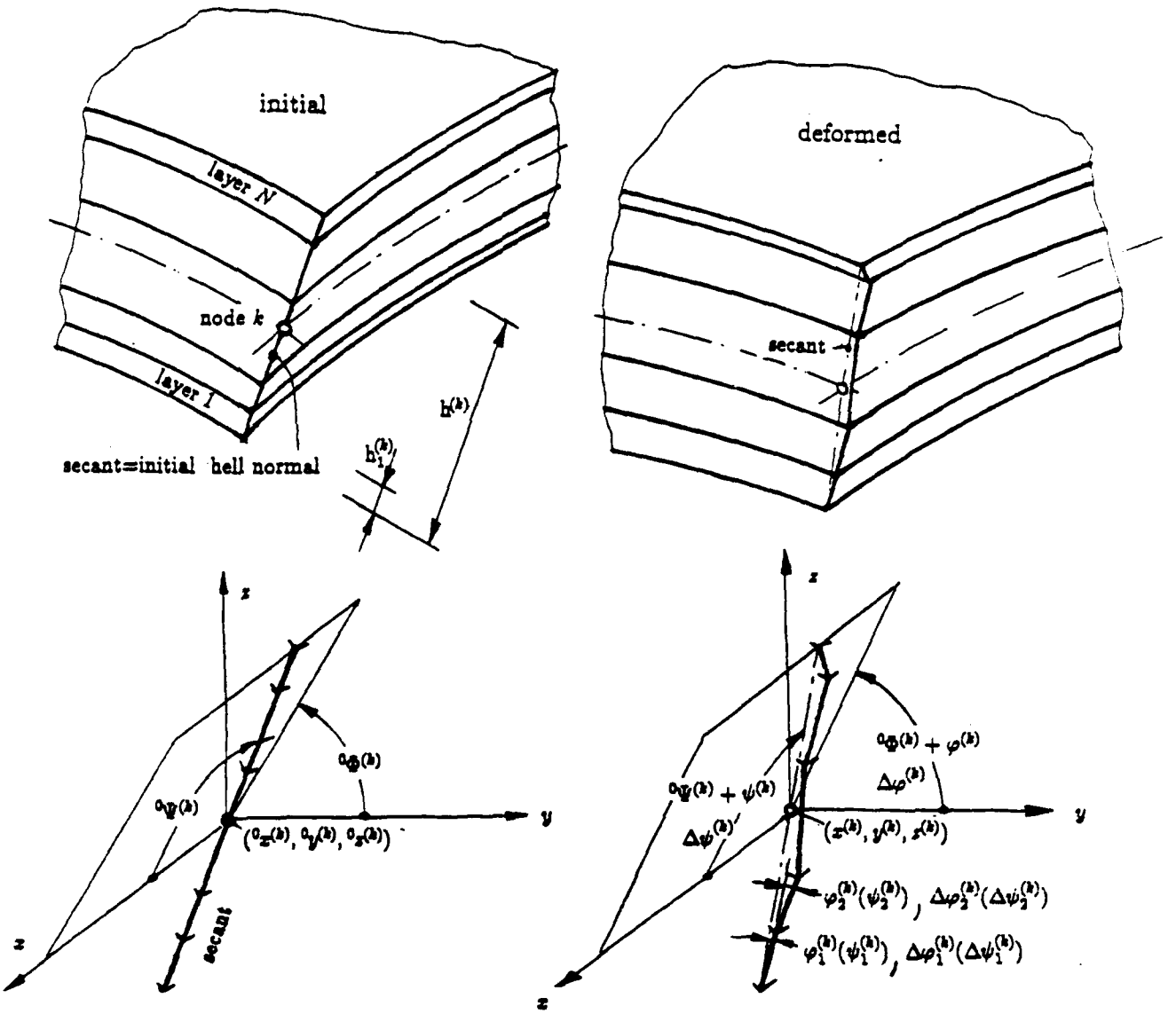

Fig. 1.3 Definition of element geometry and DOFs for the multilayer shell

To secure an easy and universal usage of the element, the definition of the element DOFs is based on the concept of "inplane" and "out-of-plane" quantities:

- Displacements of the shell's midsurface represent the "inplane" part (they are related to the membrane behavior).
- Rotations of shell-"normals" represent the "out-of-plane" part (they are related to the bending and transverse shearing behavior).

Basically, the same notation as used in the degeneration principle is employed here. The geometry of the entire shell is described in terms of:

- The coordinates of nodes (k) lying in the shell's midsurface, $x^{(k)}, y^{(k)}, z^{(k)}$,
- 2 angles at these nodes, $\Phi^{(k)}, \Psi^{(k)}$ which determine the position of the shell's "normal" (this vector is not necessarily exactly normal to the shell's midsurface),
- $2(N-1)$ additional angles at these nodes, $\varphi_n^{(k)}, \psi_n^{(k)}$ ($n = 1, \ldots, N-1$; N = number of layers), which determine the positions of the normal vectors of the layers, and
- the thickness of the shell at these nodes $h^{(k)}$, see Fig. 1.3.

Correspondingly, the following DOFs per node are defined:

- 3 displacement increments, $\Delta u^{(k)}, \Delta v^{(k)}, \Delta w^{(k)}$, and
- $2N$ angle increments, $\Delta\varphi^{(k)}, \Delta\psi^{(k)}, \Delta\varphi_n^{(k)}, \Delta\psi_n^{(k)}$ ($n = 1, \ldots, N-1$).

Initially, the normal vectors of all layers lie on one straight line, namely the shell's normal, which is determined by the initial angles ${}^0\Phi^{(k)}, {}^0\Psi^{(k)}$, and can be computed from the nodal coordinates. By using the 2/D shape functions $\phi^{(k)}(r,s)$ (see interpolation of the geometry, Eq. (6)), the shell's normal vector $\underset{\sim}{n}$ is given by

$$\underset{\sim}{n} = \begin{pmatrix} n_x \\ n_y \\ n_z \end{pmatrix} = \begin{pmatrix} {}^0x_{,r} \\ {}^0y_{,r} \\ {}^0z_{,r} \end{pmatrix} \times \begin{pmatrix} {}^0x_{,s} \\ {}^0y_{,s} \\ {}^0z_{,s} \end{pmatrix} \tag{28}$$

The formulas for the displacement derivatives $x_{,r}$, $y_{,r}$, $z_{,r}$, $x_{,s}$, $y_{,s}$, $z_{,s}$ can be found in the appendix, Eq. ($A20$).

From $\underset{\sim}{n}$, computed at node k, the angles ${}^0\Phi^{(k)}, {}^0\Psi^{(k)}$ follow as

$$\begin{aligned} {}^0\Phi^{(k)} &= \arctan \frac{n_x^{(k)}}{n_y^{(k)}} \\ {}^0\Psi^{(k)} &= \arctan \frac{\sqrt{n_y^{(k)2} + n_x^{(k)2}}}{n_z^{(k)}} \end{aligned} \tag{29}$$

Alternatively, the initial position of the shell's normal can be defined by prescribing direction cosines at nodes (in addition to the coordinates). This is sometimes useful if two adjacent elements are inclined (i.e. have no common normal), which can lead to inaccuracies in the analysis.

During loading, the normals of the layers deviate from the initial shell's normal. Due to the degeneration principle, these layer-normals remain straight, so that a piecewise linear deformation of the shell's normal occurs.

By defining a "secant" (which coincides with the shell's normal in the initial configuration) and angles $\varphi_n^{(k)}, \psi_n^{(k)}$ as corresponding deviations of the layer-normals from this secant (see Fig. 1.3) one can compute the coordinates $x_n^{(k)}$, $y_n^{(k)}$, $z_n^{(k)}$ and the total angles $\Phi_n^{(k)}$, $\Psi_n^{(k)}$ for the layers.

1.3.2 Description of Geometry

The nodal coordinates for layer n at beginning of the increment can be computed from the coordinates of the midsurface of the shell, the shell thickness, the angles of the "secant", and the angles of the layer-normals as follows:

$$
\begin{aligned}
x_n^{(k)} &= x^{(k)} - \tfrac{1}{2}\mathrm{h}^{(k)} \cos\Psi^{(k)} + \sum_{j=1}^{n-1} \mathrm{h}_j^{(k)} \cos(\Psi^{(k)} + \psi_j^{(k)}) \\
y_n^{(k)} &= y^{(k)} - \tfrac{1}{2}\mathrm{h}^{(k)} \sin\Psi^{(k)} \cos\Phi^{(k)} + \sum_{j=1}^{n-1} \mathrm{h}_j^{(k)} \sin(\Psi^{(k)} + \psi_j^{(k)}) \cos(\Phi^{(k)} + \varphi_j^{(k)}) \\
z_n^{(k)} &= z^{(k)} - \tfrac{1}{2}\mathrm{h}^{(k)} \sin\Psi^{(k)} \sin\Phi^{(k)} + \sum_{j=1}^{n-1} \mathrm{h}_j^{(k)} \sin(\Psi^{(k)} + \psi_j^{(k)}) \sin(\Phi^{(k)} + \varphi_j^{(k)}) \\
\Phi_n^{(k)} &= \begin{cases} \Phi^{(k)} + \varphi_n^{(k)} & 1 \le n \le N-1 \\ \Phi^{(k)} - \arcsin\Big(\sum_{j=1}^{N-1} \sin\varphi_j^{(k)} \frac{\mathrm{h}_j^{(k)}}{\mathrm{h}_N^{(k)}}\Big) & n = N \end{cases} \\
\Psi_n^{(k)} &= \begin{cases} \Psi^{(k)} + \psi_n^{(k)} & 1 \le n \le N-1 \\ \Psi^{(k)} - \arcsin\Big(\sum_{j=1}^{N-1} \sin\psi_j^{(k)} \frac{\mathrm{h}_j^{(k)}}{\mathrm{h}_N^{(k)}}\Big) & n = N \end{cases}
\end{aligned}
\tag{30}
$$

The corresponding equation for the initial coordinates ${}^0x_n^{(k)}, {}^0y_n^{(k)}, {}^0z_n^{(k)}$ can be found in the appendix, Eq. (*A*21).

The nodal displacements for layer n can be computed similar to Eq. (30) in terms of

the shell's nodal displacements and nodal angles:

$$
\begin{aligned}
u_n^{(k)} &= u^{(k)} - \tfrac{1}{2}h^{(k)}(\cos\Psi^{(k)} - \cos{}^0\Psi^{(k)}) \\
&\quad + \sum_{j=1}^{n-1} h_j^{(k)}\big(\cos(\Psi^{(k)} + \psi_j^{(k)}) - \cos{}^0\Psi^{(k)}\big) \\
v_n^{(k)} &= v^{(k)} - \tfrac{1}{2}h^{(k)}(\sin\Psi^{(k)}\cos\Phi^{(k)} - \sin{}^0\Psi^{(k)}\cos{}^0\Phi^{(k)}) \\
&\quad + \sum_{j=1}^{n-1} h_j^{(k)}\big(\sin(\Psi^{(k)} + \psi_j^{(k)})\cos(\Phi^{(k)} + \varphi_j^{(k)}) - \sin{}^0\Psi^{(k)}\cos{}^0\Phi^{(k)}\big) \\
w_n^{(k)} &= w^{(k)} - \tfrac{1}{2}h^{(k)}(\sin\Psi^{(k)}\sin\Phi^{(k)} - \sin{}^0\Psi^{(k)}\sin{}^0\Phi^{(k)}) \\
&\quad + \sum_{j=1}^{n-1} h_j^{(k)}\big(\sin(\Psi^{(k)} + \psi_j^{(k)})\sin(\Phi^{(k)} + \varphi_j^{(k)}) - \sin{}^0\Psi^{(k)}\sin{}^0\Phi^{(k)}\big)
\end{aligned}
\tag{31}
$$

The layer-coordinates from Eq. (30) and the layer-displacements from Eq. (31) are then used for computing the stiffness expressions of the layer (section 1.2).

1.3.3 Transformation Layer → Shell

Equation (31) can be used for deriving the displacement increments. By assuming the angle increments $\Delta\varphi^{(k)}, \Delta\psi^{(k)}, \Delta\varphi_n^{(k)}, \Delta\psi_n^{(k)}$ to be small ($\ll 1$), the trigonometric functions can be linearized with respect to these angles, which results in a linear relationship between the layer DOFs ($\Delta u_n^{(k)}$, $\Delta v_n^{(k)}$, $\Delta w_n^{(k)}$, $\Delta\overline{\varphi}_n^{(k)}$, $\Delta\overline{\psi}_n^{(k)}$) and the shell DOFs ($\Delta u^{(k)}$, $\Delta v^{(k)}$, $\Delta w^{(k)}$, $\Delta\varphi^{(k)}$, $\Delta\psi^{(k)}$, $\Delta\varphi_n^{(k)}$, $\Delta\psi_n^{(k)}$, $n = 1, \ldots, N-1$):

$$
\Delta\underset{\sim}{u}_n^{(k)} = \underset{\approx}{G}_n^{(k)}\,\Delta\underset{\sim}{u}^{(k)} \tag{32}
$$

The detailed formulas for the transformation matrix $\underset{\approx}{G}_n^{(k)}$ and the definitions of the vectors $\Delta\underset{\sim}{u}_n^{(k)}$ and $\Delta\underset{\sim}{u}^{(k)}$ can be found in the appendix, Eqs. (*A25–A27*).

The definition of the angles $\varphi_n^{(k)}$ and $\psi_n^{(k)}$ as deviations from the "secant" renders some distinct advantages:

- Enforcing a straight shell normal (e.g. as a boundary condition) can easily be done by setting the DOFs $\Delta\varphi_n^{(k)}$, $\Delta\psi_n^{(k)}$, $n = 1, \ldots, N-1$ to zero. This forces the total angles $\Phi_n^{(k)}$, $\Psi_n^{(k)}$ of all layers to be equal to the corresponding angles $\Phi^{(k)}$, $\Psi^{(k)}$ of the shell.

- The piecewise linear deformations of the shell's "normal" result directly from the analysis in terms of the deviation angles.

By applying the transformation from Eq. (32) to all nodes the following global transformation matrix can be derived:

$$\underset{\approx}{G}_n = \begin{pmatrix} \underset{\approx}{G}_n^{(1)} & \underset{\approx}{0} & \cdots & \underset{\approx}{0} & \cdots & \underset{\approx}{0} \\ & \underset{\approx}{G}_n^{(2)} & \cdots & \underset{\approx}{0} & \cdots & \underset{\approx}{0} \\ & & \ddots & \vdots & \vdots & \vdots \\ & sym. & & \underset{\approx}{G}_n^{(k)} & \cdots & \underset{\approx}{0} \\ & & & & \ddots & \vdots \\ & & & & & \underset{\approx}{G}_n^{(N)} \end{pmatrix} \tag{33}$$

with this equation, the stiffness matrix and the vector of internal nodal forces can be transformed from the layer level to the element level:

$$\underset{\approx}{K} = \sum_{n=1}^{N} \underset{\approx}{G}_n^T (\underset{\approx}{K}_e^{(n)} + \underset{\approx}{K}_g^{(n)}) \underset{\approx}{G}_n \tag{34}$$

$$\underset{\sim}{f}_{th} = \sum_{n=1}^{N} \underset{\approx}{G}_n^T (\underset{\sim}{f}^{(n)} - \Delta \underset{\sim}{f}_{th}^{(n)}) \tag{35}$$

Consequently, $\underset{\approx}{K}$ and $\underset{\sim}{f}_{th}$ are used in the incremental equilibrium equation, Eq. (1).

1.3.4 Distributed Loads

In the **LCSLFC**-element distributed loads are taken into account in a simplified manner. The equivalent nodal forces are computed for the entire shell (rather than seperately for each layer) and added to the RHS-vector of Eq. (1).

Currently, the following distributed load types U1 – U5 (this notation corresponds to the ABAQUS notation [10]) are implemented in the **LCSLFC**-element (for details on the derivation of the equations see [3]):

U1 corresponds to a uniform pressure load p. By assuming the pressure to act on the midsurface of the shell, the equivalent nodal forces $\underset{\sim}{\mathrm{R}}_{press}$ can be computed by:

$$\underset{\sim}{\mathrm{R}}_{press} = \int_{-1}^{+1}\int_{-1}^{+1} -p\, \overline{\underset{\approx}{\mathbf{N}}}^{T}(r,s)\left(\begin{pmatrix} x_{,r} \\ y_{,r} \\ z_{,r} \end{pmatrix} \times \begin{pmatrix} x_{,s} \\ y_{,s} \\ z_{,s} \end{pmatrix}\right) \det|\,\underset{\approx}{\mathbf{J}}\,|\; dr\, ds \tag{36}$$

with $\overline{\underset{\approx}{\mathbf{N}}}$ being the translational part of the interpolation matrix for the shell $\underset{\approx}{\mathbf{N}}$, see appendix, Eqs. $(A29, A30)$.

U2 correspond to a gravity load in $-z$ direction. The equivalent nodal forces $\underset{\sim}{\mathrm{R}}_{grav}$ can be computed by:

$$\underset{\sim}{\mathrm{R}}_{grav} = \int_{-1}^{+1}\int_{-1}^{+1} \left[\overline{\underset{\approx}{\mathbf{N}}}^{T}(r,s) \begin{pmatrix} 0 \\ 0 \\ -\overline{\rho}\mathrm{g} \end{pmatrix} + \widehat{\underset{\approx}{\mathbf{N}}}^{T}(r,s) \begin{pmatrix} 0 \\ 0 \\ -\widehat{\rho}\mathrm{g} \end{pmatrix}\right] \det|\,\underset{\approx}{\mathbf{J}}\,|\; dr\, ds \tag{37}$$

with $\widehat{\underset{\approx}{\mathbf{N}}}$ being the rotational part of the interpolation matrix $\underset{\approx}{\mathbf{N}}$, see appendix, Eqs. $(A29, A31)$, and g being the gravity constant. $\overline{\rho}, \widehat{\rho}$ are the following thickness integrals of the mass densities of the layers (ρ_n):

$$\begin{aligned} \overline{\rho} &= \sum_{n=1}^{N} \rho_n \frac{\mathrm{h}_n}{\mathrm{h}} \\ \widehat{\rho} &= \sum_{n=1}^{N} \rho_n \frac{\mathrm{h}_n}{\mathrm{h}} \frac{\overline{\mathrm{h}}_n}{\mathrm{h}} \qquad \text{with} \qquad \overline{\mathrm{h}}_n = \frac{\mathrm{h}_n - \mathrm{h}}{2} + \sum_{j=1}^{n-1} \mathrm{h}_n \end{aligned} \tag{38}$$

U3 correspond to a uniform body force b in x direction. The equivalent nodal forces $\underset{\sim}{\mathrm{R}}_{bfo}$ can be corr ted by:

$$\underset{\sim}{\mathrm{R}}_{bfo} = \int_{-1}^{+1}\int_{-1}^{+1} \overline{\underset{\approx}{\mathbf{N}}}^{T}(r,s) \begin{pmatrix} b \\ 0 \\ 0 \end{pmatrix} \det|\,\underset{\approx}{\mathbf{J}}\,|\; dr\, ds \tag{39}$$

U4,U5 correspond to a uniform body force b in y, z direction, respectively. The equivalent nodal forces can computed similar to Eq. (39) but the load direction has to be adjusted accordingly.

1.4 MODIFIED BUCKLING ANALYSIS

In the **LCSLFC**-element the buckling procedure implemented in ABAQUS [10] is used in a modified way in order to improve the convergence behavior in cases where thermal buckling is considered.

Instead of computing the current stiffness plus eigenvalue times an incremental stiffness (this is the ABAQUS `*BUCKLE` procedure), the stiffness matrix is decomposed into a load independent part and a load dependent part, which is used to formulate a linear eigenvalue problem.

Starting from Eq. (1) and by linearizing the nonlinear relationship between the stiffness matrix and the current load, an eigenvalue problem of the following form can be obtained (for details see [11]), leading to an estimate for the critical load:

$$(\underset{\approx}{\mathbf{K}}_e + \eta\, \underset{\approx}{\mathbf{K}}_g)\,\delta\underset{\sim}{y} = 0 \tag{40}$$

$$\text{critical load} \approx \eta_1 \times \text{current load} \tag{41}$$

with η_1 being the smallest eigenvalue of Eq. (40). The eigenvectors $\delta\underset{\sim}{y}$ correspond to the eigenvalues η and represent approximations of the buckling modes.

The error caused by the linearization mentioned above, vanishes and, hence, the estimate (Eq. (41)) becomes accurate when the lowest eigenvalue η_1 approaches 1, i.e. the current configuration approaches the critical one.

2. USER MANUAL FOR THE LCSLFC-ELEMENT

2.1 SUMMARY OF ELEMENT CAPABILITIES

The following is a list of features implemented in the **LCSLFC**-element. Sections 2.2 and 2.3 include detailed descriptions of these capabilities.

* Element formulations:
  - linear or
  - updated Lagrangian
* Variable node numbers: 4-, 8-, 9- and 16-noded elements
* Variable integration order: from 1×1 up to 4×4
* Variable shell thickness within each element
* Free definition of directions of shell quasi-normals:
  - prescribed or
  - computed from initial geometry
* Convenient definition of DOFs:
  - displacements of shell-midsurface plus
  - rotations of shell quasi-normals plus
  - seperate rotational DOFs per node for each layer
* Layerwise constant transverse shear
* Free laminate lay-up: each layer can have a
  - different layer angle
  - different thickness
  - different material
* Free distribution of layer angles within elements:
  - prescribed or
  - computed from initial geometry
* Material models:
  - linear elastic model or
  - metal-matrix-composite-type elasto-plastic model or
  - user defined material model

* Different types of material data input:
  - layer data (= homogenized data) or
  - data for fiber material and matrix material with
    - aligned continuous fibers or
    - randomly oriented fibers or
    - aligned whiskers or
    - randomly oriented whiskers
* Thermal loading in terms of temperatures at the surfaces of the shell
* Distributed loads (surface pressure and bodyforces)
* Printout of layer stresses and strains at various locations
* Full usage of ABAQUS preprocessor capabilities

2.2 INPUT STRUCTURE

The **LCSLFC**-element works in conjuction with the FE-code **ABAQUS** [10] as a user defined element by employing the UEL-interface. Therefore, the input for the **LCSLFC**-element is based on the conventions and concepts of ABAQUS. In addition, line ("card") oriented data input within the `*UEL PROPERTY` section is used to define all the element parameters necessary.

2.2.1 Introducing the LCSLFC-Element

The **LCSLFC**-element is introduced via the keyword `*USER ELEMENT` in the input-deck. In addition to the keyword, the parameters `NODES, TYPE, COORDINATES, VARIABLES, PROPERTIES` have to be entered with the following values:

`NODES=4` or `=8` or `=9` or `=16` (= number of nodes forming the element, see note (1))

`TYPE=U1` (= element identifier)

`COORDINATES=6` (= number of coordinates at each point, see note (2))

`VARIABLES=`*nn* (= number of solution dependent variables, see note (3))

`PROPERTIES=`*mm* (= number of property values given in the `*UEL PROPERTY` option, see note (4))

Notes:

(1) The 4-noded element should be used with care due to the possibility of shear-locking. The 8-noded and 9-noded shells can exhibit membrane-locking effects for curvilinear geometries. Thus they should be used primarily for planar problems.
The use of the 16-noded element is highly recommended since none of the adverse effects occur.
The local element node numbering scheme for the different elements can be found in Fig. 2.1.

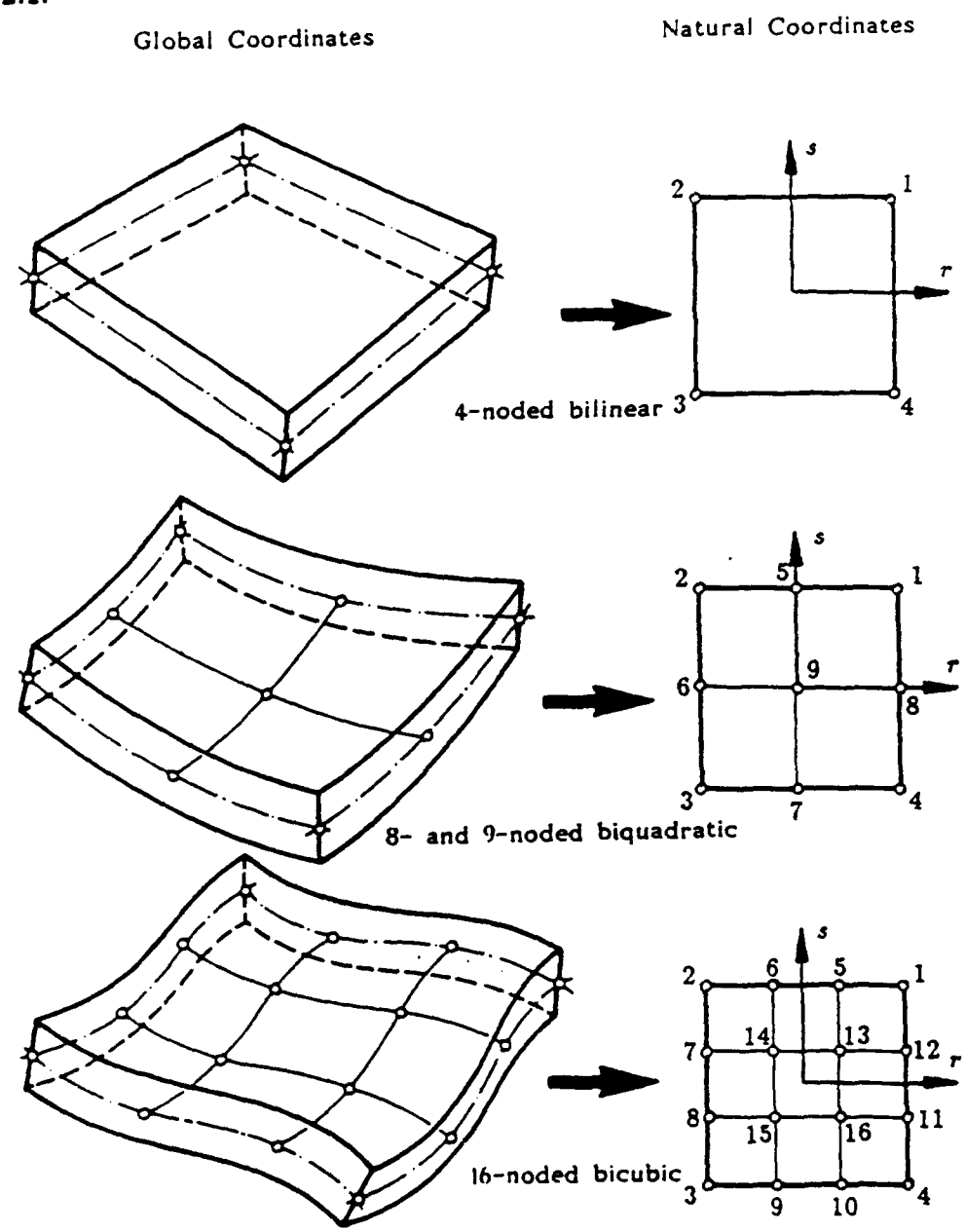

Fig. 2.1 Element node numbering scheme for 4-, 9-, 16-noded **LCSLFC**-element

(2) 6 coordinates (x, y, z coordinates plus x, y, z direction cosines) are used to define both the position of the nodes in space and the direction of the shell normal. These coordinates are entered in the *NODE section of the input-deck; input of the direction cosines is optional; if they are not specified, the direction of the initial shell normal is computed from the initial geometry of the shell (see Eqs. (28,29)). If the direction cosines are specified, these directions will be used, unless the difference between the angles computed from the geometry and those computed from the direction cosines is greater than a given value (default: DANG= 10°, or specified for each element, see *Element Data Block*). DANG should be kept small to prevent excessive initial distortion of the element. In cases where two adjacent elements are inclined (i.e. have no common normal) it is sometimes useful to specify a particular direction of normal to reduce inaccuracies in the analysis.

(3) The number of solution dependent variables nn defines the length of the array SVARS, which contains certain element data. nn depends on the number of layers (parameter MAXNUM), the number of integration points (parameters NIR, NIS), the number of element nodes (parameter NNODE) and the number of items stored at each integration point at each layer (parameter NLWA). nn is given by the following expression:

$$nn \geq \texttt{NSVARS} = (\texttt{NLWA} + 8) * 2 * \texttt{NIR} * \texttt{NIS} * \texttt{MAXNUM} + (\texttt{MAXNUM} + 3) * \texttt{NNODE} + 2$$

The program checks whether nn is sufficiently large and prints out SVARS(NSVARS).

(4) The number of property values equals 8 times the number of data lines within the *UEL PROPERTY section of the input-deck.

2.2.2 Definition of Degrees of Freedom

After the line with the keyword *USER ELEMENT, a line with a list of active DOFs per node has to be entered, which depends on the number of layers:

For a shell with only one layer, DOFs 1,2,3,4,5 have to be activated; for each additional layer two additional DOFs are necessary. For these DOFs the numbers 11,12,... should be used (ABAQUS has certain conventions for labeling the DOFs [10]), so that results can be printed out. However, if thermal load is applied, these DOFs cannot be used (these DOFs are unavailable if the keyword *TEMPERATURE is used), instead DOFs 6,...,10 can be used. In that case, however, only DOF 6 is available for print-out.

The output variable identifiers for printing the DOFs are defined as follows (see also ABAQUS Users' Manual, section 7.7.1). These identifiers can be used in the *NODE PRINT option:

DOFs	identifier
1,2,3,4,5,6	U
11,12,...	NT11,NT12,...

DOFs 1,2,3 represent the displacement increments in x, y, z directions, DOFs 4,5 correspond to the rotational increments of the shell secant, see Fig. 1.3. The remaining DOFs are rotational increments of the normals of the layers as defined in section 1.3.1, see Fig. 1.3. Due to ABAQUS input conventions (only 16 integer items can be given in a data line), the maximum number of layers is restricted to 6 (= 15 DOFs).

2.2.3 Element Properties

To define all element properties, the *UEL PROPERTY section has to be used. The data within this section are arranged in "card" form (i.e. the ordering of both the input lines and the input items within each line are essential). The arrangement of the data items is as follows (the names of the variables correspond to the **LCSLFC**-code):

```
KTEMP,NIR,NIS,ISTRES,MODEL,NUMMAT,NUMSPE
NP,NSCHDA(NP),NSCHLA,WHISKL
RHO(NP),RHOM,ALFT(1,NP),ALFT(2,NP),ALFT(3,NP),ALFT(4,NP),ALFT(5,NP)
PROP(1,NP),...,PROP(8,NP)
[PROP(9,NP),...]
[NP,...
   ⋮ (NUMMAT materials have to be defined)
 [PROP(9,NP),...]]
NLFC,NSCHI(NLFC),NSY
ISCHI,ANSCHI(ISCHI,NLFC),THSCHI(ISCHI,NLFC),IMSCHI(ISCHI,NLFC),KISCHI
next ISCHI,... (until all layers are defined)
[NLFC,...
   ⋮ (NUMSPE laminates have to be defined)
 ISCHI,...]
M,MTYP,IPS,KG,KA,ANGM1,IANGL,DANG
[HH(1,MAXNUM+1),HH(2,MAXNUM+1),...]
[ANGM(1),ANGM(2),...]
next M,... (until all elements are defined)
```

These input data are structured into 4 blocks, see Fig. 2.2.

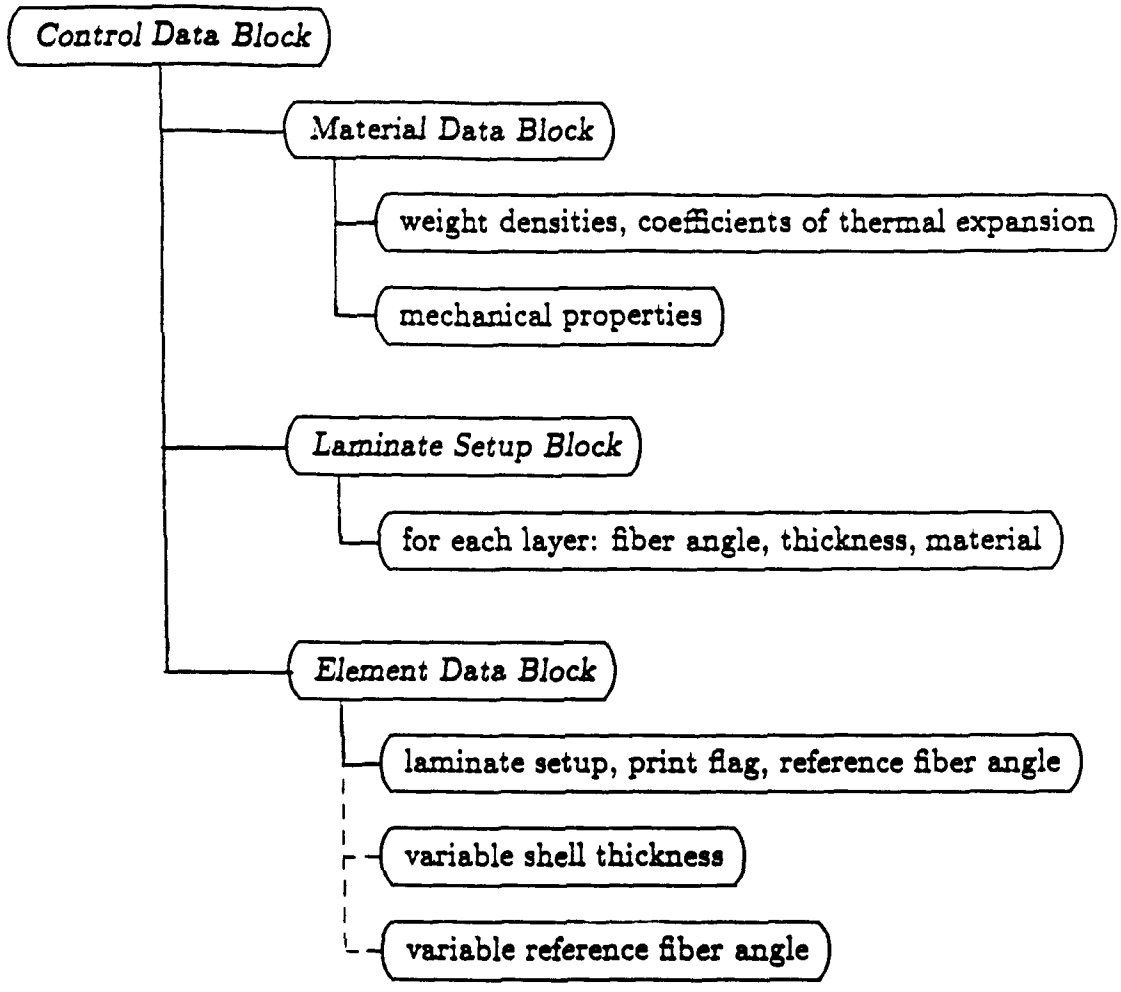

Fig. 2.2 Input data structure within the `*UEL PROPERTY` section

Control Data Block : Defines all control parameters

Variable	Entry	Note
`KTEMP`	Thermal load flag =0... no thermal load =1... thermal loading is taken into account	(1)
`NIR`	Integration order in r-direction	(2)
`NIS`	Integration order in s-direction	(2)

ISTRES	Stress/strain output flag = 0... no stress/strain output = 1... print layer stresses at layer midsurface = 2... print layer stresses at bottom and top surface = 10... print layer status (for MODEL=2) =100... print layer strains at layer midsurface =200... print layer strains at bottom and top surface	(3)
MODEL	Material model number =1... linear elastic =2... elastic-plastic (MMC) =4... user defined material	(4)
NUMMAT	Number of material specifications in the *Material Data Block* default=1	
NUMSPE	Number of laminate specifications in the *Laminate Setup Block* default=1	

Notes:

(1) "In-plane" thermal loading (i.e. temperatures at the midsurface of the shell) is applied via the standard ABAQUS option *TEMPERATURE in the history definition. Initial temperatures can be defined by using the *INITIAL CONDITIONS,TYPE=TEMPERATURE option.

"Thermal bending" loads (i.e. temperature differences between outer and inner surfaces of the shell) can be introduced via the *FIELD,VARIABLE=1 option, in which the temperature differences can be entered. Initial conditions are defined via the *INITIAL CONDITIONS,TYPE=FIELD option.

(2) NIR and NIS define the order the reference surfaces of the layers are numerically integrated (Gauss integration). The locations of these integration points with respect to the natural coordinates r, s are as follows:

integration order	r and s coordinates
1×1	0.0
2×2	$\pm\sqrt{1/3}$
3×3	0.0, $\pm\sqrt{3/5}$
4×4	$\pm$0.8611363116, $\pm$0.3399810436

(3) ISTRES defines the type of stress/strain output. Input to ISTRES consists of a number containing three digits. The first digit controls the layer strain output, the second digit controls the output of layer status, and the third digit controls the layer stress output. E.g. ISTRES=111 produces output of layer stresses, layer strains and layer status, all at the midsurface of the layers.
Output locations are the numerical integration points defined in the previous table. Stresses and strains are referred to the local layer coordinate system l, q, t (fiber direction, transverse direction, thickness direction).

(4) Three different options are available:
- A linear elastic model, in which either layer data or fiber and matrix data along with the geometrical setup can be input (see *Material Data Block*);
- A special elasto-plastic material model for fiber reinforced metal matrix composites, developed by Alfred Svobodnik, Institute of Lightweight Structures and Aerospace Engineering, Vienna Technical University [6];
- A user defined material model (see section 2.3).

Material Data Block : Defines the materials of the layers of the composite. Each different material combination (fiber and matrix) needs it's own material data sequence. Thus it is possible to define hybrid composites. NUMMAT material specifications have to be entered.

Variable	Entry	Note
Card 1:		
NP	Material set number	
NSCHDA(NP)	Flag for type of material data input =0... fiber and matrix data =1... layer data	(1)
NSCHLA	Flag for fiber orientation =0... aligned fibers =1... randomly oriented fibers	(2)
WHISKL	Length of whiskers	(2)
Card 2 (if NSCHDA(NP)=0):		
RHO(NP)	Weight density of the fiber	(3)
RHOM	Weight density of the matrix	(3)

ALFT(1,NP)	Coefficient of linear thermal expansion of the fiber in fiber direction
ALFT(2,NP)	Coefficient of linear thermal expansion of the fiber in transverse direction
ALFT(3,NP)	Coefficient of linear thermal expansion of the matrix

Card 2 (if NSCHDA(NP)=1):

RHO(NP)	Weight density of the composite
RHOM	not used
ALFT(1,NP)	Coefficient of linear thermal expansion of the composite (4) in l-direction (fiber direction)
ALFT(2,NP)	Coefficient of linear thermal expansion of the composite (4) in q-direction (transverse direction)
ALFT(3,NP)	Coefficient of linear thermal expansion of the composite (4) in lq-shear (inplane shear)
ALFT(4,NP)	Coefficient of linear thermal expansion of the composite (4) in lt-shear (transverse shear)
ALFT(5,NP)	Coefficient of linear thermal expansion of the composite (4) in qt-shear (transverse shear)

Card 3 (if NSCHDA(NP)=0):

PROP(1,NP)	Axial Young's modulus of the fiber
PROP(2,NP)	Transverse Young's modulus of the fiber
PROP(3,NP)	Poisson's ratio of the fiber
PROP(4,NP)	Axial shear modulus of the fiber
PROP(5,NP)	Transverse shear modulus of the fiber
PROP(6,NP)	Fiber volume fraction
PROP(7,NP)	Young's modulus of the matrix
PROP(8,NP)	Shear modulus of the matrix

Card 3a (only if MODEL=2):

PROP(9,NP)	Yield stress of the matrix in tension	
PROP(10,NP)	Parameter defining hardening behavior of the matrix	(5)
PROP(11,NP)	Parameter defining hardening behavior of the matrix	(5)
PROP(12,NP)	Stress correction parameter =0... no stress correction =1... correction after each increment =2... correction after each subincrement	(6)

Card 3a (only if needed for MODEL=4):

PROP(9,NP)	Additional material property	(7)
PROP(10,NP)	Additional material property	(7)
⋮	⋮	

Card 3 (if NSCHDA(NP)=1):

PROP(1,NP)	Young's modulus of the composite in l-direction
PROP(2,NP)	Young's modulus of the composite in q-direction
PROP(3,NP)	Poisson's ratio of the composite
PROP(4,NP)	Inplane shear modulus of the composite (lq-shear)
PROP(5,NP)	Transverse shear modulus of the composite (lt-shear)
PROP(6,NP)	Transverse shear modulus of the composite (qt-shear)

Notes:

(1) For NSCHDA=0 the effective properties of the composite are computed from fiber and matrix data as well as the volume fraction and the geometrical setup, which is entered on cards 2 and 3. The Mori-Tanaka averaging regime in conjunction with the parameters NSCHLA and WHISKL will be used in this case, see note (2). For NSCHDA=1 the effective properties of the composite have to be entered directly on cards 2 and 3.

(2) If WHISKL>0 then a whisker type composite is assumed, with whisker length=WHISKL. NSCHLA indicates whether the fibers (or whiskers) are aligned or randomly distributed. NSCHLA and WHISKL are used only if NSCHDA=0.

(3) The fiber volume fraction is used to compute the weight density of the composite by averaging the weight densities of the fiber and the matrix.

(4) For an orthotropic material only the coefficients of linear thermal expansion in the principal directions (l and q) are different from zero. However, for a fully anisotropic material additional coefficients for thermal shear can be entered.

(5) Two different hardening models are implemented. A detailed description of these can be found in [6].
- Bilinear hardening matrix: PROP(10,NP) is set to zero and PROP(11,NP) has to contain the value of the tangent modulus.
- Modified Ramberg-Osgood law: The classical Ramberg-Osgood approximation is:

$$\varepsilon = \frac{\sigma}{E} + (\frac{\sigma}{B})^n$$

Here σ and ε denote stress and strain in simple tension, E is the Young's modulus, B PROP(10,NP) and n PROP(11,NP) are parameters describing the plastic behavior which are determined from measured stress-strain curves.

(6) This parameter controls the stress correction. A description of the stress correction can be found in [6].
Usually this parameter should be set to 1. For very large load increments a value of 2 is recommended.

(7) For the user defined material model, additional material properties may need to be entered. The internal parameter NCON specifies the number of properties. It has to be set accordingly (see section 2.3).

Laminate Setup Block: Defines the setup of the laminated composite. The fiber angle, the thickness, and the material definition of each layer have to be entered. NUMSPE laminate definitions must be specified.

Variable	Entry	Note
Card 1:		
NLFC	Number of laminate setup	
NSCHI(NLFC)	Number of layers in this laminate setup	
NSY	Flag for symmetrical laminate setup =0... unsymmetric setup =1... symmetrical setup with respect to the mid surface of the shell	(1)
Card 2 (enter as many cards of this type as needed to define the laminate):		
ISCHI	Layer number	(2)
ANSCHI(ISCHI,NLFC)	Fiber angle for this layer	(3)
THSCHI(ISCHI,NLFC)	Layer thickness for this layer	
IMSCHI(ISCHI,NLFC)	Material label	(4)
KISCHI	Generation parameter	(2)

Notes:

(1) With NSY=1 the laminate setup is assumed to be symmetrical to the midsurface of the shell. Layer n has the same fiber angle and thickness as layer NSCHI+1-n. Thus, only the half laminate setup (ISCHI=1,2,...,NSCHI/2) has to be entered.
With NSY=0 all layers (ISCHI=1,2,...,NSCHI) have to be defined.

(2) The sequence of the input cards for defining the layers can be chosen freely. However, the highest number (=NSCHI/2 for NSY=1 or =NSCHI for NSY=0) has to be in the last line. With the parameter KISCHI layers can be generated, e.g. the card sequence
1,45.,0.1,1
7,60.,0.1,2,2
generates layers 3,5 with the same fiber angle, thickness, and material as layer 7.

(3) This angle is defined with respect to a reference axis, which, in turn, is prescribed by the element geometry and a reference angle in the *Element Data Block*.

(4) For IMSCHI the number of the material defined in the *Material Data Block* (→ NP) has to be entered. Thus, it is possible to define hybrid setups containing different materials.

Element Data Block : Contains additional element information. Elements with similar data can be generated.

Variable	Entry	Note
Card 1:		
M	Element number	
MTYP	Laminate setup for this element	(1)
IPS	Stress/strain output control flag	(2)
KG	Generation parameter	(3)
KA	Element thickness flag =0... constant element thickness (from laminate definition) =2... element thicknesses at corner nodes prescribed (requires additional card 1a) =4... element thicknesses at all nodes prescribed (requires additional cards 1a, 1b)	(4)
ANGM1	Angle between reference axis and r-axis in local element node 1	(5)

IANGL	Flag for calculation of the reference angle =0... ref. angle is constant within the element (=ANGM1) =1... ref. angles are computed from element geometry =2... ref. angles at corner nodes prescribed (requires additional card 1c) =4... ref. angles at all nodes prescribed (requires additional cards 1c, 1d)	(5)
DANG	Tolerance measure for angles of normal (default=10°)	(6)

Card 1a (only if KA=2):

HH(1,MAXNUM+1)	Shell thickness at local element node 1
HH(2,MAXNUM+1)	Shell thickness at local element node 2
HH(3,MAXNUM+1)	Shell thickness at local element node 3
HH(4,MAXNUM+1)	Shell thickness at local element node 4

Card 1a (only if KA=4):

HH(1,MAXNUM+1)	Shell thickness at local element node 1
HH(2,MAXNUM+1)	Shell thickness at local element node 2
⋮	⋮
HH(8,MAXNUM+1)	Shell thickness at local element node 8

Card 1b (only for 9- and 16-noded elements, if KA=4):

HH(9,MAXNUM+1)	Shell thickness at local element node 9
⋮	⋮

Card 1c (only if IANGL=2):

ANGM(1)	Reference angle at local element node 1
ANGM(2)	Reference angle at local element node 2
ANGM(3)	Reference angle at local element node 3
ANGM(4)	Reference angle at local element node 4

Card 1c (only if IANGL=4):

ANGM(1)	Reference angle at local element node 1
ANGM(2)	Reference angle at local element node 2
⋮	⋮
ANGM(8)	Reference angle at local element node 8

Card 1d (only for 9- and 16-noded elements, if IANGL=4):

ANGM(9)	Reference angle at local element node 9
⋮	⋮

Notes:

(1) For MTYP the number of the corresponding laminate, defined in the *Laminate Setup Block* (NLFC), has to be entered.

(2) IPS controls the stress/strain output locations within the element. The input to IPS consists of a number containing 3 digits. The last digit controls the increment of layer output, the second digit controls the increment in s-direction, and the first digit controls the increment in r-direction for output.
For IPS=1xx stresses/strains of all integration points in r-direction are printed.
For IPS=2xx, =3xx, etc. stresses/strains of every 2^{nd}, 3^{rd}, etc. integration point in r-direction are printed.
For IPS=x1x, =x2x, etc. the same syntax as described above for the r-direction is used for the s-direction.
For IPS=xx1 stresses/strains of all layers are printed.
For IPS=xx2, =xx3, etc. stresses/strains of every 2^{nd}, 3^{rd}, etc. layer are printed.

(3) KG is used for element information generation. For KG>0, information between the element data card where KG is initially entered, and the following element data card is automatically generated. Element data sets $e, e + \text{KG}, e + 2 * \text{KG}, \ldots$ are generated with all data defined in the initial set of the generation sequence (element e).

(4) For KA=0, shell thickness is constant throughout the element. Thickness is defined as the sum of the layer thicknesses given in the *Laminate Setup Block*.
For KA=2, bilinear variation of element thickness is assumed. For this purpose, an additional card 1a is required which contains the shell thicknesses at the corner nodes of the element. Thus, layer thicknesses defined in the *Laminate Setup Block* vary bilinearly, too.
For KA=4, the shape functions (bilinear, biquadratic, bicubic depending on the number of nodes) define the variability of the shell thickness throughout the element. An additional card 1a is required which contains the thicknesses for the first 8 nodes. For elements with more than 8 nodes, a 2^{nd} additional card 1b is required to define the thicknesses for the remaining nodes.

(5) IANGL defines the variation of the angle between the reference axis (for defining the laminate setup) and the local element r-axis.
For IANGL=0, the angle is constant throughout the element, with the value =ANGM1. This is typically used for rectangular elements.
For IANGL=1, the angles are computed from the element geometry and the given angle at the local element node 1 (=ANGM1). This is useful for non-rectangular element corners and curved element edges (the fibers are assumed to be parallel within the shell surface).
For IANGL=2, shape functions are used to interpolated the angles from the values given at the corner nodes. Thus, an additional card 1c is required which contains the nodal information.
For IANGL=4, shape functions are used to interpolated the angles from the values given at all nodes. Thus, an additional card 1c is required which contains the information for the first 8 nodes. For elements with more than 8 nodes, a 2^{nd} additional card 1d is required to define the angles for the remaining nodes.

(6) If the direction cosines are specified in the *NODE section of the input-deck, these directions will be used as initial shell normals, unless the difference between the angles computed from the geometry and the angles computed from the direction cosines is greater than DANG. If used, DANG should be kept small to prevent excessive initial distorsion of the element.

2.2.4 Usable ABAQUS Options

The following is a list of ABAQUS [10] options that can be used in conjunction with the **LCSLFC**-element, some of these have not been tested but they should work without problems:

Nodal Point Data: *NCOPY,*NFILL,*NGEN,*NMAP,*NODE,*NSET,*SYSTEM (not tested), *TRANSFORM (not tested)

Element Data: *ELCOPY,*ELEMENT,*ELGEN,*ELSET,*SLIDE LINE (not tested)

Kinematic Conditions: *BOUNDARY,*EQUATION,*MPC (with restrictions, see note (1))

Miscellaneous: *AMPLITUDE,*RESTART,**,*INITIAL CONDITIONS

Step: *STEP,*ENDSTEP

Procedures: *BUCKLE (modified, see note (2)),*STATIC,*MODEL CHANGE (not tested)

Loading: *CLOAD,*DLOAD (see note (3)),*FIELD, *TEMPERATURE (see note (1) in *Control Data Block*, section 2.2.3)

Prescribed Boundary Conditions: *BOUNDARY

Print and File Output Definitions: *NODE PRINT,*PRINT,*FILE FORMAT,*NODE FILE

Notes:

(1) MPCs have to be used with care due to the fact that the definitions of rotational DOFs for the **LCSLFC**-element are different from the corresponding ABAQUS definitions. MPCs 1,2,6,9,12 restrict the translational DOFs only and, therefore, can be used without problems.

(2) In the **LCSLFC**-element a modified version for computing the buckling loads is implemented, see section 1.4. Therefore, the sequence of *STEPs in the ABAQUS input-deck needed to perform a buckling analysis is a little different than described in the ABAQUS manual [10]: After loading the structure to the load level desired, two *STEPs consisting of the *BUCKLE,DEAD procedure and subsequently the *BUCKLE,LIVE procedure have to be performed. The resulting eigenvalues multiplied by the current load level give estimates for the buckling loads. The eigenmodes are estimates of the buckling modes.

$$\text{buckling load} \approx \text{eigenvalue} \times \text{current load}$$

(3) Currently, 5 different distributed load types are available (see section 1.3.4):

U1 stands for uniform pressure load acting in $-t$ direction (the t direction is defined by the shell surface and the node numbering order, see Fig. 1.1). In the data card of the *DLOAD option the magnitude of the pressure (p) has to be entered.

U2 represents gravity load in $-z$ direction. In the data card of the *DLOAD option the gravity constant (g) has to be entered.

U3–U5 stand for uniform body force in x, y, z direction, respectively. In the data card of the *DLOAD option the magnitude of the body force (b) has to be entered.

2.3 LCSMAT, MATERIAL MODEL INTERFACE

The **LCSLFC**-element provides an interface whereby the user can write his own constitutive model in the subroutine LCSMAT. The material constants that are needed in the subroutine have to be entered in the *Material Data Block* as described in section 2.2.3. If the number of material constants exceeds 8, then the parameter NCON has be adjusted accordingly in the subroutine LCSPAR.

Most constitutive models require the storage of solution dependent variables (plastic strains, failure parameter, etc.). The array WA(NLWA) can be used for this purpose; the length NLWA of this array has to be set in the subroutine LCSPAR.

The interface to the subroutine LCSMAT is simple. When it is called, it is provided with the material data, the state at the beginning of the increment (local strains, temperature, solution dependent variables), the current local strains and the temperature at the end of the increment. The subroutine must perform two functions: it must compute the current local stresses, and it must provide the current material matrix (it must also update the solution dependent variables, if used).

LCSMAT will be called at each material calculation point of the shell, i.e. the 2/d numerical integration points (Gauss-points), at the top and bottom of each layer. The sample subroutine LCSMAT for linear elastic fiber and matrix materials is included in the **LCSLFC**-program. The subroutine D3MMC represents an application of the material model interface (with some small modifications).

Interface cards:

```
      SUBROUTINE LCSMAT (EEPSL,EEPSL0,WA,NLWA,PROP,NCON,ALFT,EMAT,
     1                   STRES0,STRESS,TEMP0,TEMP,IINP)
C
      IMPLICIT REAL*8 (A-H,O-Z)
C
      DIMENSION EEPSL(5),EEPSL0(5),WA(NLWA),PROP(NCON),ALFT(5),
     1          EMAT(5,5),STRES0(5),STRESS(5)

   user coding...

      RETURN
      END
```

Variables to be defined:

EMAT(5,5) represents the current material stiffness matrix $\underset{\approx}{\mathbf{E}}_L$ of the constitutive model for modified plane stress conditions (no thickness normal stress, but transverse shear stresses and strains), defined in the local l, q, t coordinate system. All entities have to be specified. However, an unsymmetric constitutive model will not be treated correctly because the global stiffness matrix is computed assuming symmetry.

$$\underset{\approx}{\mathbf{E}}_L = \begin{pmatrix} E_{llll} & E_{llqq} & E_{lllq} & E_{lllt} & E_{llqt} \\ E_{qqll} & E_{qqqq} & E_{qqlq} & E_{qqlt} & E_{qqqt} \\ E_{lqll} & E_{lqqq} & E_{lqlq} & E_{lqlt} & E_{lqqt} \\ E_{ltll} & E_{ltqq} & E_{ltlq} & E_{ltlt} & E_{ltqt} \\ E_{qtll} & E_{qtqq} & E_{qtlq} & E_{qtlt} & E_{qtqt} \end{pmatrix}$$

with l...fiber direction,
q...inplane transverse direction,
t...thickness direction.

STRESS(5) stand the current stresses that correspond to the current strains (EEPSL) and the current state of the solution dependent variables (WA). If thermal load is applied (KTEMP=1), thermal stresses for temperature at the end of the increment (→ TEMP) have to be included.

$$\underset{\sim}{\sigma}_L = \begin{pmatrix} \sigma_{ll} \\ \sigma_{qq} \\ \tau_{lq} \\ \tau_{lt} \\ \tau_{qt} \end{pmatrix}$$

STRESO(5) (need only be defined if thermal load is applied, i.e. KTEMP=1) symbolize the current stresses that correspond to the current strains (EEPSL) and the current state of the solution dependent variables (WA) including thermal stresses for temperature at the beginning of the increment (→ TEMPO).

WA(NLWA) represents the array of solution dependent state variables. The values at the beginning of the increment are transferred to the subroutine and they have to be updated to the current values. The size of the array NLWA is defined in the subroutine LCSPAR.

Variables passed in for information:

EEPSL(5) represent the current strains in local (fiber fixed) coordinate system.

$$\underline{\varepsilon}_L = \begin{pmatrix} \varepsilon_{ll} \\ \varepsilon_{qq} \\ \gamma_{lq} \\ \gamma_{lt} \\ \gamma_{qt} \end{pmatrix}$$

EEPSLO(5) stand for the strains in local (fiber fixed) coordinate system at the beginning of the increment.

NLWA indicates the number of solution dependent state variables.

PROP(NCON) symbolizes the array of material constants entered in the *Material Data Block*.

NCON represents the number of material constants.

ALFT(5) stands for the array of coefficients of linear thermal expansion entered in the *Material Data Block*.

TEMP indicates the current temperature.

TEMPO symbolizes the temperature at the beginning of the increment.

IINP stands for the flag that defines the state of the analysis:
IINP=0...first call of LCSMAT at this point
IINP=-1...subsequent calls

2.4 RUNNING ABAQUS WITH THE LCSLFC-ELEMENT

The **LCSLFC**-element can work in conjunction with some ABAQUS elements. However, special care is needed with the rotational DOFs due to their different definitions in ABAQUS and the **LCSLFC** program, respectively.

To run ABAQUS and the **LCSLFC**-element together the standart command ABAQUS (this calls the ABAQUS command file ABAQUS.COM) can be used. However, to get proper file handling, some modifications prove necessary. The sample command file ABQ8.COM

includes all these changes. In order to run ABQ8.COM, the compiled LCSLFC program has to exist in the working directory. By typing @ABQ8 the program can be started.

The material and element information for the **LCSLFC**-element is printed on the ABAQUS .DAT file. The stresses and strains are printed on a seperate file called *file*.STR.

Plotting is not supported by ABAQUS version 4-8. However, all the necessary statements for version 5 (which is expected to support UEL-element plotting) are already included in the **LCSLFC** code. Meanwhile, an auxiliary program (PLOTA) has to be used to extract plotting data:

Once PLOTA has been started, it will request the ABAQUS .DAT filename. After the filename has been entered, PLOTA searches through this file for element connectivities and nodal displacements. Then it creates a .GEO file, which contains the nodal coordinates and the element connectivities and a .DIS file for each set of displacements. These data are formatted for use with the post processing program MOVIE.BYU (version 5).

PLOTA will not create a .GEO file, unless all the element information is included in the ABAQUS .DAT file. E.g. .DAT files from restart analyses do not contain all element information. The same can happen if the *PREPRINT option has been used.

In addition, PLOTA can be used to create imperfect geometries that can be applied for post buckling analyses:
After the filename has been entered, PLOTA will request a scaling factor. If this number is not zero, the displacements, multiplied by this factor are added to the initial (perfect) geometry. This modified geometry is then printed onto the .GEO file (formatted for use in an ABAQUS .INP file).

3. VERIFICATION EXAMPLES

3.1 PRESSURE LOADED THICK SQUARE PLATE

A simply supported thick three-layer cross-ply square plate which is subject to a sinusoidal pressure load is used to demonstrate the accuracy of the **LCSLFC**-element. Both the exact solutions and FE results [12,13] have been used for comparison.

Lay-up: [0/90/0]...three layer cross-ply, shell thickness $h = 1$ in.

Material: as specified in [12]

E_l =25000 kpsi	E_q =1000 kpsi	ν_{ql} =0.25
G_{lq} = 500 kpsi	G_{lt} = 500 kpsi	G_{qt} = 200 kpsi

Model: A quarter of the plate has been modelled by four 16-node **LCSLFC**-elements. Width of the square $a = 4$ in. Symmetry conditions: along the $x-$symmetry line $\Delta v^{(k)}$, $\Delta\varphi^{(k)}$, $\Delta\varphi_n^{(k)}$ $(n = 1,\ldots,N-1)$ have been set to zero, and along the $y-$symmetry line $\Delta u^{(k)}$, $\Delta\psi^{(k)}$, $\Delta\psi_n^{(k)}$ $(n = 1,\ldots,N-1)$ have been set to zero. The 0° layers have been divided into two sub-layers to trace the variation of transverse shear within the layers.

Distributed load:

$$q(x,y) = q_0 \sin(\pi x/a)\sin(\pi y/a)$$
$$q_0 = (\pi/a)^2$$

For comparison purposes, the following normalized quantities have been used:

$$\overline{u} = \frac{100E_q h^2}{q_0 a^3}u \qquad \overline{w} = \frac{100E_q h^3}{q_0 a^4}w \qquad \overline{z} = z/h$$
$$(\overline{\sigma}_x, \overline{\sigma}_y) = \frac{h^2}{q_0 a^2}(\sigma_x, \sigma_y) \qquad (\overline{\tau}_{xz}, \overline{\tau}_{yz}) = \frac{h}{q_0 a}(\tau_{xz}, \tau_{yz})$$

Since nonlinear effects are not taken into account in [12], only a linear load step has been performed. Figs. 3.1 to 3.3 show the through-the-thickness distribution of both the normalized inplane displacements $\overline{u}$ and the normalized stresses $\overline{\sigma}_x, \overline{\tau}_{xz}$ at specific locations. Analytical solutions and the results from classical laminate theory (CLT) are also given in these figures. Very good agreement can be observed between the **LCSLFC**-element and the analytical solution despite the fact, that this "plate" resembles a solid brick rather than a plate (the element length to thickness ratio is 1:1!).

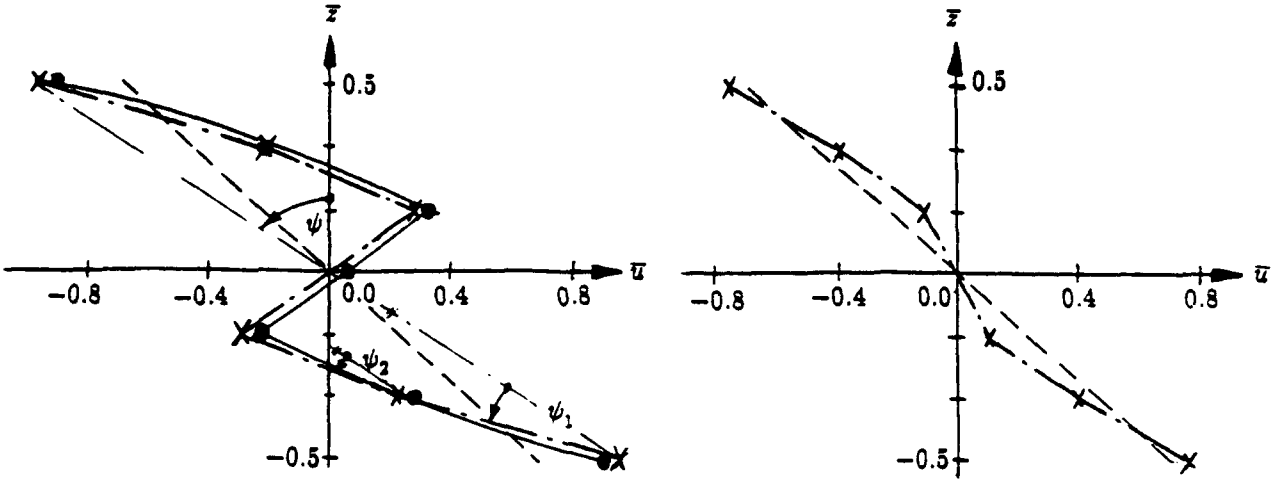

Fig. 3.1 Thickness distribution of normalized inplane displacements $\bar{u}$ of a thick cross-ply square plate at $x = 0, y = \frac{a}{2}$ for $h = 1.0$ and $h = 0.4$

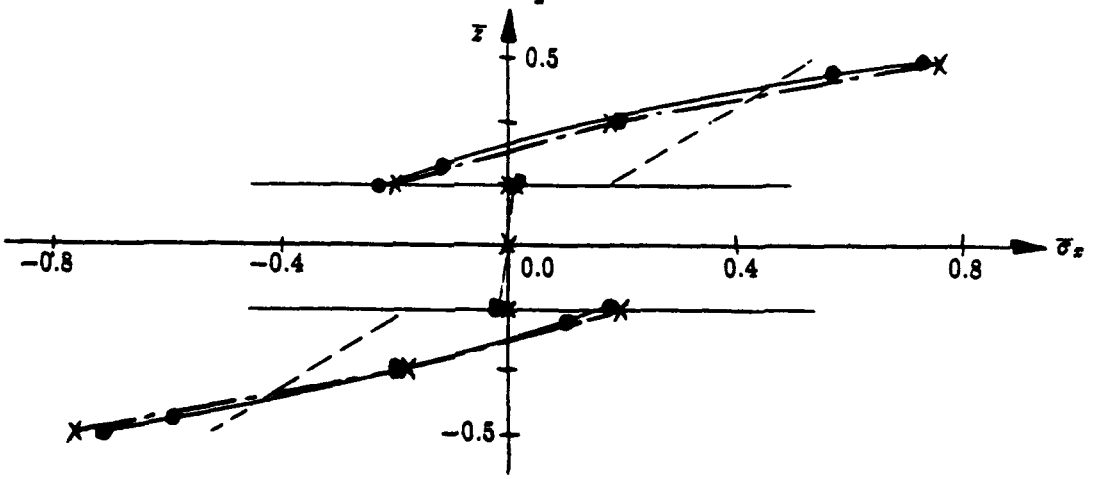

Fig. 3.2 Thickness distribution of normalized in-plane normal stresses $\bar{\sigma}_x$ at the center of a thick cross-ply square plate $(x = \frac{a}{2}, y = \frac{a}{2})$ for $h = 1.0$

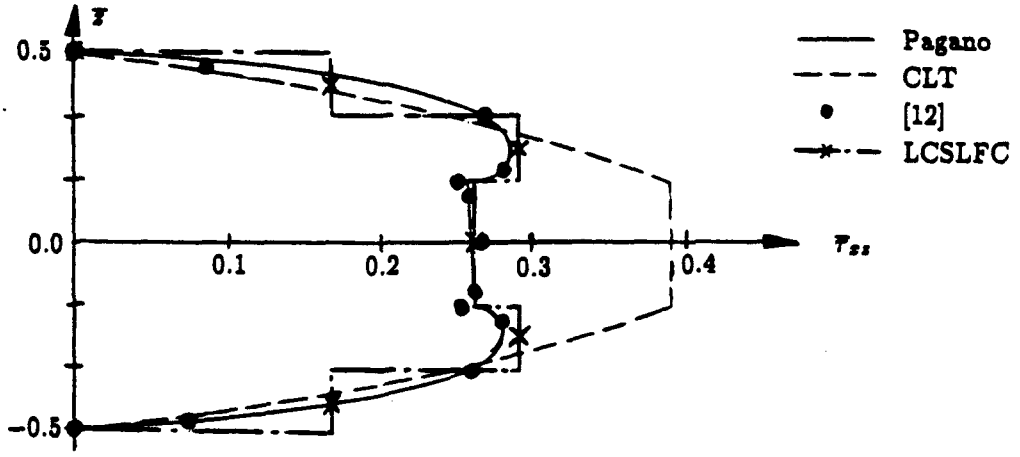

Fig. 3.3 Thickness distribution of normalized transverse shear stresses $\bar{\tau}_{xz}$ of a thick cross-ply square plate at $x = 0, y = \frac{a}{2}$ for $h = 1.0$

The same computation has been performed with a different shell thickness ($h = 0.4$) in order to investigate the importance of transverse shear. As one would expect, the differences between the classical lamination theory and more advanced methods (like the **LCSLFC**-element) become less pronounced as the thickness of the shell decreases, see Fig. 3.1. Table 3.1 lists some stresses and displacements for this case together with analytical results and other FE results.

Table 3.1: Normalized stresses and displacements for $h = 0.4$

	$\overline{\sigma}_x(\frac{a}{2}, \frac{a}{2}, \pm\frac{h}{2})$	$\overline{\sigma}_y(\frac{a}{2}, \frac{a}{2}, \pm\frac{h}{6})$	$\overline{\tau}_{xz}(0, \frac{a}{2}, 0)$	$\overline{\tau}_{yz}(\frac{a}{2}, 0, 0)$	$\overline{w}(\frac{a}{2}, \frac{a}{2}, 0)$
Pagano	± 0.590	$+0.285$ -0.288	$+0.357$	$+0.1228$	$+0.7530$
[12]	$+0.5884$ -0.5879	$+0.2834$ -0.2873	$+0.3627$	$+0.1284$	$+0.7531$
LCSLFC-element	$+0.590$ -0.586	$+0.285$ -0.283	$+0.364$	$+0.1079$	$+0.7559$

These results clearly indicate that the **LCSLFC**-element is capable of handling thick laminated shell problems with high accuracy.

3.2 CYLINDRICAL BENDING OF A PLATE STRIP

A two-layer cross-ply plate strip subject to a distributed normal load [14] has been used to investigate the influence of stacking sequence, geometrical nonlinearities and boundary conditions on the mechanical behavior of laminated plates.

Lay-up: [0/90]... two layer cross-ply, layer thickness = 0.2 in.

Material: as specified in [14]

E_l =20000 kpsi	E_q =1400 kpsi	$\nu_{ql} = 0.3$
G_{lq} = 700 kpsi	G_{lt} = 700 kpsi	G_{qt} =700 kpsi

Model: The plate strip has been modelled by four 16-node **LCSLFC**-elements; length of the strip $l = 18$ in., width $b = 3$ in. Both ends of the strip have been pinned. Each layer has been divided into two sub-layers to ensure an accurate representation of the variation of transverse shear within the layers.

Different types of meshes have been tested to evaluate the robustness of the **LCSLFC**-element. Even with an aspect ratio (length to width) of 11:1 very accurate results have been obtained.

For comparison purposes the shell normals have been forced to remain straight. This was accomplished by setting the rotational DOFs $\Delta\varphi_1^{(k)}$ $\Delta\psi_1^{(k)}$ to zero. Excellent agreement with the investigations in [14] have been obtained, see Fig. 3.4.

For simply supported ends, the magnitude of the displacements is independent of the sign of the applied load, because the plate strip is essentially in pure bending, see [14]. Due to the pinned ends of the strip in this study, in-plane stiffnesses are activated as soon as out of plane deflections occur (geometrically nonlinear effect) and, therefore, quite different results are obtained for positive and negative load directions (which can be translated into a reversed stacking sequence), respectively, see Fig. 3.4. For a detailed explanation of this phenomenon see [14].

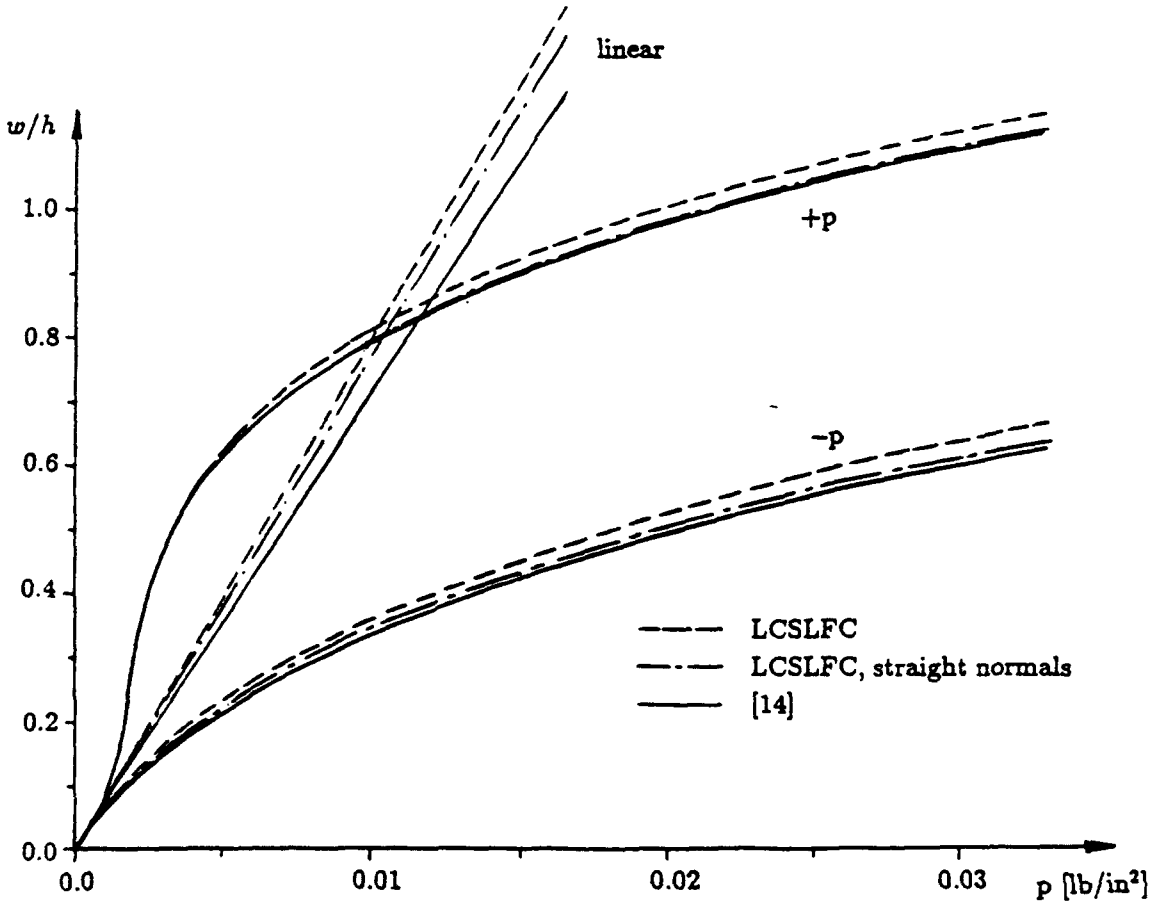

Fig. 3.4 Load-displacement path of a pinned two-layer cross-ply plate strip subject to a distributed normal load

Relaxing the boundary condition on the shell normals, which allows them to deform layerwise linearly (therefore having a more realistic model), results in somewhat larger deformationsi, as can be seen in Fig. 3.4. This indicates that transverse shear does not play a significant role in this rather thin shell application.

3.3 THERMALLY LOADED SQUARE PLATE

In order to show the thermoelastic capability of the **LCSLFC**-element a uniform temperature rise has been applied to a simply supported composite square plate. To verify the results, comparative investigations with ABAQUS shell elements have been undertaken. The following properties have been chosen:

Lay-up: [0/90]...two layer cross-ply, layer thickness = 0.2 mm

Material: Graphite/Epoxy

$E_l = 127.5\,kN/mm^2$	$E_q = 11.0\,kN/mm^2$	$\nu_{ql} = 0.35$
$G_{lq} = 5.5\,kN/mm^2$	$G_{lt} = 5.5\,kN/mm^2$	$G_{qt} = 4.6\,kN/mm^2$
$\alpha_l = -0.08\times10^{-5}\,°C^{-1}$	$\alpha_q = 2.90\times10^{-5}\,°C^{-1}$	

Model: The whole plate has been modelled by sixteen 16-node **LCSLFC**-elements, the width of the square is 300 mm; all edges were restricted to remain straight.

Fig. 3.5 shows the nonlinear load-displacement path as well as an estimate curve for the buckling load.

Because of the constant temperature rise all over the plate and the simply supported edges, no stability problem would be expected for a homogeneous isotropic plate. But, due to anisotropies occuring in the laminate, a linear buckling analysis (i.e. a buckling analysis after a very small load step, $\overline{\vartheta} = 1°C$) yields a bifurcation point at ${}^{*}\overline{\vartheta} = 4°C$. However, a detailed analysis of the buckling behavior indicates that the nonlinear pre-buckling deformations make the results of the linear buckling analysis rather meaningless. As can be seen from the estimate-curve in Fig. 3.5, the estimates of the relevant buckling mode change during the incremental increase of the temperature and the critical temperature is approximately 50 times higher than the corresponding value of the linear buckling analysis!

The comparison with the ABAQUS element has shown excellent agreement in the displacements. However, it has not been possible to compute the detailed buckling behav-

ior by using the ABAQUS elements. No convergence or only negative results have been obtained during the eigenvalue extraction. Using the **LCSLFC**-element buckling loads and buckling modes have been successfully computed by employing the modified buckling procedure described in section 1.4.

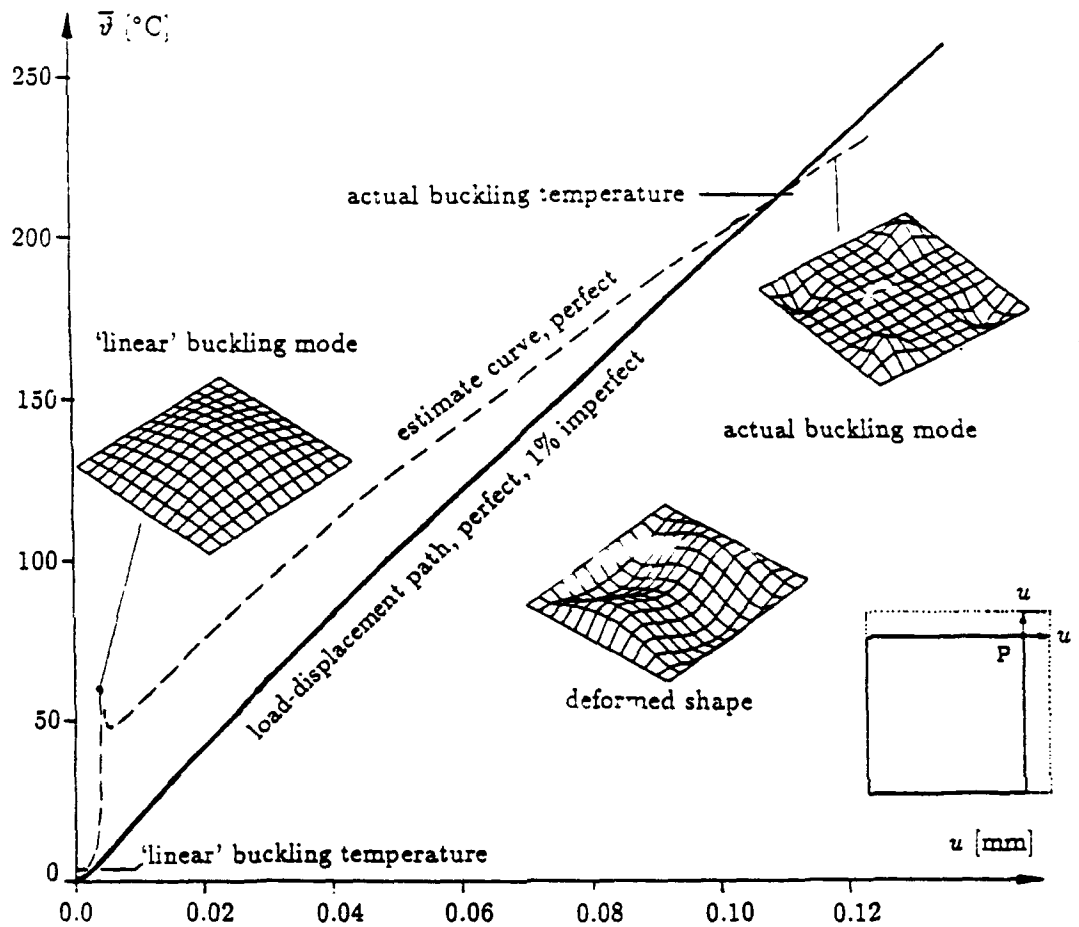

Fig. 3.5 Load-displacement path and estimate-curve for buckling load of a two layer cross-ply square plate

ACKNOWLEDGEMENT

The financial support of this project by the Fonds zur Förderung der wissenschaftlichen Forschung (Erwin Schrödinger Stipendium) is gratefully acknowledged.

REFERENCES

[1] E. Ramm, 'A Plate/Shell Element for Large Deflections and Rotations', *Formulations and Computational Algorithms in Finite Element Analysis*, Ed. K.J. Bathe, J.T. Owen, W. Wunderlich, Proc. U.S.-German Symp., MIT, Cambridge, 1977.

[2] K.J. Bathe, *Finite Element Procedures in Engineering Analysis*, Prentice-Hall, Englewood Cliffs, NJ, 1982.

[3] K. Dorninger, *Entwicklung von nichtlinearen FE-Algorithmen zur Berechnung von Schalenkonstruktionen aus Faserverbundstoffen*, Fortschritt-Berichte, VDI Reihe 18, Nr. 65, VDI Verlag, Duesseldorf, FRG, 1989.

[4] C.-M. Huang, D.C. Lagoudas, *A Fortran Program for Effective Properties of Composite Materials Based on the Mori-Tanaka Scheme*, Department of Mechanical Engineering and Mechanics and Department of Civil Engineering, Rensselaer Polytechnic Institute, Troy, NY, 1990.

[5] G.J. Dvorak, Y.A. Bahei-El-Din, 'Plasticity Analysis of Fibrous Composites', Journal of Applied Mechanics **49**, 327-335 (1982).

[6] A.J. Svobodnik, *Numerical Treatment of the Elastic-Plastic Macromechanical Behavior of Longfiber-Reinforced Metal Matrix Composites*, Dissertation, Vienna Technical University, Vienna, Austria, 1990.

[7] G.M. Stanley, *Continuum-Based Shell Elements*, Dissertation, Stanford University, Stanford, CA, 1985.

[8] E. Ramm, A. Matzenmiller, 'Large Deformation Shell Analysis Based on the Degeneration Concept', *State-of-the-Art Texts on FEM for Plate and Shell Structures*, Eds. T.J.R. Hughes, E. Hinton, Pineridge Press, Swansea, UK, 1986.

[9] G. Laschet, J.P. Jeusette and P. Beckers, 'Homogenization and Pre-Integration Techniques for Multilayer Composites and Sandwich Finite Element Models', Int. J. Num. Meths. Eng. **27**, 257–269 (1989).

[10] *ABAQUS Version 4-8 User's Manual*, Hibbit, Karlsson & Sorensen Inc., Providence, RI, 1989.

[11] F.G. Rammerstorfer, 'Jump Phenomena Associated with the Stability of Geometrically Nonlinear Structures', *Recent Advances in Non-Linear Computational Mechanics*, Eds. E. Hinton, D.R.J. Owen, C. Taylor, Pineridge Press, Swansea, UK, 1982.

[12] H.-S. Jing, M.-L. Liao, 'Partial Hybrid Stress Element for the Analysis of Thick Laminated Composite Plates', Int. J. Num. Meths. Eng. **28**, 2813–2827 (1989).

[13] Z.H. Li, D.R.J. Owen, 'Elastic-Plastic Analysis of Laminated Anisotropic Shells by a Refined Finite Element Laminated Model', Computers & Structures **32**, No. 5, 1005–1024 (1989).

[14] J.N. Reddy,'On Refined Computational Models of Composite Laminates', Int. J. Num. Meths. Eng. **27**, 361–382 (1989).

[15] T.R. Tauchert, 'Thermal Stresses in Plates – Statical Problems', *Thermal Stresses I*, Ed. R.B. Hetnarski, North-Holland, Amsterdam, 1986.

Appendix

Jacobian matrix:

$$\underset{\approx}{\mathrm{J}} = \begin{pmatrix} x_{n,r} & x_{n,s} & x_{n,t} \\ y_{n,r} & y_{n,s} & y_{n,t} \\ z_{n,r} & z_{n,s} & z_{n,t} \end{pmatrix} \tag{A1}$$

with

$$\begin{aligned} x_{n,j} &= \sum_{k=1}^{M} \phi_{,j}^{(k)} [x_n^{(k)} + t\, \mathrm{h}_n^{(k)} \cos \Psi_n^{(k)}] \\ y_{n,j} &= \sum_{k=1}^{M} \phi_{,j}^{(k)} [y_n^{(k)} + t\, \mathrm{h}_n^{(k)} \sin \Psi_n^{(k)} \cos \Phi_n^{(k)}] \qquad j = r, s \\ z_{n,j} &= \sum_{k=1}^{M} \phi_{,j}^{(k)} [z_n^{(k)} + t\, \mathrm{h}_n^{(k)} \sin \Psi_n^{(k)} \sin \Phi_n^{(k)}] \\ x_{n,t} &= \sum_{k=1}^{M} \phi^{(k)} [\mathrm{h}_n^{(k)} \cos \Psi_n^{(k)}] \\ y_{n,t} &= \sum_{k=1}^{M} \phi^{(k)} [\mathrm{h}_n^{(k)} \sin \Psi_n^{(k)} \cos \Phi_n^{(k)}] \\ z_{n,t} &= \sum_{k=1}^{M} \phi^{(k)} [\mathrm{h}_n^{(k)} \sin \Psi_n^{(k)} \sin \Phi_n^{(k)}] \end{aligned} \tag{A2}$$

Displacement derivatives:

Total displacements:

$$\begin{aligned} u_{n,j} &= \overline{u}_{n,j} + t\, \widehat{u}_{n,j} \\ v_{n,j} &= \overline{v}_{n,j} + t\, \widehat{v}_{n,j} \qquad j = x, y, z \\ w_{n,j} &= \overline{w}_{n,j} + t\, \widehat{w}_{n,j} \end{aligned} \tag{A3}$$

with

$$\begin{aligned} \overline{u}_{n,j} &= \sum_{k=1}^{M} \left[\phi_{,j}^{(k)}\, u_n^{(k)} + \phi^{(k)}\, t_{,j}\, \mathrm{h}_n^{(k)} (\cos \Psi_n^{(k)} - \cos^0 \Psi_n^{(k)}) \right] \\ \overline{v}_{n,j} &= \sum_{k=1}^{M} \left[\phi_{,j}^{(k)}\, v_n^{(k)} + \phi^{(k)}\, t_{,j}\, \mathrm{h}_n^{(k)} (\sin \Psi^{(k)} \cos \Phi_n^{(k)} - \sin^0 \Psi_n^{(k)} \cos^0 \Phi_n^{(k)}) \right] \\ \overline{w}_{n,j} &= \sum_{k=1}^{M} \left[\phi_{,j}^{(k)}\, w_n^{(k)} + \phi^{(k)}\, t_{,j}\, \mathrm{h}_n^{(k)} (\sin \Psi^{(k)} \sin \Phi_n^{(k)} - \sin^0 \Psi_n^{(k)} \sin^0 \Phi_n^{(k)}) \right] \end{aligned} \tag{A4}$$

and

$$\widehat{u}_{n,j} = \sum_{k=1}^{M} \phi_{,j}^{(k)} \mathrm{h}_n^{(k)} (\cos \Psi_n^{(k)} - \cos^0 \Psi_n^{(k)})$$

$$\widehat{v}_{n,j} = \sum_{k=1}^{M} \phi_{,j}^{(k)} \mathrm{h}_n^{(k)} (\sin \Psi_n^{(k)} \cos \Phi_n^{(k)} - \sin^0 \Psi_n^{(k)} \cos^0 \Phi_n^{(k)}) \qquad (A5)$$

$$\widehat{w}_{n,j} = \sum_{k=1}^{M} \phi_{,j}^{(k)} \mathrm{h}_n^{(k)} (\sin \Psi_n^{(k)} \sin \Phi_n^{(k)} - \sin^0 \Psi_n^{(k)} \sin^0 \Phi_n^{(k)})$$

where

$$\phi_{,j}^{(k)} = \phi_{,r}^{(k)} \, r_{,j} + \phi_{,s}^{(k)} \, s_{,j} \qquad (A6)$$

$r_{,j}, s_{,j}, t_{,j}$ correspond to the elements of the inverse of the Jacobian matrix $\underset{\approx}{\mathbf{J}}$ and ${}^0\Phi_n^{(k)}, {}^0\Psi_n^{(k)}$ are the angles of normal of the initial geometry.

Incremental displacements:

$$\begin{aligned} \Delta u_{n,j} &= \Delta \overline{u}_{n,j} + t \, \Delta \widehat{u}_{n,j} \\ \Delta v_{n,j} &= \Delta \overline{v}_{n,j} + t \, \Delta \widehat{v}_{n,j} \qquad\qquad j = x, y, z \\ \Delta w_{n,j} &= \Delta \overline{w}_{n,j} + t \, \Delta \widehat{w}_{n,j} \end{aligned} \qquad (A7)$$

with

$$\Delta \overline{u}_{n,j} = \sum_{k=1}^{M} \left[\phi_{,j}^{(k)} \, \Delta u_n^{(k)} + \phi^{(k)} \, t_{,j} \, \mathrm{h}_n^{(k)} (\mathrm{g}_x^{(k)} \Delta \overline{\varphi}_n^{(k)} + \overline{\mathrm{g}}_x^{(k)} \Delta \overline{\psi}_n^{(k)}) \right]$$

$$\Delta \overline{v}_{n,j} = \sum_{k=1}^{M} \left[\phi_{,j}^{(k)} \, \Delta v_n^{(k)} + \phi^{(k)} \, t_{,j} \, \mathrm{h}_n^{(k)} (\mathrm{g}_y^{(k)} \Delta \overline{\varphi}_n^{(k)} + \overline{\mathrm{g}}_y^{(k)} \Delta \overline{\psi}_n^{(k)}) \right] \qquad (A8)$$

$$\Delta \overline{w}_{n,j} = \sum_{k=1}^{M} \left[\phi_{,j}^{(k)} \, \Delta w_n^{(k)} + \phi^{(k)} \, t_{,j} \, \mathrm{h}_n^{(k)} (\mathrm{g}_z^{(k)} \Delta \overline{\varphi}_n^{(k)} + \overline{\mathrm{g}}_z^{(k)} \Delta \overline{\psi}_n^{(k)}) \right]$$

and

$$\Delta \widehat{u}_{n,j} = \sum_{k=1}^{M} \phi_{,j}^{(k)} \mathrm{h}_n^{(k)} (\mathrm{g}_x^{(k)} \Delta \overline{\varphi}_n^{(k)} + \overline{\mathrm{g}}_x^{(k)} \Delta \overline{\psi}_n^{(k)})$$

$$\Delta \widehat{v}_{n,j} = \sum_{k=1}^{M} \phi_{,j}^{(k)} \mathrm{h}_n^{(k)} (\mathrm{g}_y^{(k)} \Delta \overline{\varphi}_n^{(k)} + \overline{\mathrm{g}}_y^{(k)} \Delta \overline{\psi}_n^{(k)}) \qquad (A9)$$

$$\Delta \widehat{w}_{n,j} = \sum_{k=1}^{M} \phi_{,j}^{(k)} \mathrm{h}_n^{(k)} (\mathrm{g}_z^{(k)} \Delta \overline{\varphi}_n^{(k)} + \overline{\mathrm{g}}_z^{(k)} \Delta \overline{\psi}_n^{(k)})$$

where

$$
\begin{aligned}
\mathrm{g}_x^{(k)} &= 0 & \overline{\mathrm{g}}_x^{(k)} &= -\sin\Psi_n^{(k)} \\
\mathrm{g}_y^{(k)} &= -\sin\Phi_n^{(k)}\sin\Psi_n^{(k)} & \overline{\mathrm{g}}_y^{(k)} &= \cos\Phi_n^{(k)}\cos\Psi_n^{(k)} \\
\mathrm{g}_z^{(k)} &= \cos\Phi_n^{(k)}\sin\Psi_n^{(k)} & \overline{\mathrm{g}}_z^{(k)} &= \sin\Phi_n^{(k)}\cos\Psi_n^{(k)}
\end{aligned}
\tag{A10}
$$

The functions $\mathrm{g}^{(k)}$ and $\overline{\mathrm{g}}^{(k)}$ represent linearizations of the trigonometric functions in Eqs. (A4, A5) at $\Phi_n^{(k)}, \Psi_n^{(k)}$ with respect to the incremental rotations $\Delta\overline{\varphi}_n^{(k)}, \Delta\overline{\psi}_n^{(k)}$.

Strain-displacement matrices:

Linear strain-displacement matrix:

$$
\underset{\approx}{\mathbf{B}}_I = \overline{\underset{\approx}{\mathbf{B}}}_I + t\,\widehat{\underset{\approx}{\mathbf{B}}}_I \tag{A11}
$$

with

$$
\begin{aligned}
\overline{\underset{\approx}{\mathbf{B}}}_I &= \left(\overline{\underset{\approx}{\mathbf{B}}}_I^{(1)} \quad \overline{\underset{\approx}{\mathbf{B}}}_I^{(2)} \quad \cdots \quad \overline{\underset{\approx}{\mathbf{B}}}_I^{(M)}\right) \\
\widehat{\underset{\approx}{\mathbf{B}}}_I &= \left(\widehat{\underset{\approx}{\mathbf{B}}}_I^{(1)} \quad \widehat{\underset{\approx}{\mathbf{B}}}_I^{(2)} \quad \cdots \quad \widehat{\underset{\approx}{\mathbf{B}}}_I^{(M)}\right)
\end{aligned}
\tag{A12}
$$

where

$$
\overline{\underset{\approx}{\mathbf{B}}}_I^{(k)} = \begin{pmatrix}
\phi_{,x}^{(k)} & 0 & 0 & \mathrm{h}_n^{(k)}\phi^{(k)}\,t_{,x}\,\mathrm{g}_x^{(k)} & \mathrm{h}_n^{(k)}\phi^{(k)}\,t_{,x}\,\overline{\mathrm{g}}_x^{(k)} \\
0 & \phi_{,y}^{(k)} & 0 & \mathrm{h}_n^{(k)}\phi^{(k)}\,t_{,y}\,\mathrm{g}_y^{(k)} & \mathrm{h}_n^{(k)}\phi^{(k)}\,t_{,y}\,\overline{\mathrm{g}}_y^{(k)} \\
0 & 0 & \phi_{,y}^{(k)} & \mathrm{h}_n^{(k)}\phi^{(k)}\,t_{,z}\,\mathrm{g}_z^{(k)} & \mathrm{h}_n^{(k)}\phi^{(k)}\,t_{,z}\,\overline{\mathrm{g}}_z^{(k)} \\
\phi_{,y}^{(k)} & \phi_{,x}^{(k)} & 0 & \mathrm{h}_n^{(k)}\phi^{(k)}[t_{,z}\,\mathrm{g}_y^{(k)} + t_{,y}\,\mathrm{g}_z^{(k)}] & \mathrm{h}_n^{(k)}\phi^{(k)}[t_{,z}\,\overline{\mathrm{g}}_y^{(k)} + t_{,y}\,\overline{\mathrm{g}}_z^{(k)}] \\
\phi_{,z}^{(k)} & 0 & \phi_{,x}^{(k)} & \mathrm{h}_n^{(k)}\phi^{(k)}[t_{,x}\,\mathrm{g}_z^{(k)} + t_{,z}\,\mathrm{g}_x^{(k)}] & \mathrm{h}_n^{(k)}\phi^{(k)}[t_{,x}\,\overline{\mathrm{g}}_z^{(k)} + t_{,z}\,\overline{\mathrm{g}}_x^{(k)}] \\
0 & \phi_{,z}^{(k)} & \phi_{,y}^{(k)} & \mathrm{h}_n^{(k)}\phi^{(k)}[t_{,y}\,\mathrm{g}_z^{(k)} + t_{,z}\,\mathrm{g}_y^{(k)}] & \mathrm{h}_n^{(k)}\phi^{(k)}[t_{,y}\,\overline{\mathrm{g}}_z^{(k)} + t_{,z}\,\overline{\mathrm{g}}_y^{(k)}]
\end{pmatrix}
\tag{A13}
$$

and

$$
\widehat{\underset{\approx}{\mathbf{B}}}_I^{(k)} = \begin{pmatrix}
0 & 0 & 0 & \mathrm{h}_n^{(k)}\phi_{,x}^{(k)}\,\mathrm{g}_x^{(k)} & \mathrm{h}_n^{(k)}\phi_{,x}^{(k)}\,\overline{\mathrm{g}}_x^{(k)} \\
0 & 0 & 0 & \mathrm{h}_n^{(k)}\phi_{,y}^{(k)}\,\mathrm{g}_y^{(k)} & \mathrm{h}_n^{(k)}\phi_{,y}^{(k)}\,\overline{\mathrm{g}}_y^{(k)} \\
0 & 0 & 0 & \mathrm{h}_n^{(k)}\phi_{,z}^{(k)}\,\mathrm{g}_z^{(k)} & \mathrm{h}_n^{(k)}\phi_{,z}^{(k)}\,\overline{\mathrm{g}}_z^{(k)} \\
0 & 0 & 0 & \mathrm{h}_n^{(k)}[\phi_{,x}^{(k)}\,\mathrm{g}_y^{(k)} + \phi_{,y}^{(k)}\,\mathrm{g}_x^{(k)}] & \mathrm{h}_n^{(k)}[\phi_{,x}^{(k)}\,\overline{\mathrm{g}}_y^{(k)} + \phi_{,y}^{(k)}\,\overline{\mathrm{g}}_x^{(k)}] \\
0 & 0 & 0 & \mathrm{h}_n^{(k)}[\phi_{,x}^{(k)}\,\mathrm{g}_z^{(k)} + \phi_{,z}^{(k)}\,\mathrm{g}_x^{(k)}] & \mathrm{h}_n^{(k)}[\phi_{,x}^{(k)}\,\overline{\mathrm{g}}_z^{(k)} + \phi_{,z}^{(k)}\,\overline{\mathrm{g}}_x^{(k)}] \\
0 & 0 & 0 & \mathrm{h}_n^{(k)}[\phi_{,y}^{(k)}\,\mathrm{g}_z^{(k)} + \phi_{,z}^{(k)}\,\mathrm{g}_y^{(k)}] & \mathrm{h}_n^{(k)}[\phi_{,y}^{(k)}\,\overline{\mathrm{g}}_z^{(k)} + \phi_{,z}^{(k)}\,\overline{\mathrm{g}}_y^{(k)}]
\end{pmatrix}
\tag{A14}
$$

Nonlinear strain-displacement matrix:

$$\underset{\approx}{\mathbf{B}}_{nl} = \overline{\underset{\approx}{\mathbf{B}}}_{nl} + t\,\widehat{\underset{\approx}{\mathbf{B}}}_{nl} \tag{A15}$$

with

$$\begin{aligned} \overline{\underset{\approx}{\mathbf{B}}}_{nl} &= \left(\overline{\underset{\approx}{\mathbf{B}}}_{nl}^{(1)} \quad \overline{\underset{\approx}{\mathbf{B}}}_{nl}^{(2)} \quad \cdots \quad \overline{\underset{\approx}{\mathbf{B}}}_{nl}^{(M)}\right) \\ \widehat{\underset{\approx}{\mathbf{B}}}_{nl} &= \left(\widehat{\underset{\approx}{\mathbf{B}}}_{nl}^{(1)} \quad \widehat{\underset{\approx}{\mathbf{B}}}_{nl}^{(2)} \quad \cdots \quad \widehat{\underset{\approx}{\mathbf{B}}}_{nl}^{(M)}\right) \end{aligned} \tag{A16}$$

where

$$\overline{\underset{\approx}{\mathbf{B}}}_{nl}^{(k)} = \begin{pmatrix} \phi_{,x}^{(k)} & 0 & 0 & \mathrm{h}_n^{(k)}\phi^{(k)}\,t_{,x}\,\mathrm{g}_x^{(k)} & \mathrm{h}_n^{(k)}\phi^{(k)}\,t_{,x}\,\overline{\mathrm{g}}_x^{(k)} \\ \phi_{,y}^{(k)} & 0 & 0 & \mathrm{h}_n^{(k)}\phi^{(k)}\,t_{,y}\,\mathrm{g}_x^{(k)} & \mathrm{h}_n^{(k)}\phi^{(k)}\,t_{,y}\,\overline{\mathrm{g}}_x^{(k)} \\ \phi_{,z}^{(k)} & 0 & 0 & \mathrm{h}_n^{(k)}\phi^{(k)}\,t_{,z}\,\mathrm{g}_x^{(k)} & \mathrm{h}_n^{(k)}\phi^{(k)}\,t_{,z}\,\overline{\mathrm{g}}_x^{(k)} \\ 0 & \phi_{,x}^{(k)} & 0 & \mathrm{h}_n^{(k)}\phi^{(k)}\,t_{,x}\,\mathrm{g}_y^{(k)} & \mathrm{h}_n^{(k)}\phi^{(k)}\,t_{,x}\,\overline{\mathrm{g}}_y^{(k)} \\ 0 & \phi_{,y}^{(k)} & 0 & \mathrm{h}_n^{(k)}\phi^{(k)}\,t_{,y}\,\mathrm{g}_y^{(k)} & \mathrm{h}_n^{(k)}\phi^{(k)}\,t_{,y}\,\overline{\mathrm{g}}_y^{(k)} \\ 0 & \phi_{,z}^{(k)} & 0 & \mathrm{h}_n^{(k)}\phi^{(k)}\,t_{,z}\,\mathrm{g}_y^{(k)} & \mathrm{h}_n^{(k)}\phi^{(k)}\,t_{,z}\,\overline{\mathrm{g}}_y^{(k)} \\ 0 & 0 & \phi_{,x}^{(k)} & \mathrm{h}_n^{(k)}\phi^{(k)}\,t_{,x}\,\mathrm{g}_z^{(k)} & \mathrm{h}_n^{(k)}\phi^{(k)}\,t_{,x}\,\overline{\mathrm{g}}_z^{(k)} \\ 0 & 0 & \phi_{,y}^{(k)} & \mathrm{h}_n^{(k)}\phi^{(k)}\,t_{,y}\,\mathrm{g}_z^{(k)} & \mathrm{h}_n^{(k)}\phi^{(k)}\,t_{,y}\,\overline{\mathrm{g}}_z^{(k)} \\ 0 & 0 & \phi_{,z}^{(k)} & \mathrm{h}_n^{(k)}\phi^{(k)}\,t_{,z}\,\mathrm{g}_z^{(k)} & \mathrm{h}_n^{(k)}\phi^{(k)}\,t_{,z}\,\overline{\mathrm{g}}_z^{(k)} \end{pmatrix} \tag{A17}$$

and

$$\widehat{\underset{\approx}{\mathbf{B}}}_{nl}^{(k)} = \begin{pmatrix} 0 & 0 & 0 & \mathrm{h}_n^{(k)}\phi_{,x}^{(k)}\,\mathrm{g}_x^{(k)} & \mathrm{h}_n^{(k)}\phi_{,x}^{(k)}\,\overline{\mathrm{g}}_x^{(k)} \\ 0 & 0 & 0 & \mathrm{h}_n^{(k)}\phi_{,y}^{(k)}\,\mathrm{g}_x^{(k)} & \mathrm{h}_n^{(k)}\phi_{,y}^{(k)}\,\overline{\mathrm{g}}_x^{(k)} \\ 0 & 0 & 0 & \mathrm{h}_n^{(k)}\phi_{,z}^{(k)}\,\mathrm{g}_x^{(k)} & \mathrm{h}_n^{(k)}\phi_{,z}^{(k)}\,\overline{\mathrm{g}}_x^{(k)} \\ 0 & 0 & 0 & \mathrm{h}_n^{(k)}\phi_{,x}^{(k)}\,\mathrm{g}_y^{(k)} & \mathrm{h}_n^{(k)}\phi_{,x}^{(k)}\,\overline{\mathrm{g}}_y^{(k)} \\ 0 & 0 & 0 & \mathrm{h}_n^{(k)}\phi_{,y}^{(k)}\,\mathrm{g}_y^{(k)} & \mathrm{h}_n^{(k)}\phi_{,y}^{(k)}\,\overline{\mathrm{g}}_y^{(k)} \\ 0 & 0 & 0 & \mathrm{h}_n^{(k)}\phi_{,z}^{(k)}\,\mathrm{g}_y^{(k)} & \mathrm{h}_n^{(k)}\phi_{,z}^{(k)}\,\overline{\mathrm{g}}_y^{(k)} \\ 0 & 0 & 0 & \mathrm{h}_n^{(k)}\phi_{,x}^{(k)}\,\mathrm{g}_z^{(k)} & \mathrm{h}_n^{(k)}\phi_{,x}^{(k)}\,\overline{\mathrm{g}}_z^{(k)} \\ 0 & 0 & 0 & \mathrm{h}_n^{(k)}\phi_{,y}^{(k)}\,\mathrm{g}_z^{(k)} & \mathrm{h}_n^{(k)}\phi_{,y}^{(k)}\,\overline{\mathrm{g}}_z^{(k)} \\ 0 & 0 & 0 & \mathrm{h}_n^{(k)}\phi_{,z}^{(k)}\,\mathrm{g}_z^{(k)} & \mathrm{h}_n^{(k)}\phi_{,z}^{(k)}\,\overline{\mathrm{g}}_z^{(k)} \end{pmatrix} \tag{A18}$$

Stress-integrals:

$$\underset{\sim}{S} = \begin{pmatrix} S_{xx} \\ S_{yy} \\ S_{zz} \\ S_{xy} \\ S_{xz} \\ S_{yz} \end{pmatrix} \qquad \underset{\approx}{\mathbf{S}} = \begin{pmatrix} S_{xx} & S_{xy} & S_{xz} & & & & & & \\ S_{xy} & S_{yy} & S_{yz} & & \underset{\approx}{0} & & & \underset{\approx}{0} & \\ S_{xz} & S_{yz} & S_{zz} & & & & & & \\ & & & S_{xx} & S_{xy} & S_{xz} & & & \\ & \underset{\approx}{0} & & S_{xy} & S_{yy} & S_{yz} & & \underset{\approx}{0} & \\ & & & S_{xz} & S_{yz} & S_{zz} & & & \\ & & & & & & S_{xx} & S_{xy} & S_{xz} \\ & \underset{\approx}{0} & & & \underset{\approx}{0} & & S_{xy} & S_{yy} & S_{yz} \\ & & & & & & S_{xz} & S_{yz} & S_{zz} \end{pmatrix} \tag{A19}$$

Displacement derivatives at shell's midsurface:

$$\begin{aligned} x_{,j} &= \sum_{k=1}^{M} \phi_{,j}^{(k)} x^{(k)} \\ y_{,j} &= \sum_{k=1}^{M} \phi_{,j}^{(k)} y^{(k)} \qquad\qquad j = r, s \\ z_{,j} &= \sum_{k=1}^{M} \phi_{,j}^{(k)} z^{(k)} \\ x_{,t} &= 0 \\ y_{,t} &= 0 \\ z_{,t} &= 0 \end{aligned} \tag{A20}$$

Initial nodal coordinates for layer n:

$$\begin{aligned} {}^{0}x_{n}^{(k)} &= {}^{0}x^{(k)} + \Big(\sum_{j=1}^{n-1} \mathrm{h}_{j}^{(k)} - \tfrac{1}{2}\mathrm{h}^{(k)}\Big) \cos {}^{0}\Psi^{(k)} \\ {}^{0}y_{n}^{(k)} &= {}^{0}y^{(k)} + \Big(\sum_{j=1}^{n-1} \mathrm{h}_{j}^{(k)} - \tfrac{1}{2}\mathrm{h}^{(k)}\Big) \sin {}^{0}\Psi^{(k)} \cos {}^{0}\Phi^{(k)} \\ {}^{0}z_{n}^{(k)} &= {}^{0}z^{(k)} + \Big(\sum_{j=1}^{n-1} \mathrm{h}_{j}^{(k)} - \tfrac{1}{2}\mathrm{h}^{(k)}\Big) \sin {}^{0}\Psi^{(k)} \sin {}^{0}\Phi^{(k)} \\ {}^{0}\Phi_{n}^{(k)} &= {}^{0}\Phi^{(k)} \\ {}^{0}\Psi_{n}^{(k)} &= {}^{0}\Psi^{(k)} \end{aligned} \tag{A21}$$

Relation between layer DOFs and shell DOFs:

Explicit:

$$\begin{aligned}
\Delta u_n^{(k)} &\approx \Delta u^{(k)} - \tfrac{1}{2}h^{(k)}(g_x^{(k)}\Delta\varphi^{(k)} + \overline{g}_x^{(k)}\Delta\psi^{(k)}) \\
&\quad + \sum_{j=1}^{n-1} h_j^{(k)}(g_x^{(k)}(\Delta\varphi^{(k)} + \Delta\varphi_j^{(k)}) + \overline{g}_x^{(k)}(\Delta\psi^{(k)} + \Delta\psi_j^{(k)})) \\
\Delta v_n^{(k)} &\approx \Delta v^{(k)} - \tfrac{1}{2}h^{(k)}(g_y^{(k)}\Delta\varphi^{(k)} + \overline{g}_y^{(k)}\Delta\psi^{(k)}) \\
&\quad + \sum_{j=1}^{n-1} h_j^{(k)}(g_y^{(k)}(\Delta\varphi^{(k)} + \Delta\varphi_j^{(k)}) + \overline{g}_y^{(k)}(\Delta\psi^{(k)} + \Delta\psi_j^{(k)})) \\
\Delta w_n^{(k)} &\approx \Delta w^{(k)} - \tfrac{1}{2}h^{(k)}(g_z^{(k)}\Delta\varphi^{(k)} + \overline{g}_z^{(k)}\Delta\psi^{(k)}) \\
&\quad + \sum_{j=1}^{n-1} h_j^{(k)}(g_z^{(k)}(\Delta\varphi^{(k)} + \Delta\varphi_j^{(k)}) + \overline{g}_z^{(k)}(\Delta\psi^{(k)} + \Delta\psi_j^{(k)}))
\end{aligned} \tag{A22}$$

$$\Delta\overline{\varphi}_n^{(k)} = \begin{cases} \Delta\varphi^{(k)} + \Delta\varphi_n^{(k)} & 1 \le n \le N-1 \\ \Delta\varphi^{(k)} - \sum_{j=1}^{N-1} \Delta\varphi_j^{(k)} \frac{h_j^{(k)}}{h_N^{(k)}} & n = N \end{cases}$$

$$\Delta\overline{\psi}_n^{(k)} = \begin{cases} \Delta\psi^{(k)} + \Delta\psi_n^{(k)} & 1 \le n \le N-1 \\ \Delta\psi^{(k)} - \sum_{j=1}^{N-1} \Delta\psi_j^{(k)} \frac{h_j^{(k)}}{h_N^{(k)}} & n = N \end{cases}$$

with

$$\begin{aligned}
g_x^{(k)} &= 0 & \overline{g}_x^{(k)} &= -\sin\Psi^{(k)} \\
g_y^{(k)} &= -\sin\Phi^{(k)}\sin\Psi^{(k)} & \overline{g}_y^{(k)} &= \cos\Phi^{(k)}\cos\Psi^{(k)} \\
g_z^{(k)} &= \cos\Phi^{(k)}\sin\Psi^{(k)} & \overline{g}_z^{(k)} &= \sin\Phi^{(k)}\cos\Psi^{(k)}
\end{aligned} \tag{A23}$$

In matrix notation:

$$\Delta\underset{\sim}{u}_n^{(k)} = \underset{\approx}{G}_n^{(k)}\,\Delta\underset{\sim}{u}^{(k)} \tag{A24}$$

with

$$\Delta\underset{\sim}{u}_n^{(k)} = \begin{pmatrix} \Delta u_n^{(k)} \\ \Delta v_n^{(k)} \\ \Delta w_n^{(k)} \\ \Delta\overline{\varphi}_n^{(k)} \\ \Delta\overline{\psi}_n^{(k)} \end{pmatrix} \qquad \Delta\underset{\sim}{u}^{(k)} = \begin{pmatrix} \Delta u^{(k)} \\ \Delta v^{(k)} \\ \Delta w^{(k)} \\ \Delta\varphi^{(k)} \\ \Delta\psi^{(k)} \\ \Delta\varphi_1^{(k)} \\ \Delta\psi_1^{(k)} \\ \vdots \\ \Delta\varphi_n^{(k)} \\ \Delta\psi_n^{(k)} \\ \vdots \\ \Delta\varphi_{N-1}^{(k)} \\ \Delta\psi_{N-1}^{(k)} \end{pmatrix} \tag{A25}$$

and the transformationmatrix $\underset{\approx}{G}_n^{(k)}$ (size $5 \times (2N+3)$):

- for layers $n \leq N-1$

$$\underset{\approx}{G}_n^{(k)} = \begin{pmatrix} 1 & 0 & 0 & \overline{h}_n^{(k)} g_x^{(k)} & \overline{h}_n^{(k)} \overline{g}_x^{(k)} & h_1^{(k)} g_x^{(k)} & h_1^{(k)} \overline{g}_x^{(k)} & \dots & h_{n-1}^{(k)} g_x^{(k)} & h_{n-1}^{(k)} \overline{g}_x^{(k)} & 0 & 0 & \dots & 0 \\ 0 & 1 & 0 & \overline{h}_n^{(k)} g_y^{(k)} & \overline{h}_n^{(k)} \overline{g}_y^{(k)} & h_1^{(k)} g_y^{(k)} & h_1^{(k)} \overline{g}_y^{(k)} & \dots & h_{n-1}^{(k)} g_y^{(k)} & h_{n-1}^{(k)} \overline{g}_y^{(k)} & 0 & 0 & \dots & 0 \\ 0 & 0 & 1 & \overline{h}_n^{(k)} g_x^{(k)} & \overline{h}_n^{(k)} \overline{g}_x^{(k)} & h_1^{(k)} g_x^{(k)} & h_1^{(k)} \overline{g}_x^{(k)} & \dots & h_{n-1}^{(k)} g_x^{(k)} & h_{n-1}^{(k)} \overline{g}_x^{(k)} & 0 & 0 & \dots & 0 \\ 0 & 0 & 0 & 1 & 0 & 0 & 0 & \dots & 0 & 0 & 1 & 0 & \dots & 0 \\ 0 & 0 & 0 & 0 & 1 & 0 & 0 & \dots & 0 & 0 & 0 & 1 & \dots & 0 \end{pmatrix} \tag{A26}$$

- for layer N

$$\underset{\approx}{G}_N^{(k)} = \begin{pmatrix} 1 & 0 & 0 & \overline{h}_N^{(k)} g_x^{(k)} & \overline{h}_N^{(k)} \overline{g}_x^{(k)} & h_1^{(k)} g_x^{(k)} & h_1^{(k)} \overline{g}_x^{(k)} & \dots & h_{N-1}^{(k)} g_x^{(k)} & h_{N-1}^{(k)} \overline{g}_x^{(k)} \\ 0 & 1 & 0 & \overline{h}_N^{(k)} g_y^{(k)} & \overline{h}_N^{(k)} \overline{g}_y^{(k)} & h_1^{(k)} g_y^{(k)} & h_1^{(k)} \overline{g}_y^{(k)} & \dots & h_{N-1}^{(k)} g_y^{(k)} & h_{N-1}^{(k)} \overline{g}_y^{(k)} \\ 0 & 0 & 1 & \overline{h}_N^{(k)} g_x^{(k)} & \overline{h}_N^{(k)} \overline{g}_x^{(k)} & h_1^{(k)} g_x^{(k)} & h_1^{(k)} \overline{g}_x^{(k)} & \dots & h_{N-1}^{(k)} g_x^{(k)} & h_{N-1}^{(k)} \overline{g}_x^{(k)} \\ 0 & 0 & 0 & 1 & 0 & -\frac{h_1^{(k)}}{h_N^{(k)}} & 0 & \dots & -\frac{h_{N-1}^{(k)}}{h_N^{(k)}} & 0 \\ 0 & 0 & 0 & 0 & 1 & 0 & -\frac{h_1^{(k)}}{h_N^{(k)}} & \dots & 0 & -\frac{h_{N-1}^{(k)}}{h_N^{(k)}} \end{pmatrix} \tag{A26}$$

with

$$\overline{h}_n^{(k)} = \sum_{j=1}^{n-1} h_j^{(k)} - \tfrac{1}{2} h^{(k)} \tag{A27}$$

Interpolation matrix for the shell:

$$\underset{\approx}{\mathbf{N}} = \overline{\underset{\approx}{\mathbf{N}}} + t_{sh}\,\widehat{\underset{\approx}{\mathbf{N}}} \qquad -0.5 \le t_{sh} \le 0.5 \tag{A28}$$

with

$$\begin{aligned} \overline{\underset{\approx}{\mathbf{N}}} &= \left(\overline{\underset{\approx}{\mathbf{N}}}^{(1)} \quad \overline{\underset{\approx}{\mathbf{N}}}^{(2)} \quad \dots \quad \overline{\underset{\approx}{\mathbf{N}}}^{(M)}\right) \\ \widehat{\underset{\approx}{\mathbf{N}}} &= \left(\widehat{\underset{\approx}{\mathbf{N}}}^{(1)} \quad \widehat{\underset{\approx}{\mathbf{N}}}^{(2)} \quad \dots \quad \widehat{\underset{\approx}{\mathbf{N}}}^{(M)}\right) \end{aligned} \tag{A29}$$

where

$$\overline{\underset{\approx}{\mathbf{N}}}^{(k)} = \phi^{(k)}(r,s) \begin{pmatrix} 1 & 0 & 0 & 0 & 0 \\ 0 & 1 & 0 & 0 & 0 \\ 0 & 0 & 1 & 0 & 0 \end{pmatrix} \tag{A30}$$

and

$$\widehat{\underset{\approx}{\mathbf{N}}}^{(k)} = \mathrm{h}^{(k)}\phi^{(k)}(r,s) \begin{pmatrix} 0 & 0 & 0 & \mathrm{g}_x^{(k)} & \overline{\mathrm{g}}_x^{(k)} \\ 0 & 0 & 0 & \mathrm{g}_y^{(k)} & \overline{\mathrm{g}}_y^{(k)} \\ 0 & 0 & 0 & \mathrm{g}_z^{(k)} & \overline{\mathrm{g}}_z^{(k)} \end{pmatrix} \tag{A31}$$

$\mathbf{g}^{(k)}$ and $\overline{\mathbf{g}}^{(k)}$ can be found in Eq. (A27).

APPENDIX H

Post–Failure Analysis of Layered Composite Shells by Finite Element Method

Post-Failure Analysis of Layered Composite Shells by Finite Element Method

Konrad Dorninger*
Institute of Lightweight Structures and Aerospace Engineering
Vienna Technical University, Vienna, Austria

ABSTRACT

Using the UEL-interface (user-defined element) a special shell finite element developed for layered composite material (LFC-element) has been implemented in ABAQUS. The element formulation is based on the degeneration principle including large displacements with an efficient analytical thickness integration. Examining suitable failure criteria and taking into account post-cracking stiffnesses allows for the investigation of progressive damage.

For load cases without failure analysis comparison of results obtained by the LFC-element with those of the ABAQUS shell element shows the efficiency and accuracy of the new element. Some examples illustrate that an extended range of composite specific problems can be covered by this LFC-element.

1. INTRODUCTION

In designing shell structures the prediction of the limit load is crucial for fully utilizing the material capabilities. Either buckling of the structure or the strength of the material (or both) limit the sustainable load of the shell. In this paper special emphasis will be put on investigating these two limiting factors, especially for layered composite shells.

By using a special shell finite element developed for laminated fiber-reinforced composites (LFC-element, *Dorninger, 1989*) in conjunction with ABAQUS (*ABAQUS, 1989*) these limit load analyses including the post failure regime can be conducted for arbitrary shell structures.

* Current address: Department of Civil Engineering, Rensselaer Polytechnic Institute, Troy, NY 12180-3590, U.S.A.

The onset of failure and the effective safety margin to overall collapse can be computed, which is of considerable practical relevance.

The complexity of the internal stress state typically found in layered composite materials and, in addition, the number of failure modes possible necessitate the introduction of some simplifications and assumptions in order to make post-failure analyses feasible. The basic assumptions are:

- Only inplane normal and shear stresses and out-of-plane shear stresses are considered (no interlaminar stresses).
- No variation of stresses along the layer thickness is assumed.
- Only two inplane failure modes together with the corresponding post-failure stiffnesses are considered: matrix cracking and fiber failure (either by cracking or by buckling).

The LFC-element is capable of handling thermal loading and material nonlinearities in terms of the stiffness degradation mentioned above as well as geometrical nonlinearities due to large deformations. By using the ABAQUS buckling procedure the buckling behavior of layered composite plate and shell structures, including nonlinear pre-buckling deformations, can be computed.

2. LFC-ELEMENT FORMULATION

A detailed description of the theoretical background of the LFC-element along with a number of illustrative examples can be found in *Dorninger, 1989*. In this chapter only the outline of the element formulation is presented with special emphasis on the failure analysis modelling.

2.1 Basics

The element formulation is based on the well known degeneration principle, see e.g. *Ramm, 1976, Bathe, 1982*. By using objective strain and stress measures, geometrically nonlinear behavior in terms of large deformations is included.

The incremental finite element equation has the well known form:

$$[{}^{m}\mathbf{K}_e + {}^{m}\mathbf{K}_g](\Delta\mathbf{u})^1 = {}^{m+1}\mathbf{r} - ({}^{m}\mathbf{f} - \Delta\mathbf{f}_{th}) \tag{1}$$

The usual iterative application of Eq. (1) in each increment improves the result up to a given accuracy.

For the updated Lagrange formulation the stiffness matrices and the nodal force vectors for one element (e) are given by the following integrals over the element volume (^{m}V):

$${}^{m}\mathbf{K}_e^{(e)} = \int_{{}^{m}V} {}^{m}\mathbf{B}_L^T \, {}^{m}\mathbf{C} \, {}^{m}\mathbf{B}_L \, d^{m}\mathrm{V} \tag{2}$$

$${}^{m}\mathbf{K}_g^{(e)} = \int_{{}^{m}V} {}^{m}\mathbf{B}_{NL}^T \, {}^{m}\mathbf{T} \, {}^{m}\mathbf{B}_{NL} \, d^{m}\mathrm{V} \tag{3}$$

$$ {}^{m}\mathbf{f}^{(e)} = \int_{{}^{m}V^{(e)}} {}^{m}\mathbf{B}_L^T \, {}^{m}\tau \, d^{m}V \tag{4} $$

$$ \Delta\mathbf{f}_{th}^{(e)} = \int_{{}^{m}V^{(e)}} {}^{m}\mathbf{B}_L^T \, {}^{m}\mathbf{C} \, \alpha \Delta\vartheta \, d^{m}V \tag{5} $$

In Eq. (1) the sum in square brackets is often referred to as the current global tangent stiffness matrix ${}^{m}\mathbf{K}$ at state m, comprised of ${}^{m}\mathbf{K}_e$ (material stiffness matrix, depending on the current material matrix ${}^{m}\mathbf{C}$ which, in turn, depends on the local state of damage) and ${}^{m}\mathbf{K}_g$ (initial stress or geometrical stiffness matrix, depending explicitely on the Cauchy stress tensor, ${}^{m}T$). The external load vector at the current state $m+1$, ${}^{m+1}\mathbf{r}$, is given by the surface and body forces, concentrated or distributed. ${}^{m}\mathbf{f}$ is the vector of internal forces corresponding to the stresses at state m (vector ${}^{m}\tau$) and $\Delta\mathbf{f}_{th}$ is the vector of internal nodal forces equivalent to stress increments resulting from a temperature increment $\Delta\vartheta$ and computed by using the direction dependent coefficients of linear thermal expansion (vector α).

The general theory used to describe the degenerated shell element's geometry and its deformations as well as the assumptions with respect to modified plane stress conditions are in close analogy to *Bathe, 1982*, and are described in detail in *Dorninger, 1989*. For example, the interpolation of the geometry is performed by

$$ {}^{m}x_i(r,s,t) = \sum_{k=1}^{M} \phi^{(k)}(r,s)\left[{}^{m}x_i^{(k)} + t\frac{\mathrm{h}^{(k)}}{2}\cos{}^{m}\Psi_i^{(k)}\right] \tag{6} $$

where $\phi^{(k)}(r,s)$ represent the standard 2/D shape functions (i.e. Lagrangian polynomials); M is the number of nodes forming the element, $\mathrm{h}^{(k)}$ is the thickness of the shell at node k and the angles $\Psi_i^{(k)}$ are used to determine the position of the shell's normal at node k.

2.2 Material Description of the Multilayer Composite

Due to the anisotropic and layered setup of composite shells the overall material matrix $\mathbf{C}$ in Eqs. (2,5) and the vector of coefficients of thermal expansion α in Eq. (5) become position and orientation dependent. Each layer is assumed to have orthotropic material behavior with respect to its individual fiber-fixed local coordinate system l,q. The definition of the local system and the nomenclature for the material setup of the **LFC**-element are shown in Fig. 1.

Assuming a linear elastic material (in terms of Cauchy stresses and Almansi strains) the elasticity matrix and the vectors of stresses and strains can be defined corresponding to the modified plane stress conditions ($\tau'_{33} = 0$) resulting from the degeneration principle:

$$ {}^{m}\tau' = {}^{m}\mathbf{C}'({}^{m}\varepsilon' - \alpha' \, {}^{m}\vartheta) \tag{7} $$

with ${}^{m}\vartheta$ being the temperature difference with respect to a stress-free reference temperature, and

$$ \tau' = \begin{pmatrix} \tau'_{11} \\ \tau'_{22} \\ 0 \\ \tau'_{12} \\ \tau'_{13} \\ \tau'_{23} \end{pmatrix}, \qquad \varepsilon' = \begin{pmatrix} \varepsilon'_{11} \\ \varepsilon'_{22} \\ 0 \\ \gamma'_{12} \\ \gamma'_{13} \\ \gamma'_{23} \end{pmatrix}. \tag{8} $$

Eqs. (7,8) are referred to a local cartesian coordinate system $\mathbf{x}'$ (x_1' being tangential to the natural coordinate r and x_3' being normal to the shell's midsurface), see Fig. 2.

The material matrix and the vector of coefficients of linear thermal expansion of the unidirectionally reinforced layer (UD-layer) are defined in the local layer coordinate system denoted by subscript L. A rotation transformation serves for computing $\mathbf{C}'$ and α' from $\mathbf{C}_L$ and α_L. Since element geometry and fiber-direction are independent of each other the angle Θ, which denotes the fiber angle with respect to the $\mathbf{x}'$ coordinate system, is not necessarily constant within the element (see Fig. 2). Two ways of accounting for this are implemented in the LFC-element:

a) By assuming the fibers to be parallel within the layer one can find a geometric relationship for the change of Θ (see *Dorninger, 1989*).

b) By specifying the Θ-angles at each nodal point of the element and using the 2/D shape functions $\phi^{(k)}(r,s)$ (from the interpolation of the geometry, Eq. (6)) one can interpolate the Θ-angle at any point.

After transforming the locally defined material laws of all UD-layers of the laminate into the x_1', x_2', x_3' coordinate system and using the isoparametric concept one can express the material matrix and the vector of coefficients of linear thermal expansion of layer n as a function of the natural coordinates r, s and obtain

$$\mathbf{C}'(r,s,t) = \begin{cases} {}^1\mathbf{C}'(r,s) \\ {}^2\mathbf{C}'(r,s) \\ \vdots \\ {}^N\mathbf{C}'(r,s) \end{cases} \qquad \alpha'(r,s,t) = \begin{cases} {}^1\alpha'(r,s) & -1 \le t \le {}^1t \\ {}^2\alpha'(r,s) & {}^1t < t \le {}^2t \\ \vdots & \vdots \\ {}^N\alpha'(r,s) & {}^{N-1}t < t \le +1 \end{cases} \tag{9}$$

with

$${}^nt = -1 + \frac{2}{\mathrm{h}} \sum_{j=1}^{n} {}^j\mathrm{h} \qquad \text{(definition of } {}^j\mathrm{h} \text{ see Fig. 1)} \tag{10}$$

for the multi-layer compound with layer number $n = 1, \ldots, N$.

The degeneration principle includes the assumption that normal vectors (or quasi-normals) remain straight during the deformation. In order to reduce the error resulting from this kinematic restriction, which in many cases is negligibly small, shear-correction factors can be introduced. *Noor, Peters, 1989*, proposed a predictor-corrector approach which not only improves the overall shear response but also the computation of interlaminar stress quantities. As long as rather thin shells are considered the use of such corrections can be omitted.

2.3 Stiffness Expressions

Computation of the element stiffness matrix requires a three-dimensional integration (see Eqs. (2–5)) which usually is performed by some sort of numerical integration technique. Since we are dealing with multi-layer shells (with a very large number of layers allowed), where each layer requires at least one (even better two or more) integration points over its thickness, the numerical effort increases rapidly with the number of layers. An effective way to overcome this difficulty is the use of a quasi-analytical thickness integration as described for homogeneous shells e.g. in *Stanley, 1985, Ramm, Matzenmiller, 1986*. This, however, requires

an assumption on the $t-$dependence of the Jacobian matrix (see e.g. *Laschet, Jeusette, Beckers, 1989*). In the present work the $t-$dependence is neglected. This approximation is acceptable as long as the shells are thin, their curvature is moderate and their thickness does not vary too much. The neglection of the $t-$dependence of $\mathbf{J}$ has been successfully used by *Stegmüller, 1985*, for homogeneous shells and by *Chao, Reddy, 1984*, for layered composite shells.

The displacements follow from the description of the geometry (Eq. (6)) and, therefore, the $t-$dependence of the displacement derivatives can be formulated explicitely:

$$ {}^{m}u_{i,j}(r,s,t) = {}^{m}x_{i,j} - {}^{0}x_{i,j} = {}^{m}\overline{u}_{i,j}(r,s) + t\,{}^{m}\widehat{u}_{i,j}(r,s) \qquad i,j = 1,2,3 \tag{11} $$

Using this relation the Almansi strains ε_{ij} can be decomposed into a $t-$independent part ($\rightarrow \overline{\varepsilon}$), a part linear in t ($\rightarrow \widehat{\varepsilon}$) and a t^2-dependent part ($\rightarrow \widetilde{\varepsilon}$). Together with the material matrix for the multi-layer compound and the vectors of linear thermal expansion (Eq. (9)), both transformed properly to the global x_1, x_2, x_3 system, the vector of Cauchy stress components (Eq. (7)) becomes:

$$ {}^{m}\tau(r,s,t) = {}^{m}\mathbf{C}(r,s,t)\left(\left[{}^{m}\overline{\varepsilon}(r,s) - {}^{m}\alpha(r,s,t)\,{}^{m}\overline{\vartheta}(r,s)\right] + t\left[{}^{m}\widehat{\varepsilon}(r,s) - {}^{m}\alpha(r,s,t)\,\frac{{}^{m}\widehat{\vartheta}(r,s)}{2}\right] + t^2\,{}^{m}\widetilde{\varepsilon}(r,s)\right) \tag{12} $$

where

$$ {}^{m}\mathbf{C}(r,s,t) = {}^{m}\mathbf{G}^{T}(r,s)\,\mathbf{C}'(r,s,t)\,{}^{m}\mathbf{G}(r,s) \tag{13} $$

$$ {}^{m}\alpha(r,s,t) = {}^{m}\mathbf{G}^{-1}(r,s)\,\alpha'(r,s,t) \tag{14} $$

The matrix ${}^{m}\mathbf{G}$ represents the transformation from the global x system to the local x' system. $\mathbf{G}$ is composed of the elements of the Jacobian matrix and, therefore, if $\mathbf{J}$ is independent of t so is $\mathbf{G}$. The temperature field is assumed to be linearly distributed over the thickness of the shell, with $\overline{\vartheta}$ being the temperature load of the midsurface and $\widehat{\vartheta}$ the temperature difference between opposite points on the two surfaces of the shell.

The $\mathbf{B}_L$ and $\mathbf{B}_{NL}$ matrices are constructed from derivatives of the shape functions and, therefore, they can be decomposed into a $t-$independent part ($\rightarrow \overline{\mathbf{B}}_L, \overline{\mathbf{B}}_{NL}$) and a part linear in t ($\rightarrow \widehat{\mathbf{B}}_L, \widehat{\mathbf{B}}_{NL}$). Now the stiffness matrices and nodal force vectors of Eqs. (2-5) can be rewritten and the quasi-analytical thickness integration can be performed. By introducing some abbreviations $\mathbf{K}_e^{(e)}, \mathbf{K}_g^{(e)}, \mathbf{f}^{(e)}, \Delta\mathbf{f}_{th}^{(e)}$ follow as:

$$ {}^{m}\mathbf{K}_e^{(e)} = \int_{-1}^{+1}\int_{-1}^{+1} \left({}^{m}\overline{\mathbf{B}}_L^{T}\left({}^{m}\mathbf{C}1\,{}^{m}\overline{\mathbf{B}}_L + {}^{m}\mathbf{C}2\,{}^{m}\widehat{\mathbf{B}}_L\right) + {}^{m}\widehat{\mathbf{B}}_L^{T}\left({}^{m}\mathbf{C}2\,{}^{m}\overline{\mathbf{B}}_L + {}^{m}\mathbf{C}3\,{}^{m}\widehat{\mathbf{B}}_L\right)\right)\det|\,{}^{m}\mathbf{J}\,|\,dr\,ds \tag{15} $$

$$ {}^{m}\mathbf{K}_g^{(e)} = \int_{-1}^{+1}\int_{-1}^{+1} \left({}^{m}\overline{\mathbf{B}}_{NL}^{T}\left({}^{m}\mathbf{S}1\,{}^{m}\overline{\mathbf{B}}_{NL} + {}^{m}\mathbf{S}2\,{}^{m}\widehat{\mathbf{B}}_{NL}\right) + {}^{m}\widehat{\mathbf{B}}_{NL}^{T}\left({}^{m}\mathbf{S}2\,{}^{m}\overline{\mathbf{B}}_{NL} + {}^{m}\mathbf{S}3\,{}^{m}\widehat{\mathbf{B}}_{NL}\right)\right)\det|\,{}^{m}\mathbf{J}\,|\,dr\,ds \tag{16} $$

$$ {}^{m}\mathbf{f}^{(e)} = \int_{-1}^{+1}\int_{-1}^{+1} \left({}^{m}\overline{\mathbf{B}}_L^{T}\,{}^{m}s1 + {}^{m}\widehat{\mathbf{B}}_L^{T}\,{}^{m}s2\right)\det|\,{}^{m}\mathbf{J}\,|\,dr\,ds \tag{17} $$

$$ {}^{m}\Delta\mathbf{f}_{th}^{(e)} = \int_{-1}^{+1}\int_{-1}^{+1} \left({}^{m}\overline{\mathbf{B}}_L^{T}\left({}^{m}c1_{th}\,\Delta\overline{\vartheta} + {}^{m}c2_{th}\,\frac{\Delta\widehat{\vartheta}}{2}\right) + {}^{m}\widehat{\mathbf{B}}_L^{T}\left({}^{m}c2_{th}\,\Delta\overline{\vartheta} + {}^{m}c3_{th}\,\frac{\Delta\widehat{\vartheta}}{2}\right)\right)\det|\,{}^{m}\mathbf{J}\,|\,dr\,ds \tag{18} $$

where the following abbreviations are used:

$$
\begin{aligned}
{}^{m}s1 &= {}^{m}C1\,{}^{m}\bar{\varepsilon} - {}^{m}c1_{th}\,{}^{m}\bar{\vartheta} + {}^{m}C2\,{}^{m}\hat{\varepsilon} - {}^{m}c2_{th}\,\frac{{}^{m}\bar{\vartheta}}{2} + {}^{m}C3\,{}^{m}\tilde{\varepsilon} \\
{}^{m}s2 &= {}^{m}C2\,{}^{m}\bar{\varepsilon} - {}^{m}c2_{th}\,{}^{m}\bar{\vartheta} + {}^{m}C3\,{}^{m}\hat{\varepsilon} - {}^{m}c3_{th}\,\frac{{}^{m}\bar{\vartheta}}{2} + {}^{m}C4\,{}^{m}\tilde{\varepsilon} \\
{}^{m}s3 &= {}^{m}C3\,{}^{m}\bar{\varepsilon} - {}^{m}c3_{th}\,{}^{m}\bar{\vartheta} + {}^{m}C4\,{}^{m}\hat{\varepsilon} - {}^{m}c4_{th}\,\frac{{}^{m}\bar{\vartheta}}{2} + {}^{m}C5\,{}^{m}\tilde{\varepsilon}
\end{aligned}
\tag{19}
$$

are "stress integrals" and

$${}^{m}Ci(r,s) = {}^{m}G^{T}(r,s)\sum_{n=1}^{N}{}^{n}C'(r,s)\frac{{}^{n}t^{i} - {}^{n-1}t^{i}}{i}\,{}^{m}G(r,s) \qquad i = 1,\ldots,5 \tag{20}$$

$${}^{m}ci_{th}(r,s) = {}^{m}G^{T}(r,s)\sum_{n=1}^{N}{}^{n}C'(r,s)\,{}^{n}\alpha'(r,s)\frac{{}^{n}t^{i} - {}^{n-1}t^{i}}{i} \qquad i = 1,\ldots,4 \tag{21}$$

are thickness integrals of the material matrix and the vector of linear thermal expansion. ${}^{m}S1$, ${}^{m}S2$, ${}^{m}S3$ are equivalent to ${}^{m}s1$, ${}^{m}s2$, ${}^{m}s3$, but the elements are rearranged in special matrix form, see *Dorninger, 1989*.

The summations in Eqs. (20,21) are independent of the state m (as long as local failure is not taken into account), thus they only have to be computed once (prior to the incremental analysis). This results in a decrease in the numerical effort in each increment due to the reduction of the 3/D numerical integration to a 2/D one. The more layers there are within the laminate the more efficient the analytical thickness integration becomes compared to the fully 3/D numerical integration.

2.4 Effects of Local Failure

Due to the nature of composite material the failure behavior is very complex with numerous different failure modes possible. Therefore an accurate prediction of failure with reasonable effort is almost impossible so that some restrictions have to be made. In this paper a simple way of dealing with this kind of behavior was chosen:

As outlined in the introduction failure is considered to occur within the layers only and delamination is not taken into account. With respect to this and by assuming a linear elastic stress-strain relationship up to failure (which is valid for many fiber reinforced plastics, see e.g. *Tsai, Hahn, 1980*) one can use proper strength criteria to determine onset of failure. Although the following procedures are based on "homogenized" material, the local damage of the composite, i.e. matrix or fiber cracking, can be estimated, compare *Tsai, Hahn, 1980*. In this paper failure is indicated by a combination of two failure criteria, and two distinct failure modes are assumed:

A quadratic strength criterion, the Tsai-Wu-criterion (*Tsai, Hahn, 1980, Chawla, 1987*) serves for predicting failure for stress states with relatively large transverse stress components which affect the matrix material rather than the fibers. Therefore, violation of this criterion can be related to matrix failure. Endurable stress states lie within a failure surface in the stress space

$$F_{01}\sigma_{ll} + F_{11}\sigma_{ll}^2 + F_{12}\sigma_{ll}\sigma_{qq} + F_{02}\sigma_{qq} + F_{22}\sigma_{qq}^2 + F_{44}\tau_{lq}^2 < 1 \tag{22}$$

with

$$F_{01} = \frac{1}{\sigma_{lTu}} + \frac{1}{\sigma_{lCu}} \qquad F_{11} = \frac{-1}{\sigma_{lTu}\sigma_{lCu}} \qquad F_{44} = \frac{1}{\tau_{lqu}^2}$$
$$F_{02} = \frac{1}{\sigma_{qTu}} + \frac{1}{\sigma_{qCu}} \qquad F_{22} = \frac{-1}{\sigma_{qTu}\sigma_{qCu}} \qquad F_{12} = -\sqrt{F_{11}F_{22}} \tag{23}$$

$\sigma_{ll}, \sigma_{qq}, \tau_{lq}$ are the inplane engineering stresses. With respect to material damage we use the same laws for Cauchy stresses, too. The following notations are used

σ_{lCu} maximum endurable, i.e. ultimate uniaxial compression stress in fiber direction,
σ_{lTu} ultimate tensile stress in fiber direction,
σ_{qCu} ultimate compression stress normal to fiber direction,
σ_{qTu} ultimate tensile stress normal to fiber direction,
τ_{lqu} ultimate shear stress.

Since in many cases the Tsai-Wu-criterion overestimates the strength of the UD-layer in the case of stresses acting predominantly in fiber direction, a maximum stress limit in fiber direction is imposed (the failure surface corresponding to the combination of Eqs. (22) and (24) is shown in Fig. 3):

$$\sigma_{lCu} < \sigma_{ll} < \sigma_{lTu} \tag{24}$$

Post-cracking stiffnesses are introduced according to the two assumed failure modes. In the case of matrix cracking they take the form:

$$\mathbf{C}_L = \begin{pmatrix} E_{11} & E_{12} & 0 & 0 & 0 & 0 \\ & E_{22} & 0 & 0 & 0 & 0 \\ & & 0 & 0 & 0 & 0 \\ & sym. & & E_{44} & 0 & 0 \\ & & & & E_{55} & 0 \\ & & & & & E_{66} \end{pmatrix} \xrightarrow{\text{matrix-cracking}} \begin{pmatrix} \beta_E E_{11} & 0 & 0 & 0 & 0 & 0 \\ & 0 & 0 & 0 & 0 & 0 \\ & & 0 & 0 & 0 & 0 \\ & sym. & & 0 & 0 & 0 \\ & & & & E_{55} & 0 \\ & & & & & E_{66} \end{pmatrix} \tag{25}$$

E_{12}, E_{22} and E_{44} are set to zero, which is a simple representation of the matrix stiffness being removed. The reason for introducing a correction factor β_E is twofold: First, a damaged matrix also reduces the stiffness in fiber direction and, second, for nonstraight (e.g. wavy) fibers the reduced support by the damaged matrix can lead to a further loss of stiffness. β_E depends on the composition of the layer and must be given as an additional material parameter.

In the case of fiber failure the reduced stiffnesses are modeled by:

$$\mathbf{C}_L = \begin{pmatrix} E_{11} & E_{12} & 0 & 0 & 0 & 0 \\ & E_{22} & 0 & 0 & 0 & 0 \\ & & 0 & 0 & 0 & 0 \\ & sym. & & E_{44} & 0 & 0 \\ & & & & E_{55} & 0 \\ & & & & & E_{66} \end{pmatrix} \xrightarrow{\text{fiber-failure}} \begin{pmatrix} E_{22} & E_{12} & 0 & 0 & 0 & 0 \\ & E_{22} & 0 & 0 & 0 & 0 \\ & & 0 & 0 & 0 & 0 \\ & sym. & & E_{44} & 0 & 0 \\ & & & & E_{55} & 0 \\ & & & & & E_{66} \end{pmatrix} \tag{26}$$

As can be seen from Eq. (26), E_{11} is set equal to E_{22}. This is a simple representation of the assumption that after fiber failure only the matrix stiffness remains.

By assuming thin layers it is sufficient to investigate the stress state in the layers' midsurface only. In addition, if cracking occur the corresponding failure mode is taken to be valid through the entire thickness of the layer. Thick layers with significant stress gradients in thickness direction can be treated by subdividing them into several "thin" sublayers.

Equations (25,26) represent "secant"-stiffnesses of the material and, therefore, stresses can be computed directly from the total strains. The following procedure, applied at each load step m at each stiffness sampling point r_i, s_j (= 2/D integration points) for all N layers of the laminate, accounts for stiffness changes due to material cracking:

- The local inplane strains ${}^n\varepsilon_L$ at the midsurface of layer n with respect to the layer's local axis are derived from the global strain vector ${}^m\varepsilon$.
- With ${}^n\varepsilon_L$ and the corresponding local elasticity matrix ${}^n\mathbf{C}_L$ of the previous step an estimate of the stresses is computed.
- In the next step the combined failure criterion is examined. If failure is indicated by a violation of Eq. (22) or Eq. (24) the local stiffness matrix is changed according to Eq. (25) or Eq. (26), respectively. The elements of ${}^n\mathbf{C}_L$ to be reduced are properly subtracted from the $\mathbf{C}i$ matrices (Eq. (20)) and the ci_{th} vectors (Eq. (21)).

A flow chart of the complete algorithm along with some investigations on the influence of the iteration scheme and the mesh size on the accuracy of the algorithm can be found in *Dorninger, 1989.*

3. NUMERICAL EXAMPLES

3.1 Buckling and Postbuckling of a Multilayer Square Plate

This problem has been chosen to show the accuracy of the LFC-element, to quantify the efficiency compared to the ABAQUS shell element and to conduct post-buckling analyses. The practical purpose of this example can be seen in optimizing an inplane loaded plate with given geometry and given material with regard to buckling.

Lay-up: $[(+\Theta/-\Theta)_{6s}]$... 24-layer angle-ply, layer thickness = 0.0529 mm

Material: Graphite/Epoxy

$E_l = 127.5\,kN/mm^2$	$E_q = 11.0\,kN/mm^2$	$\nu_{ql} = 0.35$
$G_{lq} = 5.5\,kN/mm^2$	$G_{lt} = 5.5\,kN/mm^2$	$G_{qt} = 4.6\,kN/mm^2$

Model: The whole plate has been modelled by sixteen 16-node LFC-elements, the width of the square being 900 mm, see Fig. 4; boundary conditions: a) simply supported, b) clamped.

For several fiber angles Θ the buckling load has been computed by using the standard buckling procedure implemented in ABAQUS. Fig. 5 indicates a strong dependence of the buckling load and the corresponding buckling mode on the fiber angle. To verify this result a similar FE-analysis by *Nemeth, 1986,* has been used for comparison. Fig. 5 shows the very close agreement between these two analyses. For a few angles Θ the buckling load has also been computed by employing 36 ABAQUS S9R5 shell elements (so that the number of nodes

remains unchanged). Again, the results are almost exactly the same as obtained with the 16-node LFC-element (less than 1% difference in the buckling loads; no observable differences in the displacements).

The advantage of the quasi-analytical thickness integration becomes evident in the following example: For the 16-node LFC-element the CPU-time for one load step has been about 40% less than for the ABAQUS S9R5 element. For the 9-node LFC-element, which has the same number of nodes as the ABAQUS element, the time savings have been increased to 66%! The 9-node LFC-element, however, yields somewhat higher buckling loads and, therefore, has not been used in subsequent analyses. To find out how the number of layers affects the CPU-time the same plate has been investigated with only 4 layers: For the LFC-elements no influence of the number of layers on the CPU-time has been observed. For the ABAQUS element, in contrast, this reduction of layers by a factor 6 resulted in a decrease of CPU-time by a factor 3.

To get some idea on the post-buckling behavior of the plate a nonlinear load-displacement analysis for fiber angle $\Theta = 60°$ has been carried out. In order to achieve this an imperfection was introduced into the geometry of the plate: the calculated mode shape with its amplitude scaled to 1% of the shell thickness has been superimposed on the original (perfect) geometry. Due to these imperfections the original bifurcation point vanishes and the plate exhibits a nonlinear (nearly bilinear) behavior, see Fig. 6. The corresponding deformation figures indicate that, after reaching the buckling load, out-of-plane deformations (corresponding to the shape of the buckling mode) develop, which, in turn, drastically lower the overall stiffness of the plate.

3.2 Thermally Loaded Cross-Ply Square Plate

A simply supported composite square plate has been loaded by a uniform temperature rise. The following properties have been chosen:

Lay-up: [0/90]... two layer cross-ply, layer thickness = 0.2 mm

Material: Graphite/Epoxy

$E_l = 127.5\,kN/mm^2$	$E_q = 11.0\,kN/mm^2$	$\nu_{ql} = 0.35$
$G_{lq} = 5.5\,kN/mm^2$	$G_{lt} = 5.5\,kN/mm^2$	$G_{qt} = 4.6\,kN/mm^2$
$\alpha_l = -0.08\times10^{-5}\,°C^{-1}$	$\alpha_q = 2.90\times10^{-5}\,°C^{-1}$	

Model: The whole plate has been modelled by sixteen 16-node LFC-elements, the width of the square being 300 mm; all edges were restricted to remain straight.

Fig. 7 shows the nonlinear load-displacement path as well as an estimate curve for the buckling load. The deformed shape of the plate is in good agreement with an analytically derived solution, see *Tauchert, 1986.*

Because of the constant temperature rise all over the plate and the simply supported edges, no stability problem would be expected for a homogeneous isotropic plate. But, due to anisotropies occuring in the laminate, a linear buckling analysis (i.e. a buckling analysis after a very small load step, $\overline{\vartheta} = 1°C$) yields a bifurcation point at ${}^{*}\overline{\vartheta} = 4°C$. However, a detailed

analysis of the buckling behavior indicates that the nonlinear pre-buckling deformations make the results of the linear buckling analysis rather meaningless. As can be seen from the estimate curve in Fig. 7, the estimates of the relevant buckling mode change during the incremental increase of the temperature and the critical temperature is approximately 50 times higher than the corresponding value of the linear buckling analysis!

Again the comparison with the ABAQUS element has shown excellent agreement in the displacements. It has not been possible to compute the detailed buckling behavior by using the ABAQUS elements, no convergence or only negative results having been obtained during the eigenvalue extraction. With the LFC-element buckling loads and buckling modes have been successfully computed after introducing a slight modification to the buckling analysis:

Starting from Eq. (1) an eigenvalue problem of the following form can be obtained, for details see *Rammerstorfer, 1982*:

$$\left({}^{m}\mathbf{K}_{\sigma} + {}^{m}\overline{\eta}\,{}^{m}\mathbf{K}_{g}\right){}^{m}\delta\overline{\mathbf{u}} = 0 \tag{28}$$

leading to an estimate for the critical load multiplier

$${}^{*}\lambda \approx {}^{m}\overline{\eta}_{1}\,{}^{m}\lambda \tag{29}$$

with ${}^{m}\lambda$ being the actual load multiplier and ${}^{m}\overline{\eta}_{1}$ the smallest eigenvalue of Eq. (28). ${}^{m}\delta\overline{\mathbf{u}}$ represents the eigenvector corresponding to the eigenvalue ${}^{m}\overline{\eta}$.

An imperfect plate (produced in the same way as described in example 3.1 by superimposing the actual buckling mode, scaled to 1% of the plate thickness, onto the original geometry) displays almost exactly the same behavior as the perfect plate, except that the actual bifurcation point does not occur any more, instead the estimate curve deviates from the load-displacement path.

3.3 Bending of a Flexural Specimen

In this example the procedure for taking into account the local stiffness degradation has been applied. For testing the ultimate flexural strength and modulus of a laminate of the type typically used in aircraft structures a simple flexural specimen (i.e. a three point bending bar) is used. This bar is loaded up to complete failure and the load-displacement path is recorded. A comparison of the measured results with the finite element investigations shows the applicability of the strength calculations included in the LFC formulation.

Lay-up: 30 layers of Kevlar29 fabric, effective layer thickness = 0.09 mm
For the FE model each fabric layer is subdivided into two sublayers in order to approximate the woven reinforcement by UD-layers.

→ assumed lay-up: $[(0/90)_{15s}]$... cross-ply, layer thickness = 0.045 mm

Model: one quarter of the bar has been modeled by eight 16-node elements

Material: Kevlar29 (UD)

E_l = 57.2 kN/mm^2	E_q = 3.9 kN/mm^2	ν_{ql} =0.35
G_{lq} = 2.3 kN/mm^2	G_{lt} = 2.3 kN/mm^2	G_{qt} = 2.3 kN/mm^2
σ_{lT_u} =1300. N/mm^2	σ_{lC_u} =227. N/mm^2	τ_{lq_u} = 34. N/mm^2
σ_{qT_u} = 12. N/mm^2	σ_{qC_u} = 53. N/mm^2	β_E = 0.2

Fig. 8 shows the calculated and the measured load-displacement path of the flexural specimen. Reasonably good agreement is obtained. First-ply-failure occurs at a relatively low load level and might be interpreted as the beginning of the nonlinear deformations of the experimentally obtained curve. However, in the FE calculations a noticable deviation from the linear path is observed only at a much higher load level. The calculated deformations and the calculated ultimate load are slightly lower than the measured values but for estimating the nonlinear behavior of the material the procedure appears to be satisfactory.

4. CONCLUSIONS

The successful implementation of a special shell finite element into ABAQUS has been shown. The theoretical background of this element (LFC-element) which is based on the degeneration principle has been outlined and a simple way of taking into account fiber failure and matrix cracking in terms of materially nonlinear behavior has been introduced.

By comparing the CPU time requirements it has been shown that the LFC-element becomes more efficient than the ABAQUS shell element with increasing number of layers. The accuracy of the LFC-element in terms of displacements has been proven excellent compared to analytical results as well as compared to ABAQUS shell element results.

Post-failure analyses in terms of post-buckling behavior have been conducted for a mechanically loaded composite plate as well as for a thermally loaded composite plate. Somewhat unexpected phenomena occurred with thermal loading and tracing the buckling behavior has been a difficult task.

The investigation of a flexural specimen in terms of failure has shown the applicability of the proposed simple failure analysis procedure.

Acknowledgement

The financial support of this project by the Federal Republic of Austria (Ministry of Science and Research) and the Fonds zur Förderung der wissenschaftlichen Forschung is gratefully acknowledged.

References

ABAQUS Version 4-8 User's Manual, Hibbit, Karlsson & Sorensen Inc., Providence, RI, 1989.

Bathe, K.J., *Finite Element Procedures in Engineering Analysis*, Prentice-Hall, Englewood Cliffs, NJ, 1982.

Chao, W.C. and J.N. Reddy, 'Analysis of Laminated Composite Shells Using a Degenerated 3-D Element', Int. J. Num. Meths. Eng. **20**, 1981-2007 (1984).

Chawla, K.K., *Composite Materials*, Springer Verlag, New York, NY, 1987.

Dorninger, K., *Entwicklung von nichtlinearen FE-Algorithmen zur Berechnung von Schalenkonstruktionen aus Faserverbundstoffen*, Fortschritt-Berichte, VDI Reihe 18, Nr. 65, VDI Verlag, Düsseldorf, FRG, 1989.

Laschet, G., J.P. Jeusette and P. Beckers, 'Homogenization and Pre-Integration Techniques for Multilayer Composites and Sandwich Finite Element Models', Int. J. Num. Meths. Eng. **27**, 257–269 (1989).

Nemeth, M.P., 'Importance of Anisotropy on Buckling of Compression-Loaded Symmetric Composite Plates', AIAA Journal **24**, No. 11, 1831–1835 (1986).

Noor, A.K. and J.M. Peters, 'A Posteriori Estimates for Shear Correction Factors in Multilayered Composite Cylinders', J. Eng. Mechs. **115**, No. 6, 1225–1244 (1989).

Ramm, E., *Geometrisch nichtlineare Elastostatik und finite Elemente*, Habilitationsschrift, University of Stuttgart, FRG, 1975.

Ramm, E., 'A Plate/Shell Element for Large Deflections and Rotations', *Formulations and Computational Algorithms in Finite Element Analysis*, Ed. K.J. Bathe, J.T. Owen, W. Wunderlich, Proc. U.S.-German Symp., MIT, Cambridge, MA, 1977.

Ramm, E. and A. Matzenmiller, 'Large Deformation Shell Analysis Based on the Degeneration Concept', *State-of-the-Art Texts on FEM for Plate and Shell Structures*, Eds. T.J.R. Hughes, E. Hinton, Pineridge Press, Swansea, UK, 1986.

Rammerstorfer, F.G., 'Jump Phenomena Associated with the Stability of Geometrically Nonlinear Structures', *Recent Advances in Non-Linear Computational Mechanics*, Eds. E. Hinton, D.R.J. Owen, C. Taylor, Pineridge Press, Swansea, UK, 1982.

Stanley, G.M., *Continuum-Based Shell Elements*, Dissertation, Stanford University, Stanford, CA, 1985.

Stegmüller, H., *Grenzlastberechnungen flüssigkeitsgefüllter Schalen mit "degenerierten" Schalenelementen*, Dissertation, University of Stuttgart, Stuttgart, FRG, 1985.

Tauchert, T.R., 'Thermal Stresses in Plates — Statical Problems', *Thermal Stresses I*, Ed. R.B. Hetnarski, North-Holland, Amsterdam, 1986.

Tsai, S.W. and H.T. Hahn, *Introduction to Composite Materials*, Technomic Publishing Co., Lancaster, PA, 1980.

Figures

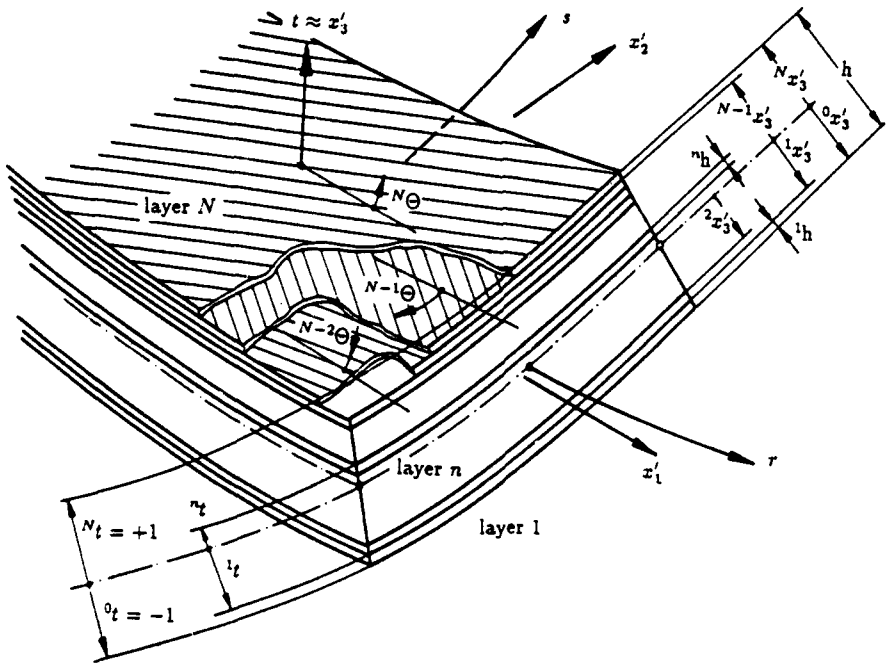

Fig. 1 Geometry and material setup of the LFC-element

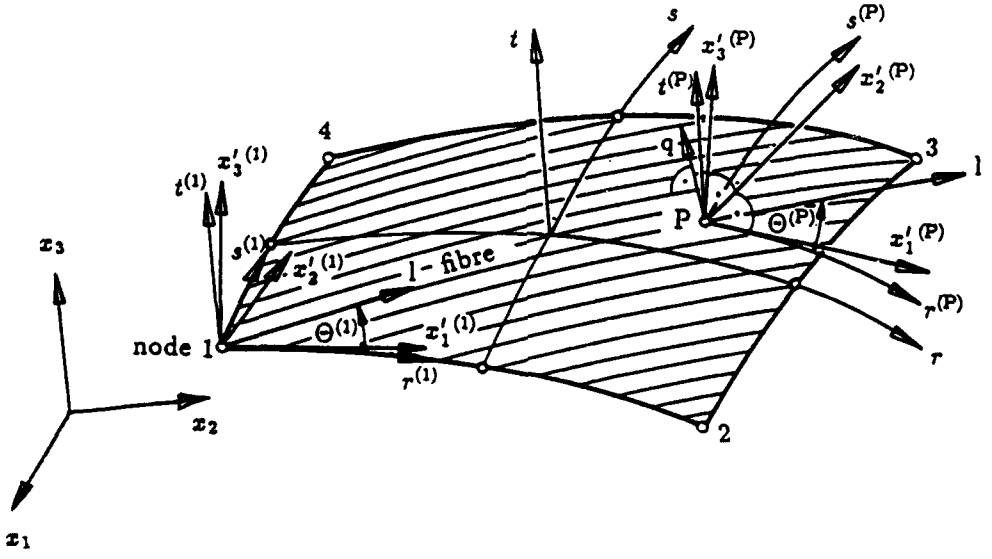

Fig. 2 Coordinate systems of the LFC-element:
local layer system l, q, natural coordinates r, s, t,
local cartesian system x'_1, x'_2, x'_3 global cartesian system x_1, x_2, x_3

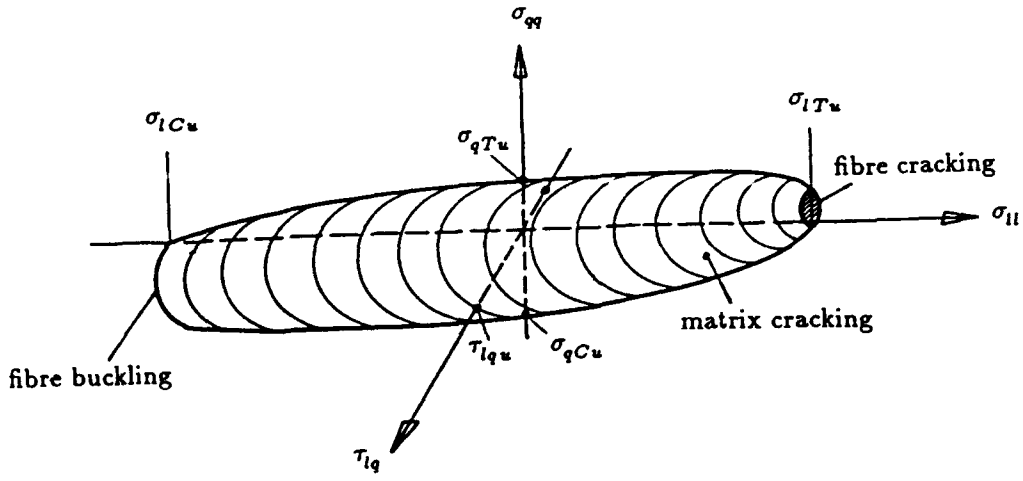

Fig. 3 Failure surface in stress space of the combined failure criterion

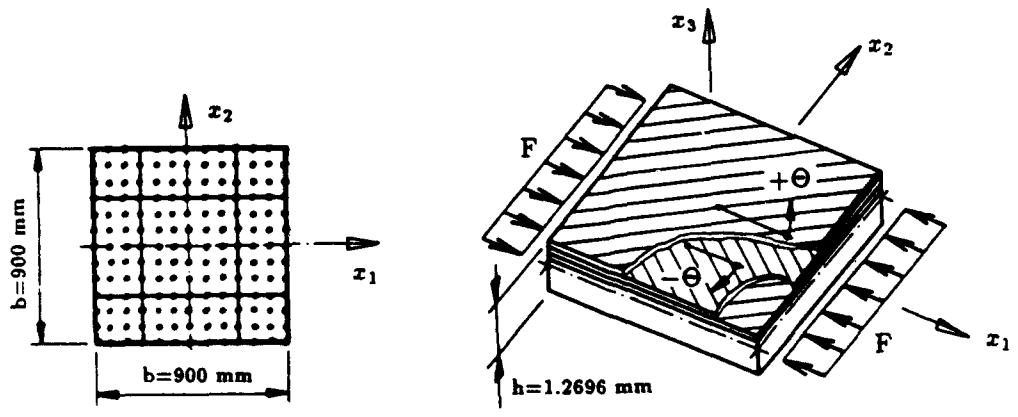

Fig. 4 Model of inplane loaded angle-ply square plate

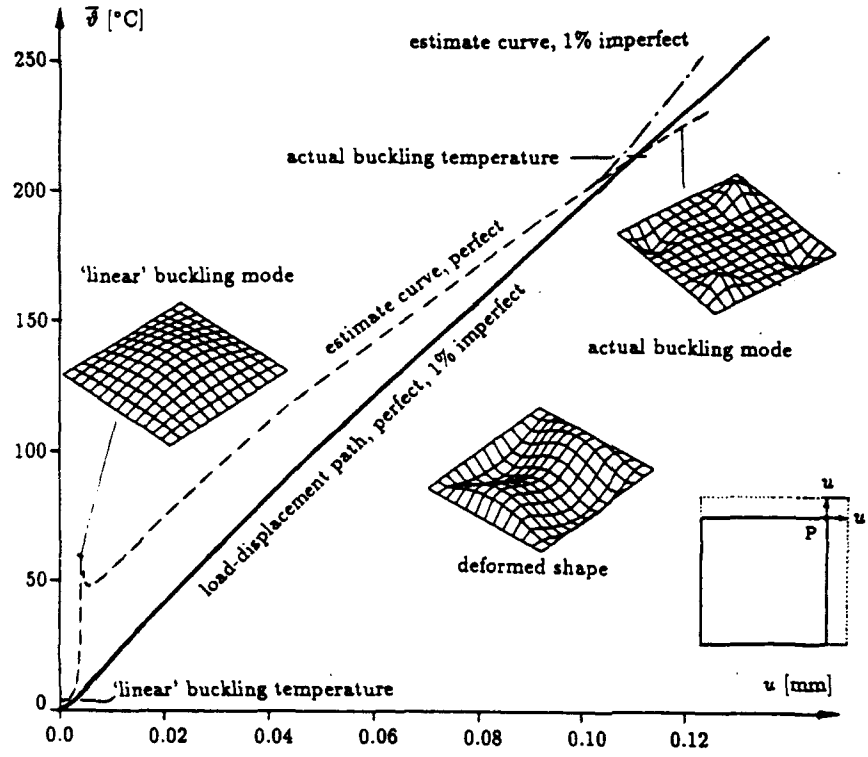

Fig. 7 Load-displacement path and estimate curves for buckling loads of a thermally loaded two-layer cross-ply plate

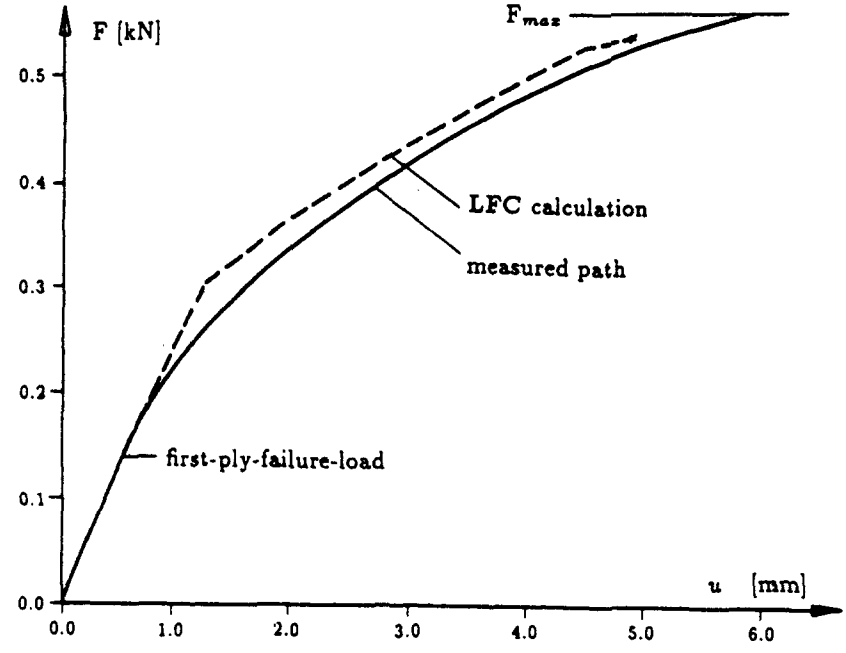

Fig. 8 Load-displacement path of a flexural specimen

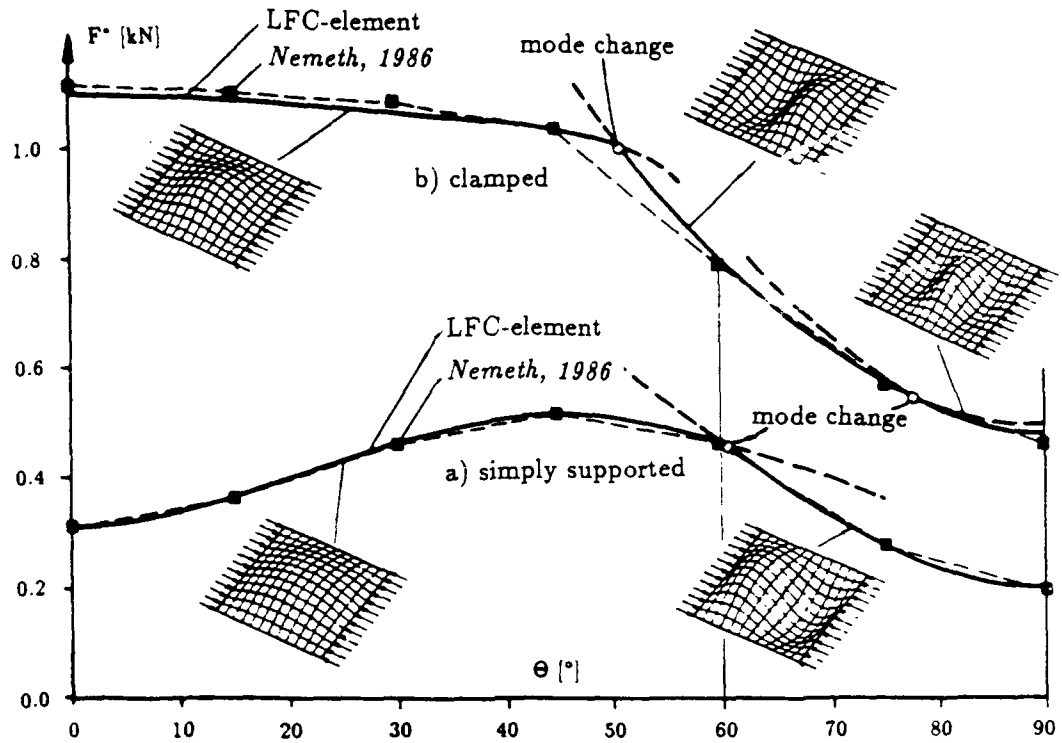

Fig. 5 Buckling load and buckling modes of inplane loaded square plates as a function of fiber angle and boundary conditions

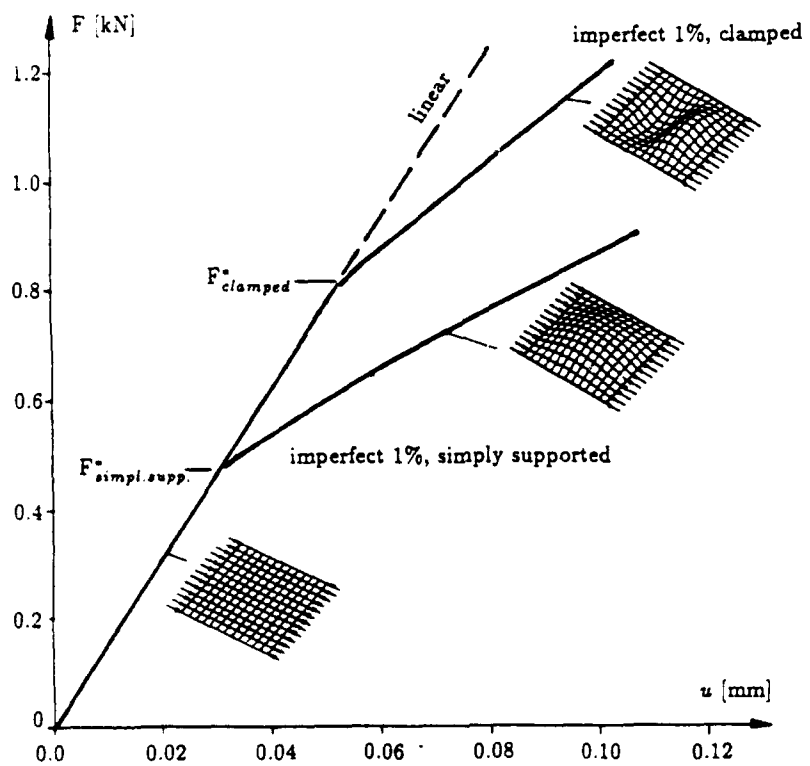

Fig. 6 Post-buckling behavior of an inplane loaded square plate with fiber angle $\Theta = 60°$

APPENDIX I

Composite Material Models in ABAQUS

COMPOSITE MATERIAL MODELS IN ABAQUS

N.D. Lambropoulos, J.F. Wu, M.S. Shephard,
S.S. Sternstein and G.J. Dvorak

Rensselaer Polytechnic Institute
Troy, NY 12180-3590

ABSTRACT

A finite element based procedure that accounts for micromechanical level nonlinear behavior of the matrix material in continuous fiber composites is presented. The micromechanical level model is a periodic hexagonal array with elastic fibers and nonlinear matrix material. A bilinear elastoplastic relation for metal matrix and a nonlinear time-dependent relation for thermoplastic matrix are used with this micromechanical model to provide the overall instantaneous material properties of a macromechanical finite element model of the composite structure being analyzed. Example problems of simple composite systems analyzed with this procedure are presented.

INTRODUCTION

The proper analysis of many composite material systems requires a proper consideration of nonlinear material behavior. Common examples where nonlinear behavior should be considered include: 1) the design of metal matrix composites where the strain to yield of the matrix is only a fraction of the strain to failure of the fiber; 2) thermoplastic composites with substantial transverse loads; and 3) metal matrix composites subject to high temperature creep. A key feature of composites with nonlinear material behavior is that the nonlinearities are due to nonlinear behavior of the individual constituents. Typically the type and degree on nonlinearity in the constituents is not the same. In the cases above, the matrix undergoes nonlinear deformations while the

fibers are essentially linear until failure. Therefore, any analysis of a composite which attempts to account for nonlinear material behavior must consider the micromechanical behavior of the constituents. Unlike the linear range, simple models to combine the behavior of the constituents in the nonlinear range to arrive at a macromechanical constitutive relationship do not yield satisfactory results. This paper presents a composite material model which can account for micromechanical level nonlinearities in a macromechanical level finite element analysis. This procedure has been integrated into ABAQUS through a user defined material procedure.

The key to accounting for local matrix material nonlinearities is the micromechanical mixing model. In this work the periodic hexagonal array (PHA) model [TEPLY 84], [DVORAK and TEPLY 85] is used. The PHA is capable of predicting the macromechanical stiffness properties, as well as the stress and strain concentration factors at a material point given the constituent material properties, volume fraction of the constituents, and the overall stress and strain field. One of the major advantages of the PHA is its modular structure which can accommodate almost any kind of constitutive relation for the matrix material. Currently, a bilinear elastoplastic material model with a Mises type of yield function and a kinematic hardening rule is used for metal matrix, and a nonlinear time-dependent relation is also being used for thermoplastic matrix.

ABAQUS and its user-defined material subroutine UMAT provided the platform for implementing all these composite material models. The example cases which illustrate the behavior of these models have also been analyzed by ABAQUS.

PERIODIC HEXAGONAL ARRAY FOR CONTINUOUS FIBER COMPOSITES IN ABAQUS

The development of models that can accurately predict the macromechanical behavior of composites based on a knowledge of the constituent materials is critical to the ability to carrying out engineering analysis of composite structures. These models become complex when micromechanical level nonlinear behavior of the constituents must be considered to predict the macromechanical behavior.

The Periodic Hexagonal Array (PHA) model [TEPLY 84], [TEPLY

and DVORAK 88] addresses the difficulties of accounting for micromechanical nonlinearities by explicitly modeling the microstructural geometry. The analysis of the PHA begins with the selection of an appropriate representative volume element (RVE) and the identification of an appropriate set of boundary conditions which allows an analysis of the RVE that will yield useful information on the overall behavior. The assumption that yields a convenient set of boundary conditions is a uniform strain far-field on the micromechanical volume containing the RVE. Although there are gradients in the solution at the macromechanical level, the uniform strain field assumption is adequate for the purposes of determining the material properties of the composite at that point.

In the PHA the fibers are assumed to be periodically distributed throughout the matrix material in a topologically hexagonal configuration. In this case the simplest RVE is a triangle created by connecting the centers of adjacent fibers (Fig. 1). This RVE can be isolated [TEPLY 84], by the proper specification of periodic displacement boundary conditions. Although limited to a single triangle, the complexities introduced by the presence of two distinct phases and the nonlinear behavior of the matrix phase, make it too difficult to obtain a closed form solution. Therefore an analysis based on a finite element discretization of the RVE is necessary. The coarseness of the finite element mesh is dictated by the minimum number of elements which allow a meaningful handling of the periodic boundary conditions and at the same time yield useful results, by avoiding overconstraint.

The primary purpose of the RVE analysis is to provide the overall material properties needed to support a macromechanical analysis. To achieve this goal an equivalent homogeneous volume (EHV) of unknown material properties is introduced. It is the instantaneous stiffness parameters of the EHV that are needed for the macromechanical analysis. They can be determined by applying the periodic boundary conditions to both the EHV and RVE and equating the total energy change of the two.

Both upper and lower bound finite element formulations are being employed [TEPLY 84], to qualify the amount of approximation error introduced by the finite element discretization of the RVE used in the energy change calculation. The calculation of the displacement-based upper bound technique follows the basic steps

below. The energy change $\Delta\Pi$ in the EHV and RVE, is given by:

$$\text{EHV} \Rightarrow \quad \Delta\Pi = \frac{1}{2}\,\Delta\bar{a}^{T}\,\bar{B}^{T}\,L\,\bar{B}\,\Delta\bar{a} - \Delta\bar{F}^{T}\,\Delta\bar{a} \qquad [1]$$

$$\text{RVE} \Rightarrow \quad \Delta\Pi = \frac{1}{2}\,\Delta\bar{a}^{T}\,K\,\Delta\bar{a} - \Delta\bar{F}^{T}\,\Delta\bar{a} \qquad [2]$$

where

$\Delta\bar{a}$ a common set of nodal displacements for the EHV and RVE
$\bar{B}$ the strain-displacement matrix for EHV
$\Delta\bar{F}$ the nodal forces equivalent to surface tractions
L the overall instantaneous stiffness of the EHV
K the overall stiffness matrix of the RVE finite element mesh, which is the assembly of fiber and matrix subelement stiffness matrices and as a result, it is also a function of fiber and matrix subelement material matrices.

The final step in the process is to equate the energy change of the RVE [Equ.1] and EHV [Equ.2], where the second terms (potential due to applied loads) in both energy expressions drop out, due to identical boundary conditions. This yields the explicit form of the overall instantaneous stiffness matrix L, as:

$$L = \left(\bar{B}^{T}\right)^{-1} K \left(\bar{B}\right)^{-1} \qquad [3]$$

which takes into account the material matrix L^{k} of each phase subelement.

In the general nonlinear finite element formulation the solution of the equilibrium equations requires the updating of the global stiffness matrix of the structure being analyzed at every step of the analysis. This implies the re-evaluation of the individual element stiffness matrix for each element that has demonstrated nonlinear behavior in that load step. This requires the evaluation of the instantaneous material stiffness matrix, L, at each sampling point in the element. It is this evaluation that invokes the micromechanical level finite element analysis of the PHA. Thus, the PHA calculations are the inner most loop of the nonlinear finite element process (Fig. 2). Therefore, computational efficiency of the PHA calculation is critical.

The integration of the PHA into a large scale nonlinear finite

element code is greatly facilitated in the case of ABAQUS [V4.5 85] by the modular separation of models (in particular material models). The ability to tailor ABAQUS to deal with functions not directly available within the program, is through a set of user defined routines. Each one allows the analyst to carry out a particular type of operation that alters data within ABAQUS's data structures. For example, the user defined material routine (UMAT) is invoked by indicating that the material type for a particular set of elements is the user defined material. With this capability users can define their own constitutive relation for cases where the existing models are not adequate for predicting the material behavior.

Two basic functions have to be performed by UMAT at each sampling point in the finite element mesh:

1. Update the stresses and the solution dependent variables to their values at the end of the increment.
2. Provide the material instantaneous stiffness matrix according to the constitutive model.

To carry out these operations the UMAT routine must be supplied with the appropriate information. The generalized interface allows the main program to pass the state information used by the other portions of the program, as well as any specific state information that is needed for the operation of the material model, into the UMAT routine. The primary information provided to UMAT for driving the solution process are strain and temperature increments which have been determined by the global iterative scheme in ABAQUS for the current load increment, as well as the values of the state variables from the previous step. The UMAT routine then updates the instantaneous stiffness and stresses for the given increment and returns this information. This operation has to be repeated until overall convergence for the current loading step, is achieved.

METAL MATRIX COMPOSITE PHA

A complexity that arises in PHA for metal matrix composites is that it was developed using a stress-space plasticity formulation. This means that it uses a stress increment to calculate the instantaneous stiffness and strain increment. However, ABAQUS provides the UMAT routine with a strain increment and wants back

the instantaneous stiffness and corresponding stress. Therefore it was necessary to introduce a local iteration into the UMAT routine [WU et al 88]. This procedure typically converges in two or three iterations.

When UMAT is called during a load increment including mechanical and/or thermal loads, ABAQUS provides the current state (the results at the end of the previous increment) of stress ($\sigma_{(A)}$), strain ($\varepsilon_{(A)}$) and temperature (T). At the start of the current load increment, that is on the initial iteration, the strain increment is zero ($\Delta\varepsilon_{(A)}=0$) and the temperature increment (ΔT) is the value for that load increment. The function of this initial iteration is to provide the macromechanical analysis procedure (ABAQUS) with an appropriate instantaneous stiffness matrix including the effects of any thermal load for that increment. Unlike the typical finite element procedure where thermal effects are treated by the construction of an initial strain vector, the approach used here is to convert the thermal increment into an equivalent mechanical load through the use of an initial stress vector. The determination of this initial stress vector must be carried out at the micromechanical level on the PHA accounting for the different thermal characteristics of the matrix and fibers. The analysis is done using Dvorak's decomposition procedure [DVORAK 86]. The instantaneous stiffness matrix and initial stress matrix are returned to ABAQUS where the effects of the pure mechanical load are combined with the initial stress vector to predict the strain increments for this load increment. From this point through the remainder of this load increment, the UMAT routine treats all load types as pure mechanical load at temperature equal to (T+ΔT).

In each one of the global iterations after the initial one, UMAT receives a non-zero strain increment predicted using the given instantaneous stiffness and the overall load increment. This strain increment must be converted into a stress increment ($\Delta\sigma_{(A)}$) and added to the stress at the current state ($\sigma_{(A)}$) to form a new stress vector ($\sigma_{(U)}{}^{(1)}$):

$$\sigma_{(U)}^{(1)} = \sigma_{(A)} + L\,\Delta\varepsilon_{(A)} \qquad [4]$$

where: L is the stiffness at the beginning of this increment.

The PHA procedure calculates a new strain vector ($\varepsilon^{(i)}{}_{(U)}$)

which must be compared with the strain vector given to UMAT by the global iterative scheme $(\varepsilon_{(A)} + \Delta\varepsilon_{(A)})$. If they are not nearly equal, a local iteration in the UMAT routine is initiated where the stress vector used in the PHA is updated by:

$$\sigma_{(U)}^{(i+1)} = \sigma_{(U)}^{(i)} + L_{(U)}^{(i)} \left(\varepsilon_{(A)} + \Delta\varepsilon_{(A)} - \varepsilon_{(U)}^{(i)} \right), \quad i=1,2,\ldots \qquad [5]$$

where:

$L_{(U)}^{(i)}$ is the instantaneous stiffness at the end of i^{th} local iteration (given by PHA based on stress state $\sigma_{(U)}^{(i)}$).

$\varepsilon_{(U)}^{(i)}$ is the strain at the end of i^{th} local iteration (given by PHA based on stress state $\sigma_{(U)}^{(i)}$).

The convergence criteria on the UMAT local level iterations is:

$$\frac{\left| (\varepsilon_{(A)} + \Delta\varepsilon_{(A)}) - \varepsilon_{(U)}^{(i+1)} \right|}{\left| \varepsilon_{(A)} + \Delta\varepsilon_{(A)} \right|} \leq \text{tolerance} \qquad [6]$$

EXAMPLE OF METAL MATRIX COMPOSITE

A P-100 Gr/Al metal matrix composite system of $(\pm\phi)_s$ laminates with different ϕ and different tangent modulus in the matrix was analyzed for thermal cyclic loads in the range of $\pm 120^{\circ}C$ with an ambient temperature at $20^{\circ}C$. The material model outlined above was applied, and two layers of 8-noded three-dimensional elements with a 2x2x2 integration scheme were used. Uniform displacements on each surface of the model were specified as boundary conditions. For the laminates with a fixed volume fraction for both phases, the variations of axial coefficient of thermal expansion (C.T.E.) are shown in (Fig. 3). One can see that there are several points at zero C.T.E. condition. These are caused by the cancellation of the contributions of both phases to overall response. From these three curves one can predict the axial strain range of any $(\pm\phi)_s$ lay-ups under thermal cyclic loads, provided that the initial yield temperature for each lamina is known [WU et al 88].

TIME-DEPENDENT CONSTITUTIVE RELATION FOR THERMOPLASTIC MATRIX

A nonlinear viscoelastic material model with the essential

mechanical characteristics of thermoplastics such as rate dependence, stress component interactions and transient behavior has been developed. A phenomenological approach was taken which led to a minimum of material parameters, all of which can be determined from straight forward mechanical tests.

The model is based on a one-dimensional rheological equation which was used [CESSNA and STERNSTEIN 67] to describe time and path dependent processes at the tip of a crack in glassy polymers. This approach successfully related constant strain rate failure data to constant load (creep) times to failure. Recently, the model has been made three-dimensional [BANKERT, et al 86] for use as a matrix constitutive equation for composite materials. In summary, the hydrostatic component of strain is assumed to be linear elastic

$$\sigma_{kk} = 3B\,\varepsilon_{kk} \qquad [7]$$

while the deviatoric strain is nonlinear viscoelastic and coupled to the hydrostatic stress component as follows:

$$\dot{S}_{ij} = 2G_1\,\dot{e}_{ij} - \frac{2G_1}{\eta}\,S_{ij} - 2G_1\,K\,e^{\frac{\beta}{3}\sigma_{kk}}\sinh \left\{\alpha\left[S_{ij} - 2G_2\left(e_{ij} - \frac{S_{ij}}{2G_2} - \int_0^t \frac{S_{ij}}{\eta}\,dt\right)\right]\right\} \qquad [8]$$

where: S_{ij} and $\dot{S}_{ij}$ the deviatoric stress and stress rate components

e_{ij} and $\dot{e}_{ij}$ the deviatoric strain and strain rate components

σ_{kk} and ε_{kk} the hydrostatic stress and strain components

The physical interpretation of the parameters is the following:

K	activation energy needed to overcome potential barrier.
α	activation volume of the polymer segment which has to move as a whole for flow to take place.
β	describes the pressure effect on shear 'yield' stress.
B	elastic bulk modulus.
G_1	shear modulus before 'yield'.
G_2	shear modulus after 'yield'.
η	solid state viscosity.

The implementation of this constitutive relation for the matrix material inside the User Defined Subroutine UMAT, is primarily concerned with the deviatoric part. This requires an integration in time which is carried out in the following steps:

Let us consider a time step $\Delta t = t(n) - t(n-1)$

1. ABAQUS supplies the stresses $\{\sigma\}$ and $\{S\}$, and the strains $\{\varepsilon\}$ and $\{e\}$ at $t = t(n-1)$, and an estimate of the increment in strains $\{\Delta\varepsilon\}$ corresponding to Δt.

2. Transform the constitutive relation [Equ.8] into an incremental relation between deviatoric stresses $\{\Delta S\}$ and total strains $\{\Delta\varepsilon\}$ using an explicit central-difference approximation as a time integration operator.

3. Solve the resulting six nonlinear equations for $\{\Delta S\}$ by Newton-Raphson iteration. The resulting algebraic equations are uncoupled because of the assumption of linear hydrostatic component.

4. Update the total stress vector $\{\sigma\}$ at time $t(n)$, according to the formula:

$$\{\sigma\} = \{S^\circ\} + \{\Delta S\} + B\,[D2]\,\{\varepsilon\} \qquad [9]$$

5. Determine the material Jacobian matrix, $[\partial\Delta\sigma/\partial\Delta\varepsilon]$, which yields the incremental relation between total stresses $\{\sigma\}$ and total strains $\{\varepsilon\}$ as:

$$\left[\frac{\partial\Delta\sigma}{\partial\Delta\varepsilon}\right] = B[D2] + \frac{2G_1[D1] + C_3\cosh(A)\ G_2[D1] - C_3\sinh(A)\ \frac{1}{2}\beta B[D2]}{1 + \frac{1}{2}C_1 + C_3\cosh(A)\ \frac{1}{2}\alpha C_2} \qquad [10]$$

where

$$A = \alpha\left\{C_2\left(\{S^\circ\} + \tfrac{1}{2}\{\Delta S\}\right) - 2G_2[D1]\left(\{\varepsilon^\circ\} + \tfrac{1}{2}\{\Delta\varepsilon\}\right) + \frac{2G_2}{\eta}\{P\}\right\}$$

and $\{S^\circ\}$, $\{\varepsilon^\circ\}$ are the deviatoric stress and total strain at the end of the previous increment, $\{\Delta S\}$, $\{\Delta\varepsilon\}$ the deviatoric stress and total strain increments during the current loading step, $\{P\}$ a recursive vector used for

keeping track of the solution of the integral term in time C_1, C_2, C_3 constants, and [D1], [D2] coefficient matrices.

EXAMPLE OF THERMOPLASTIC MATRIX COMPOSITES

The desirable features that can also be recovered by the predictions of the model are: 1) proper rate-dependency of the onset of nonlinear response; 2) onset of nonlinear response at a higher absolute value of hydrostatic compression than tension; and 3) 'Ratcheting' effect in cycling loading [LAMBROPOULOS 88].

To show the significance of using a realistic material constitutive relation, the material model presented above was incorporated into a detailed Mode II specimen analysis [BANKERT et al 87]. A beam specimen with a midplane blunt-tip crack is subjected to bending loading, which produces an overall Mode II stress-state at tne crack tip. A thin resin-rich layer with isotropic but nonlinear viscoelastic behavior is introduced in front of the crack tip, while orthotropic linear elastic material properties are used for the rest of the beam. A qualitative presentation of results is presented in (Fig. 4). In-plane shear stress contours at three different steps of the loading history illustrate the progressive redistribution of stresses around the crack tip. Load factor 1 corresponds to the elastic range of the material's behavior, therefore the response is fully symmetric. As the stresses at both the highest concentration areas increase and reach the onset of nonlinear response (load factor 6), significant variations are observed. The upper half of the crack tip which is under tension can no longer support stresses as high as the lower half which is under compression. This can be explained by the different behavior of the model in tension versus compression. For load factor 6 the compressive part is still in the linear elastic range, while the tensile one has already entered the 'post-yield' range. When the compressive part also enters its 'post-yield' range (load factor 10), the variations in stress distribution are found to be even more dramatic.

PHA FOR THERMOPLASTIC MATRIX COMPOSITES

The structure of the PHA can accommodate any kind of constitutive model for the matrix material including the one for thermoplastics just presented. The basic steps of the PHA

formulation remain the same, with slight differences described below.

The expression for the overall instantaneous stiffness **L** in terms of local moduli $\mathbf{L}^k$ requires the evaluation of the stiffness matrix **K** of the RVE finite element mesh, as prescribed by [Equ.3]. The fiber contribution to stiffness is based on a linear elastic material relation, while the matrix contribution is based on the time-dependent nonlinear constitutive relation [Equ.10]. Since this matrix constitutive relation is defined in strain-space (given strain - return stress), it is compatible with the displacement-based finite element method. This avoids the local iterative scheme needed by the stress-space plasticity model used for the metal matrix.

Because of the history-dependence of the model, information must be stored at the end of each step, in order to be used in subsequent ones. The storage is done in an optimal way (minimum memory required), and special care is taken to recall this information when and where it is appropriate.

Preliminary results from the testing of the PHA mixing model with the viscoelastic constitutive relation for the matrix, are presented next. A simple structure consisting of two 8-noded 3-D elements, with a 2x2x2 integration scheme, is subjected to uniaxial tension, in directions parallel and perpendicular to the fiber orientation.

The tensile stress-strain curve for the composite is plotted in (Fig. 5), along with the corresponding behavior of fiber and matrix independently subjected to the same type of loading. A soft fiber is chosen to illustrate the effect of matrix. However, it is obvious that while the fiber response is linear elastic and the matrix nonlinear, the composite lies in between, slightly nonlinear starting at the point where the matrix 'yields'. The initial slope of the curve, which determines the elastic longitudinal modulus, follows approximately the well known "rule of mixtures". The longitudinal (L) case is closer to the fiber, since it is mainly fiber-dependent, while the transverse (T) response is closer to the matrix behavior.

CLOSING REMARKS

The basic argument for the use of mixing models in composites is the level of scale that the analyst wants to look at. For small scale systems where the fiber-matrix interactions, local plastic deformations, debonding, delamination or even random fiber distribution cannot be ignored, the use of a mixing model which smoothes properties out, is inaccurate. On the other hand, when the macroscopic behavior of a composite system is under consideration, say for structural design purposes, the Periodic Hexagonal Array model provides an accurate estimate of the overall properties, still being able to capture those matrix dominated phenomena.

An important issue in the further development of these techniques is to improve their computational efficiency. The most critical area is the current need to use three-dimensional through the thickness discretization on the structural level. This problem can be eliminated by constructing a PHA for application at the lamina level using the correct reduced dimension strain space. This could then be combined with laminated shell finite elements to more efficiently predict the response of composite structures.

ACKNOWLEDGMENTS

This work was supported in part by a grant from the Office of Naval Research under contract number N000014-85-K-0733, and the National Aeronautics and Space Administration and the Air Force Office of Scientific Research under grant number NGL-33-018-003. Thanks are also due to Hibbitt, Karlsson, and Sorensen, Inc., Providence, Rhode Island, for permitting the use of the ABAQUS program in this project.

REFERENCES

[ABAQUS 85]
ABAQUS Theory and User's Manual, Hibbitt, Karlsson and Sorensen, Inc., 100 Medway St., Providence, Rhode Island, 02906-4402, July, 1985, Version 4.5(a).

[BANKERT et al 86]
Bankert, R.J., Sternstein, S.S. and Shephard, M.S., unpublished research, Rensselaer Polytechnic Institute, Troy, N.Y., 1986.

[BANKERT et al 87]
Bankert, R.J., Lambropoulos, N.D., Shephard, M.S. and Sternstein, S.S., "Thermoplastic Matrix Composites: Finite Element Analysis of Mode I and Mode II Failure Specimens", ASTM Symposium on Advances in Thermoplastic Matrix Composite Materials, 1987.

[CESSNA and STERNSTEIN 67]
Cessna, L.C.Jr. and Sternstein, S.S., "Viscoelasticity and Plasticity Considerations in the Fracture of Glasslike High Polymers", Fundamental Phenomena in the Material Sciences, vol. 4, Fracture of Metals, Polymers and Glasses, edited by L.J. Bonis, J.J. Duga and J.J. Gilman, Plenum Press, N.Y. (1967), p. 45.

[DVORAK and TEPLY 85]
Dvorak, G.J. and Teply, J.L., "Periodic Hexagonal Array Model for Plasticity Analysis of Composite Materials", Plasticity Today: Modeling, Methods and Application, W. Olszak Memorial Volume, A. Sawczuk and V. Bianchi, editors, Elsevier Scientific Publishing Co., Amsterdam, (1985), pp.623-642.

[DVORAK 86]
Dvorak, G.J., "Thermal Expansion of Elastic-Plastic Composite Materials", J. Appl. Mech., 53 (1986), pp.737-743.

[LAMBROPOULOS 88]
Lambropoulos, N.D., "Numerical Analysis of Composite Materials", Master's Thesis (in preparation), Rensselaer Polytechnic Institute, Troy NY, 1988.

[TEPLY 84]
Teply, J.L., "Periodic Hexagonal Array Model for Plasticity Analysis of Composite Materials", Ph.D. Dissertation, University of Utah, 1984.

[TEPLY and DVORAK 88]
Teply, J.L. and Dvorak, G.J., "Bounds on Overall Instantaneous Properties of Elastic-Plastic Composites", J. Mech. Phys. Solids, to appear in 1988.

[WU et al 88]
Wu, J.F., Shephard, M.S., Dvorak, G.J. and Bahei-El-Din, Y.A., "A Material Model for the Finite Element Analysis of Metal Matrix Composites", Composites Science and Technology, submitted for publication, 1988.

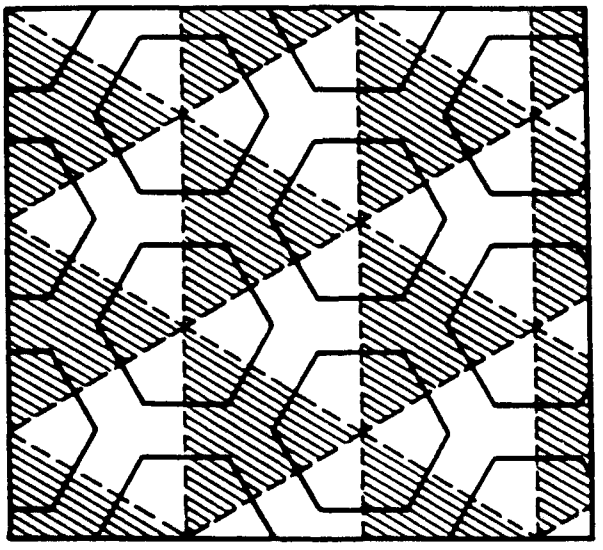

Figure 1. Representative volume element

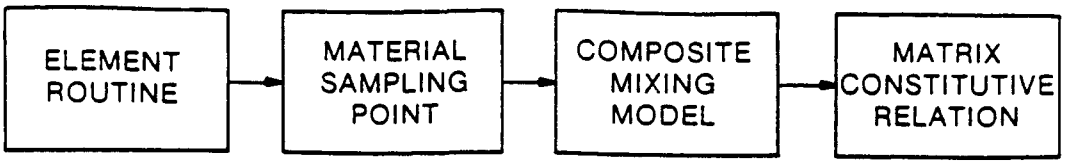

Figure 2. Placement of Composite Material Models into ABAQUS

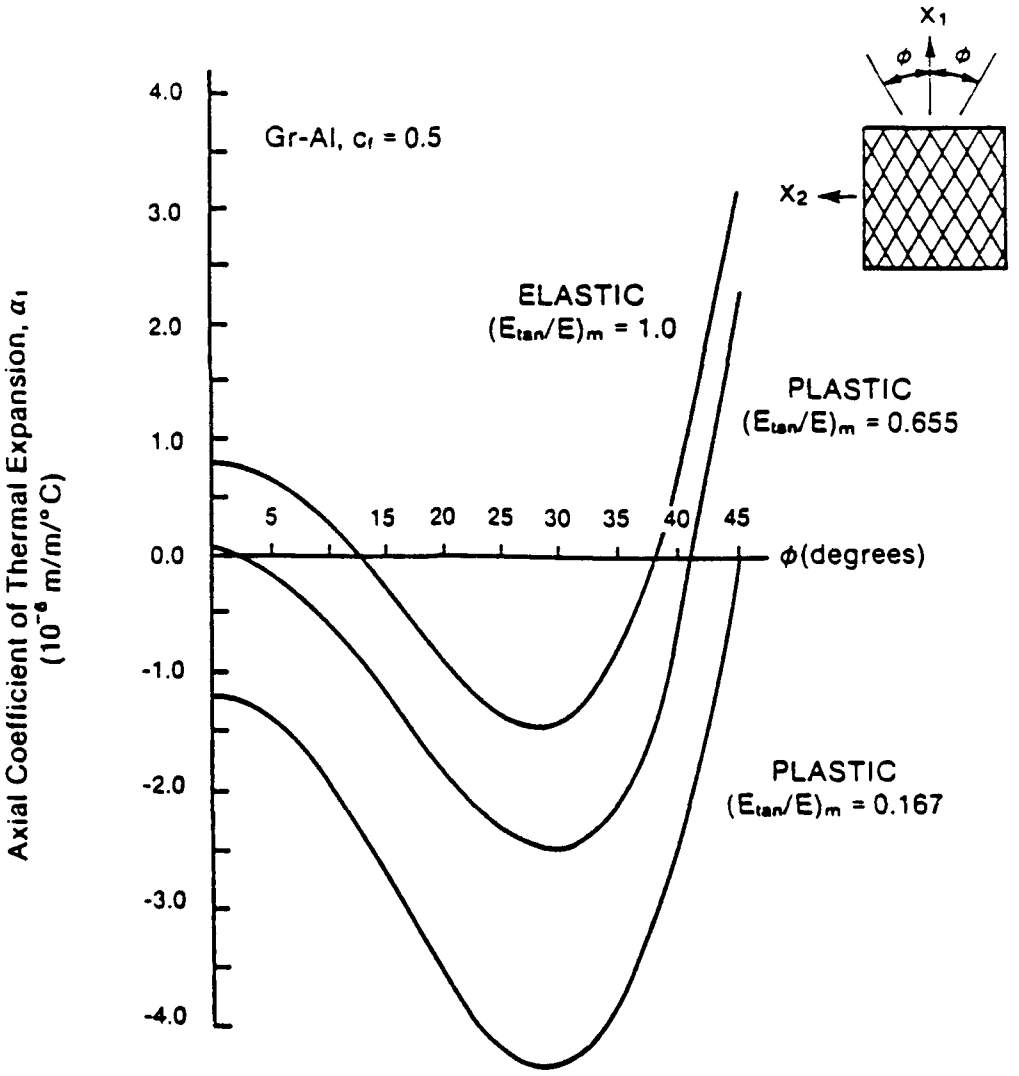

Figure 3. Variation of axial coefficient of thermal expansion for ±φ composite plates

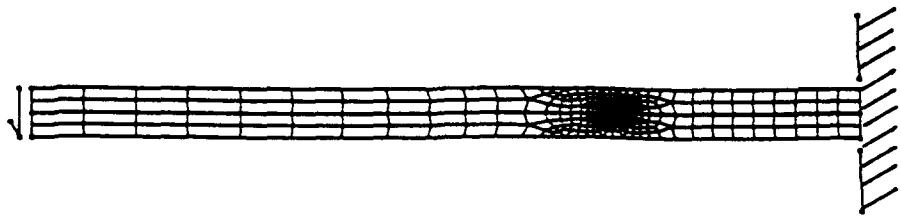

Overall specimen configuration

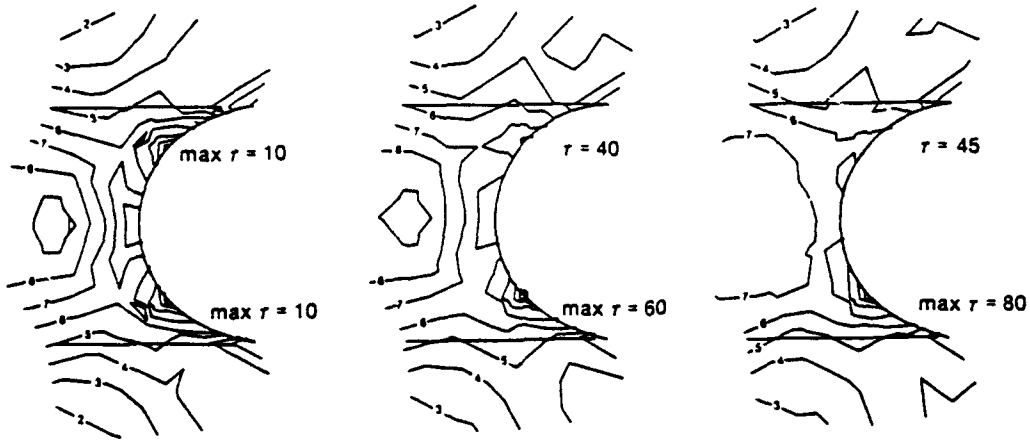

Close-up of shear stress contours at the crack tip for different levels of applied load

Figure 4. Orthotropic cracked beam with nonlinear viscoelastic thin layer

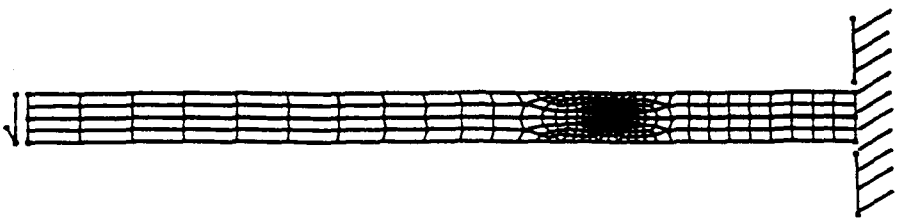

Overall specimen configuration

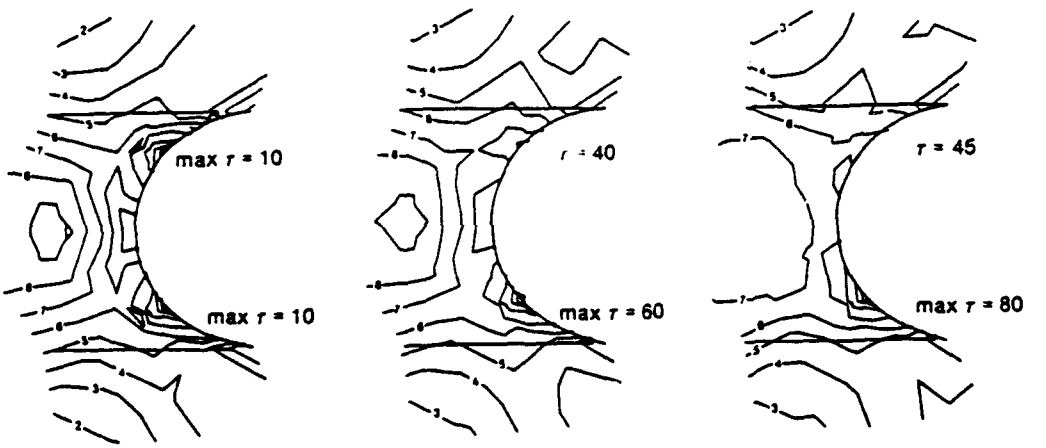

Close-up of shear stress contours at the crack tip for different levels of applied load

Figure 4. Orthotropic cracked beam with nonlinear viscoelastic thin layer

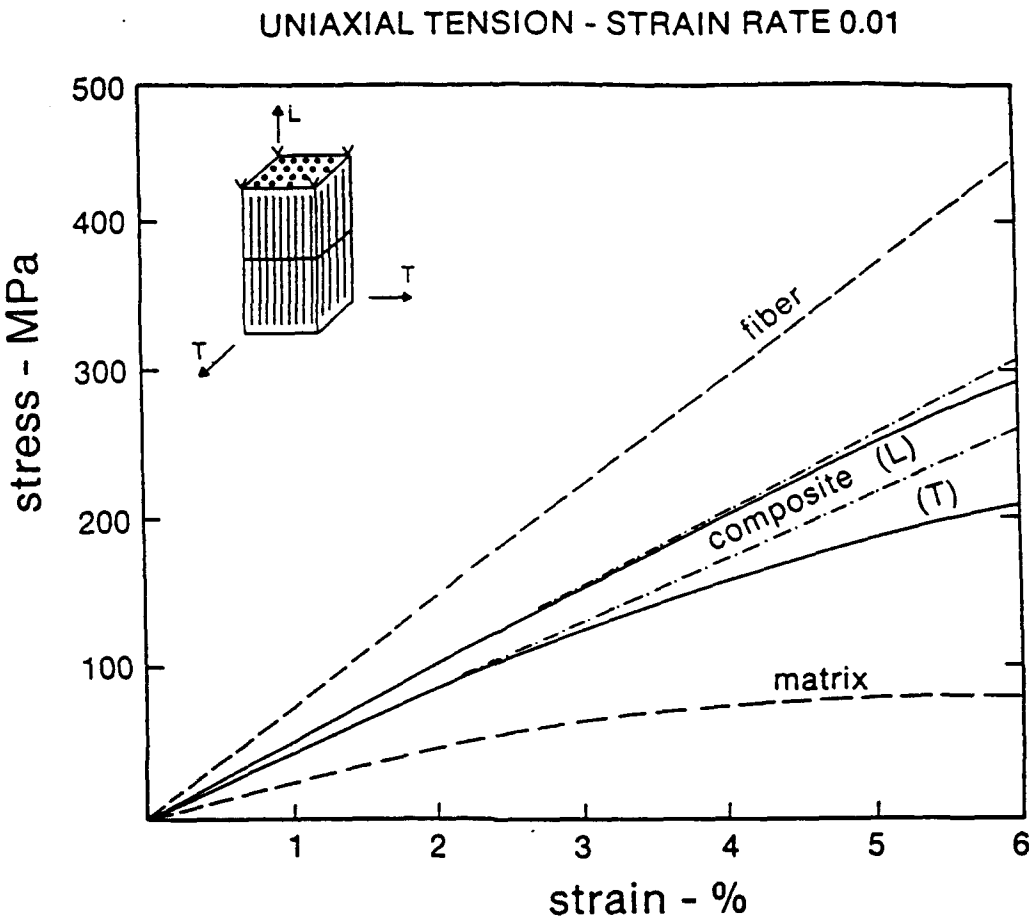

Figure 5. Longitudinal and Transverse tension of a unidirectional composite specimen

SECURITY CLASSIFICATION OF THIS PAGE

REPORT DOCUMENTATION PAGE

Form Approved OMB No. 0704-0188

1a. REPORT SECURITY CLASSIFICATION Unclassified	1b. RESTRICTIVE MARKINGS
2a. SECURITY CLASSIFICATION AUTHORITY	3. DISTRIBUTION/AVAILABILITY OF REPORT Approved for public release. Distribution unlimited.
2b. DECLASSIFICATION/DOWNGRADING SCHEDULE	
4. PERFORMING ORGANIZATION REPORT NUMBER(S)	5. MONITORING ORGANIZATION REPORT NUMBER(S)
6a. NAME OF PERFORMING ORGANIZATION Rensselaer Polytechnic Institute 6b. OFFICE SYMBOL (If applicable)	7a. NAME OF MONITORING ORGANIZATION
6c. ADDRESS (City, State, and ZIP Code) Troy, NY 12180-3590	7b. ADDRESS (City, State, and ZIP Code)
8a. NAME OF FUNDING/SPONSORING ORGANIZATION Mechanics Division Office of Naval Research 8b. OFFICE SYMBOL (If applicable)	9. PROCUREMENT INSTRUMENT IDENTIFICATION NUMBER
8c. ADDRESS (City, State, and ZIP Code) 800 North Quincy Street Arlington, Virginia 22217	10. SOURCE OF FUNDING NUMBERS PROGRAM ELEMENT NO. / PROJECT NO. / TASK NO. / WORK UNIT ACCESSION NO.

11. TITLE (Include Security Classification)
Mechanics of Composite Materials for Spacecraft (unclassified)

12. PERSONAL AUTHOR(S)
George J. Dvorak, Mark S. Shephard and Yehia A. Bahei-El-Din

13a. TYPE OF REPORT	13b. TIME COVERED	14. DATE OF REPORT (Year, Month, Day)	15. PAGE COUNT
Final	FROM 1985 TO 3/31/90	July 1992	263

16. SUPPLEMENTARY NOTATION

17. COSATI CODES			18. SUBJECT TERMS (Continue on reverse if necessary and identify by block number)
FIELD	GROUP	SUB-GROUP	Composite materials, inelastic deformation, finite element analysis

19. ABSTRACT (Continue on reverse if necessary and identify by block number)

This report presents the work performed under ONR contract number N00014–85–K–0733 during the period 1985–1990. The main objective of the project was to develop a computational facility for inelastic analysis of fibrous composite materials based on micromechanics. The theoretical work focused on development of micromechanical models for thermoplastic and thermoviscoplastic fibrous composites based on experimental observations of certain phenomena found in unreinforced and fiber reinforced metals. Implementation of the material models in computational procedures for analysis of composite materials and structures was an important part of the research. Accomplishments in these areas and in development of a layer–wise composite shell element, also performed under this contract, are described.

20. DISTRIBUTION/AVAILABILITY OF ABSTRACT	21. ABSTRACT SECURITY CLASSIFICATION
☒ UNCLASSIFIED/UNLIMITED ☐ SAME AS RPT. ☐ DTIC USERS	
22a. NAME OF RESPONSIBLE INDIVIDUAL YAPA RAJAPAKSE	22b. TELEPHONE (Include Area Code) (202) 696-4404 / 22c. OFFICE SYMBOL

DD Form 1473, JUN 86 *Previous editions are obsolete.* SECURITY CLASSIFICATION OF THIS PAGE